MECHANICS AND DYNAMICS OF MULTI-AXIS MACHINING OPERATIONS

by

ERDEM ÖZTÜRK

Submitted to the Graduate School of Engineering and Natural Sciences
in partial fulfillment of the requirements for the degree of
Doctor of Philosophy

Sabanci University

August 2010

MECHANICS AND DYNAMICS OF MULTI-AXIS MACHINING OPERATIONS

APPROVED BY:

Assoc. Prof.Dr. Erhan Budak   …………....
(Dissertation Supervisor)

Assist. Prof.Dr. Volkan Patoğlu   …………....

Assist. Prof.Dr. Mustafa Bakkal   …………....

Prof.Dr. Asıf Şabanoviç   …………....

Assist. Prof.Dr Kemal Kılıç   …….……..

DATE OF APPROVAL: …………………………..

ABSTRACT

Machining process with a single cutting tool is called multi-axis machining if more than 3-axis are involved in the operation. On the other hand, parallel machining processes where more than one cutting tool simultaneously cut a workpiece is also called multi-axis machining. 5-axis ball-end milling where a single cutting tool is employed, parallel turning and parallel milling processes with two cutting tools are in the scope of the thesis. Moreover, face-milling process with inserted tools is also modeled.

5-axis ball-end milling operations are common in several industries such as aerospace, automotive and die/mold for machining of complex sculptured surfaces. Additional two degree of freedoms, namely, lead and tilt angles make it possible to machine complex parts by providing extra flexibility in cutting tool orientation. However, they also complicate the geometry of the process. In these operations, productivity, dimensional tolerance integrity and surface quality are of utmost importance. Part and tool deflections under high cutting forces may result in unacceptable part quality, whereas using conservative cutting parameters results in decreased material removal rate. Process models can be used to determine the proper or optimal milling parameters for required quality with higher productivity. The majority of the existing milling models are for 3-axis operations, even the ones for ball-end mills. In the thesis, geometry, force and stability models are presented for 5-axis ball-end milling operations. The effect of lead and tilt angles on the process geometry, cutter and workpiece engagement limits, scallop height, and milling forces are analyzed in detail. In addition, tool deflections/form errors and stability limits are also formulated for 5-axis ball-end milling. The use of the model for selection of the process parameters such as lead and tilt angles which result in minimum cutting forces or maximum stability limits are demonstrated. The model predictions for cutting forces, form error and stability limits are compared and verified by experimental results.

Parallel machining operations are advantageous in terms of productivity since there are more than one cutting tools in operation. Due to the increased number of cutting tools, they have the potential for considerable increase in productivity as a result of higher material removal rate (MRR). However, the dynamic interaction between these parallel tools may create additional stability problems and the advantage of parallel machining may not be utilized to full extent. For that reason, dynamics and

stability of parallel machining processes need to be modeled. In the thesis, dynamics of parallel turning and parallel milling operations where two cutting tools cut a common workpiece are modeled. The predicted stability limits for parallel turning are also compared with experimental results where good agreement is demonstrated.

Die manufacturing is a very critical part of the overall production chain in many industries. Depending on shape and size of a die, machining time can be very time consuming. Furthermore, since usually one die is manufactured, the chance for testing is very limited. Machining processes in die manufacturing can be limited by many factors. Process models can be used in order to select process conditions which will yield the required quality in the shortest possible time. In this study, force and chatter models are developed for face milling processes with inserted cutters. Using the developed models, process parameters are modified and their effects on productivity are demonstrated.

ÖZET

Tek kesici takım kullanılan talaşlı imalat süreçlerinde 3 eksenden fazla eksen bulunması durumunda, bu süreçler çok eksenli talaşlı imalat olarak adlandırılırlar. Diğer yandan, paralel talaşlı imalat süreçlerinde olduğu gibi birden fazla kesme takımının eş zamanlı parça kesmesi de çok eksenli talaşlı imalat olarak tanımlanır.. Tek kesici takım kullanılan 5-eksenli küresel uçlu frezeleme, iki kesici takımlı paralel tornalama ve paralel frezeleme işlemleri bu tezin kapsamı dahilindedir. Ayrıca, bu tezde takma uçlu yüzeysel frezeleme süreci de modellenmiştir.

5-eksenli küresel uçlu frezeleme süreci havacılık, otomotiv ve kalıpçılık gibi sektörlerde karmaşık şekilli yüzeylerin üretiminde sıklıkla kullanılır. 3 eksen frezelemeye ek olarak gelen eğilme ve yatma açıları kesme takımı pozisyonlamasında ekstra serbestlik kazandırarak karmaşık parçaların işlenmesine olanak sağlar. Diğer yandan ise bu açılar süreç geometrisini karmaşıklaştırırlar. Bu tarz süreçlerde verimlilik, boyutsal toleranslar ve yüzey kalitesi büyük öneme sahiptir. Yüksek kesme kuvvetlerinde oluşan parça ve takım esnemeleri kabul edilemez parça kalitesine, oldukça güvenli seçilen süreç parametreleri de düşük anlık talaş kaldırma hızına sebep olmaktadır. Süreç modelleri en iyi frezeleme parametrelerini belirlemek için kullanılabilir. Bu sayede yüksek verimlilik ile gerekli kalite aynı anda sağlanabilir. Genelde var olan frezeleme modelleri küresel uçlu frezeleme süreçleri de dâhil olmak üzere 3-eksenli işlemleri kapsamaktadır. Bu tezde 5-eksenli küresel uçlu frezeleme süreçleri için geometri, kuvvet ve kararlılık modelleri sunulmaktadır. Eğilme ve yatma açılarının işlem geometrisi, kesici ve iş parçası kesişim limitleri, yüzey kalitesi ve kesme kuvvetleri üzerine etkisi detaylı olarak incelenmiştir. Ayrıca, 5-eksen küresel uçlu frezeleme operasyonu için takım esnemeleri/şekil hataları ve kararlılık limitleri hesaplanmıştır. Minimum kesme kuvvetleri veya maksimum kararlılık limitlerine sebep olan eğilme ve yatma açıları seçimi için sunulan modelin nasıl kullanılacağı gösterilmiştir. Kesme kuvvetleri, şekil hataları ve kararlılık limitleri için model kullanılarak tahmin edilen değerler deneylerle karşılaştırılmış ve deney sonuçlarıyla doğrulanmıştır.

Paralel talaşlı imalat operasyonları birden fazla kesme takım içermeleri nedeniyle verimlilik açısından avantajlıdır. Artan sayıdaki kesme takımına bağlı olarak, artan talaş kaldırma hızı verimlilik artışına sebep olur. Ancak paralel kesici takımların arasında oluşan dinamik etkileşim kararlılık problemlerine sebep olabilir ve böylece paralel

süreçlerin sunduğu avantajlardan tam olarak fayda sağlanamayabilir. Bu nedenle, paralel talaşlı imalat süreçlerinin için dinamiği ve kararlılığın modellenmesi gerekmektedir. Bu tezde, iki kesme takımının ortak bir iş parçasını kestiği, paralel tornalama ve frezeleme süreçlerinin dinamiği modellenmiştir. Paralel tornalama için hesaplanan kararlılık limitleri deney sonuçlarıyla karşılaştırılmıştır ve hesaplanan değerler ile deney sonuçlarının yakın olduğu gösterilmiştir.

Birçok sanayide kalıp imalatı genel üretim zincirinin en kritik kısmıdır. Kalıbın şekline ve büyüklüğüne bağlı olarak talaşlı imalat süresi uzun zaman alabilir. Bununla beraber, her seferde tek bir kalıp üretildiği için kalıp üretimini test etme şansı çok sınırlıdır. Kalıp üretiminde, talaşlı imalat süreçleri birçok etken tarafından sınırlandırılmıştır. Süreç modelleri en kısa zamanda gerekli kaliteyi sağlayacak süreç parametrelerini seçmek için kullanılabilir. Bu çalışmada takma uçlu takımlar ile yüzey frezeleme süreçleri için kuvvet ve kararlılık modelleri geliştirilmiştir. Geliştirilen modelleri kullanarak, süreç parametreleri ayarlanmış ve seçilen parametrelerin verimliliğe etkileri gösterilmiştir.

Anahtar Kelimeler: 5-eksen küresel uçlu frezeleme, kesme kuvvetleri, kararlılık, tırlama titreşimleri, paralel talaşlı imalat, takma uçlu takımlar ile yüzey frezeleme.

TABLE OF CONTENTS

LIST OF FIGURES

LIST OF TABLES

1. INTRODUCTION

Machining is a material removal process from bulk material. The final shapes of the most of the mechanical parts are obtained by machining operations [1]. The bulk material to be processed is defined as workpiece and the tool that removes material from the workpiece is named as cutting tool. The machining processes are categorized depending on the type of the cutting tool and the type of relative motion between the tool and workpiece. The most common machining operations are turning, milling, drilling, boring, broaching and grinding.

Multi-axis machining term defines the machining processes where more than one translational or rotational axis is involved in the process. Multi-axis machining can be grouped into two main categories depending on how many cutting tools are used in the process. In the first group, only one cutting tool is used in the process. Multi-axis term is mainly used in milling and grinding operations when there is more than 3-axis is involved since the standard process in these operations includes three translational axes. 4- or 5-axis milling and grinding are the example machining processes in this group.

In the second group, more than one cutting tools are employed in the process. These operations are also named as parallel (simultaneous) machining processes. Parallel turning and parallel milling processes are the example processes in this category.

Performances of machining processes are evaluated according to the productivity and quality of them. Certain phenomena such as cutting forces, tool and workpiece deflections and chatter vibrations play a major role on hindering the productivity and quality of a process. For example, cutting forces may result in tool and workpiece deflections which may cause dimensions out of tolerances. In case of higher cutting forces, even tool breakages can occur. Furthermore, chatter vibrations deteriorate the resulting surface quality by leaving chatter marks on the surface.

Cutting forces and form errors are subject of process mechanics while chatter vibrations are related to the dynamics of the processes. Understanding of mechanics and dynamics of processes helps to develop process models that can predict cutting forces, form errors and chatter vibrations before actual machining. As a result, undesirable outcomes in terms of productivity and quality can be eliminated using process models.

In this thesis, the first process of interest is the 5-axis ball-end milling process which includes two additional rotational degrees of freedom to the three linear axes that is standard in 3-axis milling. It's a multi-axis machining operation where only one cutting tool is used. Then, the contributions in dynamics of parallel machining operations where two cutting tools simultaneously cut a common workpiece are presented. Finally, mechanics and dynamics of the face milling processes where inserted tools with different insert geometries are employed are modeled.

1.1. 5-axis Ball-end Milling Processes

5-axis ball-end milling is mainly used in machining of complex surfaces such as turbine blades and compressors as shown in Figure 1.1(a). Lead and tilt angles (Figure 1.2) which are two additional parameters with respect to three axis milling make it possible to machine complex surfaces by providing increased flexibility in cutting tool orientation. 5-axis milling technology is well established. Application of lead and tilt angles is possible by addition of two rotational axes on the machine tools which have different kinematic designs. Rotational axes can be on the tool side, on the workpiece side or combination of both depending on the machine tool. Lead and tilt angle should not be confused with rotational angles of the axes. Rotational angles on the rotational axes which results in the desired combination of lead and tilt angles depend on the kinematics of the machine tool. In addition, there is several powerful CAM software with 5-axis milling solutions. Some of the widely used ones are NX CAM, CATIA Machining, hyperMILL and ESPRIT CAM ([2]-[5]). However, they consider only the geometry of the process; they process CAD data, take the process parameters selected by the process planner as input, and generate tool path for the process that results in the required final shape. They do not include the physics of the process in tool path generation. Hence, the process planner has no information about the cutting forces, form errors and chatter vibrations which have considerable effects on the productivity and quality of the process. He can only use his previous experience while selecting the process parameters to generate the tool path.

Work flow that is generally followed to produce a part with 5-axis milling is presented in Figure 1.3(a). Firstly CAD model of the workpiece is prepared, and then process planner generates the tool path by selecting a machining strategy, cutting tools and associated process parameters in CAM. CL file, which contains all the required tool path information, is obtained as output of the CAM part. Using a post processor

program, the CL file is converted into the G code (part program) which is specific to the machine tool that will be used, and finally the G code is uploaded to the machine tool. Up to this point, physics of the process is not considered. Physics come into the picture when the machine tool starts cutting the work material according to the uploaded G code. During the process, torque/power limits of spindle may be reached; high cutting forces, high form errors and chatter vibrations may arise depending on the selected process parameters. In such a case, the CAM program is modified, and then with the modified G code the process is re-run on the machine tool. Since this workflow includes iterations both on the software side (CAM) and on the hardware side (machine tool), this is not a preferable work flow. Instead, it is proposed to add process models into the workflow as presented in Figure 1.3(b), and thus eliminate the iterations on the hardware side by predicting the problems and taking necessary precautions on the software side using process models.
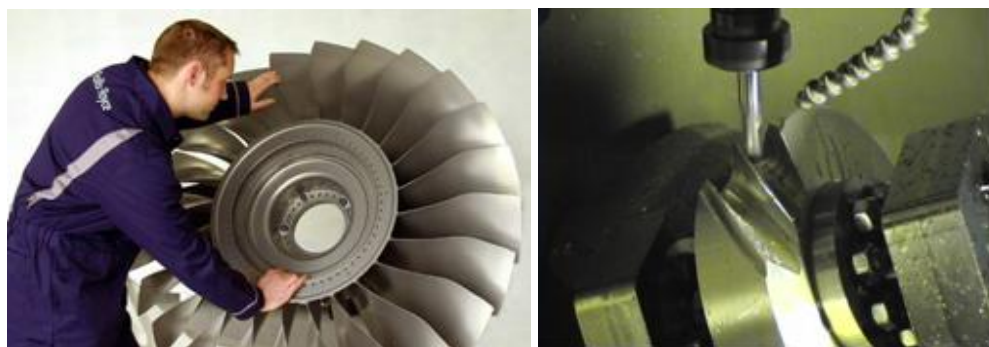
(a)   (b)

Figure 1.1: (a) A compressor manufactured for the Joint Strike Fighter (JSF) project(Source: http://www.lockheedmartin.co.uk) (b) An example 5-axis ball-end milling process
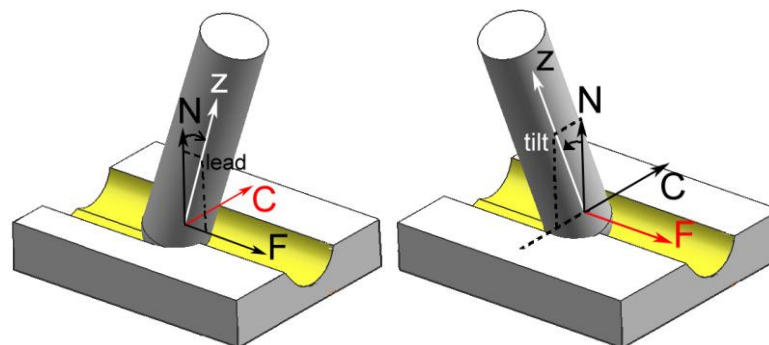
Figure 1.2: Lead and tilt angles.

3

Process models work in two ways (Figure 1.3(b)). Firstly, the process models provide input to the CAM part. In this case, they help process planner select process parameters while designing a new process. The process planner can see the effect of process parameters on cutting forces, form errors and chatter vibrations and select them accordingly. Secondly, process models may take a CL file obtained for a given process as input and the given tool path is simulated to see if there are any problematic regions in terms of cutting forces, form errors and chatter vibrations along the tool path. If so, modifications on the tool path can be performed in CAM. Reading of CL files and calculating process parameters from CL files have been performed by another parallel work which is performed by Tunc and Budak [6].

CAD → CAM → CL file → Post processor → G code → Machine tool → Product

Problems
- Torque/power limits
- High form errors, tool breakage
- Chatter vibrations

(a)

CAD → CAM → CL file → Post processor → G code → Machine tool → Product

Process Models
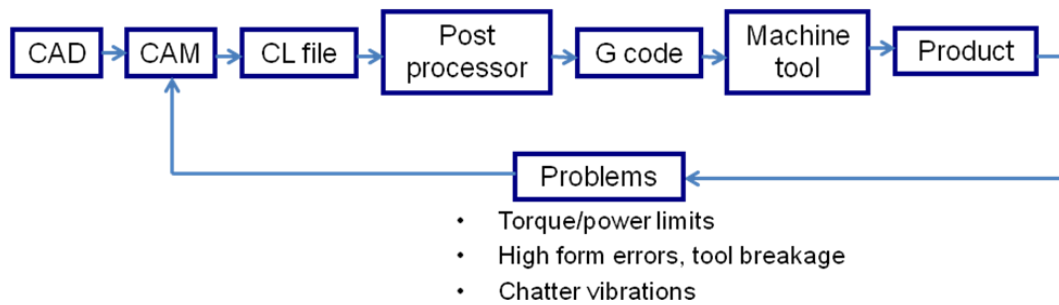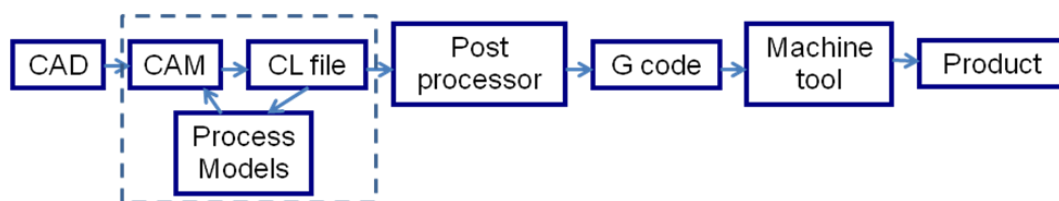
(b)

Figure 1.3: (a) General work flow (b) Proposed work flow to produce a part in 5-axis milling

Lead and tilt angles increase the flexibility of the tool orientation but they also complicate the process geometry. They change the engagement region between the cutting tool and workpiece. The determination of this engagement region is important since it affects the mechanics and dynamics of the process. Hence, process models need the engagement region information.

Using process geometry knowledge, an engagement model is developed for calculation of engagement regions. In the master thesis work [7], an engagement model had been developed but it was only able to determine the engagement region when ball-

part of the tool is in cut with the workpiece. The new engagement model is able to take care of engagement regions on both ball and cylinder part of the ball-end mill. Scallop height and material removal rate (MRR) which are measures of productivity and surface quality, respectively, are also formulated. With this formulation, different processes can be compared in terms of MRR and heights of scallops left on the resulting surface.

Cutting forces on a 5-axis ball-end milling process may result in form errors out of tolerances and tool breakages. It is critical to be able to calculate cutting forces and tool deflections which result in form errors. Using the calculated engagement regions and applying the cutting mechanics equations on the engagement region, cutting forces are calculated. After cutting forces are predicted, these forces are applied on to the structural model of the cutting tools and workpiece. Deflections of cutting tool and workpiece are calculated. Finally, form error which is defined as the summation of tool and workpiece deflections in the surface normal direction of the resulting surface is predicted.

An unfavorable cutting condition exists in 5-axis ball-end milling when tip of the ball-end mill is in contact with the workpiece. Due to the ball-end mill geometry, the cutting speed at the tool tip is zero. Hence, the phenomenon at the tool tip cannot be explained by cutting mechanics. It is more like a ploughing/indentation process which results in additional ploughing/indentation forces and decreases the final surface quality by leaving tool tip marks on the surface. A procedure to be followed was developed in order to avoid this undesirable condition.

Being one of the most important problems in machining, chatter vibrations must be avoided as they result in high cutting forces, poor surface finish and unacceptable part quality. Using stability diagrams is an effective method to predict chatter free cutting conditions. Although, there have been numerous works in milling dynamics, the stability of 5-axis ball-end milling has not been studied in detail. In this thesis, stability of the 5-axis ball-end milling is analyzed using analytical (frequency domain), numerical (time domain) and experimental methods. Firstly, a single-frequency method is used to generate stability diagrams, and then the multi-frequency dynamics of the process and its stability are considered. The analytical model presented considers 3D dynamics of the 5-axis ball-end milling process including effects of all important process parameters such as lead and tilt angles. Due to the complex geometry and mechanics of the process, the resulting analytical equations are solved with an iterative procedure in order to generate the stability diagrams. The predicted stability diagrams

are compared with experiments. Using the model and experimental results, the effects of lead and tilt angles on stability diagrams are shown. The presented model can be used in analysis of 5-axis milling stability as well as selection of milling conditions for increased stability.

Due to the time varying nature of the milling dynamics, a multi frequency response may be present resulting in flip bifurcation especially for cases with small radial depth of cut causing stronger variation in directional coefficients which has been demonstrated for standard milling applications. These frequencies are seen in the system response in the form of addition and subtraction of the chatter frequency and harmonics of the tooth passing frequency. In the thesis, the multi-frequency effects in 5-axis milling are analyzed using analytical (frequency domain), numerical (time domain) and experimental methods. Unlike other standard milling cases, it is observed that adding multi-frequency effects in the solution has marginal influence on the stability diagrams for 5-axis ball-end milling operations, even for cases with low radial depth. This is due to the effects of complex 5-axis ball-end milling geometry on the engagement region between the tool and workpiece, thus on the directional coefficients. The predicted stability diagrams are compared with cutting tests and an acceptable agreement is observed.

1.2. Parallel Machining Processes

The use of parallel machining processes is increasing in various industries due to several advantages of these machine tools. Parallel machining processes are the processes where more than one cutting tools cut a common workpiece. Due to the higher number of cutting tools, these processes have potential for increased productivity. However, dynamic interactions among the cutting tools may result in additional stability problems and the advantage of using parallel processes may be compromised. In the thesis, dynamics of parallel turning and parallel milling operations with two cutting tools are modeled.

There are two different scenarios in parallel turning operations. In the first case, two turning tools are clamped on a specially designed tool holder on a standard turning centre as shown in Figure 1.4(a). The movements of the tools are dependent on each other since they are on the same turret; but they cut different surfaces on the workpiece. In the second case, two turning tools are clamped on different tool holders on different turrets on a parallel machining centre as presented in Figure 1.4(b). Although the turrets

can move independently, they cut the same surface on the workpiece. The stability formulation of each case in time and frequency domain is presented separately. The predicted stability diagrams are compared by experimental cuts and the predictions agree with the experimental results.
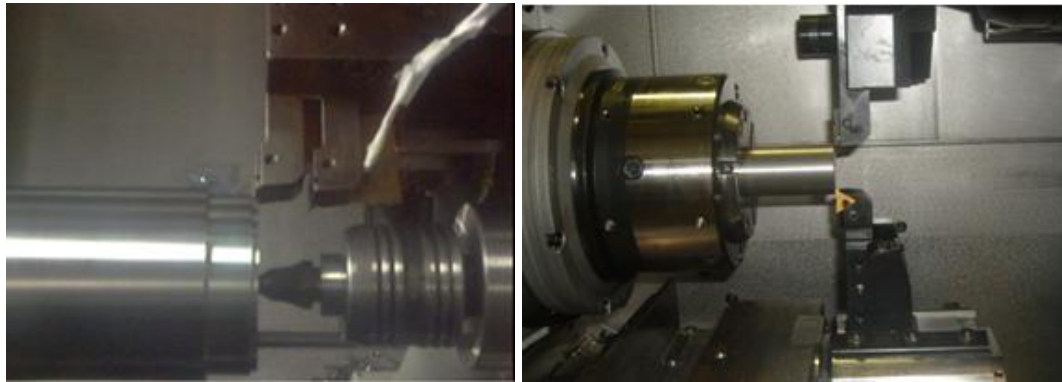
<table>
<tr><td>(a)</td><td>(b)</td></tr>
</table>

Figure 1.4: Parallel turning cases (a) two turning tools on the same turret (b) two turning tools on different turrets

The milling tools are generally on independent turrets in parallel milling machine tools. Direct dynamic coupling between two milling tools on such machines is weak since they are located on different turrets. However, there can be a strong dynamic coupling in case of milling a flexible workpiece. In this case, the vibrations caused by one of the tools may have regenerative effects on the other one. In order to address this problem, a stability model that works in time domain has been developed. The model is capable of simulating cases where two flexible milling tools are cutting a flexible workpiece. Several example cases are simulated with the model and results are presented.
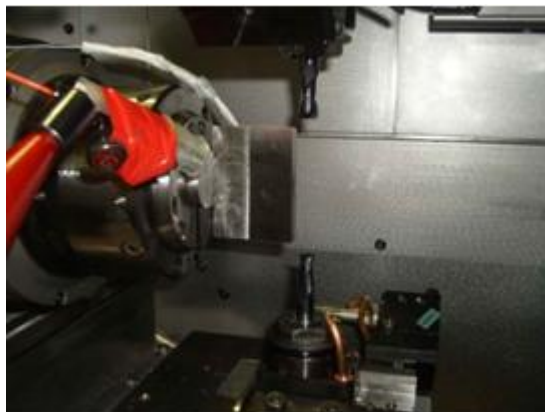
Figure 1.5: Parallel milling process

7

1.3.   Face-Milling Processes with Inserted Tools

Inserted face milling tools (Figure 1.6) are widely used in many machining applications including die machining since they are economically advantageous. Die machining applications can be time consuming depending on size of dies. On the other hand, process problems such as high cutting forces and chatter vibrations may cause low productivity and quality issues. Trial productions can be used to overcome these problems. However, the chance for trial testing is limited in die machining since usually only one die is manufactured each time. Alternatively process models can be employed in order to select process conditions yielding the required quality in the shortest possible time. In the thesis, cutting edges of face milling tools with several different inserts, which are used in an automotive die shop, are modeled. Orientation angles on the inserts are also included in the model so that cutting edges can be defined mathematically in a fixed tool coordinate system. Force and chatter models are developed to predict cutting forces and stability diagrams. After these models are verified experimentally, they are used to modify process parameters and the improvements on productivity are demonstrated.

Figure 1.6: Face milling tools (Source: http://www.lmtfettetools.com)

1.4.   Objective

High cutting forces, form errors that are out of the tolerances and chatter vibrations that decrease the surface quality are among the most important problems in machining processes. Right selection of process parameters is very critical to avoid these problems. In industry, the process parameters are usually selected by trial and error. Since the iterations in the trial and error phase occupy rather expensive equipment availability, this is not a very desirable approach.

The main motivation behind this thesis is to help the industry manufacture a product right at the first time while satisfying the productivity and quality requirements. With this motivation in mind, the process models that model the mechanics and dynamics of multi-axis machining operations are developed. Using process models, the potential problems can be predicted before actually machining a product. They can predict the effect of process parameters on the cutting forces, form errors and chatter vibrations. The process planner selects the process parameters according to the prediction of the process models in the software environment by avoiding iterations on the real set-up. Hence, the potential problems can be eliminated before machining which saves considerable time and cost.

1.5. Layout of the Thesis

Henceforth, the thesis is organized as follows:

A review of related literature is presented in the next chapter. In Chapter 3, process geometry and mechanics of the 5-axis ball-end milling are explained. Chapter 4 includes the formulation of 5-axis ball-end milling dynamics and explanation of the developed stability models. In Chapter 5, the effect of lead and tilt angles on process geometry, mechanics and dynamics are presented. Chapter 6 deals with dynamics of parallel turning formulation. Stability models in frequency and time domain models are presented for parallel turning. In Chapter 7, a time domain model to simulate the dynamics of parallel milling is presented. Mechanics and dynamics of face milling process with different insert geometries are modeled in Chapter 8. Conclusions are presented and future research directions are suggested in Chapter 9. In the Appendix, the measurement procedure to determine the center coordinates of the rotary axes on a 5-axis machining center is presented.

2. LITERATURE SURVEY

The literature related to the thesis is presented under several headlines. Firstly, the previous works about modeling of 5-axis ball-end milling are presented. Then, the literature about dynamics of parallel machining is introduced. Finally, the previous works about modeling of face-milling processes with inserted tools are explained.

2.1. 5-axis ball-end milling

5-axis milling technology has been possible by previous works in several different areas. One of the challenges with 5-axis milling was generation of tool paths that result in the final required shape once the geometry of the raw material is given. [7]-[12] are some of the notable works about tool path generation in 5-axis milling. After the tool paths are calculated, they should be transformed to the multi-axis machine tools. At this point, the studies about forward and inverse kinematics of multi-axis machine tools [12]-[18] have been valuable. Furthermore, several researchers such as [19]-[24] investigated the multi-axis control strategies of the feed drives help to obtain the required motion by the machine tool with minimum contouring error.

In the thesis, the concentration is on the mechanics and dynamics of the process of 5-axis ball-end milling. However, process geometry affects both mechanics and dynamics of the process. For that reason, before going into the details about the mechanics or dynamics the process geometry needs to be understood well. Literature about 5-axis ball-end milling geometry is introduced firstly. Then the related literature about mechanics and dynamics of the 5-axis ball-end milling is presented, respectively.

2.1.1. Geometry

5-axis ball-end milling is a geometrically complex process since there are two additional rotational degrees of freedom, namely lead and tilt angles, compared to 3-axis milling. They define the cutting tool orientation with respect to surface normal direction. Visualization of their effect on the process geometry is not straightforward; however, the understanding of the process geometry is a very important step in process modeling.

There have been considerable amount of work done on modeling of sculptured surface geometry in 3-axis ball-end milling. Although rotational degrees of freedoms are not available in 3-axis ball-end milling, there may be inclination in both feed and

cross-feed directions due to CNC interpolations on the sculptured surface. Geometry of these processes is similar to the 5-axis ball-end milling geometry. Imani et al. [25] presented machining cases with up-hill angle in 3-axis ball-end milling which corresponds to application of positive lead angle in 5-axis ball-end milling. For different up-hill angles they showed the calculated engagement boundaries which are determined using the ACIS geometric engine [26]. Later, Kim et al. [27] included the effect of tilt angle on the engagement region. In their notation, ramping corresponds to application of lead angle while contouring matches with the application of tilt angle. Combined effect of lead and tilt angle on the engagement region on the ball-part of the tool was shown by Lamikiz et al. [28] by cutting an inclined plane with a sloped feed direction in a 3-axis milling machine tool. Later, Fontaine et al. [29] applied the same notation with Kim et al. [27] for different machining strategies but added the effect of cross-feed direction where they refer to it as up/down milling. Lately, Ozturk and Budak [30] presented the combined and independent effects of lead and tilt angles on engagement regions between the tool and workpiece using CAD models and an engagement model [31].

The engagement model is presented in Chapter 3 and the effect of the lead and tilt and angles are presented in Chapter 5.

2.1.2. Mechanics

There have been numerous efforts for modeling the mechanics of the ball-end milling processes. These can be grouped into three categories according to how material data is obtained, varying from completely analytical [1],[32] to completely experimental [33]-[35]. One analytical approach is to use the flow stress and thermal properties of the workpiece material to predict cutting forces in 3-axis ball-end milling [1]. Similarly, in the so-called thermo-mechanical modeling, the cutting behavior of work material is described by a model such as the Johnson–Cook law which considers thermal and strain rate effects on the flow stress. This is the approach used by Fontaine et al. [32] to predict cutting forces in 3-axis ball-end milling. Mechanistic modeling is an experimental approach where the cutting force coefficients are calibrated for a given milling tool and workpiece pair at different axial depth of cuts. Gradisek et al. [33] , Lazoglu [34], Ozturk et al. [35] are some of the authors who employed mechanistic method to predict ball-end milling forces in 3-axis milling. Budak et al. [36] presented a hybrid method named as *mechanics of milling* for milling force modeling based on the

orthogonal cutting data and the oblique cutting model. The *mechanics of milling* approach was employed by several authors in 3-axis ball-end milling [37]-[42].

Although there have been several works on the modeling of 3-axis ball-end milling processes, these have been very limited for 5-axis ball-end milling operations. Due to the lead and tilt angles, the determination of the engagement boundaries is more complicated in 5-axis milling, and has been mainly done using non-analytical methods. Larue and Altintas [43] used ACIS solid modeling environment to determine engagement between the milling tool and the workpiece for flank milling. Clayton et al. [44] proposed a mechanistic force model for 5-axis ball-end milling using a discretized cutting edge model to determine the engagement zone. In another mechanistic 5-axis model, Zhu et al. [45] modeled the cutting edge profile, and determined the engaged cut geometry by classification of the cutting point positions with respect to the workpiece surface. Later, Fussell et al. [46] used discrete geometric models of the tool and workpiece to determine the contact area, and simulated 5-axis ball-end milling forces mechanistically.

There are only a few studies about calculation of tool deflections and form errors in the literature. Kim et al. [47] predicted the cutting forces in 3-axis ball-end milling by using Z-mapping, and estimated the form errors by modeling the milling tool as a cantilever beam. In another study, Lopez de Lacalle et al. [48] determined preferable local machining directions and tool orientation in finishing operations with respect to tool deflections In the previous works on 5-axis ball-end milling, the effects of lead and tilt angle on the process geometry and mechanics, and the surface finish have not been shown explicitly.

In Chapter 3, the cutting forces in 5-axis ball-end milling are modeled by using the *mechanics of milling* approach. This method needs orthogonal cutting data for a given work material. However, once this data is obtained, it can be applied to different machining processes and cutting tools, unlike mechanistic approach where the force coefficients have to be calibrated for each material and milling tool pair. This is especially critical for ball-end mills where cutting speed continuously varies along the cutting edges which is why the calibration tests are repeated for different axial depth of cut values in the mechanistic models [33]-[35]. The milling forces in different modes of 5-axis ball-end milling are investigated and model predictions are verified. After the cutting forces are predicted, tool deflections can be determined as well. For this, the

predicted cutting forces are applied on the tool structure which is modeled as a beam, and the tool deflections in 5-axis ball-end milling are calculated.

2.1.3. Dynamics

Analysis of chatter in metal cutting and modeling of stability limits started about half a century ago [51]. The initial work was mostly done on the stability of orthogonal cutting and turning processes resulting in discovery of stability limits by Tobias and Fiswick [51] and Tlusty and Polacek [52]. The stability of milling differs from the classical orthogonal chatter stability due to several reasons. The rotating tool and multiple cutting edges in milling result in a time-varying dynamic system. Minis et al. [53] solved two-dimensional dynamic milling problem iteratively, using Nyquist stability criterion. Later, Budak and Altintas [54] proposed single-frequency and multi-frequency methods for the stability analysis of milling. In the single-frequency method, the chatter stability diagrams were obtained analytically without any iteration by using only the average term in the Fourier series expansions of the time varying coefficients [55]. In the multi-frequency method, on the other hand, the higher order terms in the Fourier series expansions are included in the solution [54]. In 3-axis flat-end milling, Budak and Altintas [54], [56] showed that stability diagrams calculated by single-frequency and multi-frequency solutions are very close for high radial depth of cut values. The multi-frequency response may be present especially for cases with small radial depth of cut causing stronger variation in directional coefficients. Davies et al. [57] showed that the number of the stability lobes doubled when the time ratio of cutting to non-cutting decreases, i.e. the radial immersion of the tool decreases. Later on, Bayly et al. [58] used time temporal finite element analysis while Insperger and Stepan [59] employed semi-discretization method to model the stability of low immersion milling. Both of these studies verified the stability lobes presented by Davies et al.[57]. Gradisek et al. [60] evaluated the single-frequency method of Budak and Altintas [54],[56] and the semi-discretization method of Insperger and Stepan [59]. They concluded that prediction of these two methods diverges as the radial immersion decreases. However, Merdol and Altintas [61] applied the multi-frequency method [54] to low immersion milling cases, and demonstrated that it can predict the added stability lobes accurately.

The single-frequency method was later applied to the stability analysis of 3-axis ball-end milling by Altintas et al. [62]. The stability limits were determined by solution

of a quadratic equation since the dynamics in two dimensions were considered. Altintas [63] extended this model to three dimensional stability analysis by adding the dynamics in the tool axis direction. Unlike orthogonal cutting and standard milling processes, the literature on the stability of 5 axis milling is very limited. Khachan and Ismail [64] applied time-domain approach to multi-axis milling, but presented results for 3-axis milling tests only. Shamoto and Akazawa [65] modeled the effects of lead and tilt angles on stability limits using a frequency domain model; however they only showed the effect of the tilt angle.

Running time domain simulations is an alternative way of obtaining stability diagrams. In the literature, there are several studies [66]-[69] that use time-domain simulations for the stability of 3-axis flat-end milling operations. The advantage of time domain simulations is that nonlinearities such as loss of tool-material contact can be taken into account. However, obtaining a stability diagrams this way is computationally expensive.

The stability models presented in Chapter 4 extends the three dimensional chatter stability model [63] to 5 axis ball-end milling by adding the effects of lead and tilt angles on the process. Both the single-frequency and multi-frequency methods are employed. Moreover, a time domain model that simulates the 5 axis ball-end milling process at discrete time intervals is developed. The work is also presented in a journal article [70].

2.2. Dynamics of Parallel Machining

The stability of single tool turning processes has been studied in detail by many researchers. Tobias and Fishwick [51], and Tlusty and Polacek [52] demonstrated regenerative effect between dynamic cutting forces and dynamic displacements which results in chatter vibrations. Moreover, they predicted the stability limits in order to eliminate these vibrations. Later, Tlusty and Ismail [71] performed time domain simulations and acquired more accurate results for stability limits. Moufki et. al [72] applied thermo-mechanical model of cutting to the one dimensional stability formulation. Chen et al. [73] and Vela-Martinez, et al. [74] added the workpiece dynamics in the stability formulations. Rao et al. [75] extended the stability formulation to 3D for three-dimensional oblique turning operations. They included the cross-coupling between radial and axial vibrations in the force model. Similarly, Ozlu and Budak [76] formulated the stability considering the displacements of tool and workpiece

in radial and axial directions. Moreover, they showed the effect of nose radius on the stability limits. In another study, Ozlu and Budak [77] showed that when inclination angle or nose radius exists on the tool, multi-dimensional solution is needed since the one dimensional stability formulation [52] fails to represent the dynamics of the process accurately.

Although there are substantial amount of work done on chatter stability for standard turning operations, there are only a few studies on parallel turning process stability. Lazoglu et. al [78] formulated a parallel turning process in time domain where each tool cuts a different surface. There is no direct interaction between the tools in the presented case; the dynamic coupling between the tools occurs through the flexible workpiece. By simulations, they showed that parallel working tools decrease the stability limits of each other. Later, Ozdoganlar and Endres [79] developed a parallel turning process on a modified vertical milling machine where they cut different surfaces. Dynamic interaction between the tools is achieved using an angle plate and the workpiece is rigid. The analytical solution provided is valid for symmetric systems. They validated the developed formulation through experimental results.

There has been considerable number of works in 3-axis milling stability formulation. Minis, et al. [53] solved the 2-dof milling stability in an iterative manner. Later, Budak and Altintas [54] formulated the milling stability analytically and developed single and multi-frequency methods to obtain stability diagrams. Added lobe phenomenon which is seen in low radial immersion conditions has been presented by several authors (Davies et al., [57], Bayly, et al.[58], Insperger, et al. [59], Gradisek, et al. [60], Merdol and Altintas, [61]). Campomanes and Altintas [68] and Sims [69] are among the authors who developed time-domain models to simulate milling process dynamics. The most notable advantage of time-domain models is that nonlinearities such as loss of tool-material contact can be taken into consideration. Generating stability diagrams using time-domain models, on the other hand, is computationally expensive.

There are only very few works on dynamics of parallel milling operations. Olgac and Sipahi [80] developed an analytical method for prediction of stability diagrams for simultaneous machining. They basically determine the stability limits by analyzing the characteristic roots of the system. Shamoto et al. [81] presented a parallel milling

method to suppress chatter vibrations in face milling flexible plates. They eliminated regenerative effects by rotating the two spindles at different speeds.

In Chapter 6, the parallel turning processes are classified as the processes where cutting tools are on the same turret and processes where cutting tools are on different turrets. Dynamics of the both cases is modeled in both frequency and time domain. Advantage of parallel turning over single tool turning is presented although previous literature shows the negative effect of the tools on each other. Moreover, a time-domain model is presented in Chapter 7 in order to model the dynamics of parallel milling. Effects of up milling, down milling and lag angle between the milling tools are shown. These studies about parallel turning and milling are also presented in articles [82] and [83], respectively.

2.3. Force and Stability Models for Inserted Face-Milling Tools

There has been considerable research on cutting force and stability predictions in milling. In die machining, generally cutting tools with inserts are used. However, only a few of the models considered modeling of cutting tools with inserts. Altintas and Lee [84] predicted forces and stability diagrams for helical end mills. Elbestawi et al. [85] showed the effect of process parameters in high speed die machining experimentally. Later, Li et al. [86] developed a force model for calculation of forces in face milling with inserted cutters. They included dynamics of the structure and run out in force calculations. For inserted cutting tools, the orientations of cutting inserts with respect to the tool body complicate the definition of cutting edge geometry. Until the work of Engin and Altintas [87], these orientation angles had not been taken into account. Engin and Altintas [87] proposed a general model for modeling of the mechanics and dynamics of the inserted cutters and verified them experimentally. They presented experimental results only for rectangular inserts. Kim et al. [88] modeled cutting forces for cutting tools with rectangular and circular inserts. They verified their model experimentally for both rectangular and circular inserts. They also employed feed rate scheduling to keep cutting forces around a predefined value during the process. Lopez de Lacalle et al. [89] developed force and deflection models and used them in die machining. Considering hardness variations in workpiece and calculated tools deflections, they modified the process parameters, and demonstrated benefits of the model for die industry. Afterwards, Campa et al. [90] modeled the dynamics of bull-nose end mills and verified the predicted stability diagrams experimentally.

In Chapter 8, mathematical models of cutting edges on the inserts are formulated which is needed in force and stability models. Cutting edges are represented mathematically using rotation angles. It should be noted that these rotation angles are usually not equal to the angles on the inserts. They should be calculated using the angles on the cutting edges. Then, cutting force and stability models are presented. Finally, applications of the models to the machining of dies are demonstrated. The result of this work is also presented in an article [91].

3. GEOMETRY AND MECHANICS OF 5-AXIS BALL-END MILLING

This chapter is organized as follows: The geometry of ball-end mill is explained in the next section. Coordinate systems used in this thesis, lead and tilt angles are defined in Section 3.2. Local uncut chip area which is important for cutting force formulation is presented in Section 0. In Section 3.4 engagement model that determines the engagement region between the cutting tool and workpiece is defined for 5-axis ball-end milling. It can consider the engagements in both in ball and cylinder part of the ball-end mill. Determination of scallop height and material removal rate (MRR) is presented in the sections in Section 3.5 and in Section 3.6, respectively. Then, force and form error models are presented together with experimental verifications.

3.1. Ball-end mill geometry

Ball-end mills are mainly used in 3-axis and 5-axis milling. Since modeling of the mechanics and dynamics of 5-axis ball-end milling processes requires determination of local cutting edge geometry, geometry of the ball-end mill is presented here. The detailed geometry of a ball-end mill is shown in Figure 3.1. A Cartesian tool coordinates system TCS (*xyz*) is defined at the ball center. The *z*-axis is the axial direction of the cutter. At the tool tip, the local radius *R(z)* is zero, and it increases along the *z*-axis in the ball part whereas it has a constant value of R_o in the cylindrical part:

$$\left.\begin{array}{l} R(z) = \sqrt{R_o{}^2 - z^2} \; for \quad ball \quad part \\ R(z) = R_o \qquad for\, cylindrica\, l\; part \end{array}\right\} \qquad (3.1)$$
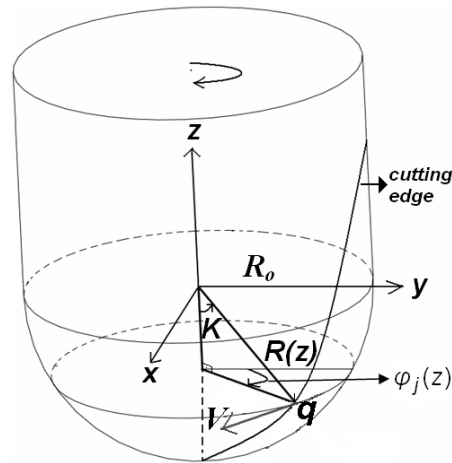
Figure 3.1: 3D view of a ball-end mill.

A point q on a cutting edge has local radius of $R(z)$, axial immersion angle of $K = K(z)$ (Figure 3.1) and radial lag angle of $\psi(z)$ (Figure 3.2). The axial immersion angle K is defined as the angle between the tool axis and normal of the cutting edge at point q. The axial immersion angle K can be calculated as:

$$K = \sin^{-1}(\frac{R(z)}{R_o})$$

(3.2)

The radial lag angle $\psi(z)$ is the angle on the xy plane between the line which connects the point q to the point $(0, 0, z)$, and the cutting edge tangent at the tip of the cutter (Figure 3.2). Radial lag angle $\psi(z)$ is due to the helix angle and is calculated using the following equation [37], where i_o is the helix angle at the meeting point of the ball and the cylinder parts:
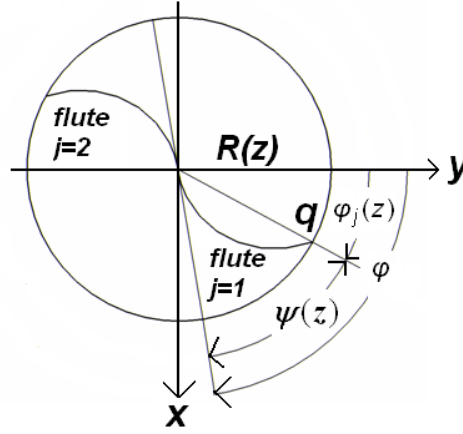
Figure 3.2: Top view of ball-end mill.

$$\psi(z) = \frac{R_o + z}{R_o} \tan i_o$$

(3.3)

Immersion angle $\varphi_j(z)$ shown in Figure 3.1 and Figure 3.2 defines the angular orientation of a point on the cutting edge of flute j, measured from $+y$ direction whereas φ is the immersion angle of the reference tooth at the tool tip. $\varphi_j(z)$ can be expressed as follows:

$$\varphi_j(z) = \varphi + (j-1)\varphi_p - \psi(z)$$

(3.4)

where φ_p is the pitch angle between the preceding flutes. The pitch angle depends on the total number of teeth on the tool, n:

$$\varphi_p = \frac{2\pi}{n}$$

(3.5)

19

3.2. Coordinate systems, lead and tilt angles

In order to define the position and orientation of a cutting tool in 5-axis milling, three coordinate systems are needed as shown in Figure 3.3. Machine coordinate system (MCS) is a fixed coordinate system attached to the X, Y, and Z axes of the machine tool whereas TCS consists of the z axis which is along the tool axis, and the two perpendicular transversal axes (x) and (y). Depending on the machine tool configuration, rotational axes may be on the spindle or on the table side. Figure 3.3 represents a case where both rotational axes are on the table side. In this case, the tool axis z and Z axis of the machine tool become parallel. In FCN coordinates system, F represents the feed direction, N stands for the surface normal direction of the workpiece and C is the cross-feed axis. The origin of the tool coordinate system (TCS) and the process coordinate system (FCN) is at the ball-center.
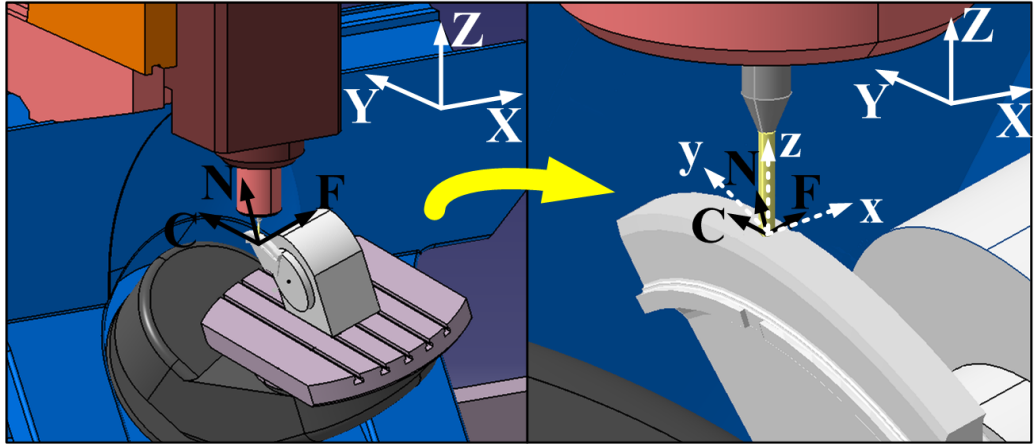
Figure 3.3: Coordinate systems

In 5-axis milling, the tool orientation is determined by lead and tilt angles which are measured with respect to the surface normal. The lead angle (l_e) is the rotation of the tool about the cross-feed axis C, and the tilt angle (t_i) is the rotation about the feed axis F. The lead and tilt angles are demonstrated in Figure 1.2. TCS is the rotated form of the FCN coordinates system by the lead and tilt angles. Transformation matrix T is used to transform TCS coordinates to FCN coordinates as follows:

$$\begin{bmatrix} F \\ C \\ N \end{bmatrix} = T \begin{bmatrix} x \\ y \\ z \end{bmatrix} \tag{3.6}$$

where T is the combination of two Euler transformations for the lead and tilt angles:

20

$$T = \begin{bmatrix} 1 & 0 & 0 \\ 0 & \cos t_i & -\sin t_i \\ 0 & \sin t_i & \cos t_i \end{bmatrix} \begin{bmatrix} \cos l_e & 0 & \sin l_e \\ 0 & 0 & 0 \\ -\sin l_e & 0 & \cos l_e \end{bmatrix} \tag{3.7}$$

The order of the rotation matrices in the above matrix is important. It should be noted that firstly lead angle and then tilt angle is applied.

3.3. Uncut chip area

Uncut chip area is the area removed instantaneously by a differential element on the cutting edge. It is defined as the multiplication of uncut chip thickness and uncut chip width. Uncut chip thickness is the thickness that a point on the cutting edge faces in the outward normal direction. In ball-end milling, uncut chip thickness at a point on the cutting edge depends on the immersion angle $\varphi_j(z)$ of the point. The uncut chip thickness ct at a point on the cutting edge depends on feed vector t and the unit outward surface normal vector u of the tool at the cutting point (Figure 3.4):
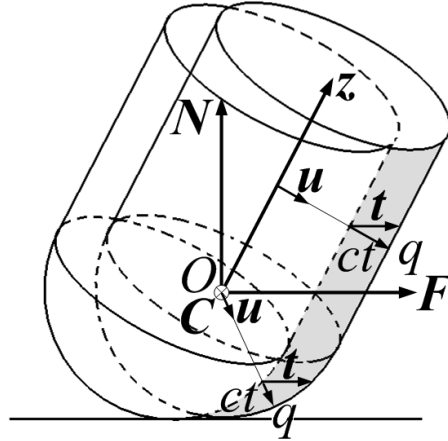
Figure 3.4: Uncut chip thickness ct.

The feed vector t is defined in FCN coordinate system as follows:

$$t = f_t f \tag{3.8}$$

where f_t is the feed per tooth and f is the unit vector in the feed direction F. Unit outward surface normal vector u at a point on the cutting edge is calculated for the ball part ($z \leq 0$), and the cylinder part $z > 0$ in tool coordinate system (TCS) as follows:

$$u = \begin{cases} \dfrac{1}{R_o} \left[R(z)\sin(\varphi_j(z)) & R(z)\cos(\varphi_j(z)) & z \right] & ,z \leq 0 \\ \left[\sin(\varphi_j(z)) & \cos(\varphi_j(z)) & 0 \right] & z > 0 \end{cases} \tag{3.9}$$

The uncut chip thickness ct at a point on the cutting edge can be determined by the scalar product of the feed vector and the unit outward surface normal vector of the tool at the cutting point. However, the feed vector and the unit outward surface normal vector should be written in the same coordinate system. For that reason, the unit outward surface normal vector u in TCS is transformed to FCN coordinate system using transformation matrix T (Equation(3.7)). The resulting unit outward normal vector in FCN coordinates system is represented by u_{FCN}. Finally, the uncut chip thickness can be calculated as follows:

$$ct = t \cdot u_{FCN} \tag{3.10}$$

The uncut chip width db that is tangent to cutting edge can be defined as follows:

$$db = \frac{dz}{\sin K} \tag{3.11}$$

3.4. Engagement Model

Engagement regions where the cutting tool is in contact with the workpiece depend on lead and tilt angles, ball-end mill geometry and cutting depths. Three different cutting types can be considered in the engagement analysis. In the first case, the tool cuts a non-machined cubic solid (first-cut, Figure 3.5(a)), whereas in the second case it cuts a previously machined surface (following-cut, Figure 3.5(b)). Finally, the last type is slotting (Figure 3.5(c)). The engagement regions for a representative following cut case with two different lead and tilt angle combinations are presented in Figure 3.6.

| (a) | (b) | (c) |
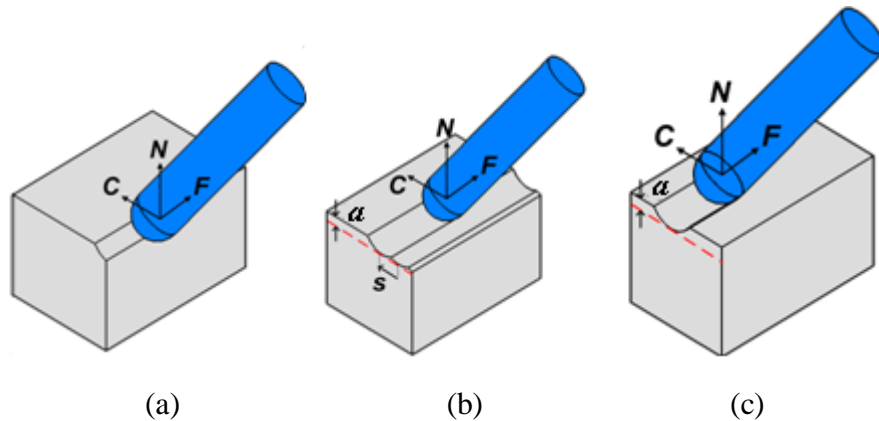
Figure 3.5: Cutting types a) first-cut b) following cut c) slotting cut
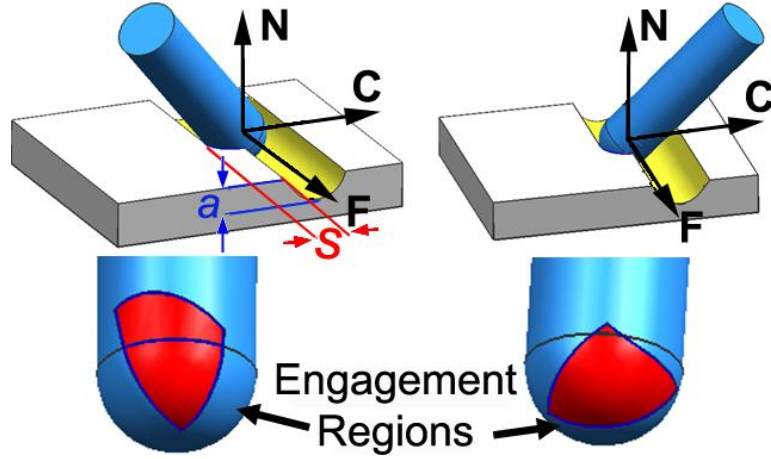
Figure 3.6: Engagement regions in two following cut operations (R_o=6mm, s=5mm, a=5mm) (a) for positive lead (15°), positive tilt (40°) (b) for positive lead (15°), negative tilt (-40°)

In the engagement analysis, firstly coordinates of points on cutting edge on ball-end mill are determined in the TCS. Starting from tool tip, ball-end mill is divided into differential disc elements, having height of *dz,* along tool axis. For a disc element at a height of *z*, *x* and *y* coordinates of points on cutting edge are found in terms of local radius *R(z)* and $\varphi_j(z)$:

$$x = R(z)\sin\varphi_j(z)$$
$$y = R(z)\cos\varphi_j(z)$$

(3.12)

However, engagement conditions are given in the FCN coordinate system. Thus, coordinates (*x*, *y*, *z*) of a point on the cutting edge need to be transformed from TCS to FCN using the transformation matrix ***T*** (Equation (3.7)) so as to check whether the corresponding point satisfies engagement conditions. The ones that satisfy these conditions are in cut with the workpiece. The milling mode, i.e. up and down milling, definitions can be ambiguous for 5-axis ball-end milling. For example, the start and exit angles may not be 0° and 180°, respectively, due to the effect of lead and tilt angles in 5-axis ball-end milling. In order to define the direction of the uncut material, another parameter, cross-feed direction is used. If uncut material is in the positive *C* axis with respect to the milling tool, the cross-feed direction is positive. On the other hand, if uncut material is in the negative *C* axis with respect to the milling tool, the cross-feed direction is negative which is the case in Figure 3.7.

(a)   (b)
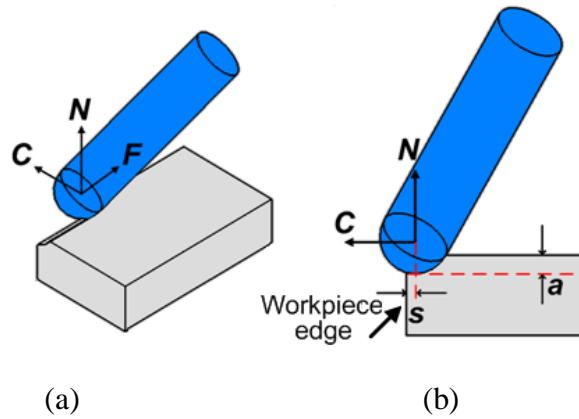
Figure 3.7: a) A first-cut process (cross feed direction is negative)

b) The step over s and the cutting depth a in the first-cut case

The common engagement conditions for all the cutting types are that chip thickness ct at points on the cutting edge are equal or greater than 0 and N coordinates of the points are equal to or less than $a\text{-}R_o$ (i.e. $N \leq a\text{-}R_o$) where a is the cutting depth. a is the distance between the tool's lowest point and workpiece's upper face in the surface normal direction N (Figure 3.5 and Figure 3.7). In other words, it's the depth of the stock removed in the surface normal direction N. It should be noted that due to the lead and tilt angles, in 5-axis ball-end milling the cutting depth is different than the axial depth which is along the tool axis. The other engagement conditions depend on cutting types and are presented for the corresponding cutting types separately.

Table 3.1: Engagement criteria for the first-cut case.

Case	Cross-feed direction	Condition for engagement
1	Positive	$C \geq -s$
2	Negative	$C \leq -s$

In the first-cut case, step over s is the distance in the cross-feed axis (C) from the workpiece edge to the tool's lowest point in the surface normal direction (N) (Figure 3.7(b)). Hence, if the C coordinate of the workpiece edge is positive, the step over is negative (Figure 3.7); otherwise it's positive. In addition to the common engagement criteria which are independent of the cutting type, a point on the cutting edge is in cut with the workpiece if the C coordinate of the point is higher than $-s$ for a positive cross-feed direction case, or it is smaller than $-s$ for a negative cross-feed direction case (Table 3.1).

In the following-cut cases, the step over s is the distance between the adjacent tool paths in C axis as shown in Figure 3.5 (b) and Figure 3.6. Depending on the cross-feed direction, step over s, tilt angle t, ball-end mill radius R_o and N coordinate of the point on the cutting edge; there are different engagement conditions in C coordinate of the points. The engagement conditions for the following cut cases are tabulated in Table 3.2 and Table 3.3 for the positive and negative cross-feed directions, respectively.

For following cut cases, depending on the step over value, the successive tool paths may intersect on the parts machined by the ball section of the tool or on the parts machined by the cylinder section of the tool in one pass and the ball section in the other pass as shown in Figure 3.8(a) and Figure 3.8(b), respectively. The step over value that discriminates these two cases is represented by s_b (Figure 3.8(c)) and it's calculated by the geometry as follows:

$$s_b = 2R_o \cos t \tag{3.13}$$

When the step over is less than s_b, the ball parts of the two passes intersect (Figure 3.8 (a)). On the other hand, if step over is higher than s_b, the ball part of one pass intersects with the cylinder part of the other pass (Figure 3.8 (b))

The engagement conditions given in Table 3.2 for the positive cross-feed direction case are explained here to be representative for the following-cuts. If s is less than s_b, there are three different engagement zones. In the first engagement zone, where the N coordinate of a cutting point on the cutting edge is below N_i, the point is in cut with the workpiece (Zone 1). N_i is the N coordinate of the intersection point of ball part of the milling tool with the ball part of the previous pass and it depends on the radius of ball-end mill R_o and step over s:

$$N_i = -\sqrt{R_o{}^2 - \frac{s^2}{4}} \tag{3.14}$$

The second engagement zone is bounded by the ball parts of the current and previous passes, $N=N_i$ plane and $N = R_o \sin t_i$ plane. In this zone, the C coordinate of the cutting point should be equal to or higher than $\sqrt{R_o{}^2 - N^2} - s$ to be in cut (Zone 2). The last engagement zone is bounded by the cylinder parts of the current and previous passes, $N = R_o \sin t_i$ plane and $N = a - R_o$ plane. In this third zone, if the

cutting point's C coordinate is equal to or higher than $\dfrac{R_o - N\sin t_i}{\cos t_i} - s$, the point is in

cut with the workpiece (Zone 3).
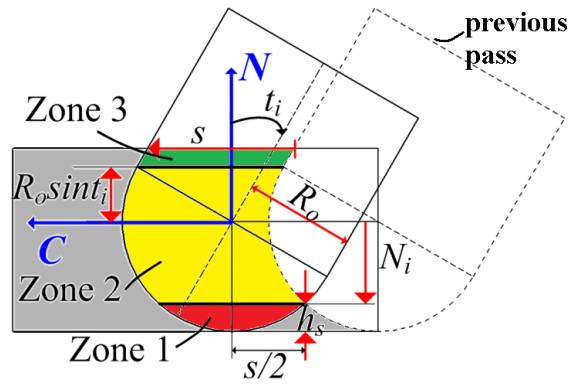
(a)
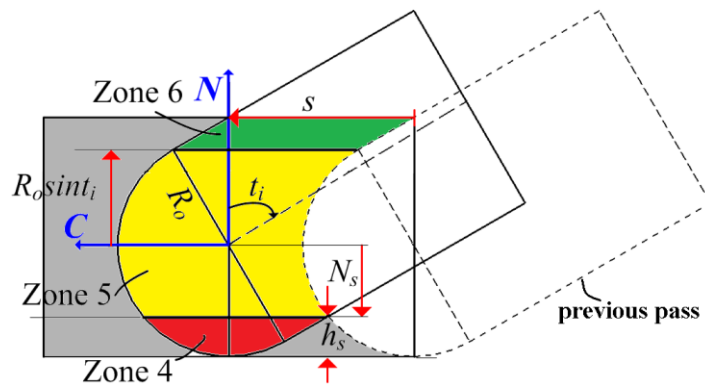
(b)
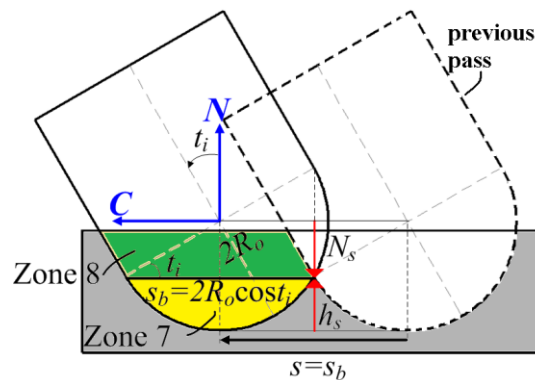
(c)

Figure 3.8 Engagement zones (cross feed direction positive) a) $s < s_b$ b) $s \geq s_b, t > 0$ c)

$$s \geq s_b, t \leq 0$$

In the other case, where step over is greater than s_b depending on the sign of the tilt angle there are two different conditions. An example situation where tilt angle is

positive is demonstrated in Figure 3.8(b). In this case, the cylinder part of the milling tool intersects with the ball part of the previous pass at a point whose N coordinate is equal to N_s, where N_s is determined by the below equation 15 in terms of radius of ball-end mill R_o, the step over s and the tilt angle t_i:

$$N_s = -\sqrt{R_o{}^2 - (R_o - s\cos t_i)^2}\, \cos t_i - (R_o - s\cos t_i)\sin|t_i| \qquad (3.15)$$

Table 3.2 Engagement conditions for the following-cut case (positive cross-feed direction)

Zone	Step over	Tilt angle	N coordinate	Condition for engagement
1	$s < s_b$		$N \le N_i$	-
2			$N_i < N \le R_o \sin t_i$	$C \ge \sqrt{R_o{}^2 - N^2} - s$
3			$N > R_o \sin t_i$	$C \ge \dfrac{R_o - N\sin t_i}{\cos t_i} - s$
4	$s \ge s_b$	$t_i > 0$	$N \le N_s$	-
5			$N_s < N \le R_o \sin t_i$	$C \ge \sqrt{R_o{}^2 - N^2} - s$
6			$N > R_o \sin t_i$	$C \ge \dfrac{R_o - N\sin t_i}{\cos t_i} - s$
7		$t_i \le 0$	$N \le N_s$	-
8			$N > N_s$	$C \ge \dfrac{R_o - N\sin t_i}{\cos t_i} - s$

For this case, there are three different engagement zones. In the first region where N coordinate of the cutting point is below $N=N_s$ plane, the point is in cut with the workpiece (Zone 4). The second region is bounded by the ball parts of the current and the previous passes, $N=N_s$ plane and $N = R_o \sin t_i$ plane (Zone 5). Engagement condition in this case is the same as zone 2. Finally, the third engagement zone is bounded by the cylinder parts of the current and the previous passes, $N = R_o \sin t_i$ plane and $N = a - R_o$ plane (Zone 6). In this case engagement condition is the same as

zone 3. On the other hand, if tilt angle is negative (zone 7 and zone 8 in Table 3.2), there are two different engagement zones, i.e. the first one is below the $N=N_s$ plane and the second one is above the $N=N_s$ plane (Figure 3.8(c)). In the first zone, the cutting point is in cut with the workpiece. The second zone is bounded by the cylinder parts of the current and the previous passes, $N=N_s$ plane and $N = a - R_o$ plane. Engagement condition in this zone is the same as the one for zone 3.

Table 3.3 Engagement conditions for the following-cut case (negative cross-feed direction).

Zone	Step over	Tilt angle	N coordinate	Condition for engagement
1			$N \leq N_i$	-
2	$s < s_b$		$N_i < N \leq -R_o \sin t_i$	$C \leq -\sqrt{R_o^2 - N^2} + s$
3			$N > -R_o \sin t_i$	$C \leq -\dfrac{R_o + N \sin t_i}{\cos t_i} + s$
4		$t > 0$	$N \leq N_s$	-
5			$N > N_s$	$C \leq -\dfrac{R_o + N \sin t_i}{\cos t_i} + s$
6	$s \geq s_b$		$N \leq N_s$	-
7		$t \leq 0$	$N_s < N \leq -R_o \sin t_i$	$C \leq -\sqrt{R_o^2 - N^2} + s$
8			$N > -R_o \sin t_i$	$C \leq -\dfrac{R_o + N \sin t_i}{\cos t_i} + s$

3.5. Scallop Height

Scallop height h_s is a measure of surface quality for the following-cut cases. In 3-axis ball-end milling, it depends on the radius of ball-end mill R_o and step over s. However, in 5-axis ball-end milling the tilt angle may also affect the scallop height. If step over is less than s_b, the ball part of the milling tool intersects with the ball part of the previous cut; thus, scallop height calculation is the same as the 3 axis ball-end milling (Figure 3.8(a)). On the other hand, if the step over is higher than s_b, the cylindrical and the ball parts intersect as shown in Figure 3.8 (b), and scallop height also

depends on tilt angle. Scallop height formulations are given in Table 3.4 for both of the cases.

Table 3.4 Scallop height formulation in 5-axis ball-end milling

Step over	Scallop height h_s
$s \leq s_b$	$R_o + N_i$
$s > s_b$	$R_o + N_s$

In the following-cuts, the step over can be as high as $2R_o / \cos t_i$. In this case the maximum scallop height is $h_{s,\max} = R_o(1 + \sin|t_i|)$ provided that the cutting depth is sufficiently high. In order to show the effect of the step over on the scallop height, a normalized form of scallop height is used. The normalized scallop height is the ratio of the scallop height to the radius of the ball-end mill whereas normalized step over is the ratio of the step over to the maximum possible step over, i.e. $2R_o / \cos t_i$. As a representative case, for a fixed tilt angle of 60°, the variation of the normalized scallop height with the normalized step over is presented in Figure 3.9. In 3-axis ball-end milling, the maximum scallop height is equal to the radius of the ball-end mill. However, in 5-axis ball-end milling, the scallop height can be higher than the radius of the ball-end mill depending on the tilt angle and the step over as presented in Figure 3.9.
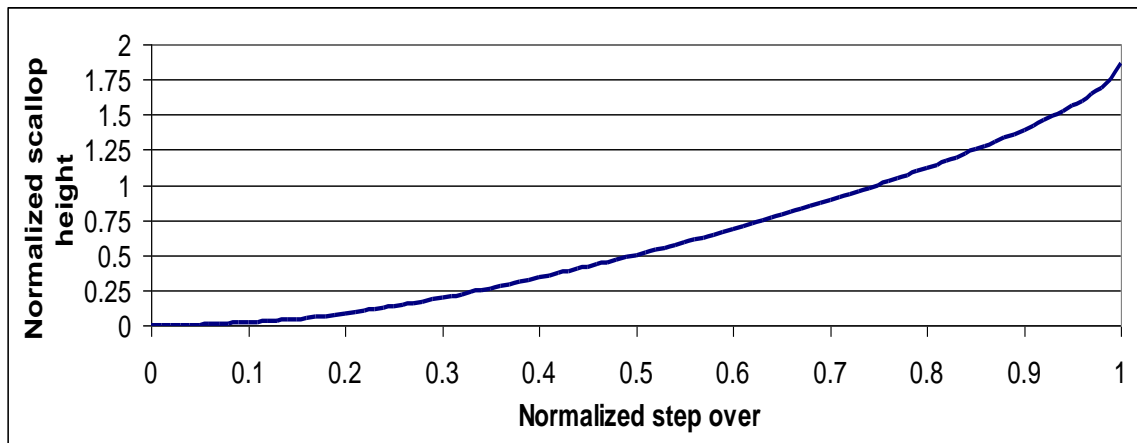
Figure 3.9 Normalized scallop height analysis

3.6. Material removal Rate (MRR)

Material removal rate (MRR) is defined as the volume of the material that a cutting tool removes from the workpiece in unit time. If increase in MRR decreases the total number of cutting steps, machining time for an operation decreases. Hence, proper

29

machining conditions should be selected to increase MRR for high productivity. In the case where step over is higher than s_b, increase in tilt angle increases the MRR while it decreases the scallop height at the same time.

(a) (b)

(c)

(d)
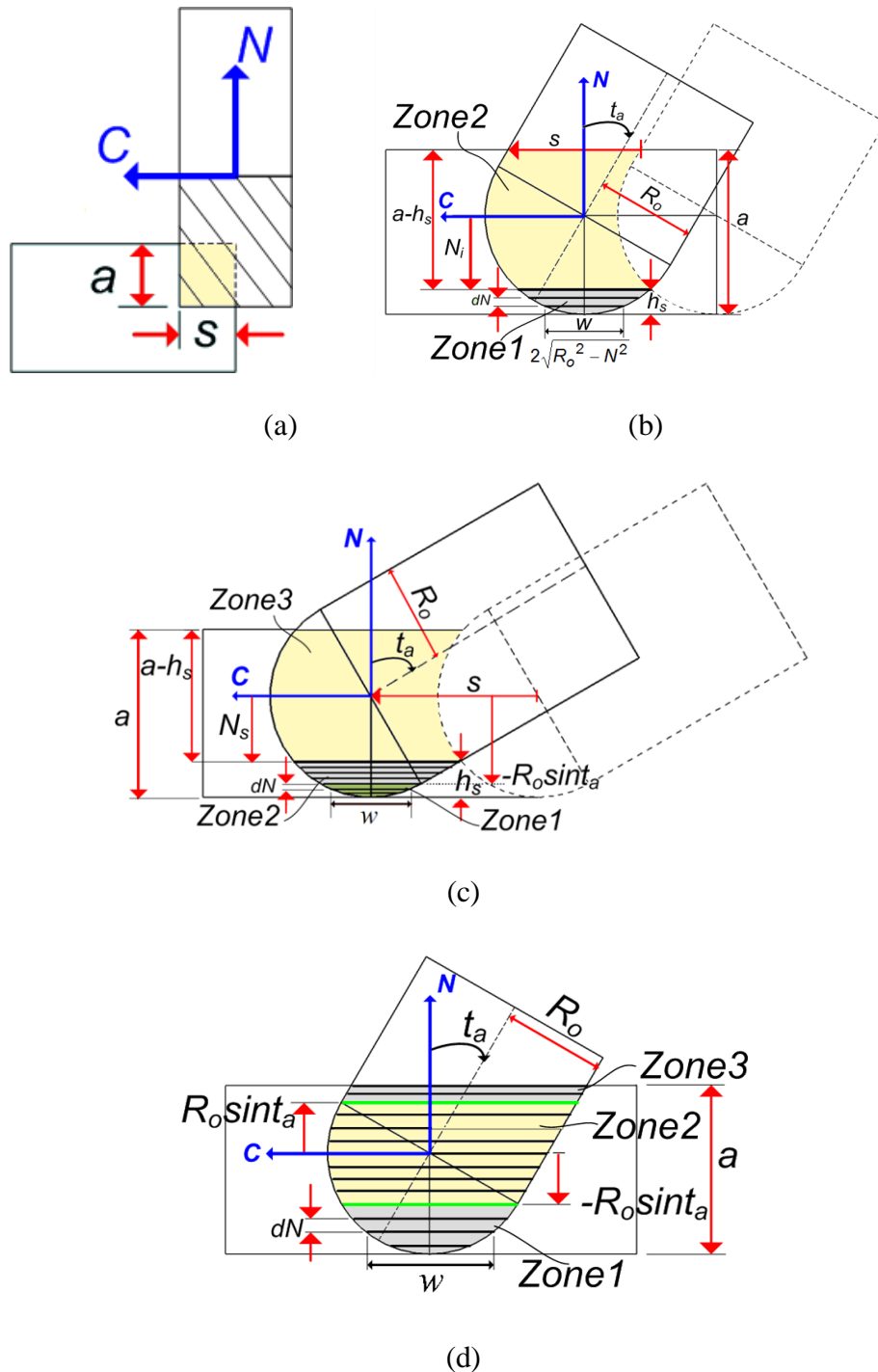
Figure 3.10: (a) Projected area in 3-axis flat end milling (b) following cut, $s \leq s_b$

(c) following cut, $s > s_b$ (d) slotting

MRR is calculated by the product of the feed velocity (F_{vel}) and the projected area ($Area_{proj}$) as follows:

$$MRR = F_{vel} * Area_{proj} \qquad (3.16)$$

Feed velocity (F_{vel}) is defined as the distance that milling tool travels in unit time in the feed direction. $Area_{proj}$ is the projection of the volume removed by the cutting tool instantaneously in the feed direction (Figure 3.10). As explained in the engagement boundary section (Section 3.4), there are 3 different cutting types in 5-axis ball-end milling. Since first cut constitutes a small portion of machining cycles in general, the MRR calculation for following cut and slotting cases are considered.

The projected area in 3-axis flat-end milling is rectangular, and can be calculated by the multiplication of axial depth and radial depth (Figure 3.10 (a)). However, in 5-axis ball-end milling, the calculation of the projected area is more complicated due to the geometry of ball-end mill and the effect of the tilt angle. It is divided into differential area elements along the surface normal direction and by integration of these elements projected area is calculated. The projected area in 5-axis ball-end milling depends on the following parameters: radius of the ball-end mill, cutting depth, step over, tilt angle and cutting mode. On the other hand, lead angle, sign of the tilt angle and cross-feed direction do not affect the projected area, and hence they do not have any effect on the MRR.

The projected area, $Area_{proj}$, is calculated by integrating the differential area of the element (wdN) between $N=-R_o$ and $N=-R_o+a$ as follows (Figure 3.10):

$$Area_{proj} = \int_{-R_o}^{-Ro+a} wdN \qquad (3.17)$$

where w is the width and dN is the height of the differential area element (Figure 3.10 (b), (c), and (d)). Firstly, calculation of the projected area is explained for following cut cases. For the cases where the cutting depth is higher than the scallop height h_s, the area above the scallop height (Zone 2 in Figure 3.10(b) and Zone 3 in Figure 3.10(c)) can be calculated simply by multiplying s and $a-h_s$. In this case, the calculation of the projected area given in (3.17) is re-written by changing the integration limits and including the area of this region as follows:

$$Area_{proj} = \int_{-R_o}^{-Ro+h_s} wdN + \int_{-Ro+h_s}^{-Ro+a} wdN = \int_{-R_o}^{-Ro+h_s} wdN + (a - h_s)s \qquad (3.18)$$

As noted in the engagement boundary section (Section 3.4), for the following cut cases, depending on the step over value, the successive tool paths may intersect on the parts machined by the ball section of the tool or on the parts machined by the cylinder section of the tool in one pass and the ball section in the other pass as shown in Figure 3.10(b) and Figure 3.10(c), respectively. The widths of the differential rectangular elements, w, are calculated using geometric relations for these two different cases. For example, for the first case, it is calculated by the following equation which is obtained using the geometry as presented in Figure 3.10 (b):

$$w = 2\sqrt{R_o^2 - N^2} \tag{3.19}$$

This and the other relations for w are tabulated depending on the (N) coordinate of the differential area element in Table 3.5. The parameter t_a which is used in Table 3.5 is defined as the absolute value of the tilt angle, t_i.

In slotting cases, there are three different zones in the calculation of the width of the differential element w depending on the N coordinate of the differential element. These are also tabulated in Table 3.5 and illustrated in Figure 3.10 (d).

Table 3.5: Calculation of w in following cut and slotting cases

Cutting mode	Step over	Zone	N coordinate	w
Following cut	$s \le s_b$	1	$N \le N_i$	$w = 2\sqrt{R_o^2 - N^2}$
	$s > s_b$	1	$N \le -R_o \sin t_a$	$w = 2\sqrt{R_o^2 - N^2}$
		2	$-R_o \sin t_a < N \le N_s$	$w = \sqrt{R_o^2 - N^2} + (\dfrac{R_o}{\sin t_a} + N) \tan t_a$
Slotting	-	1	$N \le -R_o \sin t_a$	$w = 2\sqrt{R_o^2 - N^2}$
		2	$-R_o \sin t_a < N \le R_o \sin t_a$	$w = \sqrt{R_o^2 - N^2} + (\dfrac{R_o}{\sin t_a} + N) \tan t_a$
		3	$N > R_o \sin t_a$	$w = \dfrac{2R_o}{\cos t}$

3.7. Force Model

Magnitude of cutting forces is an important limitation in milling processes. If cutting forces reach high values, resulting deflections may cause unacceptably high form errors. Furthermore, high cutting forces may cause milling tool breakage due to excessive bending stresses as well as spindle overload. Thus, predicting cutting forces in 5-axis ball-end milling operations is important for selection of machining conditions.
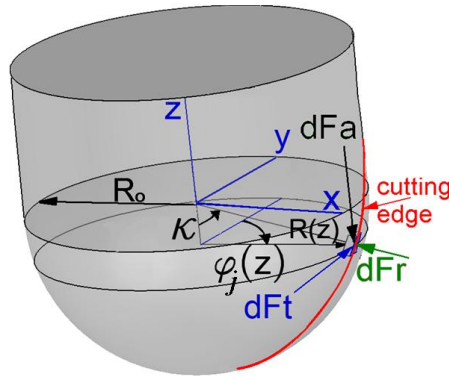
Figure 3.11: Representation of local cutting forces.

In order to model cutting forces, the ball-end mill is divided into differential cutting elements where oblique cutting mechanics is used to determine differential cutting forces. Cutting force and edge force coefficients are determined using the *mechanics of milling* method [36]. In this approach, parameters (shear angle, friction angle and the shear stress) required for the calculation of cutting force coefficients are obtained from an orthogonal cutting database. The force model integrates the contribution of the differential cutting elements that are engaged with the workpiece for each rotational position of the tool, and calculates the cutting forces in TCS, FCN and MCS coordinate systems.

The orthogonal databases are generated for different rake angles, feed rates and cutting speeds for a work-cutting tool material pair [36]. In ball-end mills, in addition to the cutting speed and uncut chip thickness, radial, or velocity rake angle [49], may also vary along the cutting edge depending on the path and the wheel profile used during the grinding of the flutes. Thus, together with the local cutting speed and uncut chip thickness value, corresponding normal rake angle must also be determined, and used in the calculation of the local cutting force coefficients. For the tools used in this study, the radial rake angle variation can be modeled as a sinusoidal one along the tool axis as follows:

$$\alpha_v = \begin{cases} \alpha_{vo} \sin K & z < 0 \\ \alpha_{vo} & z \geq 0 \end{cases} \tag{3.20}$$

where α_{vo} is the radial rake angle at the ball-cylinder meeting boundary and K is axial immersion angle given by (3.2). Corresponding local normal rake angle, α_n, can be determined from the geometric relationship between two rake angles [49].

$$\tan \alpha_n = \tan \alpha_v \cos i \tag{3.21}$$

where i is the inclination, or the local helix angle.

Cutting forces are separated into edge and shear cutting components in the linear edge force model. The cutting force coefficients, K_{rc}, K_{tc}, K_{ac}, and the edge force coefficients, K_{re}, K_{te}, K_{ae}, in radial, tangential and axial directions, respectively, are determined using the orthogonal database and the oblique cutting model [36]. Thus, the differential cutting forces for the tooth j in the radial, tangential and axial directions at a point on the cutting edge can be determined as follows[37]:

$$\begin{aligned} dF_{rj}(\varphi_j(z)) &= K_{re} dS + K_{rc}(ct) db \\ dF_{tj}(\varphi_j(z)) &= K_{te} dS + K_{tc}(ct) db \\ dF_{aj}(\varphi_j(z)) &= K_{ae} dS + K_{ac}(ct) db \end{aligned} \tag{3.22}$$

In (3.22), dS is the differential cutting edge length [37]. The differential forces in radial, tangential and axial directions can be transformed into the tool coordinate system TCS as follows [37]:

$$\begin{bmatrix} dF_{xj}(\varphi_j(z)) \\ dF_{yj}(\varphi_j(z)) \\ dF_{zj}(\varphi_j(z)) \end{bmatrix} = \boldsymbol{T_{xyz}} \begin{bmatrix} dF_{rj}(\varphi_j(z)) \\ dF_{tj}(\varphi_j(z)) \\ dF_{aj}(\varphi_j(z)) \end{bmatrix} \tag{3.23}$$

where $\boldsymbol{T_{xyz}}$ is the transformation matrix that transforms the cutting forces in radial, tangential and axial directions to x, y and z directions:

$$\boldsymbol{T_{xyz}} = \begin{bmatrix} -\sin K \sin \varphi_j(z) & -\cos \varphi_j(z) & -\cos K \sin \varphi_j(z) \\ -\sin K \cos \varphi_j(z) & \sin \varphi_j(z) & -\cos K \cos \varphi_j(z) \\ \cos K & 0 & -\sin K \end{bmatrix} \tag{3.24}$$

The total cutting forces on the tool are calculated by integrating the differential forces acting on the oblique elements engaged with the workpiece for each immersion angle, and summing up the contribution of each cutting flute as follows:

$$F_x(\varphi) = \sum_{j=1}^{n} \int dF_{xj}(\varphi_j(z))$$

$$F_y(\varphi) = \sum_{j=1}^{n} \int dF_{yj}(\varphi_j(z)) \qquad (3.25)$$

$$F_z(\varphi) = \sum_{j=1}^{n} \int dF_{zj}(\varphi_j(z))$$

Cutting forces can also be transformed to FCN using the transformation matrix $\boldsymbol{T}$:

$$\begin{bmatrix} F_F(\varphi) \\ F_C(\varphi) \\ F_N(\varphi) \end{bmatrix} = \boldsymbol{T} \begin{bmatrix} F_x(\varphi) \\ F_y(\varphi) \\ F_z(\varphi) \end{bmatrix} \qquad (3.26)$$

3.8. Form Error Model

Form error is a measure of dimensional part quality which is usually maintained using conservative cutting parameters such as low feed rates and depth of cuts, or by compensation. The former approach results in decreased productivity whereas the latter one may result in several scrap parts and time consuming tests until the right offsets are identified. If form error is modeled for a cutting process before machining, the part can be machined correctly at the first try by offsetting the tool path based on the form errors predicted. This is the motivation behind the modeling of form errors.

For form error prediction, the predicted cutting forces are used together with the tool and workpiece structural models in order to determine the deflections. The form error is the relative deflection between the tool and the workpiece at a surface generation point. In this thesis, only the deflections of the milling tool are considered for simplicity, however part deflections can also be determined through the Finite Element Analysis [50].
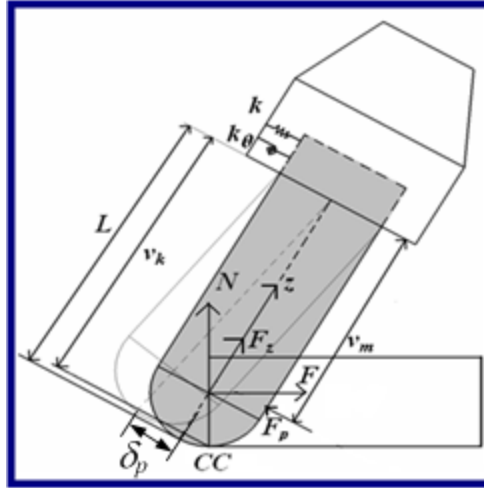
Figure 3.12 Structural model of the ball-end mill

A ball-end mill can be modeled as a cantilever beam which is connected to the tool holder with linear and torsional spring elements as shown in Figure 3.12. The spring constants for these spring elements need to be calibrated for each cutting tool. For this, predefined forces are applied on the cutting tool and corresponding deflections of the tool are measured with a dial gauge. Using the force and corresponding deflection values, the linear and torsional spring constants are calibrated. The set-up used for the calibration of spring constants is presented in Figure 3.13.
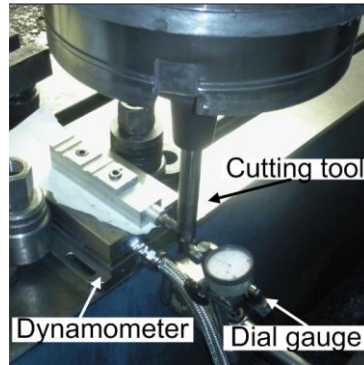
Figure 3.13 : Calibration of spring constants

Cutting forces F_x, F_y and F_z on the tool when generating the cutter contact point CC are inserted into the beam deflection equations [50] to find the deflections *in x*, *y* and *z* axes (δ_x, δ_y, δ_z). Since the tool is very rigid in z-axis with respect to *x* and *y* axis, deflection in the *z* direction can be neglected unless the part is flexible in *z* direction. Deflections in feed, cross-feed and surface normal axes ($\delta_F, \delta_C, \delta_N$) are also calculated using transformation matrix ***T*** (Equation (3.6))

CC point is defined as the tool's lowest point in surface normal axis *N* that is engaged with the workpiece. In first-cut cases, *CC* point coordinates in the FCN coordinate system depend on step over *s*, cross-feed direction. There are 4 different cases in *CC* point calculation and coordinates of the *CC* point in FCN are tabulated for the first-cut cases in Table 3.6. On the other hand, in the following-cut and slotting cases the coordinates of the *CC* point are $[0, 0, -R_o]^T$. Superscript *T* represents the transpose operation.

Table 3.6 Coordinates of the CC point for the first cut case in FCN coordinate system.

Cross-feed direction	*s*	*CC point in FCN*
Positive	$s \geq 0$	$[0, 0, -R_o]^T$
	$s < 0$	$[0,-s,-\sqrt{R_o^2 - s^2}\,]^T$
Negative	$s \geq 0$	$[0,-s,-\sqrt{R_o^2 - s^2}\,]^T$
	$s < 0$	$[0, 0, -R_o]^T$

3.9. Verification Tests

3.9.1. Comparison of measured and simulated cutting forces

In order to verify the model, 5-axis ball-end milling tests on Ti6Al4V material were performed at a DMG 50 evolution 5-axis machining center (Figure 3.14). 12 mm diameter ball-end mills clamped by a shrink fit tool holder were used in the tests. A Kistler table type dynamometer (Type 9257BA) was used together with the signal conditioner (Type 5233A1) to measure cutting forces. Cutting force signals are low pass filtered at 200 Hz with an integrated low pass filter in signal conditioner.

In order to demonstrate the model's effectiveness in different cases, comparisons between simulated cutting forces and measured ones for one revolution of the milling tool are presented here for 9 different cases to be representative. However, totally 70 tests were carried out. 12mm diameter carbide ball-end mills with 2 teeth, 8° rake angle and helix angle of 30° were used in the tests. The cutting conditions are given in Table 3.7. These cutting parameters are used in the 5-axis ball-end milling force model and the cutting forces are simulated for one revolution of the milling tool. The comparisons

for 9 different cutting conditions are shown in Figure 3.15(a)-(i). The full lines are the simulation results whereas dotted lines are the measured force values. Except the first case where the forces are plotted in the FCN coordinate system, in other cases forces are in the TCS (*xyz*).

Figure 3.14: DMG 50 evolution 5-axis machining center

Table 3.7 Cutting parameters.

Case	Lead,tilt (°)	Step over (mm)	Cutting type	Cross feed direction	Cutting depth(mm)	feed mm/tooth	n (rpm)
(a)	30,30	Slotting	-	-	1.5	0.1	500
(b)	10,-15	Slotting	-	-	1.5	0.1	3000
(c)	15,0	1.8	First cut	Positive	3	0.1	500
(d)	-15,0	1.2	First cut	Positive	3	0.1	500
(e)	15,-15	-1.8	First cut	Negative	3	0.1	500
(f)	15,15	7	Following Cut	Positive	3	0.1	1000
(g)	15,15	1.8	First cut	Positive	3	0.1	500
(h)	15,-15	7	Following Cut	Negative	3	0.1	500
(i)	15,0	-0.6	First cut	Positive	3	0.1	500

38

(a)

(b)

(c)

39

(d)

(e)

(f)

40
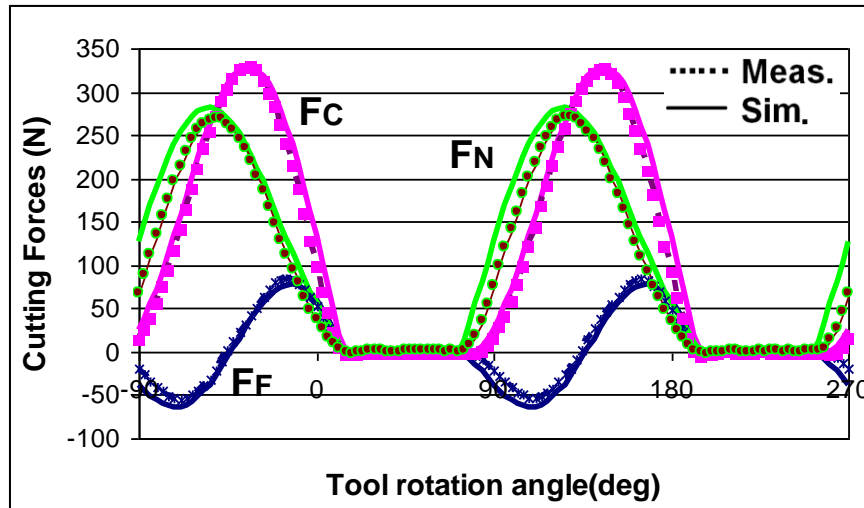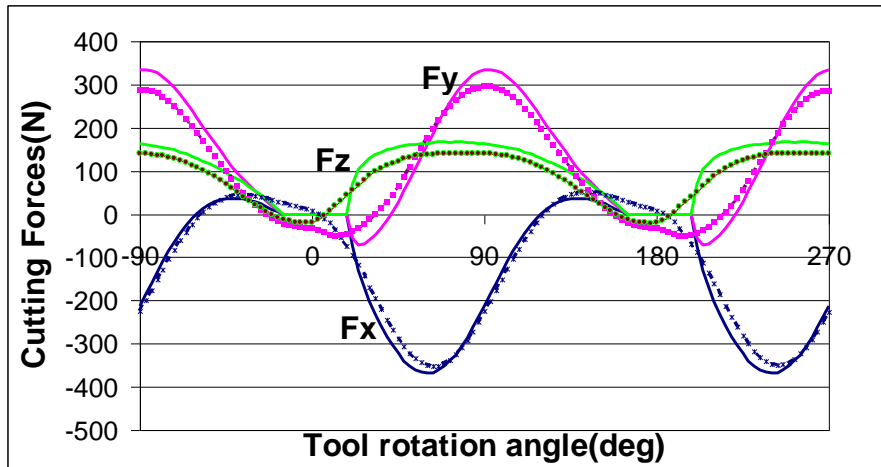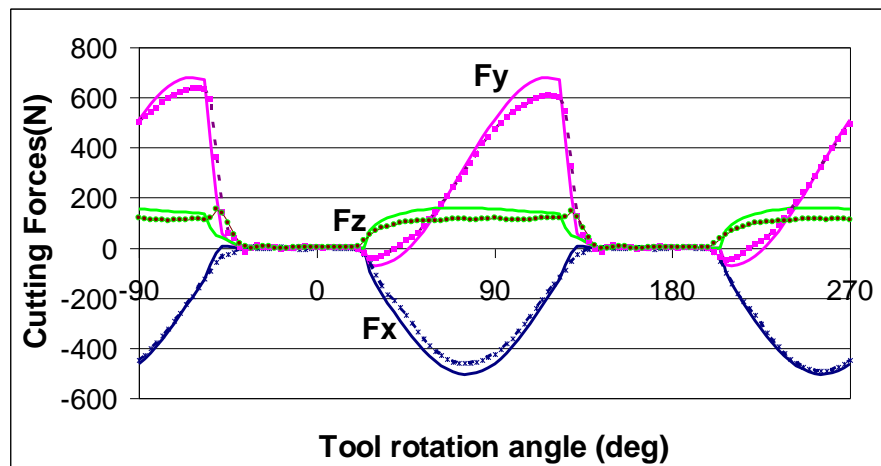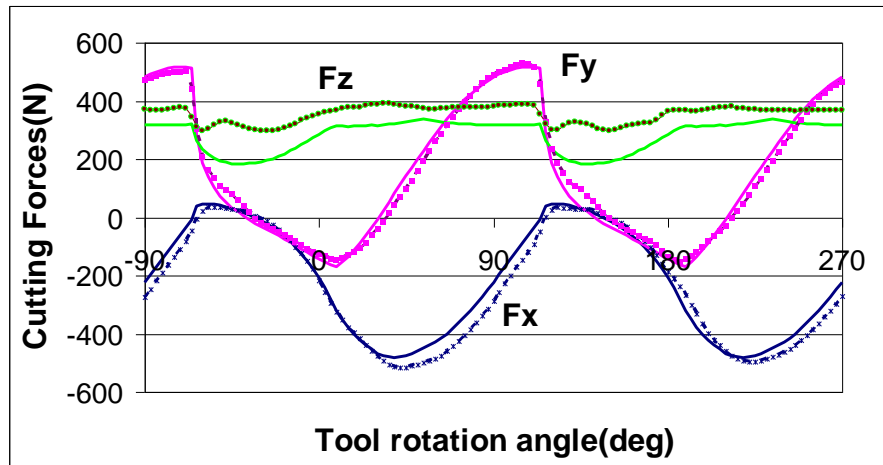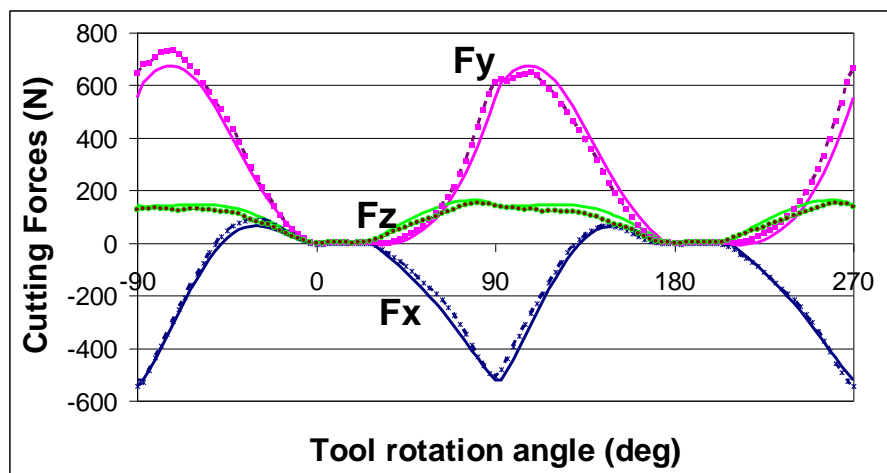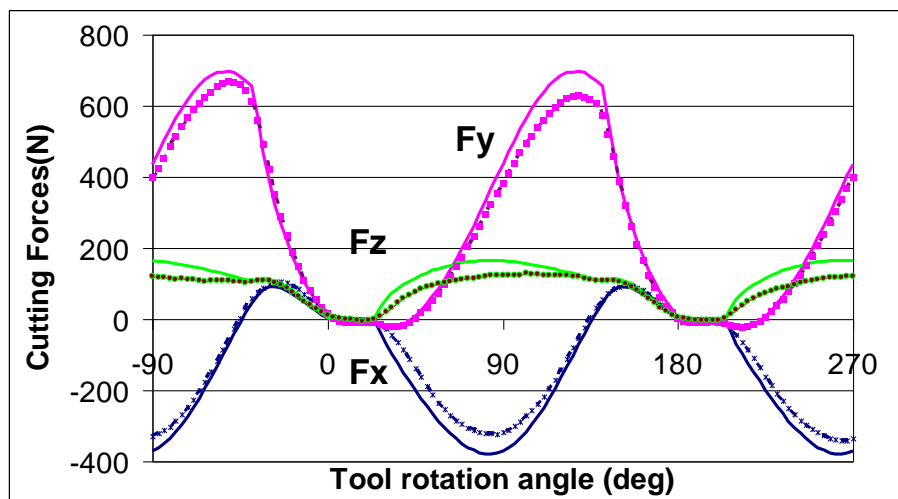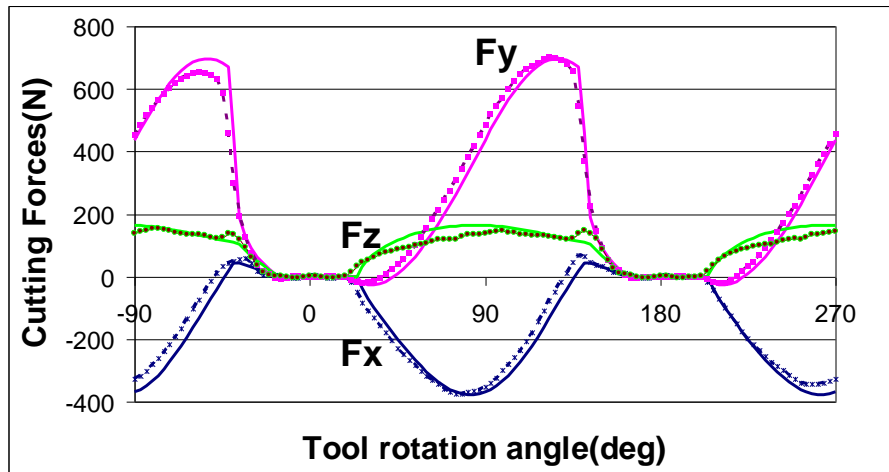
(g)
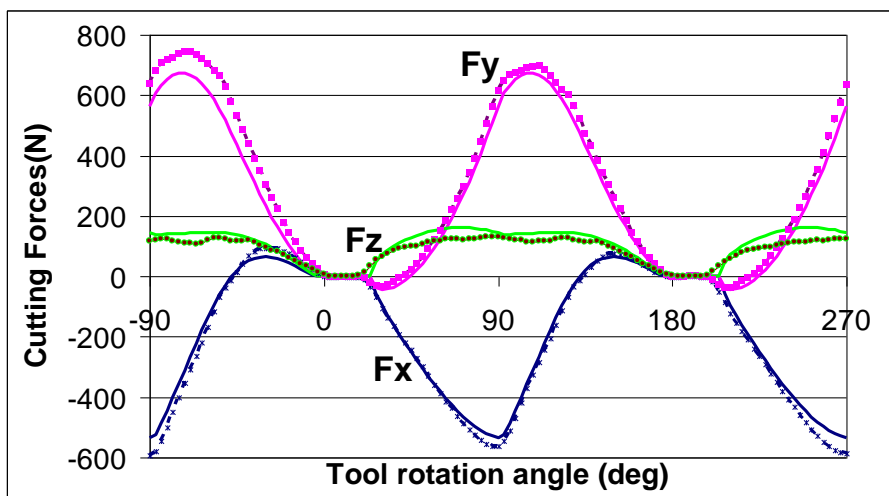
(h)
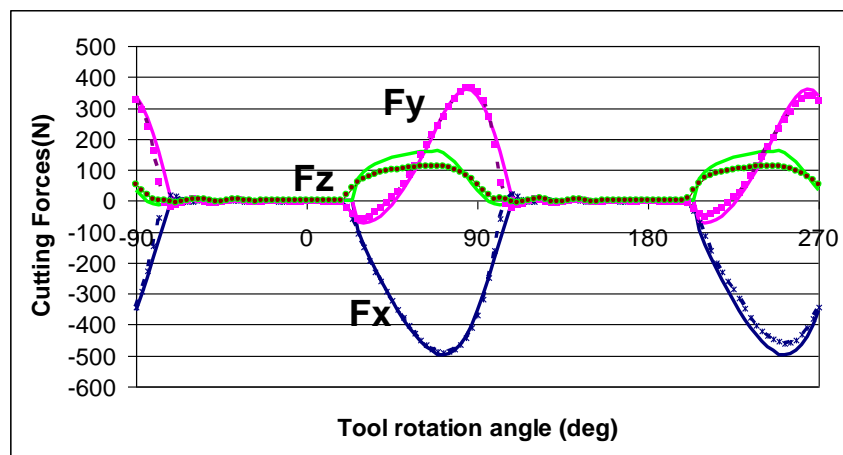
(i)

Figure 3.15 Comparison of measured and simulated cutting forces for cases (a)-(i),
respectively.

3.9.2. Statistical Analysis of the Results

A statistical analysis was performed to compare the cutting force predictions with the measurements for 70 cutting tests. The prediction error was defined as the difference between the absolute maximum value of measurement and absolute maximum value of prediction in percentage. The analysis was done for the forces in the TCS, i.e. F_x, F_y and F_z.
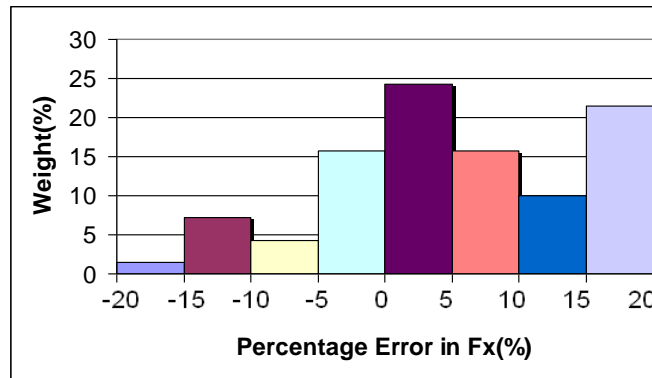
(a)
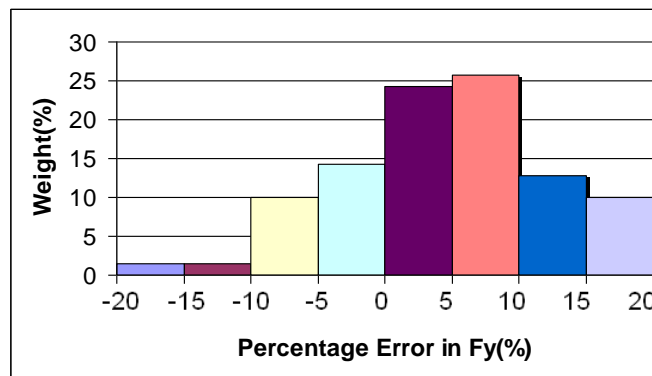
(b)
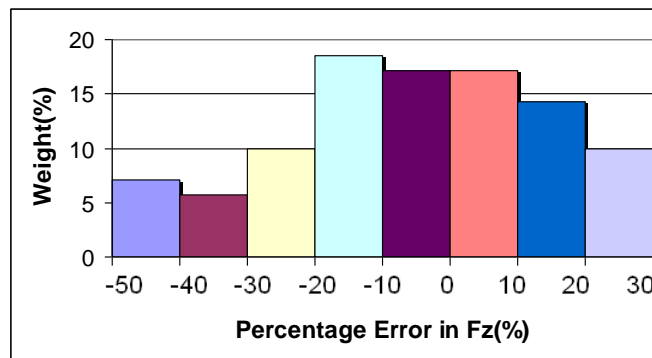
(c)

Figure 3.16 Statistical analysis for prediction error in (a) F_x (b) F_y (c) F_z

The distributions of prediction errors are shown for F_x, F_y and F_z in Figure 3.16. The mean of the prediction errors are 5%, 4% and -6% in F_x, F_y and F_z forces, respectively. The prediction accuracy for maximum force value in the x and y axis is in the 20% range. In some cases, it is observed that the prediction error in z direction may reach up to 50%. However, this is due to the fact that in these cases the F_z force is considerably lower in magnitude compared to F_x and F_y forces. An example of such a case is shown in Figure 3.15(i) where the maximum measured force in the z direction is 113 N, and the prediction for maximum F_z is 161 N. Although there is an error of about 50%, the difference is only 48N. It should be noted that the *mechanics of milling* method was used in the cutting force coefficient calculations, i.e. the orthogonal database generated for Ti6Al4V alloy by Budak et al.[36] was directly used. Thus, the calibrations for the force coefficients were not performed for the milling tool used in the tests unlike the mechanistic method. Considering this, it can be claimed that the model predictions are reasonable. However, in cases where the lead angle is negative and the tool tip is cutting into the workpiece, which is the case shown in Figure 3.17, the simulations underestimate the cutting forces in the z direction, e.g. the case shown in Figure 3.15(d). This is explained in the following section.

3.9.3. The Effect of the Tool Tip Contact

When the lead angle (l_e) is negative and the tool tip is cutting into the workpiece, the tip of the ball-end mill moves towards the workpiece since the feed vector has a nonzero component in the tool axis direction. Hence, the tool tip tries to penetrate into the workpiece. This phenomenon cannot be modeled by the cutting mechanism since the cutting speed is zero at the tool tip. As a result of this contact between the tool tip and the workpiece, the tool faces an extra indentation force.
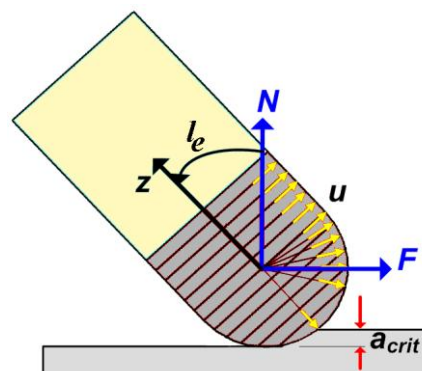
Figure 3.17: Indentation case

43

In order to show the effect of indentation force on the prediction accuracy, a separate statistical analysis was performed for the cases when tool tip is in cut with the workpiece. The result of this analysis is presented in Figure 3.18. The mean of the prediction error in F_z is 18% in these cases. The increase in the mean of the prediction error in F_z force verifies the existence of indentation force for those cases. The indentation force can be modeled, or calibrated for more accurate predictions. However, it is well known that this tool orientation, i.e. negative tilt angle with tool tip in cut, is not a preferred mode of milling, and that is why this has not been taken as a priority for the force modeling.
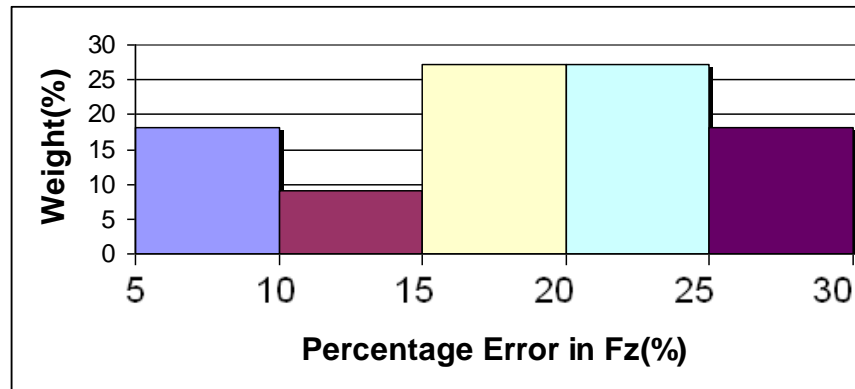
Figure 3.18: Statistical analysis for cases where the tilt angle is negative and the tool tip is in cut with workpiece.

3.9.4. Effect of Lead and Tilt Angles on Cutting Forces

The presented model can be used as an optimization tool while designing a new 5-axis ball-end milling process. The effect of the parameters such as feed rate and the depth of cut are usually predictable. On the other hand, the effects of the lead and the tilt angles on the process are not well known. Thus, the model can be used to determine the lead and tilt angles which will result in minimum milling forces. As an example, for a 5-axis ball-end milling process, the effects of the lead and the tilt angles are demonstrated next. A slotting case with 5 mm cutting depth and 0.05 mm/tooth feed rate is considered where the spindle speed is 1000 rpm. The milling tool is the same tool that was used in the previous tests, and the workpiece material is Ti6Al4V. In order to see the effects of the lead and the tilt angles on the forces, $[0^o, 60^o]$ range for the lead angle, and $[-60^o, +60^o]$ range for the tilt angle with 5° increments were used in the simulations. The objective can be to determine the minimum of the cutting forces, tool deflection or surface error, power etc. In this sample analysis, the resultant force in the

xy plane, F_{xy}, is selected to be minimized. Maximum F_{xy} force in one revolution of the milling tool is plotted as a function of the lead and the tilt angles in Figure 3.19.
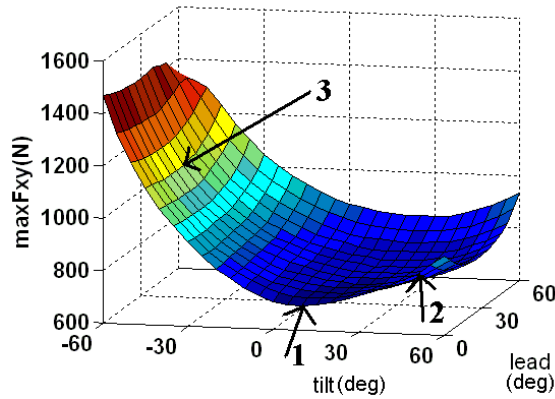
Figure 3.19 Maximum F_{xy} force in one revolution of the milling tool vs. lead and tilt angles.

From the figure, for this case one can conclude that the effect of the tilt angle on the F_{xy} is more than the effect of the lead angle, and the negative high tilt angles must be avoided. In addition, the minimum F_{xy} is obtained when the lead angle is 0° and the tilt angle is 10° (point 1 in Figure 3.19). In order to verify these predictions, cutting tests were performed for 3 points on the surface in Figure 3.19. The comparison between the predictions and the measurements is presented in Table 3.8. It is seen that there is a good agreement between the simulated and experimental results. As a result, it can be concluded that the presented 5-axis ball-end milling force model can be used in the selection of the lead and tilt angle combination that will result in minimum cutting forces for given cutting conditions.

Table 3.8 Simulation and measurement comparison for sample case.

Point	lead, tilt (^{o})	Simulated maximum F_{xy}(N)	Measured maximum F_{xy}(N)
1	0,10	692	653
2	0,50	821	786
3	30,-50	1190	1110

3.9.5. Tool Deflection Predictions

Once the cutting forces are calculated, tool deflections can be predicted. Since the workpiece used in the tests is a rigid block, its deflections were neglected. For two of the cases presented in Figure 3.15(g) and Figure 3.15(h), the errors in the surface

45

normal direction δ_N were measured using a dial gauge and are compared with the model predictions in Table 3.9. The cutting tool used in the cutting tests has 63 mm overhang length and the linear spring k and torsional spring constant k_θ are calibrated as 47458 N/mm and $3*10^7$ N.mm/rad, respectively using the set-up demonstrated in Figure 3.13 for forces less than 1000N.

Case	δ_N Simulation (mm)	δ_N Measurement (mm)
g	0.045	0.040
h	0.017	0.014

Table 3.9 The predicted and measured form errors in the surface normal direction.

As can be seen from the above table, the agreement between the measurements and the predictions for the form errors is acceptable. The small difference can be attributed to the measurement errors, run-out of the tool, and the variation of the clamping stiffness k and k_θ during cutting.

4. STABILITY MODELS FOR 5-AXIS BALL-END MILLING

Chatter is a self excited vibration type resulting from the regeneration mechanism between dynamic chip thickness and cutting forces. Hence, the formulation of dynamic chip thickness and cutting forces is essential for the stability model. In this chapter, firstly dynamic chip thickness is formulated, and then some difficulties in the stability formulation are presented. Afterwards, single-frequency formulation of 5-axis ball-end milling stability is presented and the procedure to construct the stability diagrams is explained. The details of the multi-frequency stability formulation, procedures used to calculate stability diagrams and some observations on the multi-frequency response are presented in the Section 4.5. Then, a time-domain stability model for 5 axis ball-end milling is described concisely in Section 4.6. It is also shown that depending on the kinematic configuration of machine tools, the lead and tilt angles may change the feed direction and thus the measured transfer function matrices need to be oriented accordingly. In Section 4.9, the results for stability limit predictions are demonstrated for three different cases, and they are compared with time-domain model and experimental results. Moreover, the effect of lead and tilt angles on absolute stability limits is presented on the second example case.

4.1. The dynamic chip thickness

The uncut chip thickness h at a point on the cutting edge consists of static and dynamic parts. The static part is due to the feed movement of the tool and it is ignored in the stability analysis since it does not contribute to the regeneration mechanism. On the other hand, the dynamic part h_d results from the displacements of the cutting tool and/or workpiece under the action of the cutting forces. It can be approximated by the scalar product of dynamic displacement vector $\boldsymbol{d}$ and the unit outward surface normal vector $\boldsymbol{u}$ at a cutting point on the cutting edge (Figure 4.1).

$$h_d = \boldsymbol{u} \cdot \boldsymbol{d} \tag{4.1}$$

Since both cutting tool and workpiece can be flexible, the displacements are referred as the relative displacements of the cutting tool with respect to the workpiece. The dynamic displacement vector $\boldsymbol{d}$ is defined as the difference between the current displacements $\left[x_d(t), y_d(t), z_d(t)\right]$ and the displacements one tooth period before $\left[x_d(t-\tau), y_d(t-\tau), z_d(t-\tau)\right]$ in tool coordinate system (TCS):

$$d = \begin{bmatrix} \Delta x_d \\ \Delta y_d \\ \Delta z_d \end{bmatrix} = \begin{bmatrix} x_d(t) - x_d(t-\tau) \\ y_d(t) - y_d(t-\tau) \\ z_d(t) - z_d(t-\tau) \end{bmatrix} \qquad (4.2)$$
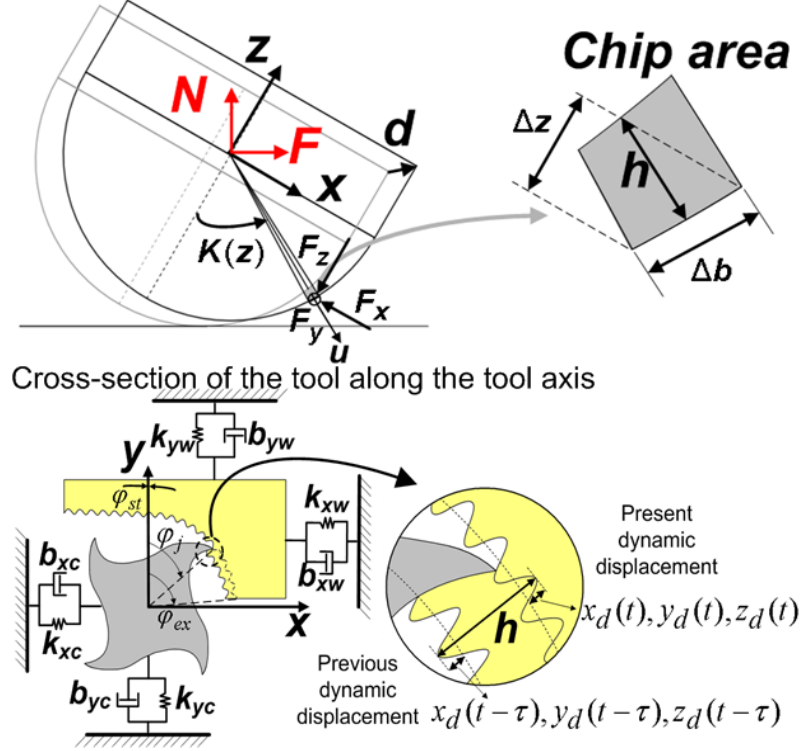
Figure 4.1: The dynamic chip thickness

Unit outward surface normal vector u at a point on the cutting edge depends on local radius and local immersion angle $\varphi_j(z)$ and it's calculated by (3.9)

4.2. Challenges in Stability Analysis of 5-axis Milling

There are some difficulties in stability formulation of 5-axis ball-end milling. Cutting force coefficients K_{rc}, K_{tc}, K_{ac} may depend on the cutting geometry, cutting speed and chip thickness. In ball-end mills, the local cutting speed V is variable along the tool axis because local radius is variable (Figure 3.1). Since determination of dynamic chip thickness magnitude is not possible in frequency domain methods, the average, i.e. the static, chip thickness is used in calculation of cutting force coefficients. Static chip thickness changes both in tool axis direction and in tangential direction (Figure 4.2(a)). For these reasons, cutting force coefficients K_{rc}, K_{tc}, K_{ac} may change along the cutting edge depending on the orthogonal cutting database [36] used. In Figure 4.2(b), variation of K_{rc}, radial cutting force coefficient for Ti6Al4V alloy, is

plotted along the cutting edge as a representative case to demonstrate that amount of variation can be substantial.
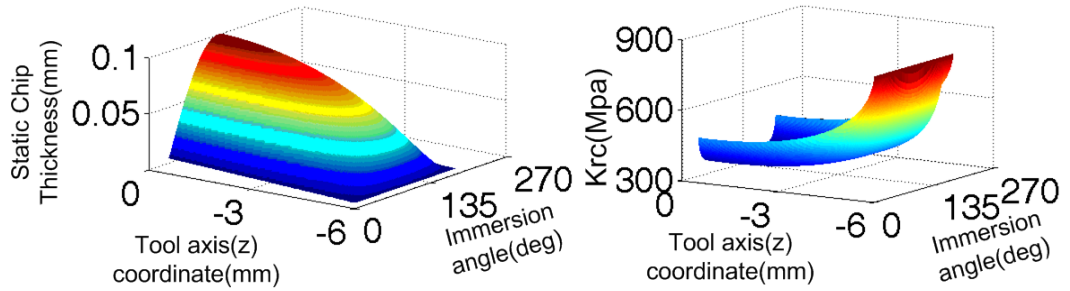
Figure 4.2: Variation of (a) static chip thickness (b) radial cutting force coefficient

Furthermore, due to the ball-end mill geometry and lead and tilt angles, start and exit angles (Figure 4.3(a)) are not constant along the tool axis. Variation of start (φ_{st}) and exit (φ_{ex}) angles along the tool axis for a representative case in 5-axis ball-end milling is presented in the Figure 4.3(b). Dotted curve represents the variation of start angle along the tool axis while the full line curve stands for the exit angle variation.

(a)   (b)
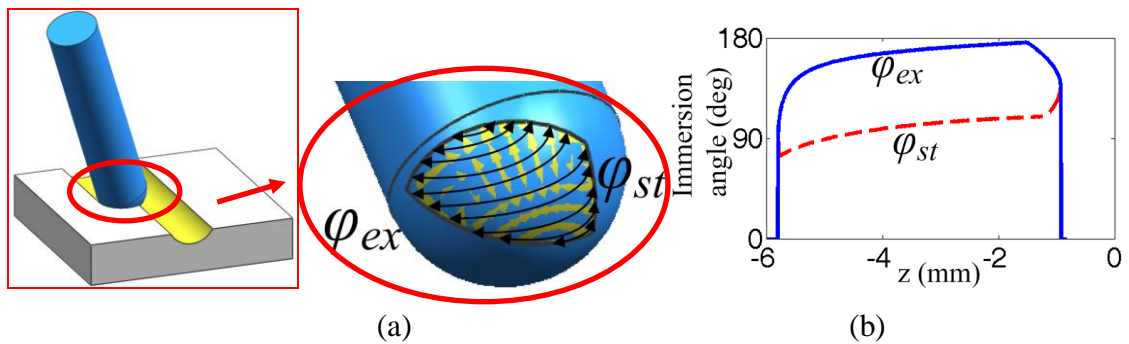
Figure 4.3: (a) A representative engagement boundary in 5-axis milling

(b) Variation of start and exit angles along the tool axis

The variation of cutting force coefficients can be handled by certain averaging techniques as done by Altintas et al.[62]. Although this may introduce some errors, the averaging of the engagement boundaries (start and exit angles) along the tool axis would lead to higher errors in stability predictions. For these reasons, in the stability analysis, ball end mill is divided along the tool axis direction into disc elements that have heights of Δz (Figure 4.4). Then, stability diagram for the process is obtained using an iterative procedure.

4.3. Formulation of the stability problem

Dynamic cutting forces cause displacements which affect chip thickness in the process, and then chip thickness changes dynamic cutting forces. This is a closed loop dynamic interaction [1] and stability of this interaction determines whether there will be chatter vibrations or not. In the previous section, dynamic chip thickness was presented in terms of unit outward normal vector u and dynamic displacement vector d. In this section, the relations for dynamic cutting forces and dynamic displacements are developed. Substituting the relations for the dynamic displacements into the cutting force equations, an eigenvalue problem is obtained. Finally, stability limits are determined by solution of the eigenvalue problem.

In the solution of stability limits, an iterative method is applied. Firstly, cutting depth (a) is incremented by steps of ΔA (Figure 4.4 (b)). For the cutting depth a, the number of disc elements m that are in cut with the workpiece is determined using the engagement model [31]. Since chatter frequencies are close to natural frequencies of the system, the chatter frequency (ω_c) is swept around the natural frequencies and for each ω_c a limiting cutting depth a_{lim} is calculated. The iteration continues by incrementing cutting depth (a) until all the calculated limiting cutting depths (a_{lim}) are less than the cutting depth (a) in the analysis.

The cutting forces in (x), (y) and (z) directions on the jth flute on a disc element l can be expressed for immersion angle φ_j as follows (Figure 4.4(a)):

$$\begin{bmatrix} F_x^{\,l}(\varphi_j) \\ F_y^{\,l}(\varphi_j) \\ F_z^{\,l}(\varphi_j) \end{bmatrix} = T_{xyz} \begin{bmatrix} K_{rc}(\varphi_j, K) \\ K_{tc}(\varphi_j, K) \\ K_{ac}(\varphi_j, K) \end{bmatrix} h_d \Delta b \tag{4.3}$$

where T_{xyz} is defined in (3.24). Edge forces are not included in the analysis since they do not contribute to the regeneration mechanism. h_d is the dynamic chip thickness and Δb is the chip width (Figure 4.1) which depends on height of the disc elements Δz and axial immersion angle K:

$$\Delta b = \frac{\Delta z}{\sin K} \tag{4.4}$$

(a)   (b)
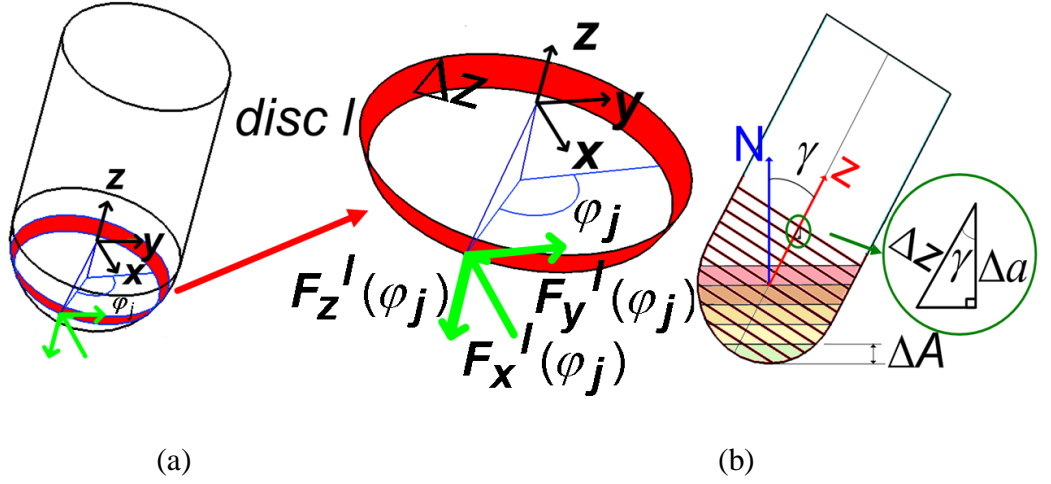
Figure 4.4: (a) Dynamic cutting forces in x, y, z directions on j^{th} flute on disc element l

(b) Discrete heights (Δz), (Δa) and (ΔA)

Cutting depth (a) is defined in the surface normal direction in 5-axis milling. Hence, in the formulation, height of disc elements Δz needs to be written in terms of the disc height along the surface normal direction Δa as follows (Figure 4.4(b)):

$$\Delta z = \frac{\Delta a}{\cos \gamma} \tag{4.5}$$

where γ_i is the inclination angle which exists between the tool axis (z) and surface normal axis (N) due to lead angle (l_e) and tilt angle (t_i) (Figure 4.4(b)). It is calculated using the equation below:

$$\gamma_i = \cos^{-1}\left[\cos(l_e)\cos(t_i)\right] \tag{4.6}$$

After the relations obtained for the dynamic chip thickness (h_d), the chip width (Δb) and disc height (Δz) are substituted into (4.3), and defining $\boldsymbol{B}^{lj}(\varphi_j)$ matrix as follows:

$$\boldsymbol{B}^{lj}(\varphi_j) = \frac{1}{\cos \gamma_i \sin K} \boldsymbol{T_{xyz}} \begin{bmatrix} K_{rc}(\varphi_j, K) \\ K_{tc}(\varphi_j, K) \\ K_{ac}(\varphi_j, K) \end{bmatrix} \boldsymbol{u} \tag{4.7}$$

Equation (4.3) can be rewritten as:

$$\begin{bmatrix} F_x^{l}(\varphi_j) \\ F_y^{l}(\varphi_j) \\ F_z^{l}(\varphi_j) \end{bmatrix} = \Delta a \boldsymbol{B}^{lj}(\varphi_j) \begin{bmatrix} \Delta x_d \\ \Delta y_d \\ \Delta z_d \end{bmatrix} \tag{4.8}$$

51

Summing the cutting forces contributed by all the teeth on disc element l, total dynamic forces at reference immersion angle φ are found as follows:

$$\begin{bmatrix} F_x^{\,l}(\varphi) \\ F_y^{\,l}(\varphi) \\ F_z^{\,l}(\varphi) \end{bmatrix} = \Delta a \boldsymbol{B}^l(\varphi) \begin{bmatrix} \Delta x_d \\ \Delta y_d \\ \Delta z_d \end{bmatrix} \tag{4.9}$$

where $\boldsymbol{B}^l(\varphi)$ is the summation of $\boldsymbol{B}^{lj}(\varphi_j)$ for all n teeth:

$$\boldsymbol{B}^l(\varphi) = \sum_{j=1}^{n} \boldsymbol{B}^{lj}(\varphi_j) \tag{4.10}$$

Since the immersion angle φ changes with time, (4.9) can also be expressed in time domain:

$$\begin{bmatrix} F_x^{\,l}(t) \\ F_y^{\,l}(t) \\ F_z^{\,l}(t) \end{bmatrix} = \Delta a \boldsymbol{B}^l(t) \begin{bmatrix} \Delta x_d \\ \Delta y_d \\ \Delta z_d \end{bmatrix} \tag{4.11}$$

where t represents time and $\boldsymbol{B}^l(t)$ is a time dependent periodic directional coefficient matrix. It can be represented by Fourier series expansion as follows:

$$\boldsymbol{B}^l(t) = \sum_{r=-\infty}^{r=\infty} \boldsymbol{B}_r^l e^{ir\omega_t t} \; , \quad \boldsymbol{B}_r^l = \frac{1}{\tau} \int_0^{\tau} \boldsymbol{B}^l(t) e^{-ir\omega_t t} \, dt \tag{4.12}$$

where ω_t is the tooth passing frequency and τ is the tooth passing period. The Fourier series expansion presented in (4.12) can also be represented in the angular domain, substituting the relation $\omega_t t = n\varphi$ where n represents the total number of flutes on the cutting tool:

$$\boldsymbol{B}^l(\varphi) = \sum_{r=-\infty}^{r=\infty} \boldsymbol{B}_r^l e^{irn\varphi} \; , \quad \boldsymbol{B}_r^l = \frac{1}{\varphi_p} \int_0^{\varphi_p} \boldsymbol{B}^l(\varphi) e^{-irn\varphi} \, d\varphi \tag{4.13}$$

φ_p is the angle between successive flutes which is defined as pitch angle and it is equal to $2\pi/n$. Depending on the number of terms used in the Fourier series expansion of the directional coefficient matrix, there are two different solution methods for the solution of stability limits, namely single- and multi-frequency solution methods. Single-frequency solution is explained in the following section while multi-frequency solution is presented in the Section 4.5.

4.4. Single-frequency Method

The Fourier series expansion in (4.13) can be truncated by using the first term only which is the average component of the Fourier series expansion of $\boldsymbol{B}^l(\varphi)$. It is represented by $\boldsymbol{B}_o{}^l$ as proposed by the single frequency method [54]. $\boldsymbol{B}_o{}^l$ is a time invariant but immersion dependent coefficient matrix and it can be calculated by averaging the $\boldsymbol{B}^l(\varphi)$ in a tooth period:

$$\boldsymbol{B}_o{}^l = \frac{1}{\varphi_p} \int\limits_{o}^{\varphi_p} \boldsymbol{B}^l(\varphi) d\varphi \tag{4.14}$$

Substituting $\boldsymbol{B}_o{}^l$, (4.11) reduces to:

$$\begin{bmatrix} F_x{}^l(t) \\ F_y{}^l(t) \\ F_z{}^l(t) \end{bmatrix} = \Delta a \boldsymbol{B}_o{}^l \begin{bmatrix} \Delta x_d \\ \Delta y_d \\ \Delta z_d \end{bmatrix} \tag{4.15}$$

Having defined the cutting forces in terms of the disc height along the surface normal direction (Δa), the average directional coefficient matrix ($\boldsymbol{B}_o{}^l$) and the dynamic displacement vector (**d**), the next step in the stability formulation is the definition of the dynamic displacement vector at the stability limit in terms of the transfer function matrix of the structure and cutting forces. In single frequency solution, dynamic displacement vector is assumed to be composed of only chatter frequency ω_c as follows:

$$\begin{bmatrix} \Delta x_d \\ \Delta y_d \\ \Delta z_d \end{bmatrix} = (1 - e^{-i\omega_c \tau}) \boldsymbol{G}(i\omega_c) \begin{bmatrix} F_x(t) \\ F_y(t) \\ F_z(t) \end{bmatrix} \tag{4.16}$$

$F_x(t)$, $F_y(t)$, $F_z(t)$ are dynamic cutting forces in TCS coordinate system. They are also assumed to have magnitudes only at chatter frequency ω_c in single-frequency solution. $\boldsymbol{G}$ is the transfer function matrix identified at the cutter workpiece contact zone oriented with respect to the TCS coordinate system. It relates the cutting forces in (x), (y) and (z) directions to displacements in the same directions. Orientation of the measured transfer function matrix is explained in the last section. In cases where both cutting tool and workpiece are flexible, the transfer function matrix $\boldsymbol{G}$ is equal to the

summation of individual transfer function matrices of the cutting tool and the workpiece.

Inserting (4.16) into (4.15), the dynamic cutting forces on disc l at the stability limit become:

$$\begin{bmatrix} F_x{}^l \\ F_y{}^l \\ F_z l \end{bmatrix} e^{i\omega_c t} = \Delta a \boldsymbol{B_o}^l (1 - e^{-i\omega_c \tau}) \boldsymbol{G}(i\omega_c) \begin{bmatrix} F_x \\ F_y \\ F_z \end{bmatrix} e^{i\omega_c t} \tag{4.17}$$

Now the dynamic elemental forces can be calculated using (4.17) for each disc element. However, in order to obtain the stability limit of the system, all the disc elements in cut have to be considered simultaneously. Therefore, it is proposed to sum the individual dynamic forces acting on each element. Writing this equation for the other disc elements and summing up the equations side by side results in the following eigenvalue problem:

$$\begin{bmatrix} F_x \\ F_y \\ F_z \end{bmatrix} e^{i\omega_c t} = \Delta a (1 - e^{-i\omega_c \tau}) \left(\sum_{l=1}^{m} \boldsymbol{B_o}^l \right) \boldsymbol{G}(i\omega_c) \begin{bmatrix} F_x \\ F_y \\ F_z \end{bmatrix} e^{i\omega_c t} \tag{4.18}$$

where m is the total number of disc elements in the analysis.(4.18) has non-trivial solutions if and only if the following determinant is equal to zero:

$$\det\{\boldsymbol{I} + \lambda\boldsymbol{\Phi}\} = 0 \tag{4.19}$$

where $\boldsymbol{\Phi}$ and complex eigenvalue λ are defined as follows:

$$\lambda = -\Delta a(1 - e^{-i\omega_c \tau}) = \lambda_R + i\lambda_I$$

$$\boldsymbol{\Phi} = \left(\sum_{l=1}^{m} \boldsymbol{B_o}^l \right) [G(i\omega_c)] \tag{4.20}$$

Since size of the $\boldsymbol{\Phi}$ matrix is 3 by 3, the solution of (4.19) produces 3 different eigenvalues for each chatter frequency ω_c. For each eigenvalue, the limiting cutting depth is calculated. However, the eigenvalue that results in the minimum positive limiting depth is used in the stability diagrams. Substituting $e^{-i\omega_c \tau} = \cos\omega_c \tau - i\sin\omega_c \tau$ into (4.20), elemental critical depth at chatter frequency ω_c can be written as [54]:

$$\Delta a_{\lim} = -\frac{1}{2}\left[\frac{\lambda_R(1 - \cos\omega_c \tau) + \lambda_I \sin\omega_c \tau}{(1 - \cos\omega_c \tau)} + i\frac{\lambda_I(1 - \cos\omega_c \tau) - \lambda_R \sin\omega_c \tau}{(1 - \cos\omega_c \tau)} \right] \tag{4.21}$$

54

Since Δa_{lim} is a real number, the imaginary part of (4.21) should disappear. Hence, the following relation is obtained:

$$\lambda_I (1 - \cos \omega_c \tau) = \lambda_R \sin \omega_c \tau \tag{4.22}$$

Defining $\kappa = \dfrac{\lambda_I}{\lambda_R} = \dfrac{\sin \omega_c \tau}{1 - \cos \omega_c \tau}$, the elemental critical depth Δa_{lim} can be found as:

$$\Delta a_{\text{lim}} = -\frac{1}{2} \lambda_R (1 + \kappa^2) \tag{4.23}$$

Since there are m discs in the analysis, limiting cutting depth (a_{lim}) at chatter frequency ω_c is calculated as follows:

$$a_{\text{lim}} = m \Delta a_{\text{lim}} \tag{4.24}$$

4.4.1. Stability diagrams

Once the limiting cutting depths are obtained by sweeping the chatter frequency around the natural frequencies of the dynamic system, the corresponding spindle speeds can be calculated as proposed in [54]. The following equation defines the relation between the chatter frequency ω_c and tooth passing period τ :

$$\omega_c \tau = \varepsilon + 2k\pi \tag{4.25}$$

where ε is the phase shift between the present and the previous vibration waves (Figure 4.1) and k is the integer number of full vibration waves marked on the cut. Phase shift depends on the phase angle $\phi_{ph} = \tan^{-1} \kappa$, and is determined by [54]:

$$\varepsilon = \pi - 2\varphi_{ph} \tag{4.26}$$

The corresponding spindle speed n_s can be determined after the tooth passing period τ is calculated as follows:

$$\tau = \frac{1}{\omega_c} (\varepsilon + 2k\pi) \rightarrow n_s = \frac{60}{n\tau} \tag{4.27}$$

Finally the stability lobes can be obtained by plotting the stability limits with respect to corresponding spindle speeds.

4.5. Multi-frequency Method

In multi-frequency solution, higher order terms of the Fourier series expansion of the directional coefficient matrix, $\boldsymbol{B}^l$ are also included in the formulation as follows:

$$\boldsymbol{B}^l(\varphi) = \boldsymbol{B}_o^l + \boldsymbol{B}_1^l e^{in\varphi} + \boldsymbol{B}_{-1}^l e^{-in\varphi} + \ldots\ldots\ldots + \boldsymbol{B}_{h_s}^l e^{h_s in\varphi} + \boldsymbol{B}_{-h_s}^l e^{-h_s in\varphi} \qquad (4.28)$$

where h_s is the number of harmonics included in the stability analysis. Response of the dynamic forces to the additional harmonic terms should be taken into consideration. In the stability limit, the dynamic forces at the integer multiples of the tooth passing frequency are added on the ones at the chatter frequency. Consequently, the dynamic cutting forces on a disc element l can be represented as follows:

$$\begin{bmatrix} F_x^l(t) \\ F_y^l(t) \\ F_z^l(t) \end{bmatrix} = e^{i\omega_c t} \left(\sum_{k=-h_s}^{k=h_s} \begin{bmatrix} F_x^l \\ F_y^l \\ F_z^l \end{bmatrix}_k e^{ik\omega_t t} \right) = \sum_{k=-h_s}^{k=h_s} \begin{bmatrix} F_x^l \\ F_y^l \\ F_z^l \end{bmatrix}_k e^{i(\omega_c + k\omega_t)t} \qquad (4.29)$$

Using superposition principle, the dynamic displacement vector in TCS can be written in terms of the transfer function matrix of the dynamic system, $\boldsymbol{G}$ and resultant dynamic cutting forces [64]:

$$\begin{bmatrix} \Delta x_d \\ \Delta y_d \\ \Delta z_d \end{bmatrix} = (1 - e^{-i\omega_c \tau}) \sum_{k=-h_s}^{k=h_s} \boldsymbol{G}(i\omega_c + ik\omega_t) \begin{bmatrix} F_x \\ F_y \\ F_z \end{bmatrix}_k e^{i(\omega_c + k\omega_t)t} \qquad (4.30)$$

As presented in single-frequency method [64], the relations developed for $\boldsymbol{B}^l$, dynamic cutting forces and dynamic displacement vector in multi-frequency solution are substituted into the (4.11). Following some simplifications [64], the pth harmonic of the dynamic cutting forces on the disc element l can be written in terms of total forces as follows:

$$\{\boldsymbol{F}\}_p = \begin{bmatrix} F_x^l \\ F_y^l \\ F_z^l \end{bmatrix}_p = \Delta a (1 - e^{-i\omega_c \tau}) \sum_{k=-h_s}^{k=h_s} \boldsymbol{B}_{p-k}^l \boldsymbol{G}(i\omega_c + ik\omega_t) \begin{bmatrix} F_x \\ F_y \\ F_z \end{bmatrix}_k \; ; \; p,k = 0, \pm 1, ..., \pm h_s \qquad (4.31)$$

After representing the above relation in matrix notation [54] and summing the corresponding relations for the m disc elements in the analysis side by side, the following eigenvalue problem is obtained.

$$\begin{Bmatrix} \{\boldsymbol{F}\}_o \\ \{\boldsymbol{F}\}_1 \\ \{\boldsymbol{F}\}_{-1} \\ ... \end{Bmatrix} = -\lambda \left(\sum_{l=1}^{m} \boldsymbol{\Phi}^l(\omega_c, \omega_t) \right) \begin{Bmatrix} \{\boldsymbol{F}\}_o \\ \{\boldsymbol{F}\}_1 \\ \{\boldsymbol{F}\}_{-1} \\ ... \end{Bmatrix} \qquad (4.32)$$

where $\boldsymbol{\Phi}^l(\omega_c,\omega_t)$ matrix corresponds to disc l and it is defined as follows:

$$\boldsymbol{\Phi}^l(\omega_c,\omega_t) = \begin{array}{c} \\ p=0 \\ p=1 \\ p=-1 \\ \\ \end{array}\begin{array}{cccc} k=0 & k=1 & k=-1 & ... \\ \left[\begin{array}{cccc} \boldsymbol{B}_o^l\boldsymbol{G}(i\omega_c) & \boldsymbol{B}_{-1}^l\boldsymbol{G}(i\omega_c+i\omega_t) & \boldsymbol{B}_1^l\boldsymbol{G}(i\omega_c-i\omega_t) & ... \\ \boldsymbol{B}_1^l\boldsymbol{G}(i\omega_c) & \boldsymbol{B}_o^l\boldsymbol{G}(i\omega_c+i\omega_t) & \boldsymbol{B}_2^l\boldsymbol{G}(i\omega_c-i\omega_t) & ... \\ \boldsymbol{B}_{-1}^l\boldsymbol{G}(i\omega_c) & \boldsymbol{B}_{-2}^l\boldsymbol{G}(i\omega_c+i\omega_t) & \boldsymbol{B}_o^l\boldsymbol{G}(i\omega_c-i\omega_t) & ... \\ ... & ... & ... & ... \end{array}\right) \end{array} \tag{4.33}$$

Eigenvalue λ is defined as $\lambda = -\Delta a(1-e^{-i\omega_c\tau})$. If the (4.32) has non-trivial solutions, the following determinant should be equal to zero.

$$\det\left\{\boldsymbol{I}+\lambda(\sum_{l=1}^{m}\boldsymbol{\Phi}^l(\omega_c,\omega_t))\right\}=0 \tag{4.34}$$

where $\boldsymbol{I}$ is the identity matrix and size of it is ($3(2h_s+1)$ by $3(2h_s+1)$). $3(2h_s+1)$ eigenvalues are determined using (4.34) and corresponding limiting cutting depths are calculated as explained in the next section.

4.5.1. Numerical Solution Procedure

Stability diagrams are obtained using an iterative procedure. Cutting depth a is incremented by steps of ΔA as presented in Figure 4.4. The presented stability formulation is applied on the m disc elements which are in cut with the workpiece for the current cutting depth a. Since (4.34) is tooth passing frequency ω_t, and chatter frequency ω_c dependent, the eigenvalues can be solved for particular ω_t and ω_c pairs. After each eigenvalue λ is calculated, limiting cutting depths corresponding to each eigenvalue can be determined as follows:

$$a_{\lim}=-m\frac{\lambda}{1-e^{-i\omega_c\tau}} \tag{4.35}$$

The following procedure is applied for determination of stability diagrams:

- Decide on the number of harmonics, h_s, to be included in the multi-frequency solution.

- Choose the spindle range of interest for the stability diagram by deciding on the minimum (n_{min}), maximum spindle speed (n_{max}) and spindle speed increment (Δn) which is the difference between the consecutive spindle speeds in the range. For each spindle speed in the range, calculate tooth passing frequency ω_t [1].

- Unlike single frequency solution where the chatter frequency is always close to one of the modal frequencies of the system, in multi-frequency case the chatter frequency can be far from the modal frequencies. The reason for that is the higher order terms in the eigenvalue matrix given by (4.33) which contain transfer functions to be calculated at addition and subtraction of chatter frequency of the system and integer multiples of tooth passing frequency. When one of these additions or subtractions is close to one of the natural modes of the system, then there is a possibility of a lobe in the stability diagram similar to the single frequency solution which results in peaks in the diagram when the chatter frequency is close to one of the modal ones. In such a case, however, the location of the lobes would be at different speeds than the ones for the regular lobes. For example, it is mathematically possible that $(\omega_c-\omega_t)$ would be close to the modal frequency ω_n if ω_c is close to $2.5\omega_n$ and ω_t is close to close to $1.5\omega_n$. In such a case an additional lobe would appear between the first and the second lobes on the stability diagram. This, of course, heavily depends on whether the higher order terms of the directional coefficients in (4.33), i.e. B_i's, are large enough compared to the fundamental one, B_o. This is closely related to the variation pattern of the directional coefficients which are strongly influenced by the total contact time between a cutting edge and the material, and thus the radial depth of cut. Hence, a larger chatter frequency zone needs to be swept for multi-frequency range of interest and solution. Considering the natural frequencies of the system, range of tooth passing frequencies in the spindle speed number of harmonics, chatter frequency range should be selected where ω_{min}, ω_{max} and $\Delta\omega$ stand for the minimum, maximum chatter frequencies and chatter frequency increment, respectively.

- In the frequency range selected, for each spindle speed, *golden section search method* [95] is applied to find the chatter frequencies that result in real stability limits, i.e. the imaginary part of stability limit in (4.35) is zero. The method determines the absolute minimum value of the imaginary parts of the calculated $3(2h_s+1)$ stability limits at each chatter frequency and stores the sign of it. If there is a sign change between consecutive chatter frequencies, it brackets the solution in the interval, $\Delta\omega$. Afterwards, it determines the chatter frequencies

and corresponding real stability limits with a predetermined error tolerance by decreasing the size of the interval at each search step as shown in Figure 4.5.
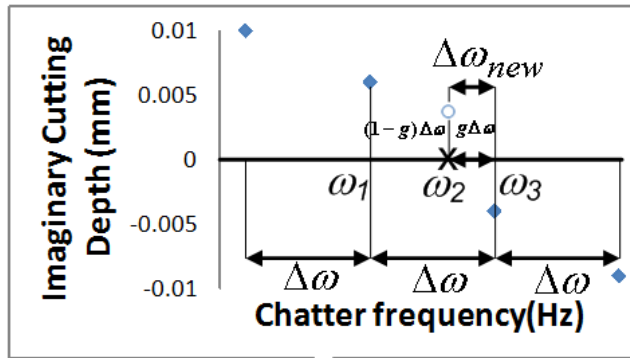
Figure 4.5: Golden section search algorithm. (1-g) is the golden ratio which is equal to 0.6180340

- Real parts of the stability limits should be positive to consider them as solutions. Therefore, chatter frequencies with negative stability limits are eliminated from the solution.

- This procedure is continued until all the calculated limiting cutting depths are less than the cutting depth a used in iterations. Otherwise, the iteration continues by increasing the cutting depth a by ΔA.

4.5.2. Effect of number of harmonics, ball-end mill geometry, lead and tilt angles on directional coefficients

As presented in (4.28), directional coefficient matrix $\boldsymbol{B}^l(\varphi)$ can be represented by different number of harmonics in multi-frequency solution. In Figure 4.6, for an example case, the effect of using different number of harmonics on the approximation of directional coefficient matrix, $\boldsymbol{B}(\varphi)$ which is the summation of directional coefficient matrices, $\boldsymbol{B}^l(\varphi)$, of each disc l in the analysis, is shown by plotting the variation of a representative element, $\boldsymbol{B}[1,1]$ along one revolution. If the directional coefficient matrix is represented by only the average term, its variation by the rotation angle is not taken into account as shown in Figure 4.6. As the number of harmonics is increased in the analysis, approximation of the Fourier series expansion gets closer to the directional coefficient matrix. For the example case, when 5 harmonics is included in the analysis, it is seen that the series approximation is very close to the actual directional coefficient matrix in Figure 4.6.
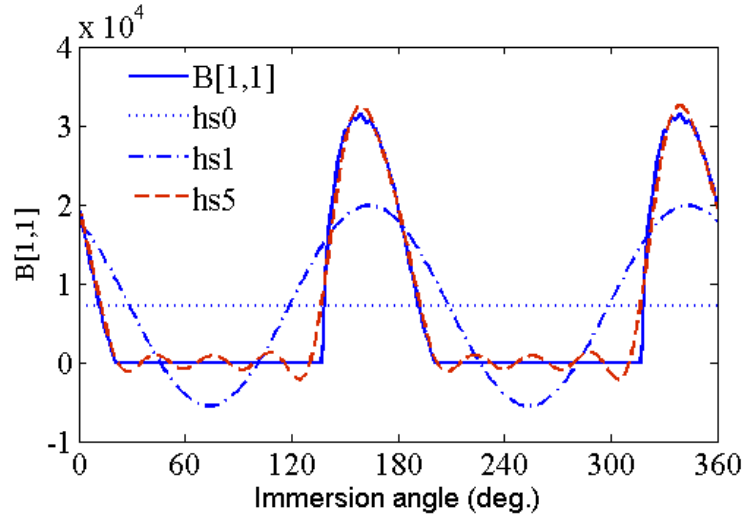
Figure 4.6: Effect of number of harmonics on an element, **B**[1,1], of the total directional coefficient matrix **B** (lead,tilt: 30°,first cut, a:2mm, s: 0mm, cross-feed direction: negative, R_o: 6mm)

5-axis ball-end milling is mostly used in finishing operations of complex surfaces where radial immersions are low. Based on the studies in 3-axis flat-end milling [57]-[61], it is expected that multi-frequency effects are observed on stability diagrams for low radial immersion operations where the ratio of time-spent in cutting to non-cutting is very low. However, in ball-end milling operations, even for the cases where the radial immersion is very low, the ratio of cutting to non-cutting time is not as low as for 3-axis flat-end milling. This statement can be validated by comparing the variation of first row first column elements of directional coefficient matrices [54] (that relates the dynamic displacements to the dynamic cutting forces in x-direction) in one revolution for a flat-end milling operation (Figure 4.7(a)) and a ball-end milling operation (lead 0,tilt 0 case in Figure 4.7(b)). These plots demonstrate the immersion angles where the cutting tools are in and out-of-cut with the workpiece. The nonzero region in the directional coefficient plot determines the immersion angles where cutting tool is in cut with the workpiece. Both of the operations are finishing processes (following cut), where the cutting tools have 12 mm diameter with two flutes and 30° helix angle. The axial depth of cut is 1 mm, and the cross-feed direction is negative with step over of 0.1mm. The only difference is in the tool geometries between the two operations (one flat end mill, the other is ball-end mill). As shown in Figure 4.7(a), the a_{xx} element of the directional coefficient matrix [64] is nonzero for only a small amount of time for flat-end milling case. However, it is seen that time in cut with the workpiece is more for the ball-end

60

mill (lead 0, tilt 0 case in Figure 4.7(b)). Moreover, lead and tilt angles also have effects on the ratio of time spent in cutting to non-cutting, since they change engagement boundaries between the cutting tool and workpiece. These effects are demonstrated in Figure 4.7(b) for two different lead and tilt angle combinations. In the first case, both lead and tilt angles are selected to be 30° in which width of immersion zone decreased slightly with respect to the (0° lead, 0° tilt) case. However, the time spent in cutting in this case is still higher than the 3-axis flat-end milling. On the other hand, application of lead and tilt angles of -30° has an increasing effect on the width of the immersion zone as presented in Figure 4.7(b). Finally, it can be concluded that multi-frequency effects in 5-axis ball-end milling are less with respect to 3-axis flat-end milling due to the effects of ball-end mill geometry, lead and tilt angles on the width of the immersion zones.
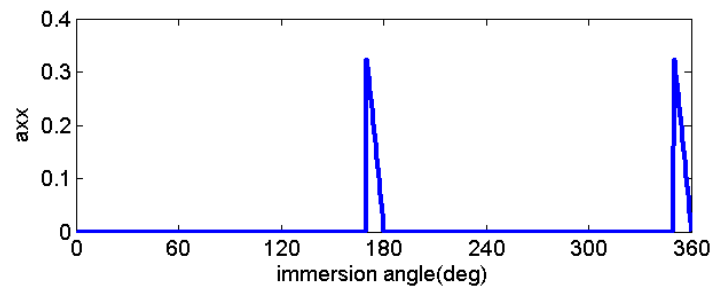
(a)
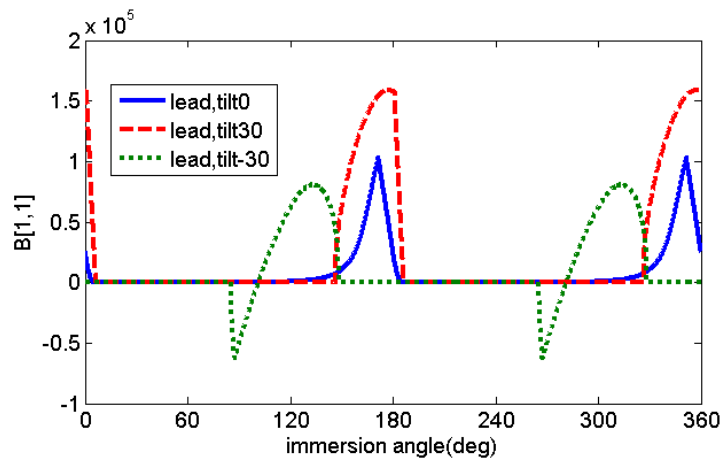
(b)

Figure 4.7: Variation of an element of the directional coefficient matrix in (a) flat-end milling (b) ball-end milling operations

61

4.5.3. Verification of the effect of ball-end mill geometry on the multi-frequency response

In order to show the of effect ball-end mill geometry on multi-frequency response, a case in the literature where multi-frequency effects are presented on a stability diagram is selected. It is a 3-axis milling flat-end milling case presented by Mann et al. [96] where the cutting tool is a 19.05mm diameter tool with one cutting flute. The feed rate is 0.1016mm/tooth, radial depth of cut is 4.515 mm and it is an up milling operation. In the experimental set-up, only the flexibility in x-direction is considered since the structure is much more rigid in other directions. The stiffness value (k), natural frequency (f_n) and damping ratio (ζ) are measured to be 2200N/mm, 146.5 Hz and 0.0032, respectively. The workpiece is aluminium 7075-T6. The cutting force coefficient in tangential direction (K_{tc}) is 550 MPa, and the one in the radial direction (K_{rc}) is 200 MPa.

Applying the proposed stability formulations and the solution procedure in this paper to 3-axis flat-end milling case, the stability diagrams are obtained using single-frequency method and multi-frequency method with five harmonics (Figure 4.8(a)). The result of multi-frequency solution is very close to the presented result in [96]. It is seen that when five harmonics are included in the multi-frequency solution, an extra lobe appears. However, this is not the case when a ball-end mill is used with the same process parameters. The predicted stability diagrams obtained by single and multi-frequency methods are shown in Figure 4.8(b). The single and multi-frequency solution gave close results in this case without an added lobe. In order to understand the reason for this result, a fictitious case is considered. Although the start and exit angles are variable along the tool axis in ball-end milling, by modifying the engagement model[31], these angles are taken as the same as the ones for the flat end milling case, i.e. fixed angles along the tool axis, 0° and 58.265^{o}, respectively. In the stability diagram for this fictitious ball-end milling case, a noticeable added lobe is seen in Figure 4.8(c) when multi-frequency solution with five harmonics is used. This observation reveals that the immersion geometry of ball-end milling is the reason for not having added lobes even when the multi-frequency solution is used.
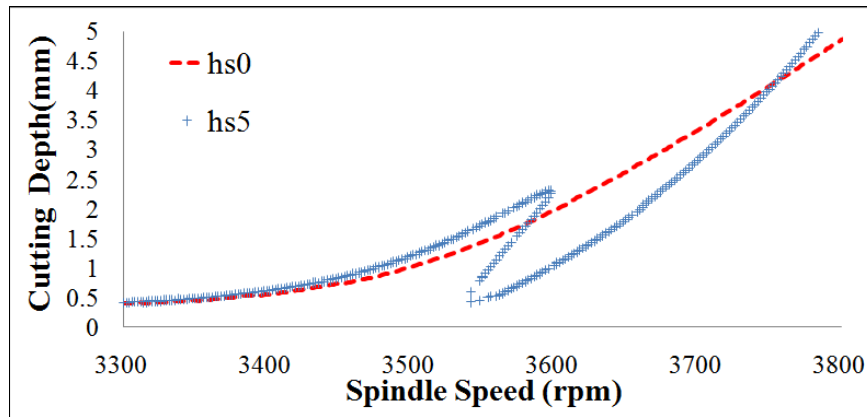
(a)
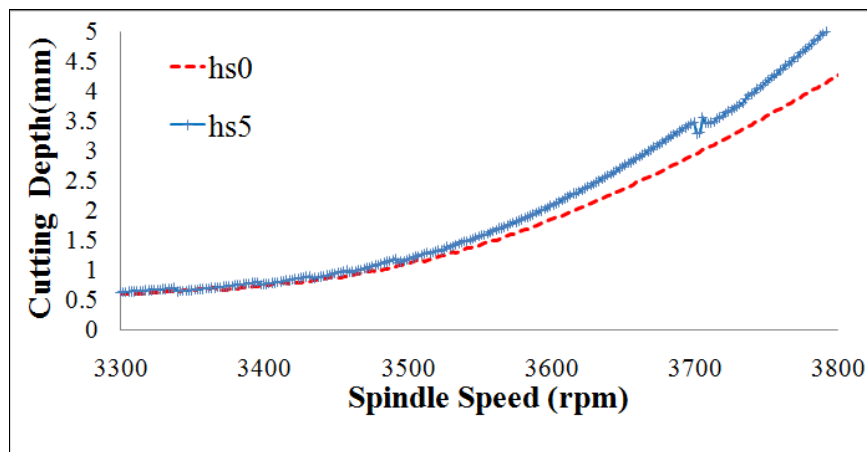
(b)
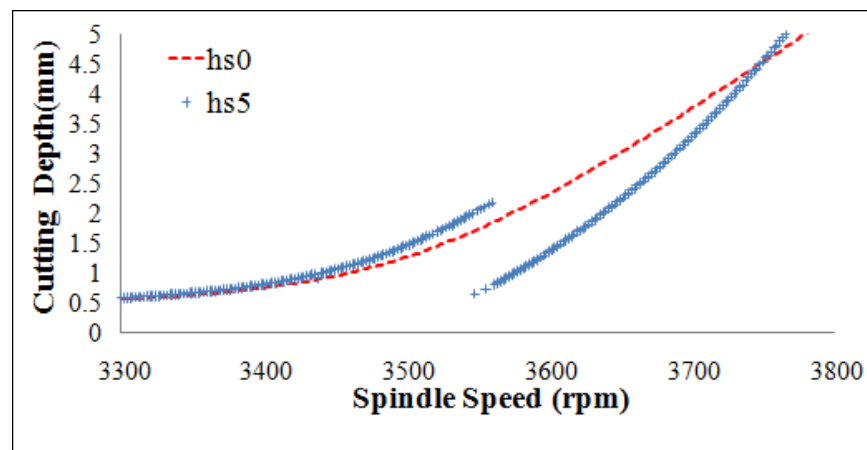
(c)

Figure 4.8: Stability diagrams(a) 3-axis flat-end milling case, radial depth is 4.515 mm (start angle and exit angle are 0° and 58.265^o) (b) A following cut ball-end milling case where step over is 4.515 mm (c) A fictitious ball-end milling case where start and exit angles are fixed as 0° and 58.265^o, respectively

In Figure 4.9, the contact zone between the cutting tool and workpiece is shown for the three different cases presented in the previous graph in order to show the effect

of ball-end mill geometry on the contact zone. The cutting depth is selected as 2 mm in each case. In Figure 4.9(a) and (b), the contact zone corresponding to the cases in Figure 4.8 (a) and Figure 4.8 (b) are presented. Increased contact zone on the ball-end tool and variable engagement limits (start and exit angles) in Figure 4.9(b) is easily observable. Moreover, in Figure 4.9(c), the engagement zone corresponding to the fictitious case of Figure 4.8(c) where start and exit angles are fixed is presented. As can be seen the contact zone is much smaller in this case. In conclusion, start and exit angles are variable along the tool axis and engagement zones are larger even for small radial depths in ball-end milling. Hence, the effects of multi-frequency terms on stability diagrams are suppressed for ball-end mills.

(a)

(b)   (c)
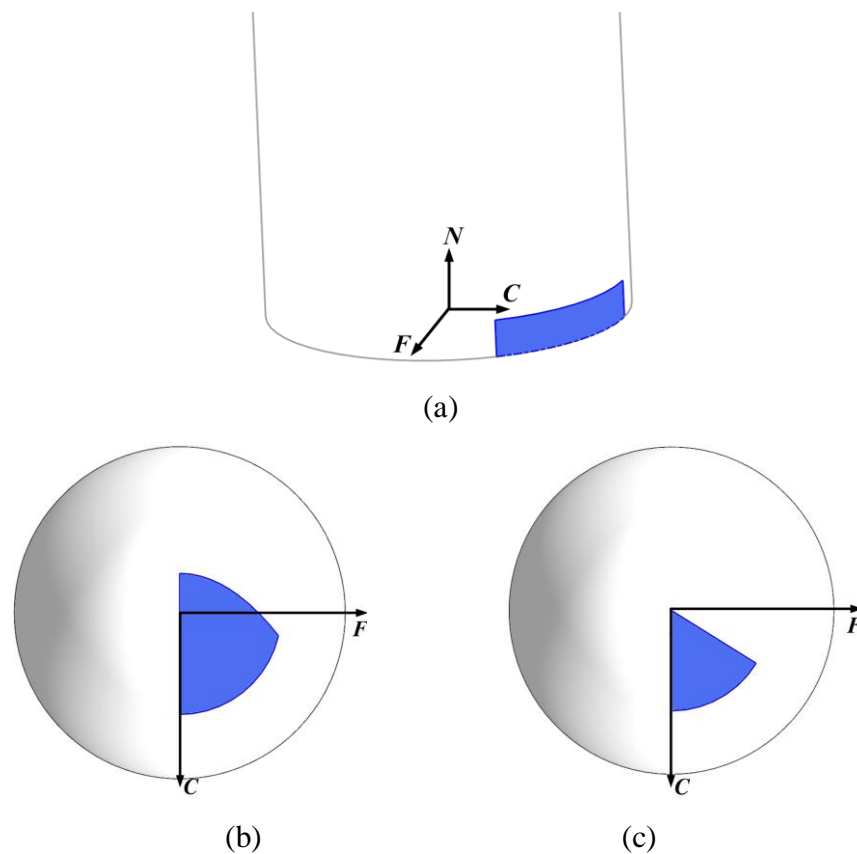
Figure 4.9: Contact zones on different operations where cutting depth is 2 mm in each case (a) 3-axis flat-end milling case, radial depth is 4.515 mm (start angle and exit angle are 0° and 58.265°) (b) A following cut ball-end milling case where step over is 4.515 mm (c) A fictitious ball-end milling case, start and exit angles are fixed as 0° and 58.265°)

4.6. Time-domain Method

A time domain stability model was developed for 5-axis ball-end milling operations in order to verify the frequency domain model's predictions. A schema showing the basic structure of the time domain model is presented in Figure 4.10 and it is described here briefly. For a given set of cutting conditions, the process under consideration is simulated in discrete time intervals. Each discrete time is related to a certain immersion angle of the milling tool by spindle speed ω_s (Figure 4.10). At each immersion angle, the dynamic cutting forces and resulting displacements are calculated. These displacements affect the dynamic chip thickness and act as a feedback loop to the dynamic cutting forces. The power spectrum of the simulated displacements and the trend of variation of dynamic displacements are used to judge the stability of the system. If the peak of the spectrum occurs at the tooth passing frequency, the process is considered to be stable whereas if it is near one of the natural frequencies of the system, then the process is declared to be unstable. In time domain simulations, nonlinearities such as tool going out-of-cut can be taken into consideration. Hence, this non-linearity has been taken into account. Moreover, frequency contents of dynamic displacements and cutting forces can be analyzed which are demonstrated in the results section. However, obtaining stability diagrams using time-domain is very time consuming.
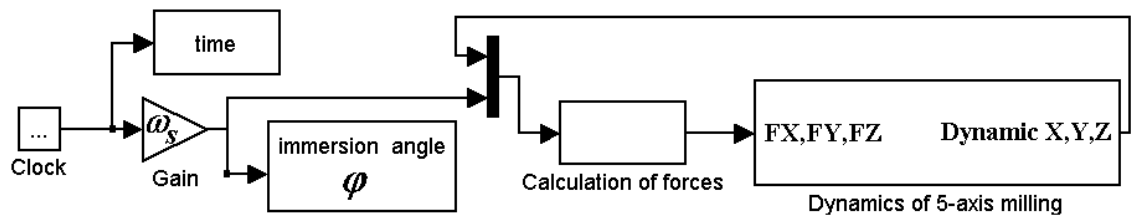
Figure 4.10: Time-domain model

4.7. Measurement of FRFs

The dynamic properties of cutting tools, i.e. transfer functions, are measured using impact tests. An impact hammer, which has a load cell on it, is used to excite the cutting tool at the tool tip and the response at the tool tip is acquired using an accelerometer (Figure 4.11). Using the force and the acceleration signals, frequency response functions (FRFs), i.e. transfer functions of the cutting tools in X and Y directions are obtained. Since the cutting tools are much more rigid in Z direction compared to X and Y directions, the flexibility in Z direction is neglected.
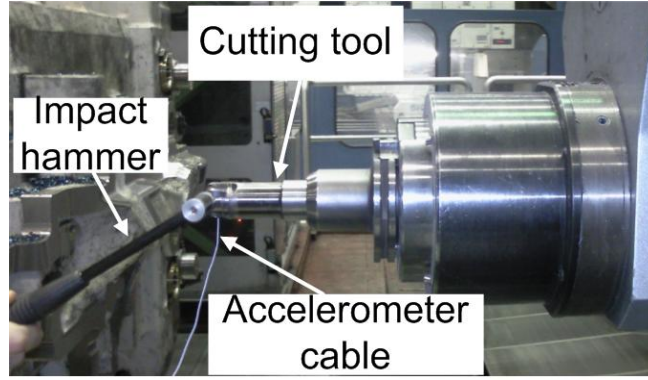
Figure 4.11 : FRF measurement

4.8. Orientation of the measured transfer function matrix

Unless measured transfer functions in two orthogonal directions are identical, feed direction may have an important effect on stability diagrams in 5-axis milling. Depending on the machine tool's kinematic configuration, the feed direction may depend on lead and tilt angles. For example, if the rotary axes of the machine tool are on the table side as shown in Figure 3.3 and Figure 4.12, the feed direction with respect to MCS depends on lead and tilt angles.

For an example 3-axis ball-end milling case feed direction with respect to the workpiece is presented in Figure 4.12(a). It coincides with the X direction in the machine coordinate system which is an inertial reference system. However, when lead and tilt angles are applied on the process, in order to satisfy the same feed direction with respect to the workpiece, the feed direction with respect to the machine coordinate system has to change as shown in Figure 4.12(b) for the machine tool configurations where rotational axes are on the table side. In order to take care of this change in the stability formulation, the measured transfer function matrices are oriented accordingly.

The transfer function matrices are measured in fixed machine coordinate system (MCS), however the transfer function matrix G used in the stability formulation is defined in TCS. Hence, orientation of measured transfer function matrix from MCS to TCS is needed. The orientation is performed using a transformation matrix T_G:

$$T_G = \begin{bmatrix} f_X & c_X & n_X \\ f_Y & c_Y & n_Y \\ f_Z & c_Z & n_Z \end{bmatrix} T \tag{4.36}$$

where f_X, f_Y, f_Z ; c_X, c_Y, c_Z; n_X, n_Y, n_Z are the measure numbers of unit feed vector, unit cross-feed vector and unit surface normal vector in MCS, respectively. The

transformation of a measured transfer function matrix $\boldsymbol{H}$ from MCS to TCS is done using below equation where superscript ($'$) denotes the transpose operation:

$$G = T_G{}' H T_G \qquad (4.37)$$

(a)   (b)
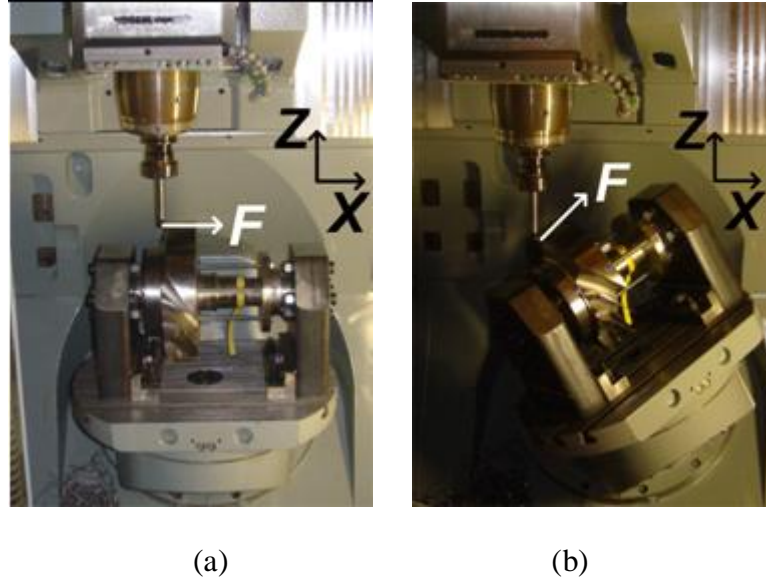
Figure 4.12: Change of feed direction with respect to MCS due to lead and tilt angles on a machine tool where rotary axes are on the table side (a) Before lead and tilt angle application (b) After lead and tilt angles are applied

In 3-axis ball-end milling slotting cases, stability diagrams are not affected by the feed direction even if the measured transfer functions in two orthogonal directions are different. In this case, the oriented transfer function matrix change, however, results of eigenvalue solution which depend on the directional coefficient matrix comes out to be identical.

4.9. Verification Tests

In order to demonstrate the application of the methods presented and verify them, several tests have been conducted. Here, three different cases are presented with experimental and simulation results. The machining center used in the tests is a 5-axis DMG 50 Evolution where 2 rotational axes are on the table side (Figure 3.14). The workpiece is a rectangular block of AISI 1050 steel that is clamped directly to the rotary table. Since the workpiece is rigid compared to the cutting tools, the flexibilities of the cutting tools are considered only. However, depending on the application, the flexibility of the workpiece can also be included in the solution. As cutting tools, ball-end mills

having 2 flutes were used. Helix angle and radial rake angle on them are 30° and 8°, respectively. Feed rate of 0.05mm/tooth is applied in the tests.

The other process parameters for these three cases are given in Table 4.1.

Table 4.1: Process parameters of experimental cases

	Example 1	Example 2	Example 3
Cutting type	Slotting	Slotting	Following cut
Cross-feed direction	-	-	Positive
Step over	-	-	0.1mm
Diameter of ball-end	12 mm	20 mm	8 mm
Overhang length	50.2 mm	62.3 mm	54.6 mm
Tool holder type	ER type	Power-chuck	Shrink-fit
Torque for fixing the tool to the tool holder	50Nm	50Nm	-

4.9.1. Cutting Force Coefficients

Cutting force coefficients are calculated using the *mechanics of milling* method [36]. An orthogonal database consisting of chip thickness ratio (r_t), friction angle (β) and shear stress (T_{shear}) is generated for AISI 1050 steel based on the uncut chip thickness ct (mm) and the cutting speed V (m/min):

$$r_t = 0.4 + 0.0005V + 0.6ct$$
$$\beta = 26.8 - 0.0313V + 11.77ct \text{ (deg)}$$
$$\tau_{shear} = 450.3 + 0.4V + 227.5ct \text{ (MPa)}$$

(4.38)

This database is valid for chip thickness and cutting speed values less than 0.32mm/tooth and 606 m/min, respectively. Since stability diagrams cover a range of spindle speeds, an average cutting speed over the range under consideration is used in calculation of local for cutting force coefficient calculations.

4.9.2. Effect of accelerometer mass on FRFs

The frequency response functions (FRFs) of the cutting tools are measured using an impact-hammer and an accelerometer at the tool tip. It is shown that addition of accelerometer to the tool may have a considerable effect on the measured FRF depending on the mass of the accelerometer and flexibility of the tool [92]. As the ratio of the accelerometer mass to the tool mass increases, the difference between original

FRF and measured FRF grows. In order to take this effect into account and obtain the original FRF of the structure without the effect of accelerometer's mass, the measured transfer function $H(\omega)$ needs to be modified as follows [92]:

$$H_{\mathrm{mod}}(\omega) = (1 + H(\omega) * (\omega^2 m_a))^{-1} * H(\omega)$$ (4.39)

where m_a represents the mass of the accelerometer and ω is the frequency. The mass of the accelerometer used in this work is 0.7 grams. Modal data is fit to measured and modified FRFs using CUTPRO software [93] in order to present the dynamic properties of the cutting tools in the paper. The tools are rigid along the tool axis direction; hence, flexibilities of the tools in z and Z directions are neglected. The cross-terms in the measured transfer function matrix $\boldsymbol{H}$ are not taken into account since their effect can be neglected compared to the direct ones. Hence, the measured transfer function matrix $\boldsymbol{H}$ is in the following form:

$$\boldsymbol{H} = \begin{bmatrix} H_{XX} & 0 & 0 \\ 0 & H_{YY} & 0 \\ 0 & 0 & 0 \end{bmatrix}$$ (4.40)

where H_{XX} and H_{YY} are direct transfer functions in X and Y directions, respectively.

4.9.3. Example 1

The first example is a 3-axis ball-end milling slotting cut. For the cutting tool which is a 12mm diameter ball-end mill, the identified modal parameters from the measured and modified FRFs are presented in Table 4.2. The measured FRFs in X and Y directions are almost identical due to the symmetry of the cutting tool. Hence, the modal data in Table 4.2 belong to both X and Y directions.

Table 4.2: Modal data for 12 mm ball-end mill

Mode#	Measured modal fit			Mass-modified modal fit		
	f_n (Hz)	ζ	m(kg)	f_n(Hz)	ζ	m(kg)
1	2971.9	$1.462e^{-2}$	0.0743	2983.8	$1.550e^{-2}$	0.0769
2	4005.2	$1.864e^{-2}$	0.0634	4022.2	$1.846e^{-2}$	0.0629

The predicted stability diagrams using the frequency domain stability model are presented in Figure 4.13 for both modal data identified from measured and mass-modified FRFs. It is seen that the accelerometer's mass does not affect the stability

diagram considerably in this case. The spindle speed range under consideration is between 13000 rpm and 20000 rpm. Since the cutting force coefficients are cutting speed dependent, average rotational speed of 16500 rpm is used in determining the force coefficients. In order to compare the results of frequency domain method, a time-domain stability model for 5-axis ball-end milling is developed.

For some of the representative spindle speeds, stability limits are determined using time domain simulations which are also shown in the Figure 4.13. It's seen that there is a close agreement between the results of the frequency domain and time-domain models.

Several cutting tests are performed to identify the stability limits experimentally and they are presented in Figure 4.13. During the tests, the sound signal was acquired using a microphone. According to the spectrum of the sound data and visual check on the machined surface, the cutting process was classified as stable, marginally stable or unstable. Marginally stable cases are in the transient region between stable and unstable regions. When predictions and experimental results are compared in Figure 4.13, it is seen that the prediction of the stability diagrams is achieved with a reasonable accuracy.

Sound spectrums at two points (point A and point B) are presented in Figure 4.14 together with surface photos. The cutting depth is common at these points and it is equal to 1.5mm. However, spindle speed is 16000 rpm at point A, while it is 17800 rpm at point B. In the sound spectrum of point A, the maximum amplitude occurs at 2916 Hz while the amplitude at tooth passing frequency of 533 Hz is nearly half of the maximum amplitude. Thus, this case is unstable with chatter frequency of 2916 Hz. The deteriorating effect of the chatter on the machined surface can also be seen in Figure 4.14. For point B, on the other hand, the maximum amplitude occurs at tooth passing frequency of 593Hz in the sound spectrum whereas around the natural frequencies of the tool, the amplitude of the spectrum is very small. For that reason, point B is declared as stable which is also visually shown in the corresponding surface photo.
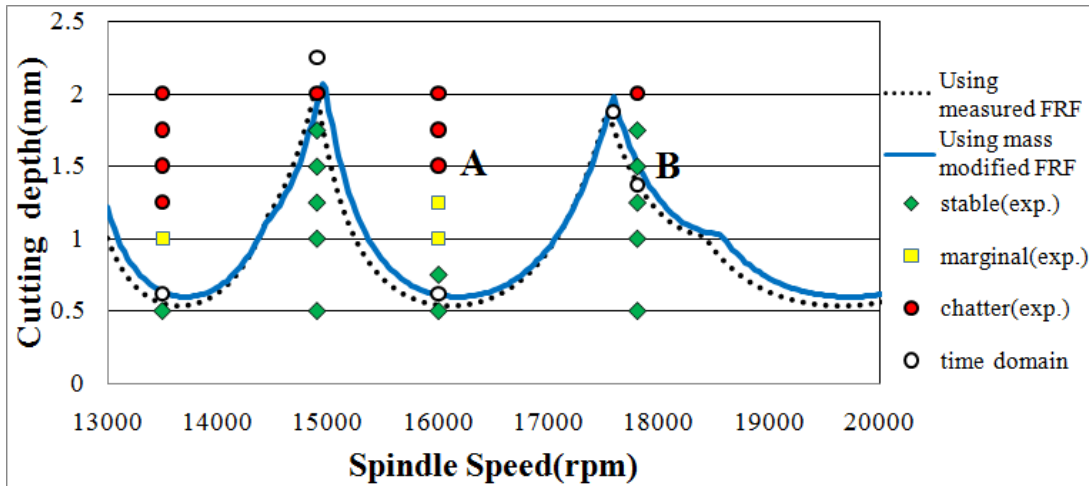
Figure 4.13: Stability diagrams of example 1
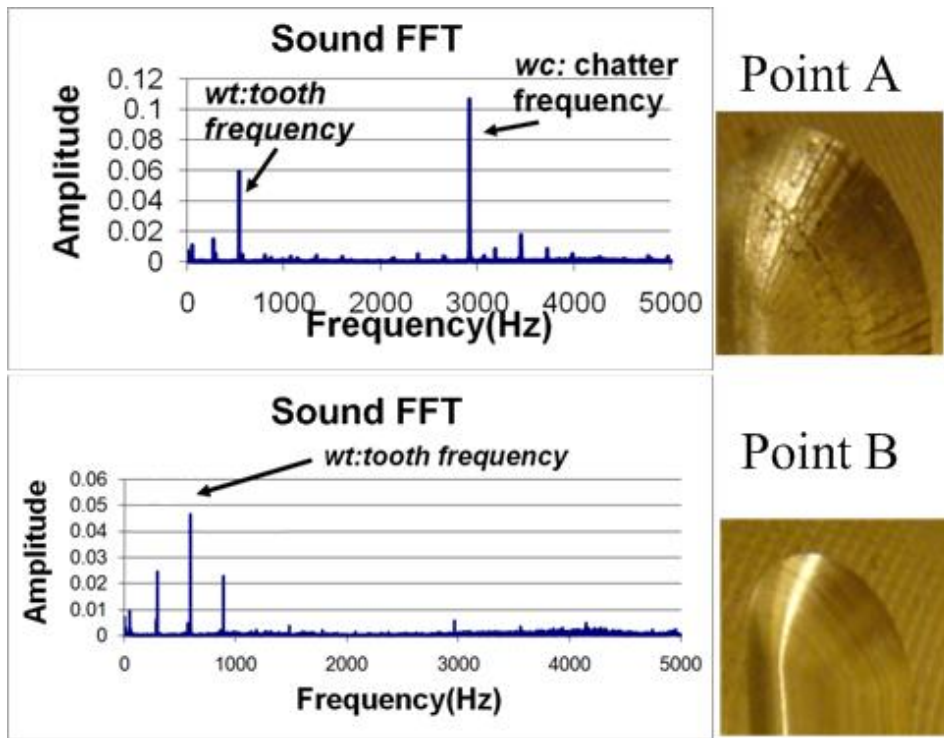
Figure 4.14: Sound spectrums and surface photos at an unstable (point A) and at a stable point (point B)

4.9.4. Example 2

In the second example, the workpiece material AISI 1050 steel is slotted using a 20 mm diameter ball-end mill. The modal data measured at the tool tip is given in Table 4.3. Since the cutting tool is even heavier than the one in the first example, the mass of the accelerometer does not have a considerable effect on the measured frequency

71

response function. Hence, in the stability diagram calculations, measured frequency response functions are used.

Table 4.3: Modal data for the example case.

Direction	f_n(Hz)	ζ (%)	k (N/mm)
X	747	3.89	26300
Y	766	3.98	36000

As stated in the Section 4.8, due to the effect of the lead and tilt angles, measured transfer function matrices need to be oriented since feed vector is changing with lead and tilt angles. In Table 4.4, the feed and normal vectors in machine coordinate system are presented for different lead angle and tilt angle combinations. Using the presented measure numbers of the vectors tabulated in Table 4.4, measured transfer function matrices are oriented using (4.37).

Table 4.4:Feed and surface normal vectors in FCN

Lead(^{o})	Tilt(^{o})	F			N		
		f_X	f_Y	f_Z	n_X	n_Y	n_Z
30	30	0.277	0.820	0.500	0.612	-0.250	0.750
30	15	0.606	0.618	0.500	-0.523	-0.163	0.837
30	0	0.834	0.232	0.500	-0.482	-0.134	0.866
30	-15	0.851	-0.162	0.500	-0.523	-0.163	0.837
30	-30	0.772	-0.392	0.500	-0.612	-0.250	0.750
15	30	0.114	0.959	0.259	-0.523	-0.163	0.837
15	15	0.530	0.808	0.259	-0.354	-0.067	0.933
15	0	0.958	0.127	0.259	-0.257	-0.034	0.966
15	-15	0.789	-0.558	0.259	-0.354	-0.067	0.933
15	-30	0.640	-0.723	0.259	-0.523	-0.163	0.837
0	30	-0.268	0.963	0	-0.482	-0.134	0.866
0	15	-0.132	0.991	0	-0.257	-0.034	0.966
0	0	0	1	0	0	0	1
0	-15	0.132	-0.991	0	-0.257	-0.034	0.966
0	-30	0.268	-0.963	0	0.482	-0.134	0.866

Effects of lead and tilt angles on the absolute stability limit using the single frequency method are demonstrated in Figure 4.15. Moreover, for three lead and tilt

angle combinations, experimentally determined absolute stability limits are also shown in this figure, namely, for lead and tilt combinations of $(15^o,-15^o)$, $(0^o,-0^o)$, $(0^o,-30^o)$. Although there is some discrepancy between simulations and experiments for the absolute stability limit, it can be concluded that the trend of variation of absolute stability limit with lead and tilt angles are predicted reasonably well by the simulations.
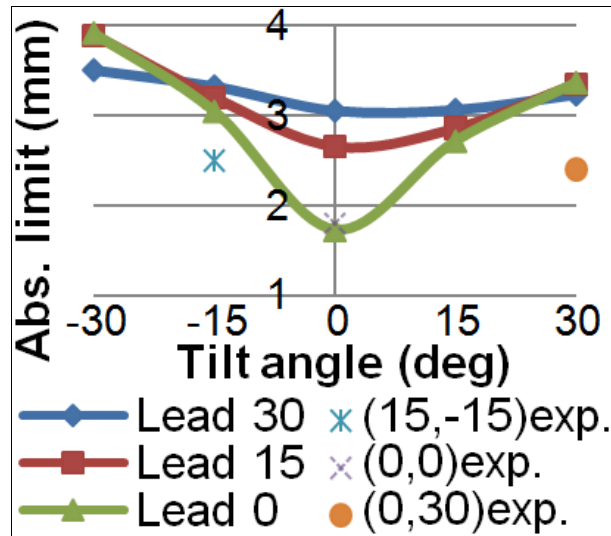
Figure 4.15: Effect of lead-tilt angle on stability.

For the lead and tilt combination of $(15^o,-15^o)$, the stability diagram using single frequency method is presented in Figure 4.16(hs0). In order to verify the predicted stability diagram, cutting tests were performed and the test cuts were classified as stable and chatter according to the stability of the cuts. These experimental results are also demonstrated in Figure 4.16. During the tests, it was observed that the measured chatter frequencies by the microphone were lower than the predicted ones. This difference can be explained if the most flexible mode presented in Table 4.3-which was measured in idle condition- is the spindle mode since it is known that due to the spindle speed effect but the modal frequencies of the spindle may shift during cutting. Mode shape of the cutting tool in X-direction is presented in Figure 4.17. The mode shape reveals that the mode presented in Table 4.3 is the spindle mode.

At high spindle speeds, the shaft softening and bearing stiffening mechanisms counteract (Lin, et al. [94]). If the shaft softening mechanism dominates, then the natural frequencies of the spindle may decrease whereas they increase if the effect of the bearing stiffening is stronger. Based on this observation, the measured frequencies under static conditions were shifted down in the simulations in order to match the measured chatter frequencies with the predicted ones. After decreasing the measured

natural frequencies (Table 4.3) by 50 Hz, it was seen that the predicted chatter frequencies were much closer to the measured values. Hence, it can be concluded that shaft softening mechanism dominated the response of the spindle for this case
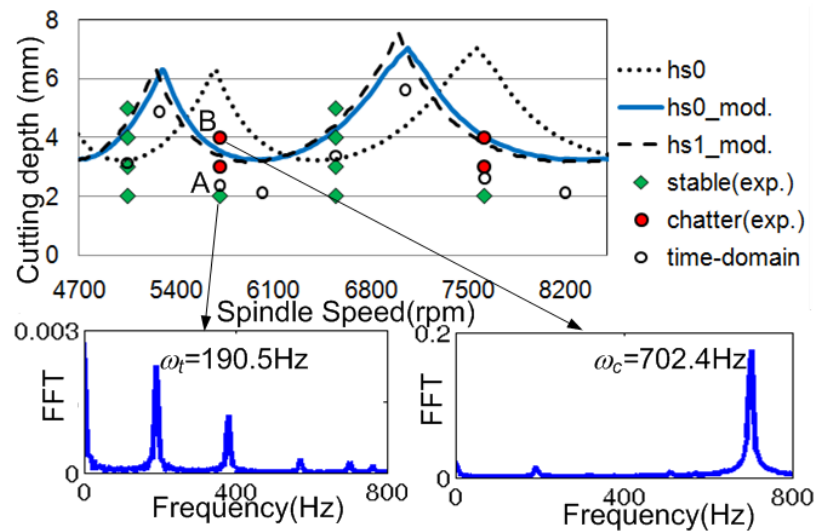
Figure 4.16: Stability diagram for $(15^o,-15^o)$ combination.
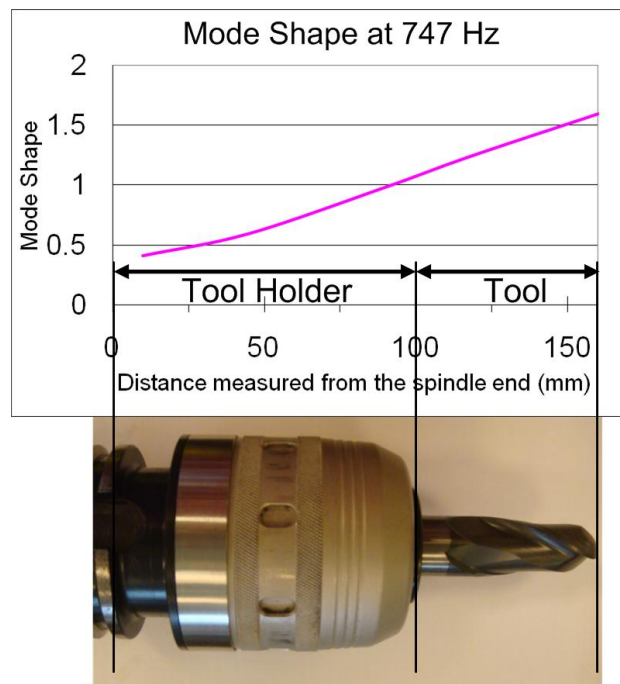
Figure 4.17: Mode shape of the tool and tool holder.

The simulation results using unmodified modal data with single frequency method (hs0), modified modal data with single frequency method (hs0_mod) and with multi-frequency method with one harmonics (hs1_mod) are presented in Figure 4.16. It is seen that the simulated stability diagrams agree better with the experimental results after modified modal data is used. Furthermore, it was observed that using higher harmonics

did not change the simulated stability diagrams. For the modified modal data, the time-domain model was run at several spindle speeds and corresponding stability limits are presented in Figure 4.16. The power spectrum of the simulated displacements is used to judge the stability of the system. There is some discrepancy between frequency domain and time-domain results which can be attributed to the discretization procedure employed. At a stable point (A) and at an unstable point (B), power spectrums of cutting tool displacements predicted by the time domain model are presented in Figure 4.16 to be representative.

4.9.5. Example 3

The third example is a following cut operation where step over is 0.1 mm. Lead and tilt angles are both 15°. For this case, the identified modal data for the measured and mass modified FRFs are presented in Table 4.5 for the 8 mm diameter ball-end mill. As in the first example, the measured FRFs in X and Y directions are nearly the same. Hence, Table 4.5 represents the modal data for both X and Y directions. Since the stiffness and mass of the 8 mm diameter tool is lower than that of the 12 mm diameter, the mass of the accelerometer has a considerable effect on the tool FRF in this case.

The stability diagrams predicted for both measured and mass modified modal data are presented in Figure 4.18. The spindle speed range in the diagram is between 11500 rpm and 15500 rpm. Average rotational speed of 13500 rpm is used in calculation of cutting force coefficients.

For several spindle speeds, the stability limits calculated by time domain model are also presented in Figure 4.18. These limits are determined by incrementing the cutting depths until the cutting forces or displacements of the cutting tool become unstable. In order to represent three different characteristic responses, namely stable, marginally stable and unstable, the variation of displacement of the cutting tool calculated by time-domain model is presented for three different cutting depths at 14650 rpm . Displacement of the cutting tool in the cross-feed direction where cutting depth is 0.5 mm is demonstrated in Figure 4.19(a). As can be seen from the figure, the variation of the displacement is stable for this cutting depth. When the cutting depth is increased to 0.9mm, the process becomes a marginally stable as presented in Figure 4.19(b). Finally, an unstable process where cutting depth is 1.25 mm is demonstrated in Figure 4.19(c). As time progresses the displacement of the cutting tool increases in an unstable manner in this case.

The stability limits determined by time-domain solution for several spindle speeds are presented in Figure 4.18. There is some discrepancy between the predictions of the frequency domain and time domain method. This can mainly be attributed to the discretization procedure employed in the frequency domain method. Moreover, numerous cutting tests were performed to obtain the stability limits experimentally. The results of these tests are also shown in Figure 4.18. It is seen that after subtracting the effect of the accelerometer's mass from the measured FRF, the agreement between the frequency domain method and the experimental results improved. Especially for low radial immersion cases like this example, the chip thickness model used in this study may be an error source and can contribute to the difference between the experimental and simulation results. This is because of the fact that the presented chip model is an approximation of the true chip thickness due to the trochoidal kinematics of the milling process.

Mode #	Unmodified modal data			Mass modified modal data		
	f_n(Hz)	ζ	m(kg)	f_n(Hz)	ζ	m(kg)
1	1810.3	$9.936e^{-3}$	0.0354	1826.7	$9.993e^{-3}$	0.0418
2	1927.3	$9.524e^{-3}$	0.1003	1934.4	$9.584e^{-3}$	0.0824
3	2020.8	$9.674e^{-3}$	0.123	2028.4	$9.726e^{-3}$	0.0852

Table 4.5: Modal data for 8 mm ball-end mill
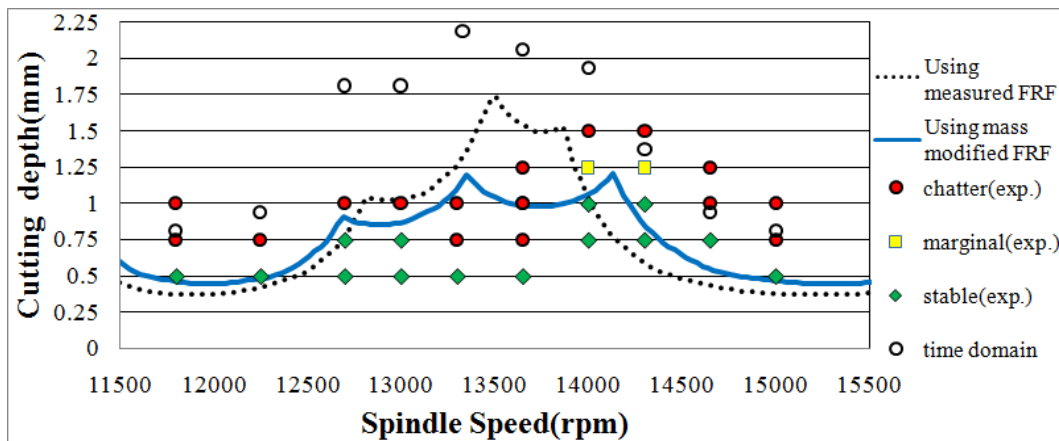
Figure 4.18: Stability diagrams of example 2
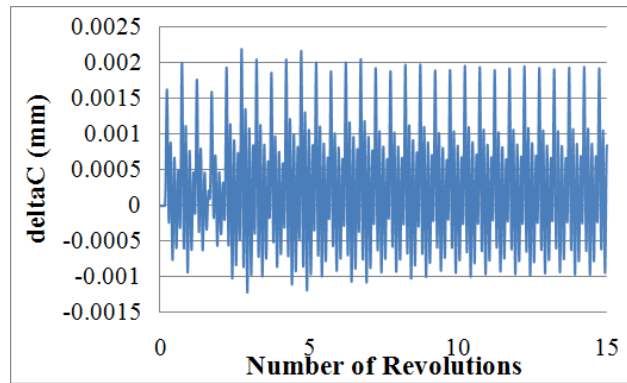
(a)
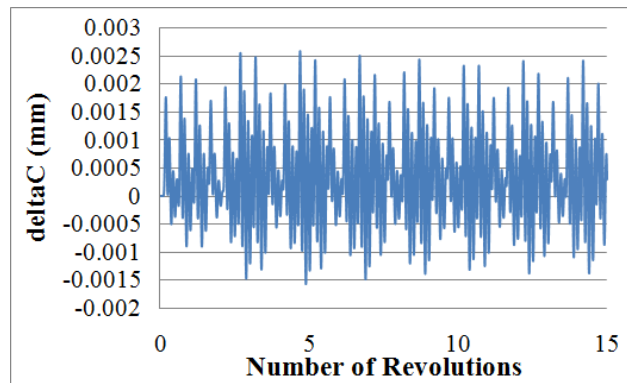
(b)
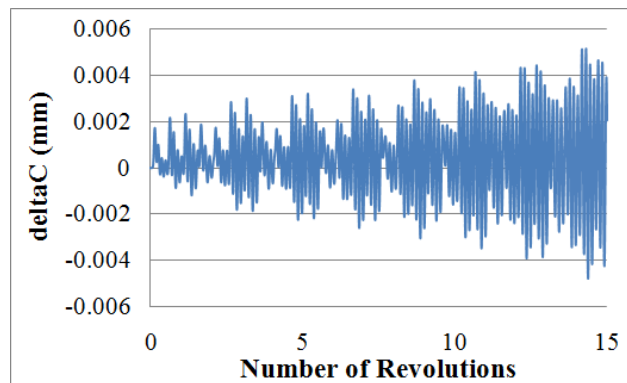
(c)

Figure 4.19: The displacement of the cutting tool at 14650 rpm (a) 0.5 mm cutting depth (stable) (b) 0.9 mm cutting depth (marginally stable) (c) 1.25 mm cutting depth (unstable)

Multi-frequency effects are expected to be observed in this example, considering the stability studies in 3-axis flat-end milling [57]-[61] since step over is low in this case. For that reason, multi-frequency solution method is applied on this example. Different number of harmonics, 1, 3 and 5, are included in the solution. The stability

diagram obtained using one harmonics (hs1) is plotted in Figure 4.20. As can be seen from the figure, adding one harmonic causes only a marginal change in the stability diagram with respect to single frequency solution (hs0). The stability diagrams calculated by using 3 harmonics (hs3) and 5 harmonics (hs5) are nearly identical and they differ from the solution with one harmonic very slightly as shown in Figure 4.20. Although step over is low in this case (0.1 mm), due to the effects of ball-end mill geometry, lead and tilt angles as explained in Section 4.5.2 , the multi-frequency terms do not have considerable effects on the stability diagram.

In order to show the multi-frequency effects, spectrum of the sound data obtained in the test with spindle speed of 14650 rpm and cutting depth of 1mm, is demonstrated in Figure 4.20. As can be seen from sound spectrum, amplitude at the chatter frequency (ω_c=1925Hz) is higher than the amplitude at the tooth passing frequency (ω_t=488Hz) which demonstrates that the process is unstable. Moreover, the frequencies at the addition and subtraction of the chatter frequency and harmonics of the tooth passing frequency can be seen at the sound spectrum. The most notable one is at the frequency (ω_c-ω_t). Spectrum of cutting forces and displacements can also be determined using the time domain model. Here, for the same case (14650 rpm, 1mm) the spectrum of the displacement of the cutting tool in feed direction is presented in Figure 4.20 to be representative. It's seen that comments made about the measured sound spectrum are also valid for the spectrum of the tool displacement in the feed direction calculated by the time-domain model.
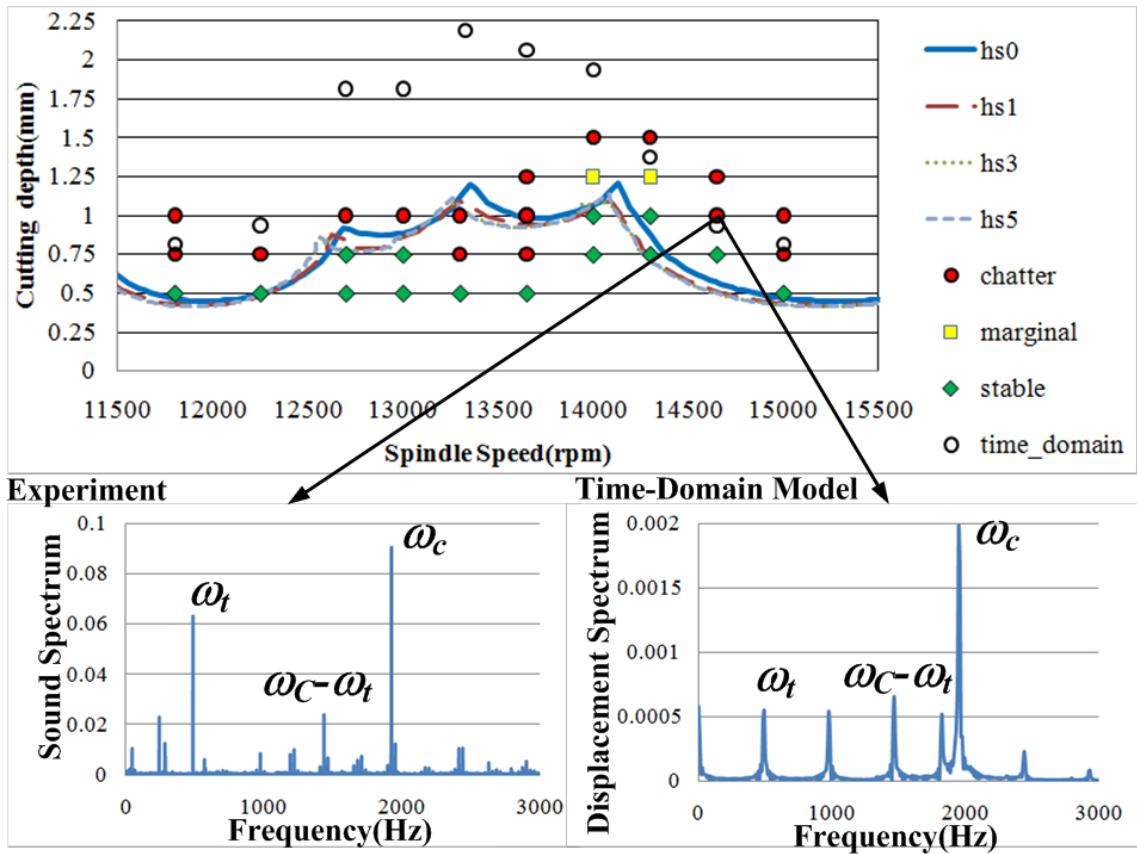
Figure 4.20: Multi-frequency effect on the stability diagrams; sound spectrum and spectrum of tool displacement in feed direction (calculated by time-domain) at 14650 rpm and 1mm.

5. INVESTIGATION OF LEAD AND TILT ANGLE EFFECTS IN 5-AXIS BALL-END MILLING PROCESSES

Being special parameters of 5-axis milling, lead and tilt angles have significant effects on the process geometry, mechanics and dynamics which have been studied very little up to now. In this chapter, combined and independent effects of lead and tilt angles on engagement regions between the tool and workpiece are explained by CAD models and calculations. For the engagement calculations, engagement model presented by Ozturk and Budak [31] is used. Effect of lead and tilt angles on maximum uncut chip thickness is also illustrated on a representative case. Moreover, a method to avoid tool tip contact condition which is undesirable due to additional ploughing forces and tool tip marks on the surface is presented. Surface finish quality is also affected by lead and tilt angles since they determine the tool-surface contact conditions. The effects of lead and tilt angles on cutting forces, torque, form errors and stability are demonstrated using modeling and experimental results. It is shown that the cutting geometry, mechanics and dynamics vary drastically and nonlinearly with these angles. For the same material removal rate, forces and stability limits can be quite different for various combinations of lead and tilt angles. All simulated effects of lead and tilt angles are verified by experiments. The results presented in this chapter are expected to enhance the understanding of complex 5-axis ball-end milling process mechanics and dynamics. The results should also help selection of 5-axis ball-end milling conditions for higher productivity and machined part quality

5.1. Engagement regions and maximum uncut chip thickness

The visualization of effects of lead and tilt angles on the engagement regions between the tool and workpiece is not very easy in 5-axis ball-end milling. In this section, their effects are shown by CAD models and simulations. For calculation of engagement regions, a previously developed engagement model [31] is applied on representative cases. In the example case, cutting depth, step over and radius of the ball-

end mill are 6 mm. Helix angle on the clockwise-rotating tool is 30° and cross-feed direction is negative.

In the absence of lead and tilt angles, CAD model of the process is shown in Fig.4. In this case, TCS and FCN coincide. The projection views of the 3D engagement region in two orthogonal planes namely, CN and CF planes, are also presented in Figure 5.1. It's seen that the engaged region is variable along the tool axis. The variation of engagement boundaries along the tool axis is plotted in Figure 5.1 where φ_{st} and φ_{ex} represent start and exit angles, respectively. There is 180° immersion close to the tool tip (z=-6mm) while the immersion width decreases for the higher z positions. As the name implies, immersion width is defined as the amount of angular immersion at a z-level.

When lead and tilt angles are applied on the cutting tool, the shape of the engagement region changes. This is illustrated for application of 30° lead and tilt angles in Figure 5.2 where the calculated engagement boundaries are also presented. In this case, it's seen that both ball and cylinder zones of the cutting tool are in contact with the workpiece.

Positive lead angle shifts the engagement region to the higher positions along the tool axis while negative lead angle moves the engagement to the lower sides of the tool. Moreover, lower immersion widths takes place with positive lead angles with respect to negative lead angle cases. In order to justify these comments, effect of lead angle on the immersion width on different z-coordinates is presented in Figure 5.3 for the example case. Since it is a 3D surface, the 2D projections of the surface in two orthogonal planes are also plotted in the figure to show the variation with more detail. Norm_z is the ratio of z-coordinate with respect to ball-end mill radius. It is seen that the comments about the effect of lead angle and observations from the Figure 5.3 match well. Although not presented here, the similar effects are also seen for lower and higher cutting depth and step over cases.
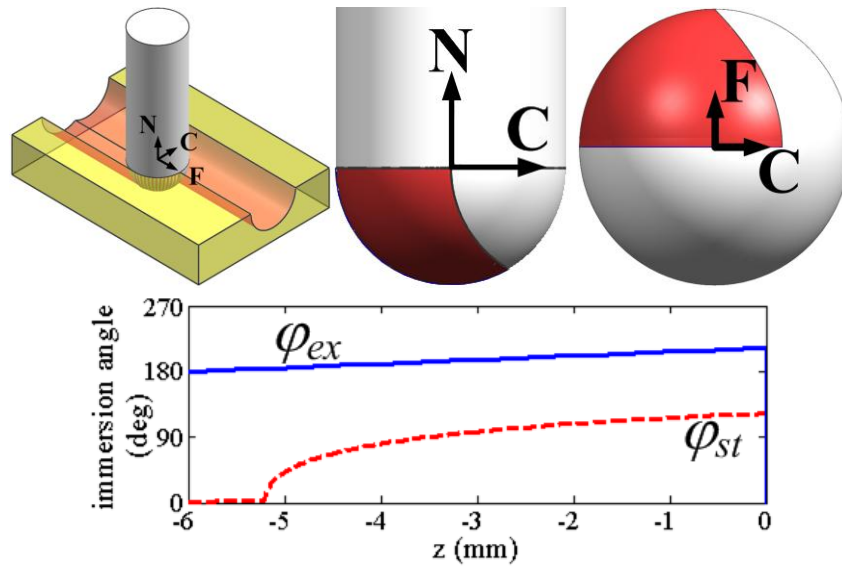
Figure 5.1: Engagement region (lead,tilt=0°)
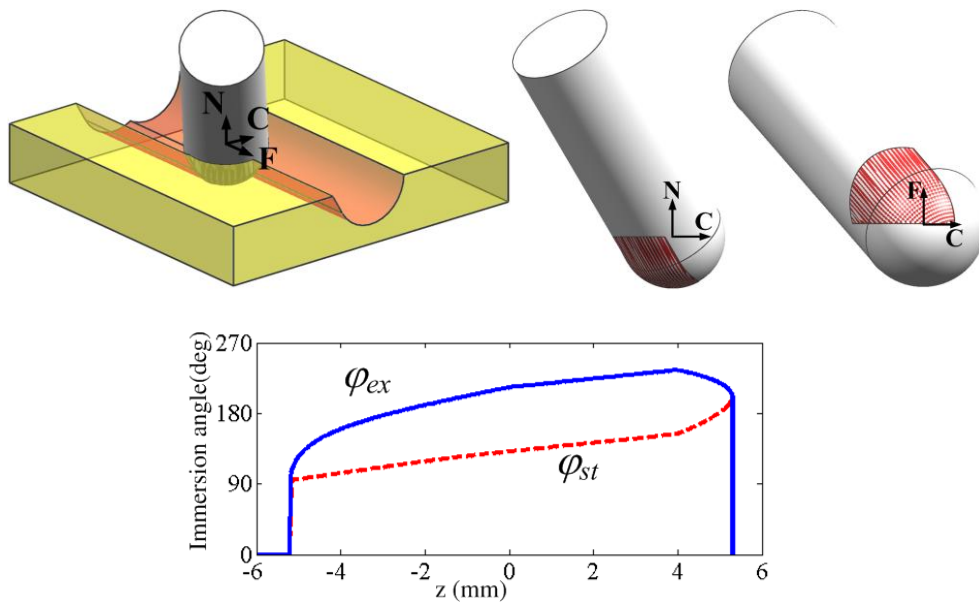
Figure 5.2: Engagement region for the example case (lead,tilt=30°)
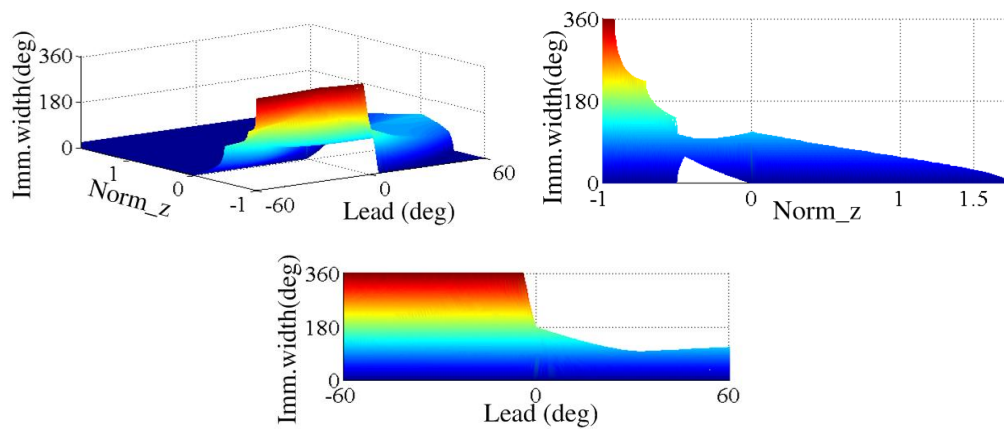
Figure 5.3: Effect of lead angle on immersion width (tilt=0°)

Local radius $R(z)$ increases as the z-coordinates of the engagement region increases (Figure 3.1). This results in higher cutting speed values in the engagement region. Since cutting speed increases tool wear, the engagement regions with higher z coordinates cause higher tool wear. Moreover, resulting cutting torque and power due to each cutting flute increases because of higher local radii and higher cutting speed. On the other hand, immersion widths decrease with higher z coordinates. In this case, the probability of having more than one flute in cut decreases since pitch angle between the flutes might be higher than immersion widths at these locations. As a result, it's difficult to derive a general conclusion about the required cutting torque and power since there are two contradicting effects.
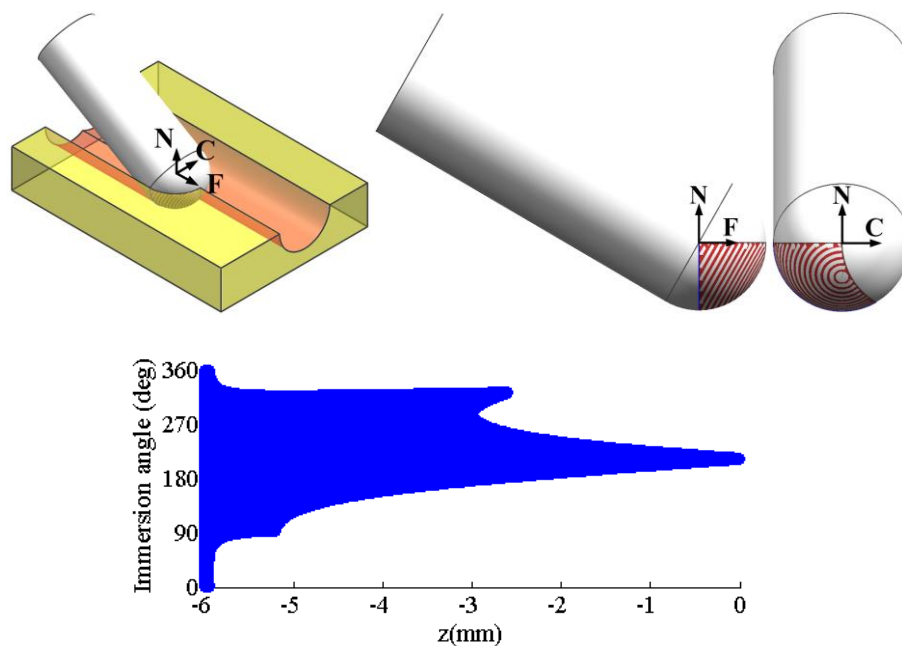
Figure 5.4: Engagement region (lead=-60°,tilt=0°)

In order to show the effect of lead angle on the engagement in more detail, for a large negative lead of -60°, 3D and 2D views of the engagement regions are presented in Figure 5.4. In this case tilt angle is 0°. Calculated engagement region is also demonstrated. In this case, it is seen that in regions close to the tool tip, the immersion width is 360° which means that there is full immersion in this zone. Tool-tip contact with the workpiece is generally not preferred due to additional ploughing/indentation forces and resulting tip marks on the finished surface. It is seen from Figure 5.4 that for higher values of z coordinates, the immersion width decreases. It is interesting to note that between z=-3 mm and z=-2.6mm positions, there are two start and exit angles, i.e. the tool engages and disengages with the workpiece two times at these z positions. In

this case, this zone on the tool stays behind the finished surface for a short duration but then tool engages with the workpiece again. This occurs depending on the step over and cutting depth for negative lead angles.

Effect of tilt angle is very much dependent on the cross-feed direction. If tilt angle and cross-feed direction have the same sign, the tool axis is oriented away from the uncut part of the workpiece. In this case, tilt angle decreases the z-coordinates of the engagement region. On the other hand, if tilt angle and cross-feed direction have opposite signs, tool axis is oriented through the uncut part of the workpiece and z-coordinates of the engagement region increase (Figure 3.6 (a)). As can be seen from the figure, positive tilt angle results in engagement regions with higher z coordinates. Effect of tilt angle on immersion width on different z coordinates is presented in Figure 5.5 for the example case. As expected, z-coordinates of the engagement region are lower when tilt angle is negative since cross-feed direction is negative in the example case. At the same time, immersion width is higher in these cases. Similar effects are seen in calculations performed for cases with lower and higher step over and cutting depth values.
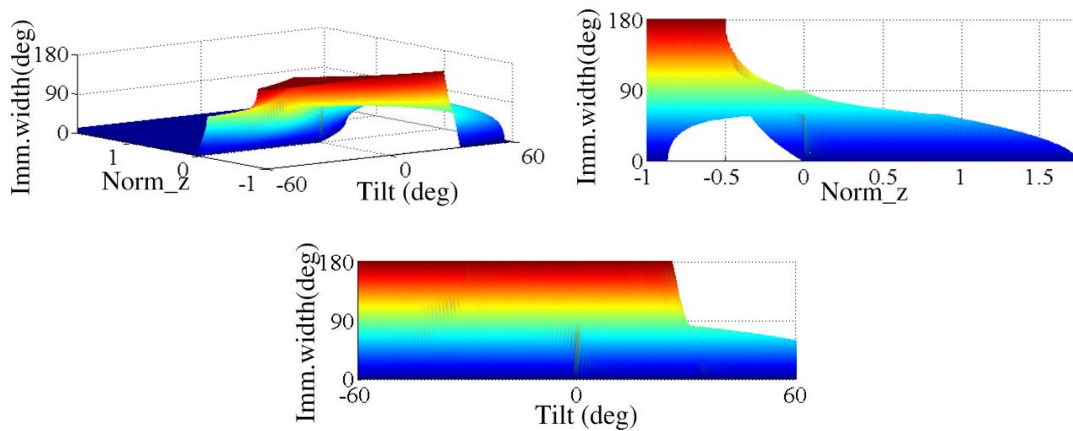
Figure 5.5: Effect of tilt angle on immersion width (lead=0°)

Tilt angle effect on the engagement region is presented on the example case with application of 0° lead and -60° tilt angle in Figure 5.6. In this case, there is 180° immersion in the regions close to the tool tip and it decreases for higher z coordinates. Two different immersion zones on the same z-position presented in the previous negative lead case, are also seen in this example between z=-0.8mm and z=0mm. In this case, the tool loses contact with the workpiece due to the material removed by the previous pass and gets into contact again which is shown better in the CN plane view of the engagement region in Figure 5.6. Negative tilt angle has an effect similar to the up-

milling effect in 3-axis flat-end milling for a clock-wise rotating tool (Figure 5.7(a)). In other words, the tool starts cutting from the final desired surface which may result in poor surface finish quality. On the other hand, positive tilt angle has a similar effect for counter-clockwise tools. Hence, positive tilt angle should be selected wherever possible considering the surface generation characteristics (Figure 5.7(b)).
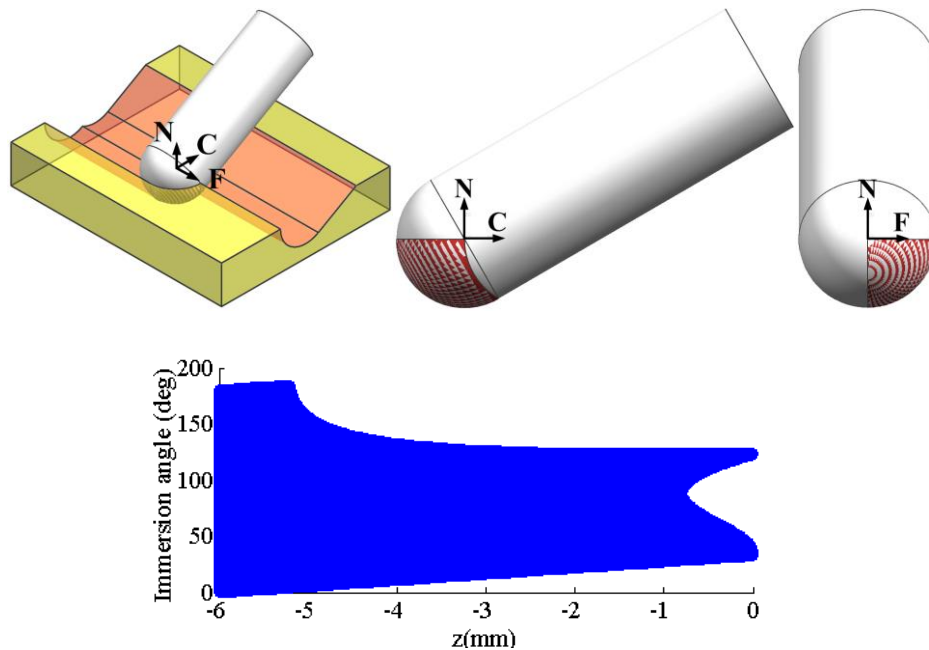
Figure 5.6:   Engagement region (lead=0°,tilt=-60°)

(a)   (b)
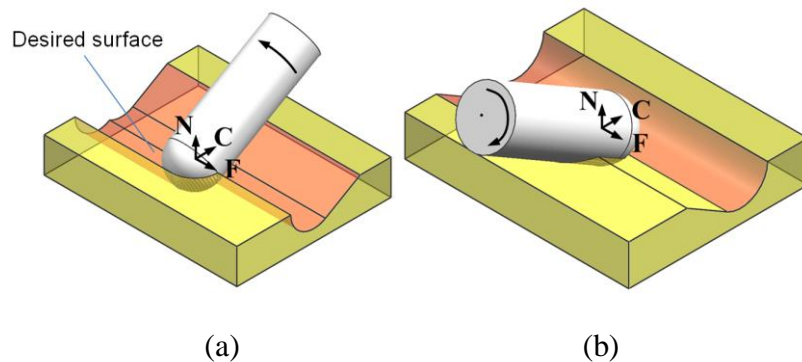
Figure 5.7: Surface generation (a) Undesirable tool orientation (b) Preferreed orientation

Lead and tilt angles also affect the local uncut chip thickness values on the cutting edge. The effect of lead and tilt angles on maximum uncut chip thickness is presented in Figure 5.8 on a representative case. Espacially when the cylindrical part of the ball-end mill is in cut, positive lead angle results in a considerable decrease in maximum uncut chip thickness since lead angle defines the inclination of the tool in feed direction. However, in cases where ball region of the tool is incut only, lead and tillt angles do not

change the maximum chip thickness. They only change the location where maximum chip thickness is reached.
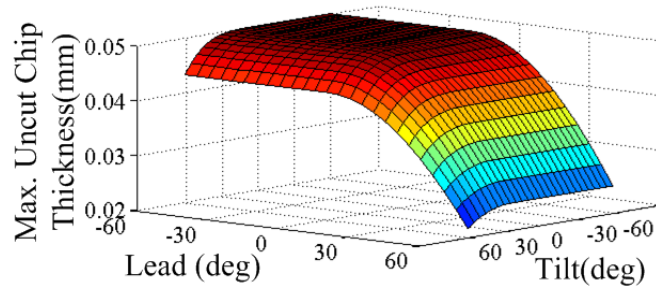
Figure 5.8: Lead and tilt angle effect on maximum uncut chip thickness. (s=6mm, a=6mm, R_o=6mm, feed per tooth=0.05mm)

5.2. Tool tip contact conditions and contact avoidance

In ball-end mills, local radius is variable along the tool axis and zero at the tool tip where cutting speed is also zero. In cases where the tool tip is in contact with the workpiece, cutting cannot be performed around the tip. Instead, it indents into the workpiece and/or ploughs over the surface depending on the lead angle. When the lead angle is negative, the feed vector has a component in the outward normal vector of the tool (**u**) at the tool tip (Figure 3.17). The non-cutting contact between the work material and the cutting tool tip results in extra indentation and ploughing forces. Although the tool tip is in contact with the workpiece in this case due to the negative lead angle, the tool tip is not in contact with the created surface. So, there are no tool tip marks on the resulting surface. On the other hand, when the lead angle is zero, the tool tip ploughs over the resulting surface. Ploughing deteriorates the surface quality of the part especially in relatively soft metals such as aluminum by leaving tool tip marks on the resulting surface. Consequently, considering either extra indentation/ploughing forces or tool tip marks on the resulting surface, the tool tip contact with the workpiece should be avoided wherever possible. The conditions for tool tip contact avoidance are discussed in this section.

The position vector of the tool tip (F_t, C_t, N_t) in FCN coordinate system is defined as follows:

$$\begin{bmatrix} F_t \\ C_t \\ N_t \end{bmatrix} = \begin{bmatrix} -R_o \sin l_e \\ R_o \sin t_i \cos l_e \\ R_o \cos t_i \cos l_e \end{bmatrix} \tag{5.1}$$

The tip contact can only occur if the lead angle is not positive, thus non-positive lead angles must be avoided if possible. However, in some cases non positive lead angle must be used due to the tool accessibility. Under such circumstances, the tip contact can be eliminated by keeping the cutting depth smaller than a critical cutting depth, a_{crit}, which is shown in Figure 3.17. The critical cutting depth depends on the N component of the tool tip position vector, N_t, and is calculated by the following equation:

$$a_{crit} = R_o(1 - \cos t_i \cos l_e) \tag{5.2}$$

If the required cutting depth is greater than the critical cutting depth, the tip contact can still be avoided if the cross-feed direction, the step over, the lead angle and the tilt angle are selected properly except the slotting cases. The conditions to avoid tool tip contact for first and following cut cases are described as follows.

In first cut cases, there are two different situations depending on the cross-feed direction (Figure 5.9). Figure 5.9(a) shows a case where cross-feed direction is positive whereas Figure 5.9(b) illustrates a case with negative cross-feed direction. In these cases, both lead and tilt angles are negative. The highlighted regions in the figures show the engagement zones of the cutting tool and workpiece. The below conditions, which are determined from the geometry, should hold in order to avoid tool tip contact in first cut cases:

$$\left.\begin{array}{l} s < -R_o \sin t_i \cos l_e \quad \text{if cross-feed direction is positive} \\ s > -R_o \sin t_i \cos l_e \quad \text{if cross-feed direction is negative} \end{array}\right\} \tag{5.3}$$

In following cut cases, when the lead angle is non-positive and the cutting depth is higher than the critical cutting depth, the tool tip is definitely in contact if both of the cross-feed direction and the tilt angle are either positive or negative. Similarly, tool tip contact cannot be avoided when tilt angle is zero. In Figure 5.9 (c), tool tip contact is illustrated for a representative case where both cross-feed direction and tilt angle are positive. On the other hand, the tool tip can be kept out of contact if the cross-feed direction and the tilt angle have opposite signs and the step over is selected properly which is illustrated in Figure 5.9 (d). As shown in the figure, the tip contact does not occur since the material at the tool tip location has been removed in the previous cutting pass. For such cases, if the step over is less than a critical step over value, s_{crit}, the tool tip is out of cut. The critical step over value depends on the cross-feed direction, lead angle, tilt angle, step over and tool tip's N coordinate, N_t. The critical step over, s_{crit} , in

terms of these parameters are given in Table 5.1 for different cases where tool tip contact can be avoided.
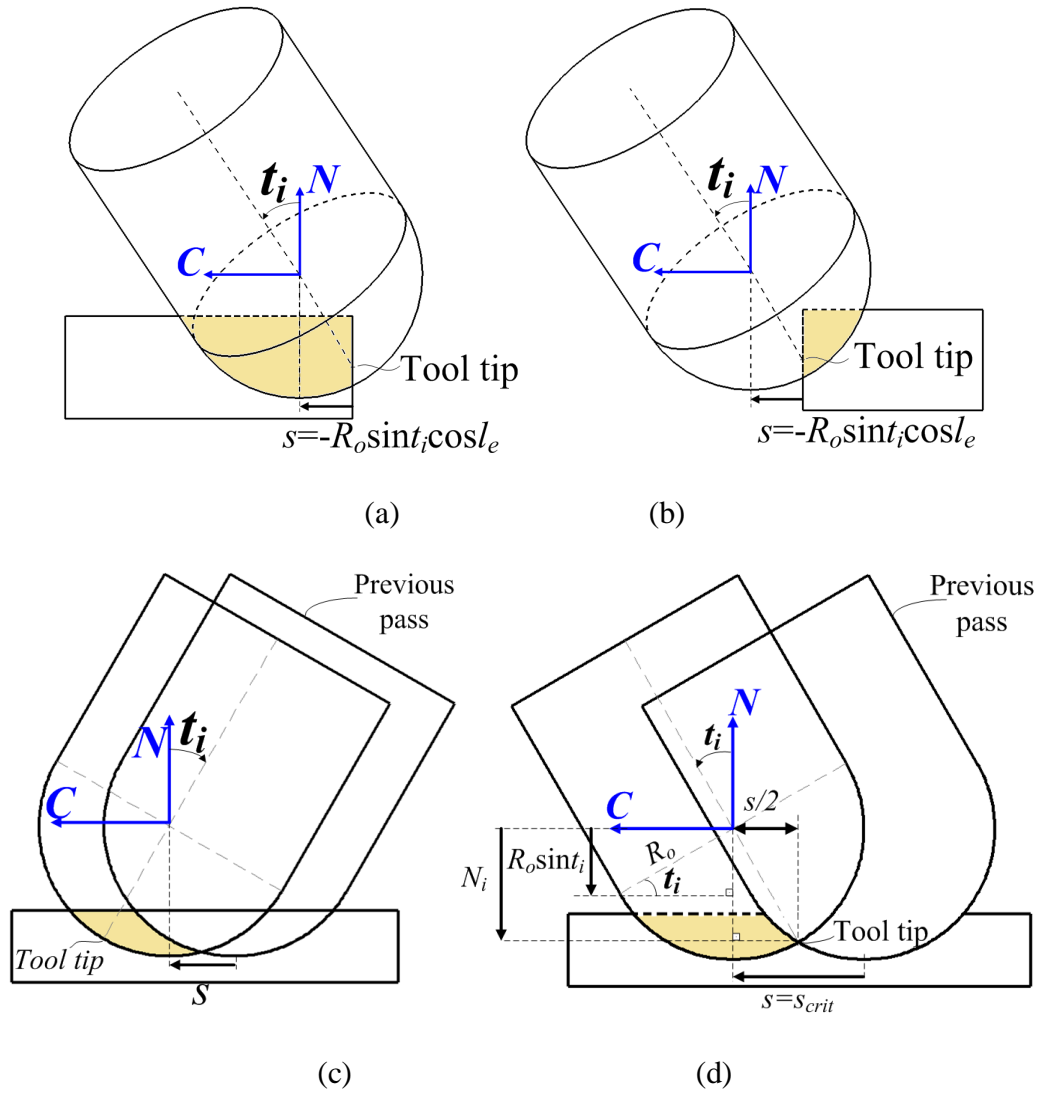
Figure 5.9 (a) Tool tip contact avoidance in first cut cases, cross-feed direction positive (b) cross-feed direction negative (c) Tool tip contact in following cut cases, cross-feed direction positive, positive tilt angle (d) negative tilt angle

In cases where the step over is less than s_b (Figure 3.8(a)), if tool tip's N coordinate, N_t, is less than N_i, the tool tip is in contact with the workpiece; otherwise, the tip contact can be avoided by selecting the step over according to the Table 5.1. On the other hand, if the step over is higher than s_b (Figure 3.8(b)), the tool tip is in contact with the workpiece if its N coordinate is less than N_s, if not, tool tip contact can be eliminated by adjusting the step over with respect to s_{crit} (Table 5.1).

Table 5.1: s_{crit} definition for following cut cases

Cross-feed direction	Tilt	Step over	Tool tip's N coordinate N_t	s_{crit}
Positive	$t_i < 0$	$s \leq s_b$	$N_i < N_t \leq R_o \sin t_i$	$R_o(\sqrt{1-\cos^2 t_i \cos^2 l_e} - \sin t_i \cos l_e)$
			$N_t > R_o \sin t_i$	$\dfrac{R_o}{\cos t_i}$
		$s > s_b$	$N_t > N_s$	$\dfrac{R_o}{\cos t_i}$
Negative	$t_i > 0$	$s \leq s_b$	$N_i < N_t \leq -R_o \sin t_i$	$R_o(\sqrt{1-\cos^2 t_i \cos^2 l_e} + \sin t_i \cos l_e)$
			$N_t > -R_o \sin t_i$	$\dfrac{R_o}{\cos t_i}$
		$s > s_b$	$N_t > N_s$	$\dfrac{R_o}{\cos t_i}$

As presented above for first cut and following cut cases, even if the lead angle is non-positive and cutting depth is higher than a_{crit}, the tool tip contact with the workpiece can be avoided by selecting step over properly when the lead and tilt angles are fixed. Alternatively, if step over is selected beforehand, the tool orientation (lead and tilt angles) can be selected accordingly considering the above conditions to prevent tool tip contact. The procedure that can be followed to prevent tool tip contact is summarized in Figure 5.10.
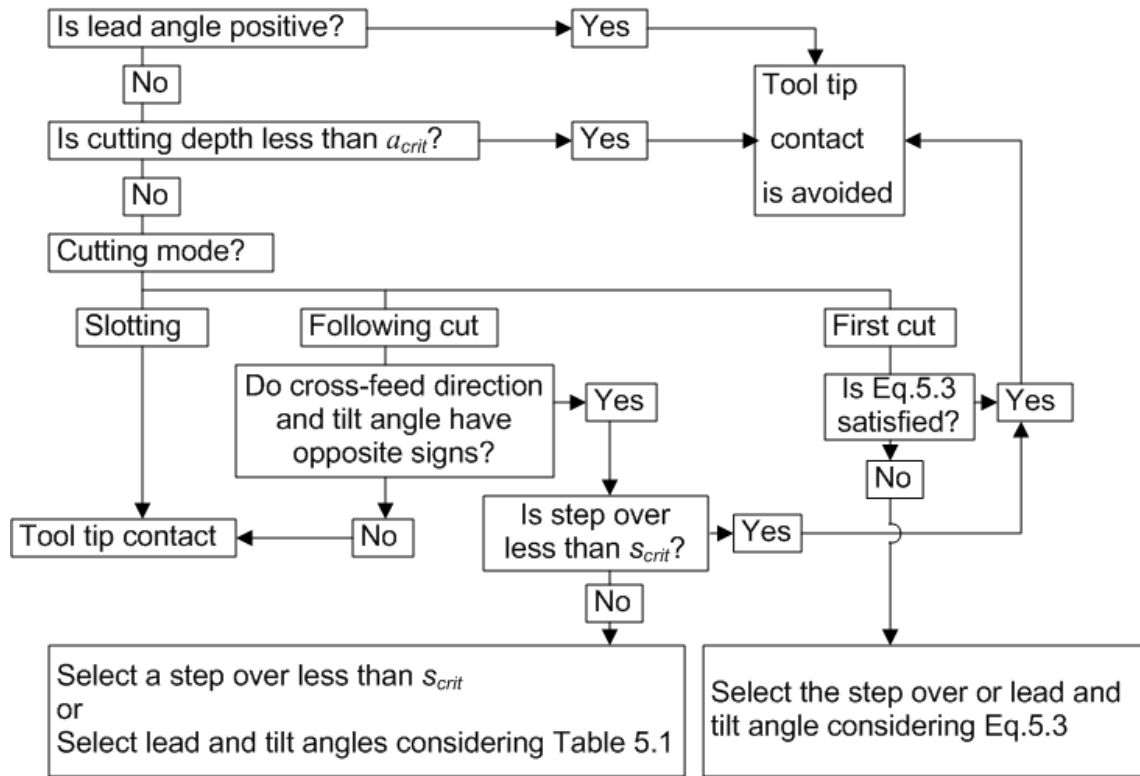
Figure 5.10: Tool tip contact avoidance procedure.

5.3. Scallop height and MRR

In finishing operations, the step over is decided according to the allowed scallop height on the resulting surface. Given the allowable scallop height, the required number of cutting steps may decrease with increasing tilt angle under certain conditions. Therefore, it is important to identify these conditions and select the tilt angle accordingly for increased productivity, which is discussed in this section.

For following cut cases, the tilt angle does not have any effect on the scallop height if the step over is less than s_b. This is in general the case for finishing operations where s is selected low in order to achieve good surface finish. However, if step over is higher than s_b, increasing tilt angle decreases the scallop heights left on the surface as shown in the following example.

In order to demonstrate the effect of tilt angle on scallop height, a following cut operation where cross feed direction is positive and cutting depth is 5 mm is considered for different step over values, i.e., 5 mm, 10 mm. The cutting tool is a 12 mm diameter ball-end mill. In Figure 5.11(a), the effect of the tilt angle on scallop height for the two cases is presented. When step over is 5 mm, the tilt angle does not affect the scallop height since $s \leq s_b$ condition holds for the given tilt angle range. However, as the step

over is increased to 10 mm, $s > s_b$ condition is satisfied when the absolute value of tilt angle exceeds 33.6^o. It is seen that the scallop height decreases for this case for higher absolute values of tilt angle in Figure 5.11.

The effect of tilt angle on the allowable step over values for four different scallop height constraints is shown in Figure 7(b). It is clearly seen that increase in tilt angle causes allowable step over value to increase, resulting in less number of cutting steps to remove the required volume of material.

(a)   (b)
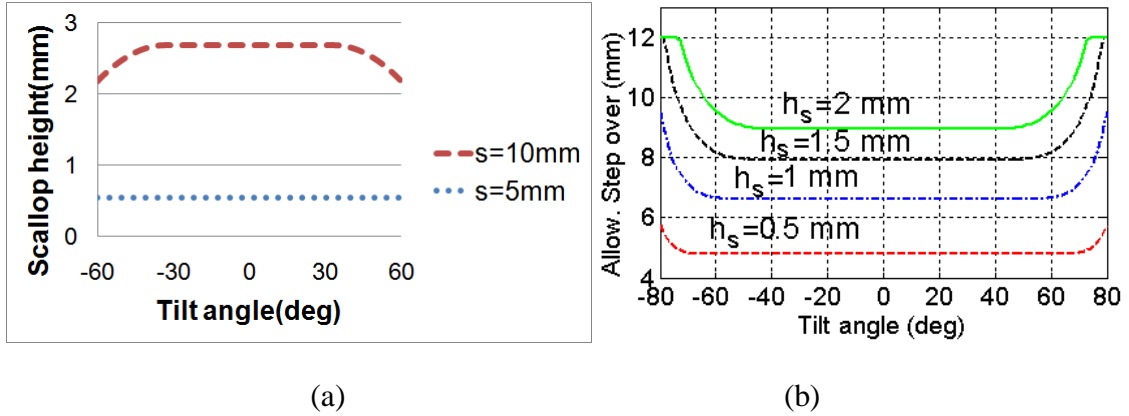
Figure 5.11: Variations of (a) scallop height (b) allowable step over with tilt angle
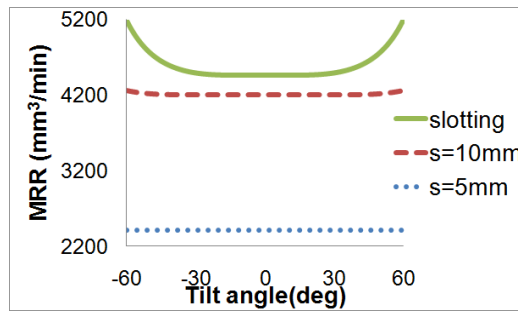
Figure 5.12: Variations of MRR with tilt angle

For the same example presented in Figure 5.11 the effect of tilt angle on MRR is demonstrated in Figure 5.12. As long as $s \le s_b$ condition holds, MRR is not affected by the tilt angle (s=5mm in Figure 5.12). But if s is higher than s_b, MRR increases as the absolute value of tilt angle increases (s=10mm in Figure 5.12). This is the reason for the increase in MRR when the tilt angle is more than 33.6^o in Figure 5.12.

For slotting cuts, the tilt angle has a considerable effect on MRR in cases where cutting depth is higher than a_b, which, depends on the radius of ball end mill and the absolute value of tilt angle, t_a:

$$a_b = R_o(1 - \sin t_a) \tag{5.4}$$

If cutting depth is higher than a_b, cylinder part of the cutting tool is also in cut with the workpiece. Hence, higher tilt angle results in higher MRR in these cases. However, if the cutting depth is less than a_b, the tilt angle has no effect on instantaneous MRR since only ball-part of the cutting tool is in engaged with the workpiece. The effect of the tilt angle on MRR is presented for a slotting case in Figure 5.12 where the other process parameters are same with the cases presented in Figure 5.11. In this case, cutting depth is higher than a_b when the value of the tilt angle is above 9.6^o, and it is seen that MRR increases for higher absolute values of tilt angle.

5.4. Cutting force, torque and form error

Effects of lead and tilt angles on cutting force, torque or form error can only be predicted through simulations using the process model [31] due to the complex geometry of the ball-end mill and non-linear variations. However, some qualitative information for the effect of the lead and tilt angles in following cut cases are given here considering the geometry and mechanics of the process for roughing and finishing operations, separately.

5.4.1. Roughing operations

For roughing operations, constraints such as cutting forces, torque, and power, and tool breakage are taken into account. F_{xy} is the resultant transversal force acting on the tool in xy-plane, and is responsible for bending stresses which may cause tool-shank breakage. Cutting power is proportional to cutting torque which is the integral of the products of local radius $R(z)$ and local tangential cutting force on the engagement zone (Figure 3.11). In ball-end mills, local radius increases along the tool axis direction (z) up to the cylindrical part. Lead and tilt angles affect cutting power and torque as they change the engagement region and local radius $R(z)$. In order to illustrate this, a lead and tilt angle combination where engagement region is on the upper side of the tool along the tool axis and another lead and tilt combination which positions the engagement zone on the lower side of the cutting tool along the tool axis are presented in Figure 3.6(a) and (b), respectively.

Lead angle can be selected as slightly positive in order to avoid tool tip contact while keeping the engagement region on the lower side of the cutting tool at the same time. If the cross-feed direction is negative, the tilt angle should be selected as negative so that the tool axis points toward the workpiece as illustrated in Figure 3.6(b). In this

case, the engaged region is kept on the lower side of the cutting tool along the tool axis. As a result, the local radii in the engaged region, and consequently cutting torque, are kept minimum. However, if the tilt angle is selected as positive, tool is inclined towards the workpiece and the engaged region shifts to the upper parts of the cutting tool as shown in Figure 3.6(a) resulting in higher local radii in the cutting zone and higher cutting torque. Similarly, if cross-feed direction is positive, for the aforementioned reason, tilt angle should be selected as positive. Nevertheless, accurate values of preferable lead and tilt angles can only be selected by running simulations by the process model.

5.4.2. Finishing operations

In finishing operations, one of the most the important limitations is the form error left on the part. It is defined as the dimensional error along the surface normal direction (N), which includes tool and workpiece deflections. Since the workpiece deflection is application specific, only the tool deflection is considered in this study.

In general, cutting tools are much stiffer in the tool axis direction (z) than (x) and (y) directions (Figure 3.11). For that reason, if the tool axis (z) is oriented in the surface normal direction (N) of the workpiece (*lead*=0 and *tilt*=0 case), tool deflection along the surface normal direction becomes minimum. However, in this case tool tip is in contact with the finished surface. As a result, the finished surface may not be of good quality especially in cutting operations of relatively softer metals such as aluminum.

An important consideration in selection of the tilt angle is over-cutting. If cutting tool starts cutting from the finished surface, depending on the magnitudes and directions of the cutting forces at the instant of surface generation, the cutting tool can deflect into the workpiece surface. This is the case when tilt angle is selected negative for a clockwise rotating cutting tool. Since over-cut cannot be corrected, negative tilt angle should be avoided for such tools in finishing operations. Similarly, for counter clockwise rotating tools negative tilt angle should be preferred to avoid over cut.

Consequently, although the quantitative effect of lead and tilt angles on the tool deflection in the surface normal direction can only be predicted through simulations using a process model [31], it can be concluded that for a clockwise rotating tool, using slightly positive lead and tilt angles would be better to obtain smaller deflections and to avoid tool tip contact.

5.5. Stability Limits

Lead and tilt angles have effects on the directional coefficient matrix (Section 4.3), which defines the relation between dynamic displacements and dynamic cutting forces (Section 4.3), since they change engagement region between cutting tool and workpiece.

Depending on the kinematic configuration of machine tools, lead and tilt angles may also have effects on the feed direction. This effect is seen when the rotational axes of the machine tool are on the table side (Figure 4.12). In this case, if the measured transfer functions of the cutting tool in two orthogonal directions, i.e., (X) and (Y) directions are not the same, the measured transfer function matrices need to be oriented accordingly. The measured transfer function matrix H can be oriented using a transformation matrix T_G as presented in (4.37):

As a result, due to their effects on the directional coefficient and oriented transfer function matrices, lead and tilt angles can change the stability limits of processes considerably. This effect is demonstrated through simulations and experiments in the next section.

5.6. Experimental and Simulation Results

The effect of lead and tilt angles on tool tip contact, overall machining time, cutting forces and cutting torque, and stability are investigated through simulations and the results are verified by a series of cutting tests

5.6.1. Tool Tip Contact consideration

The effect of tool tip contact on the resulting surface is demonstrated through two cutting tests in following cut mode. The cross-feed direction is selected as negative in the tests, where 12 mm diameter ball-end mill is used. The test conditions are given in Table 5.2. In test 1, lead and tilt angles are selected to be zero. Hence, tool tip is in contact with the created surface and leaves tool tip mark on the surface as shown in Figure 5.13(a). In test 2, by application of positive lead angle, tool tip contact is avoided. As presented in Figure 5.13 (b), the tool tip mark observed in test 1, does not exist on the surface for the test 2.

Table 5.2: Conditions for the tool tip contact tests.

Test	Lead (°)	Tilt (°)	s (mm)	a (mm)	Tip contact
1	0	0	6	1.5	Yes
2	10	0	6	1.5	No

Tool tip mark →

6mm   6mm

(a)   (b)
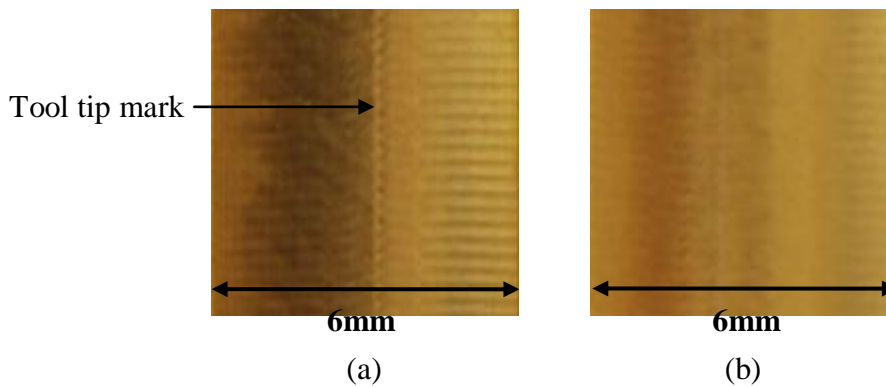
Figure 5.13: Resulting surface after (a) test1 (b) test 2

5.6.2. Scallop Height

As mentioned previously, the number of required cutting steps subject to a scallop height limit can be decreased by increasing the absolute value of the tilt angle, resulting in lower cycle time. This is demonstrated by two example cases.

The example workpiece has planar surface with 100 mm of length in the feed and cross feed directions. The cutting tool is a 12 mm diameter ball end mill. The conditions of the two cases are given in Table 5.3. Before an increase in tilt angle is applied, tilt angles are selected as -35°. In the first case scallop height limit is 2 mm, whereas it is 1 mm in the second case. Considering these limits, the allowable step over values for case 1 and case 2 are determined as 8.94 mm and 6.63 mm using the formulation in Table 3.4. By modifying the tilt angles as -71° and 75° for case 1 and case 2, respectively, allowable step over value increases to 11.28 mm in the first case and to 7.84 mm in the second case. Therefore, the total number of cutting steps decreases by 25% and 19% in case 1 and case 2, respectively. Finally, a decrease in the machining time is achieved by only changing the tilt angle.

Table 5.3: Effect of tilt angle on allowable step over while scallop height is fixed.

	Case 1	Case 2	Modified case 1	Modified case 2
Scallop Height limit (mm)	2	1	2	1
Lead, Tilt (^{o})	10, -35	10,-35	10, -71	10, -75
Allowable step over (mm)	8.94	6.63	11.28	7.84
Number of Cutting Steps	12	16	9	13

5.6.3. Cutting force, torque and form error

Effects of lead and tilt angle pairs are demonstrated by roughing and finishing examples in this section. The variation of cutting torque and maximum F_{xy} force with lead and tilt angles are demonstrated in the roughing examples while the effect of lead and tilt angles on form error is presented for a finishing case (Figure 5.14).

The first roughing case is a following cut operation where the cutting depth and the step over are 5 mm, the feed rate is 0.05 mm/tooth, the spindle speed is 1000 rpm and cross-feed direction is negative. The cutting tool is a 12 mm diameter, 2 fluted ball-end mill with 30° helix angle and 8° rake angle. It is a clock-wise rotating tool. The workpiece material is Ti6Al4V which is commonly used in aerospace industry. The cutting force coefficients are calculated using *mechanics of milling method* as presented in [36].

Using the force model presented in the Section 3.7, the variation of maximum cutting torque is calculated and plotted for different lead and tilt angle combinations in Figure 5.14(a). Since negative lead angles are generally unfavorable due to tool tip contact, negative lead angle cases are not included in the figure. As it can be seen from the figure, cutting torque is less for negative tilt angles. Moreover, simulated variation of maximum resultant lateral force F_{xy} for different lead and tilt combinations is also shown (Figure 5.14(a)). In order to verify these predictions, three points were selected on Figure 5.14(a) and cutting tests were performed. Measurement and simulation results

for maximum resultant lateral force F_{xy} in these cases are tabulated in Table 5.4. It's seen that force predictions are in good agreement with the measurements. Comparing the figures for maximum torque and maximum force F_{xy}, it is seen that variation of maximum torque and maximum resultant lateral force F_{xy} with lead and tilt angles have a similar trend.

Figure 5.14(a) reveals that low lead angles and negative tilt angles are favorable for decreased maximum resultant lateral force F_{xy} and cutting torque when cross-feed direction is negative. Hence, the qualitative remarks made about effects of tilt angle in Section 5.4, are verified by simulations and experiments in Figure 5.14(a). For this case, in order to keep cutting torque and resultant lateral force F_{xy} low, and also to avoid tool tip contact, lead angle should be selected slightly positive and tilt angle should be negative. As a result, lead and tilt angle combination of $(5^{o}, -40^{o})$ can be a good selection for this case.

In the second roughing example, all the process parameters are the same with the previous case except the cross-feed direction, which is positive. Simulated variation of the maximum torque and maximum F_{xy} force with lead and tilt angles is plotted in Figure 5.14(b). As presented in Section 5.4, it is seen that slightly positive lead angles and positive tilt angles are favorable in this case. Therefore, for this case lead and tilt angles can be selected as 5° and 40°, respectively.

The last example is a finishing example where cross-feed direction is negative. Cutting depth and step over are both 1 mm and the other process parameters are same with the previous examples. As expected, the minimum tool deflection in the surface normal direction results when the tool axis is aligned with surface normal direction of the workpiece (point 1 in Figure 5.14(c): lead and tilt angles are both zero). However, in this case, the tool tip is in contact with the finished surface and it may result in poor surface quality. Positive lead angles are favorable to avoid tool tip contact. On the other hand, in order to avoid overcut from the surface, positive tilt angles are preferred as presented in Section 5.4. In Figure 5.14(c), it is shown that negative tool deflections in the surface normal direction which results in over-cut from the surface are possible for some negative tilt angles. As a result, the lead and tilt angle pair of $(5^{o}, 5^{o})$ can be selected for this case.
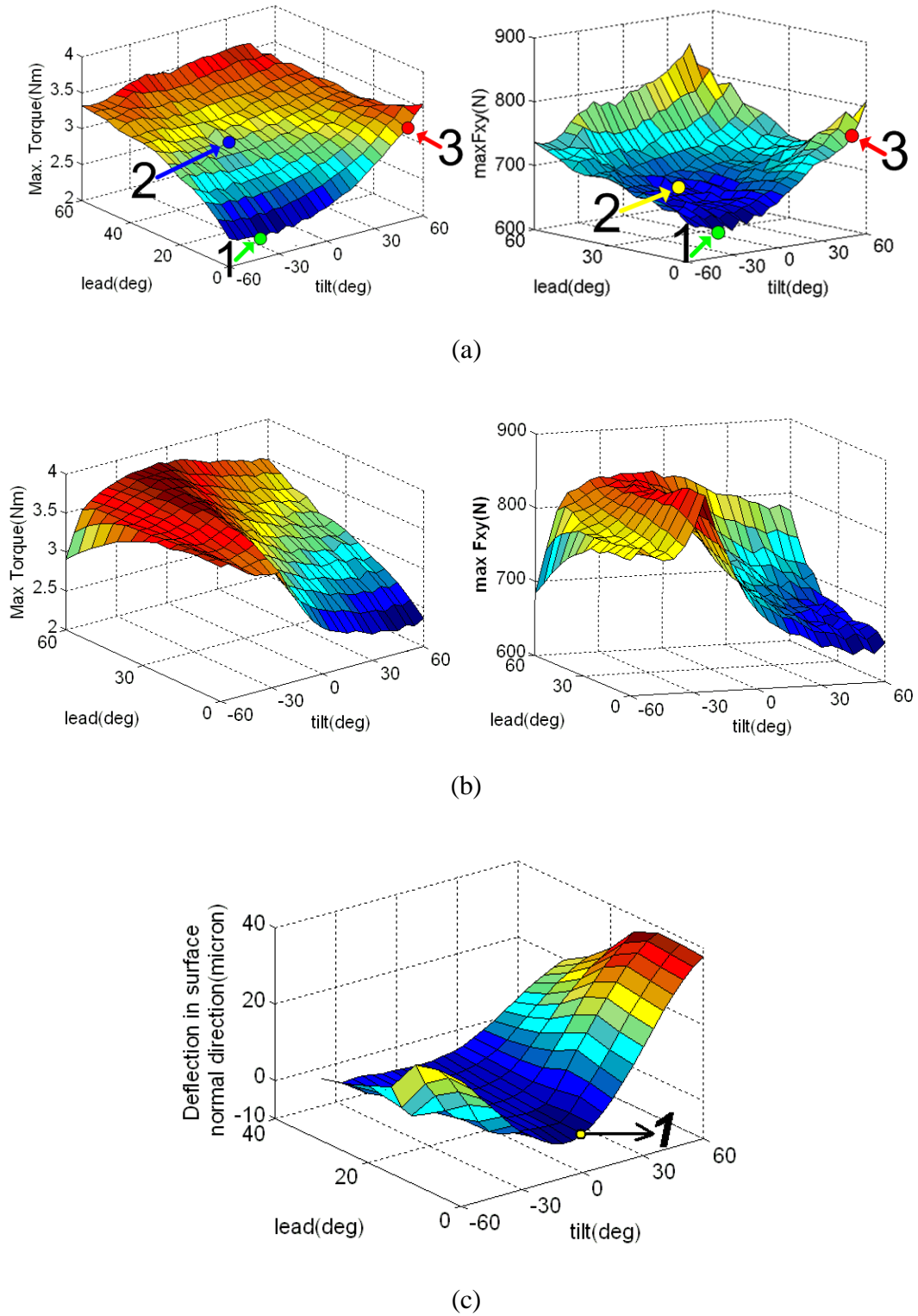
Figure 5.14: Effects of lead and tilt angles on (a) maximum torque, maximum F_{xy} force for case 1 (b) case 2 (c) tool deflection in the surface normal direction for example 3.

Table 5.4: Simulation and measurement comparison for the case in Figure 5.14(a).

Point	lead, tilt (^{o})	Simulated maximum $F_{xy}(N)$	Measured maximum $F_{xy}(N)$
1	0,-40	637	600
2	30,-15	672	652
3	0,50	752	712

5.6.4. Stability Example

Effects of lead and tilt angles on absolute stability limits are presented on an example case in this section.The example case is a following cut operation where step over is 2 mm and cross-feed direction is negative. The cutting tool is a 16 mm diameter ball-end mill with 2 flutes that has 8° rake angle and 30° helix angle. Overhang length of the tool is 75mm and it is connected to the tool holder by shrink-fit system. The machining center is DMG 50 Evolution where 2 rotational axes are on the table side (Figure 3.16), and the workpiece is a rectangular block of 1050 steel that is clamped directly to the rotary table. Only the flexibility of the cutting tool is considered and the measured frequency response functions in (X) and (Y) directions are presented in Figure 5.15. In the same figure, simulated effects of lead and tilt angles on the absolute stability limits are presented. It is seen that lead and tilt angles affect absolute stability limits considerably. In order to verify this observation, the absolute stability limits were determined experimentally for six different combinations of lead and tilt angles which are also shown on the same figure. Overall, there is a reasonable agreement between the model predictions and the experimental results.

According to the stability predictions shown in Figure 5.15, for lead and tilt combination of (0°,0°) at 2 mm cutting depth and at 9000 rpm, the process is expected to unstable which was verified experimentally. The chatter effect on the resulting surface quality is presented in Figure 5.15 where the effect of the tool tip contact is also observable on the surface. For the same cutting depth and spindle speed, the surface obtained wih (15°,0°) combination is also shown in the figure. In this case, the process is stable as predicted, and the tool tip contact is avoided with the application of 15° lead angle.
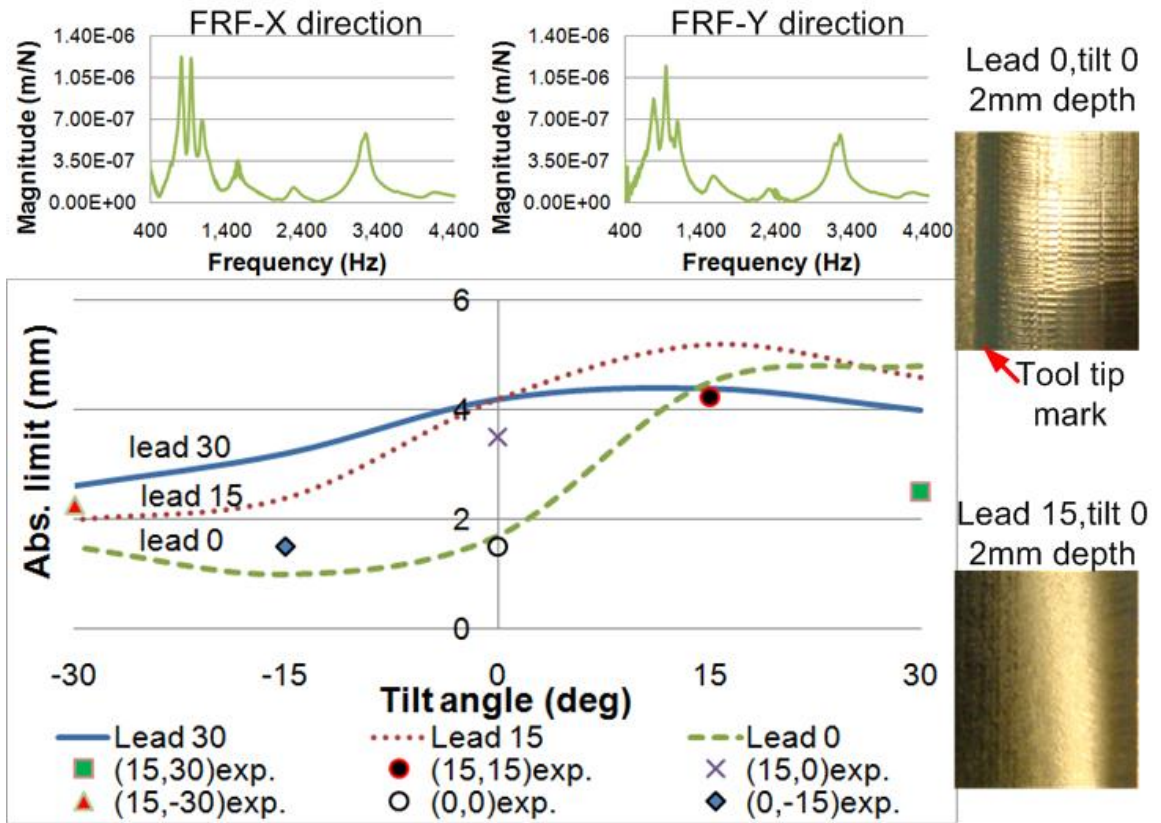
Figure 5.15: Effect of lead and tilt angles on stability

6. DYNAMICS OF PARALLEL TURNING OPERATIONS

In this chapter, dynamics of two different parallel turning operations are modeled. In the first case, a specially designed tool holder which can hold two cutting tools is used on a standard turning center. There is direct dynamic coupling between the tools since they are on the same turret location. In the second case, the turning tools are clamped on independent turrets on a parallel turning center. In this case, there is no direct dynamic coupling between the tools, but they dynamically interact through the workpiece. The formulations for both cases are presented in the next section. In Section 6.2, the procedure developed for generation of stability diagrams is explained. The stability limit predictions of the presented model are demonstrated for different cases and the simulation results are compared by experimental data in Section 6.3.

6.1. Formulation of Dynamics of Parallel Turning

6.1.1. Two turning tools on the same turret

An orthogonal turning process with two turning tools on the same turret is modeled as shown in Figure 6.1 below. These two tools move in feed direction together but cutting depths of each tool can be different. The cutting depth of tool 1 is expressed as a_1 and the cutting depth of tool 2 is expressed as a_2. Each tool can be modeled as being attached to a rigid surface of the machine with spring (k_i) and damping (b_i) elements as seen in the Figure 6.1. Moreover, there is a dynamic interaction between the cutting tools which is represented by b_{12} and k_{12} in the figure. In this model, dynamics of the workpiece can also be taken into account. However, the dynamics of the workpiece is neglected since the workpiece is considerably rigid with respect to the cutting tools along its longitudinal axis which is the Z–axis.

In order to obtain stability formulation, dynamic chip thickness of each cutting tool is formulated firstly. The feed rates (h_o) of both the tools are the same, because two tools move together in feed direction. As shown in Figure 6.1, dynamic displacements on the tools occur due to cutting forces (F_1, F_2) in the feed direction. Displacement of tool 1 is expressed as z_1 and displacement of tool 2 is expressed as z_2. Dynamic chip thicknesses (h_1, h_2) of each tool resulting from dynamic displacements are expressed as:
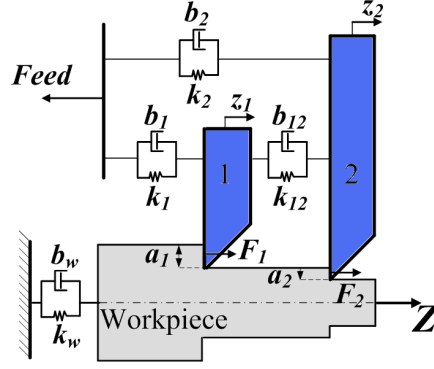
Figure 6.1 : Parallel turning on different surfaces

$$h_1(t) = h_o - z_1(t) + z_1(t-\tau)$$
$$h_2(t) = h_o - z_2(t) + z_2(t-\tau) \qquad (6.1)$$

where τ is rotation period of workpiece in terms of second. Dynamic chip thicknesses changes due to change in values of dynamic displacements between two sequential rotation periods. Static chip thickness, h_o, does not affect regeneration mechanism [1]. Hence, it can be excluded from stability formulation. Dynamic displacement values can be expressed by transfer functions of the system and dynamic cutting forces as shown below:

$$\begin{bmatrix} z_1(t) \\ z_2(t) \end{bmatrix} = \begin{bmatrix} G_{11} & G_{12} \\ G_{21} & G_{22} \end{bmatrix} \begin{bmatrix} F_1(t) \\ F_2(t) \end{bmatrix} \qquad (6.2)$$

where G_{ij} is the transfer function that represents the displacement of the *ith* tool in response to a force at *jth* tool. These transfer functions can be measured by modal analysis. Cutting forces in feed direction are expressed in terms of cutting force coefficient in feed direction K_f, cutting depths a_1 and a_2, dynamic chip thicknesses $h_1(t)$ and $h_2(t)$ as follows:

$$\begin{bmatrix} F_1(t) \\ F_2(t) \end{bmatrix} = \begin{bmatrix} K_f a_1 h_1(t) \\ K_f a_2 h_2(t) \end{bmatrix} \qquad (6.3)$$

By substituting the equation for dynamic chip thicknesses into (6.3), the below equation is obtained:

$$\begin{bmatrix} F_1(t) \\ F_2(t) \end{bmatrix} = \begin{bmatrix} K_f a_1 (z_1(t-\tau) - z_1(t)) \\ K_f a_2 (z_2(t-\tau) - z_2(t)) \end{bmatrix} \qquad (6.4)$$

The dynamic displacement values and the dynamic cutting forces when the system is marginally stable can be expressed as follows:

$$\begin{bmatrix} z_1(t) \\ z_2(t) \end{bmatrix} = \begin{bmatrix} z_1 \\ z_2 \end{bmatrix} e^{i\omega_c t}$$

$$\begin{bmatrix} F_1(t) \\ F_2(t) \end{bmatrix} = \begin{bmatrix} F_1 \\ F_2 \end{bmatrix} e^{i\omega_c t} \tag{6.5}$$

Marginal stability refers to the transition phase between the stable region and unstable region. Since the two tools are interacting with each other dynamically, they vibrate with the same chatter frequency ω_c. Additionally, the dynamic displacement values in the previous rotation can be written as follows [1]:

$$\begin{bmatrix} z_1(t-\tau) \\ z_2(t-\tau) \end{bmatrix} = \begin{bmatrix} z_1(t) \\ z_2(t) \end{bmatrix} e^{-i\omega_c \tau} \tag{6.6}$$

By substituting the relations presented in the equations (6.2), (6.5) and (6.6) into equation (6.4), the cutting forces at the stability limit in terms of cutting forces become:

$$\begin{bmatrix} F_1 \\ F_2 \end{bmatrix} e^{i\omega_c t} = K_f (e^{-i\omega_c \tau} - 1) \begin{bmatrix} a_1 & 0 \\ 0 & a_2 \end{bmatrix} \begin{bmatrix} G_{11} & G_{12} \\ G_{21} & G_{22} \end{bmatrix} \begin{bmatrix} F_1 \\ F_2 \end{bmatrix} e^{i\omega_c t} \tag{6.7}$$

In order to simplify the equation above, a new matrix $\textbf{\textit{B}}$ is defined below:

$$\textbf{\textit{B}} = K_f (e^{-i\omega_c \tau} - 1) \begin{bmatrix} a_1 & 0 \\ 0 & a_2 \end{bmatrix} \begin{bmatrix} G_{11} & G_{12} \\ G_{21} & G_{22} \end{bmatrix} \tag{6.8}$$

6.1.2. Two turning tools on different turrets

A parallel turning process with two turning tools on different turrets is demonstrated in Figure 6.2. They cut the same surface but the cutting depths of the tools can be different. According to the notation used in the model, the tool with a higher cutting depth is named as the second tool (Figure 6.2). The flexibilities of the tools in Z direction are considered only in this case. Since the workpiece is relatively rigid with respect to the cutting tools, the workpiece flexibility is neglected. Although there is no dynamical coupling between the tools, they are dynamically dependent since vibration waves left by each tooth on the workpiece surface affect the other tooth's dynamic chip thickness.
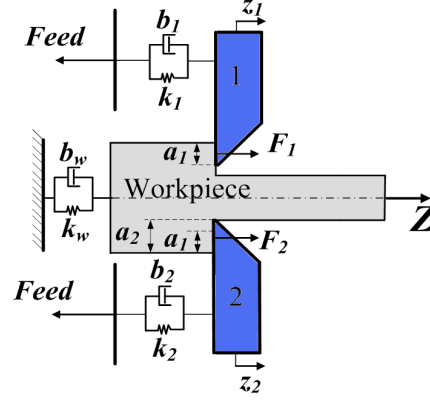
Figure 6.2 : Parallel turning on different turrets

Due to the dynamic cutting forces on each tool (F_1 and F_2), the dynamic displacements (z_1 and z_2) develop on the tools. These displacements affect the dynamic chip thickness values, and the dynamic cutting forces on each tool can be written as follows:

$$\begin{bmatrix} F_1(t) \\ F_2(t) \end{bmatrix} = K_f \begin{bmatrix} a_1(\dfrac{h_o}{2} - z_1(t) + z_2(t - \dfrac{\tau}{2})) \\ a_1(\dfrac{h_o}{2} - z_2(t) + z_1(t - \dfrac{\tau}{2})) + (a_2 - a_1)(h_o - z_2(t) + z_2(t - \tau)) \end{bmatrix} \qquad (6.9)$$

Unless the cutting depths on each tool are equal, there are two different regions with different mechanical and dynamic characteristics in the process. The region with depth of a_1 is removed by both of the tools. In this region, dynamic chip thickness on a tool is affected by the displacement of the tool at present time and the displacement of the other tool at a half rotation period ($\tau/2$) before. The feed per revolution h_o is shared between the tools in this region as the static chip thickness. On the other hand, the region with a depth of a_2-a_1 is only removed by the second tool. Hence, the dynamic chip thickness depends on the dynamic displacement of the second tool at present time and at one rotational period (τ) before. The static chip thickness on the second tool is equal to the feed per revolution in this region.

Since the static chip thicknesses on the tools do not affect the regeneration mechanism, for the stability analysis they can be removed from the formulation presented in Equation (6.9). Dynamic displacements (z_1 and z_2) can be calculated in terms of cutting forces and transfer functions as follows:

$$\begin{bmatrix} z_1(t) \\ z_2(t) \end{bmatrix} = \begin{bmatrix} G_{11}F_1(t) \\ G_{22}F_2(t) \end{bmatrix} \qquad (6.10)$$

Dynamic displacements and dynamic cutting forces on the tools at the limit of the stability can be written using Equation (6.5). Dynamic displacement of the second tool one rotational period before can be determined using Equation (6.6). Moreover, the displacements one half of the rotation period before can be calculated using the following formulation:

$$
\begin{bmatrix} z_1(t - \dfrac{\tau}{2}) \\ z_2(t - \dfrac{\tau}{2}) \end{bmatrix} = \begin{bmatrix} z_1(t) \\ z_2(t) \end{bmatrix} e^{-i\omega_c \frac{\tau}{2}}
$$

(6.11)

After the presented formulations are substituted into Equation (6.9) and re-arranged, the cutting forces at the limit of stability can be written as follows:

$$
\begin{bmatrix} F_1 \\ F_2 \end{bmatrix} e^{i\omega_c t} = B \begin{bmatrix} F_1 \\ F_2 \end{bmatrix} e^{i\omega_c t}
$$

(6.12)

where B matrix for this case is presented below:

$$
B = K_f \begin{bmatrix} -a_1 G_{11} & a_1 G_{22} e^{-i\omega_c \frac{\tau}{2}} \\ a_1 G_{11} e^{-i\omega_c \frac{\tau}{2}} & a_2 G_{22}(e^{-i\omega_c \tau} - 1) - a_1 G_{22} e^{-i\omega_c \tau} \end{bmatrix}
$$

(6.13)

6.2. Calculation of stability diagrams

The procedure for generation of stability diagrams for the two cases considered is presented in this section. After some arrangements, the relations developed for dynamic cutting forces in Equation (6.7) and Equation (6.13) take the following form:

$$
[I - B] \begin{bmatrix} F_1 \\ F_2 \end{bmatrix} = 0
$$

(6.14)

where I is the 2*2 identity matrix. In order to have non-trivial solutions, determinant of $[I\text{-}B]$ matrix should equal to zero. The determinant results in a complex valued equation with variables a_1, a_2, ω_c and τ. When the real and imaginary parts of the equation are grouped and equated to zero, two independent equations are obtained Equation (6.15). Since the resulting equations are lengthy, they are presented symbolically as follows:

$$
\begin{aligned}
\text{Real}(\det[I - B]) &= 0 \\
\text{Imaginary}(\det[I - B]) &= 0
\end{aligned}
$$

(6.15)

In the first parallel turning case presented in Section 6.1.1, the cutting depth a_2 is the height difference between tip positions of tool 1 and tool 2. It is set after the tools are fixed on the tool holder. For that reason, a_2 is a known parameter for a given configuration. Thus, the stability diagram for a_1 can be determined for a given a_2.

For the second parallel turning case explained in the Section 6.1.2, the cutting depth on the second tool, a_2, should be selected before the stability analysis. Similar to the first case, the stability diagram for a_1 can be obtained for a given a_2. But it should be remembered that that a_2 is selected as higher than a_1 in the related formulation. Hence, only the stability limit values for a_1 which are less than a_2 should be considered as solution

After these explanations, there are three unknowns, namely a_1, ω_c and τ, in the formulation for both parallel turning cases whereas there are only two independent equations at hand. Cutting depth a_1 is solved in terms of ω_c and τ using the real part of the complex equation in Equation (6.15) and this relation is substituted into the imaginary part of the complex equation in Equation (6.15). Hence, a_1 is eliminated, and the imaginary part of the complex equation is obtained with 2 parameters, ω_c and τ, only. The resulting equation includes many trigonometric functions, and thus a closed form analytical solution for ω_c is not possible to obtain. Hence, a search algorithm, named as golden section search [95], is used to solve τ for a given ω_c.

The solution procedure followed to obtain stability diagram is presented below:

- Firstly a chatter frequency range is selected where $\omega_{c,min}$, $\omega_{c,max}$ and $\Delta\omega$ represent lower limit, upper limit and increment of the frequency range, respectively. Since chatter frequencies (ω_c) are expected to be close to the natural frequency of the tools, the selected range should contain all the natural frequencies of the system.

- Then, the spindle speeds are swept with Δn increments for a given chatter frequency (ω_c). Each spindle speed n corresponds to a rotational period τ by $n=60/\tau$.

- For each ω_c and τ pair, the imaginary part of the complex equation in Equation (6.15) is calculated. If there is a sign change between consecutive τ values, a root of the equation is bracketed in an interval with a width of Δn.

- Then, using the golden ratio [95], spindle speed value that satisfies the equation is identified with a preset tolerance. For each chatter frequency, more than one spindle speed is determined corresponding to different lobe numbers in the stability diagram.

- Using calculated rotational periods and given chatter frequencies, a_1 values are calculated by the real part of Equation (6.15). ω_c and τ pairs resulting in negative a_1 values are eliminated from the solutions.

- Finally, the stability diagram can be obtained by plotting a_1 with respect to the spindle speed. Since a search algorithm is employed to obtain the stability diagrams, increments in the frequency and spindle speed ranges, which are represented by $\Delta\omega$ and Δn, have considerable effects on the accuracy of the stability diagrams. Hence, they should be selected small enough until a convergence in the solution is obtained.

6.3. Experimental Results and Simulations

In the tests, 1050 steel work material and TPGN 160304 TT1500 cutting inserts are used. For feed values between 0.005 and 0.13 and cutting speed of 200 m/min, the edge and cutting force coefficients in the feed direction are calibrated as 116N/mm and 872 MPa, respectively, using the linear-edge force model [36].

The FRFs of the flexible structures are measured using tap testing as shown in Figure 6.3. The modal data is determined using Cutpro software [93] and the transfer functions are calculated using the following equation:

$$G_{ik}(j\omega) = \sum_{r=1}^{q} \frac{1/m_r}{(j\omega)^2 + 2\xi_r\omega_{n,r}(j\omega) + \omega_{n,r}^2} \tag{6.16}$$

where q is the number of modes used to represent the transfer function. The stability results for two different examples that represent the two processes explained in Section 6.1 are presented here. In the first example, a standard turning machine tool (Mori Seiki NL 1500) is used with a special tool holder, and in the second example a parallel machine tool (Index ABC) is employed.
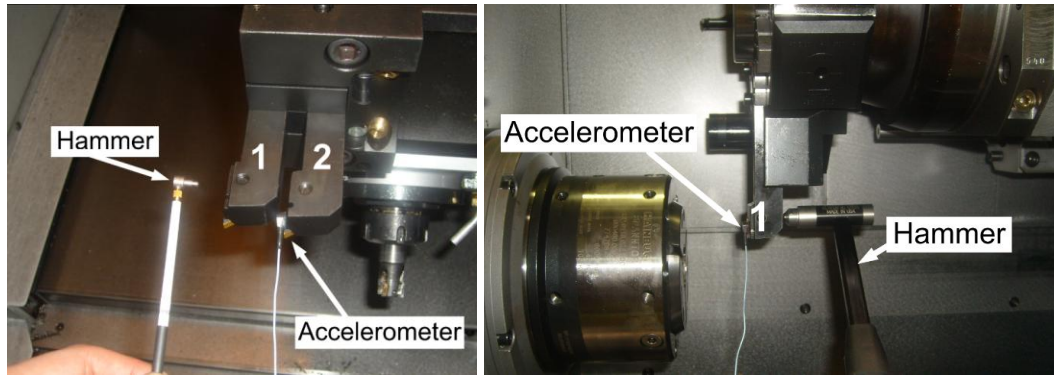
(a)   (b)

Figure 6.3 : Measurement of FRFs for different processes

6.3.1. The first example

In this example, the cutting tools are clamped on the same turret with a special tool holder in order to achieve parallel turning process on a standard turning machine (Figure 6.3). Due to the design of the tool holder, cutting depth of the second tool a_2 is fixed after the tools are clamped to the holder. Second tool is clamped in such a way that a_2 becomes 4.7mm in the parallel turning operation. The modal data determined for the tools are tabulated in Table 6.1. The workpiece is an 85 mm diameter cylinder and it's relatively rigid with respect to the tools in the feed direction.

First of all, using the orthogonal stability model [1], the stability diagram for each tool is calculated for independent operation. The absolute stability limits of the first and second tools are around 4.45 mm 5.45mm, respectively (Figure 6.4). The chatter frequencies that result in the minimum stability are quite different on each tool. The chatter frequency at the absolute stability for the first tool is 2325Hz whereas for the second tool it is 3680 Hz.
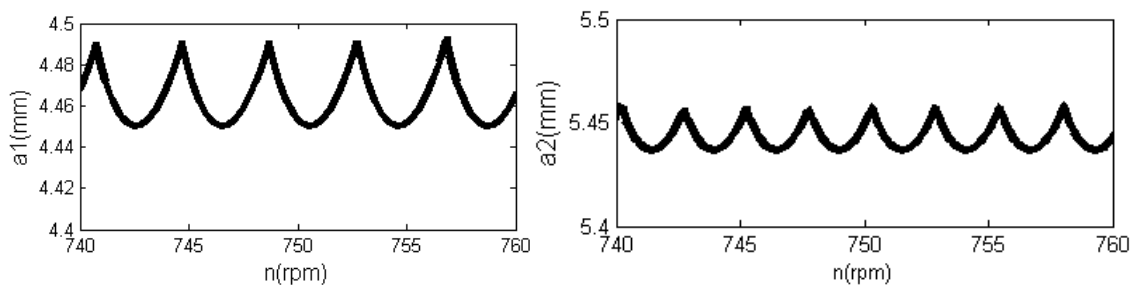
(a)   (b)

Figure 6.4 :Stability diagrams for independent turning operation (a) Tool 1 (b) Tool 2

The stability diagram for a_1 when two tools work in parallel is presented in Figure 6.5. The first tool's absolute stability limit decreases slightly due to the second tool. But comparing this decrease with the additional depth of cut of 4.7 mm removed by the second tool, it can be claimed that parallel turning is very advantageous as the total stable material removal rate nearly doubles compared to the case with only one tool is in cut.

Table 6.1: Modal data of the first example

FRF	Mode	f_n(Hz)	ζ (%)	k(N/m)
G_{11}	1	2086.1	5.71	$4.875*10^7$
	2	2290.7	1.61	$2.272*10^8$
	3	3899.9	1.22	$3.591*10^8$
$G_{12} = G_{21}$	1	2067.1	5.55	$1.635*10^8$
	2	3572.7	5.35	$-2.189*10^8$
G_{22}	1	2050.7	4.78	$6.753*10^8$
	2	2553.9	2.87	$8.602*10^8$
	3	3036.1	6.09	$5.903*10^7$
	4	3443.5	1.29	$3.141*10^8$
	5	3629.6	1.61	$3.069*10^8$
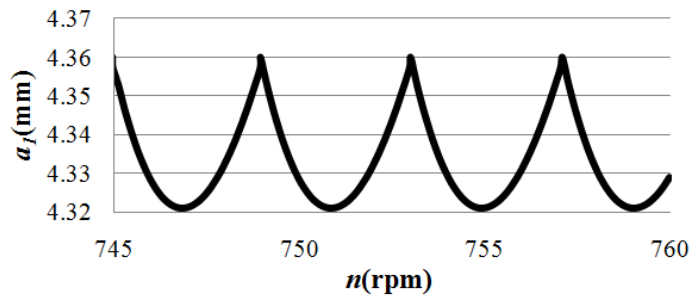
Figure 6.5 : Stability diagram for the parallel operation, a_2=4.7mm
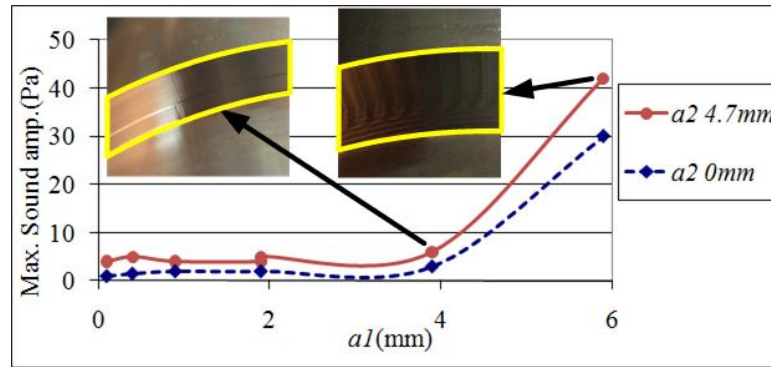
Figure 6.6: Variation of sound amplitude with a_1.

In order to verify the predictions, several cutting tests have been performed for single and parallel processes at 750 rpm. In both processes, the first tool's cutting depth a_1 was changed between 0.1 mm and 5.9 mm at 6 levels. During the tests, the sound amplitude was measured using a microphone that is fixed to the turret. Maximum sound amplitude is plotted with respect to cutting depth a_1 for both single and parallel processes in Figure 6.6. It can be seen that there is a sharp increase in sound amplitudes between a_1=3.9 mm and a_1=5.9 mm for both single and parallel processes which means that the stability limit for both cases is between 3.9 and 5.9 mm. Moreover, two photos of the surfaces created by the first tool in parallel operation are presented in Figure 6.6. The one on the right has chatter marks while they are not seen on the left one. For the single tool process, similar result is also observed. As a result, it can be concluded that the model's predictions agree with the experimental results.

6.3.2. The second example

In this example case, the cutting tools are clamped on independent turrets on a parallel machine tool as shown in Figure 1.4(b). Although they are independent, they are programmed such that there is no relative motion between the cutting tools, and their Z coordinates are the same during the parallel turning process. Hence, they cut the same surface. The modal data measured for the first and second tool in the feed direction are tabulated in Table 6.2. Note that in this case the modal frequencies of the tools are quite close to each other which has significant consequences on the parallel cutting stability as it will be shown below. The workpiece is a 35mm diameter cylinder of 1050 steel and its flexibility in the feed direction can be neglected compared to the flexibility of the cutting tools. For that reason, dynamic interaction between the tools occurs only through the effect of vibration waves left by each tool on the other tool.

Table 6.2:Modal data of the second example

Mode	f_n(Hz)	ζ(%)	k(N/m)
G_{11}	2238.9	3.23	$4.769*10^7$
G_{22}	2372.3	4.51	$1.166*10^8$

For independent operation of the cutting tools, the stability limits for the first and the second tools are calculated using the orthogonal stability model [1]. The first tool's absolute stability limit is determined around 3.6 mm at 2310Hz whereas the absolute stability limit of the second tool is calculated around 12.6 mm at 2480Hz (Figure 6.7).
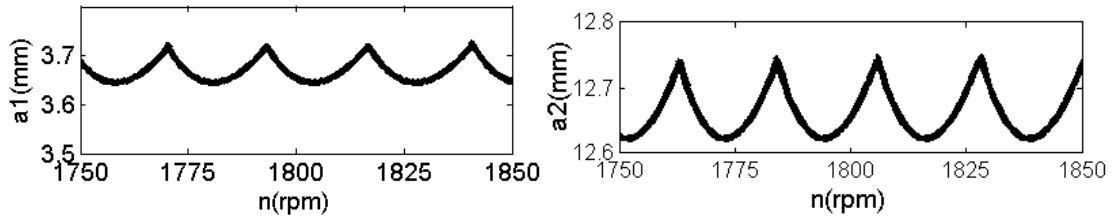
Figure 6.7: Stability diagrams for independent turning operation (a) Tool 1 (b) Tool 2
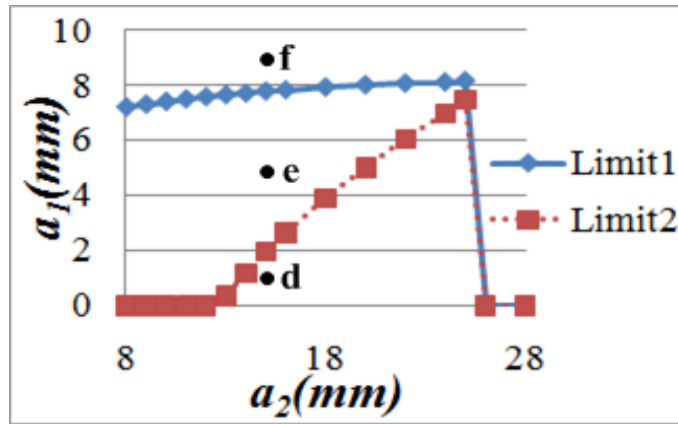
Figure 6.8: Effect of a$_2$ on absolute stability limits

When two tools work in parallel, the effect of the cutting depth a_2 on the absolute stability of the first tool is presented in Figure 6.8. In this case there are two stability limits defining the boundaries of minimum and maximum stable cutting depths for the first tool. This means that the process is stable if the cutting depth is between these boundaries. This is believed to be due to very close modal frequencies of the tools which increases the dynamic interaction effects. As it was demonstrated in the previous example, parallel cutting may increase the total stability of the system due this interaction which in this case enhanced due to close modal frequencies. One may see

this as an "absorber effect" similar to tuned vibration absorbers. The curve with legend "Limit1" in Figure 6.8 represents the higher absolute stability of the first tool. Note that increasing a_2 value has stabilizing effect on the system. This effect is seen for the a_2 values between 8 and 25 mm. For higher values of a_2, the process becomes unstable independent of a_1. For a_2 values higher than 12.6 mm the lower stable cutting depth, "Limit2", is also seen on the stability diagram. It also increases with a_2 and becomes closer to Limit1. For a_2 values higher than 25mm, Limit1 and Limit2 coincide and the system becomes totally unstable. In order to demonstrate the "two-limit" case, stability diagram calculated when a_2 is 25 mm is presented in Figure 6.9.

A time domain model is also developed for dynamics of parallel turning processes. It is used to verify the observations made in Figure 6.8. With that purpose, 3 points (d, e and f) are selected on Figure 6.8, and the variations of the displacements of first tool in time are presented in Figure 6.10 for spindle speed of 1825 rpm. Analyzing the trends of z_1 variations, points d and f are identified as unstable while point is d is clearly a stable point. These results verify the frequency model's predictions.
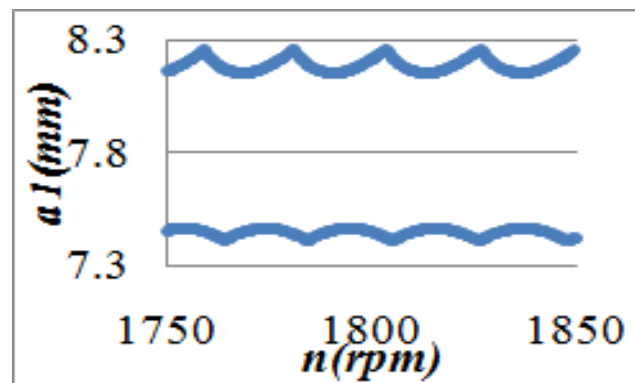
Figure 6.9: Stability diagram of tool 1 when a$_2$ is 25mm
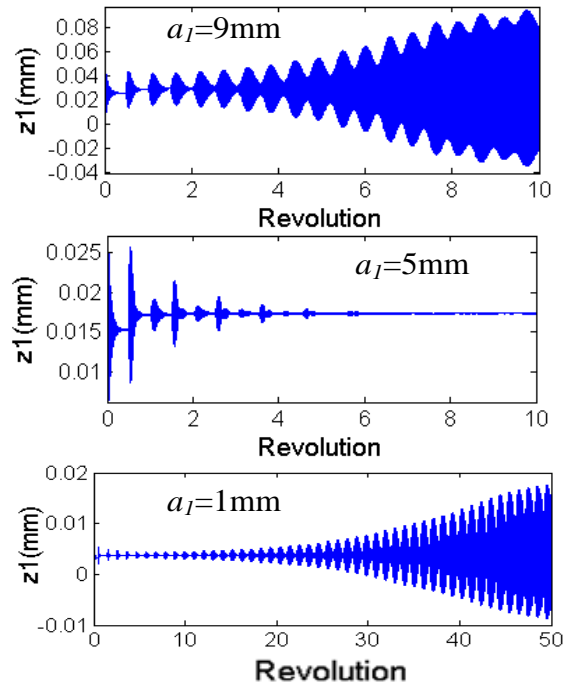
Figure 6.10: Variation of z_1 at points f, e and d on Figure 6.8

7. DYNAMICS OF PARALLEL MILLING OPERATIONS

In this chapter, a time-domain model for parallel milling processes with two milling tools cutting a common workpiece is presented. The definitions and formulations for parallel milling process dynamics are given in the next section. Time-domain model and overview of the method used to predict stability diagrams are presented in Section 7.2. Finally, the results of the model are demonstrated on example cases in the last section.

7.1. Dynamics of parallel milling

Definitions of the coordinate systems and process parameters used in the time-domain model are presented in this section. Chip thickness and cutting force formulation are given next. Then, calculation of dynamical response of tools and workpiece to cutting forces is presented.

7.1.1. Coordinate systems and Process Parameters

An example parallel milling process is illustrated in Figure 7.1. In this process, it is seen that two flexible milling tools are cutting a flexible workpiece simultaneously. The cutting tool on the upper side is numbered as the first tool and the below tool is named as the second tool. Three coordinate systems are used to represent the parallel milling process. The first coordinate system is the XYZ coordinate system on the workpiece. X, Y and Z axes are aligned with the machine tool axes. The other coordinate systems are tool coordinate systems. $x_1y_1z_1$ is the coordinate system on the first cutting tool where x_1 represents the feed direction, z_1 is the tool axis direction and y_1, which is the cross-feed direction, is determined according to the right handed coordinate system notation. Similarly, $x_2y_2z_2$ is the coordinate system on the second milling tool.

The transformations of displacements or forces between these three coordinate systems are necessary in the model. The transformation of entities from $x_1y_1z_1$ and $x_2y_2z_2$ to XYZ coordinates can be performed by the two transformation matrices. T_1 and T_2 transformation matrices which perform transformation from $x_1y_1z_1$ to XYZ and from $x_2y_2z_2$ to XYZ, respectively, are presented in the below equation:

$$T_1 = \begin{bmatrix} 0 & 0 & 1 \\ 0 & 1 & 0 \\ -1 & 0 & 0 \end{bmatrix}, \ T_2 = \begin{bmatrix} 0 & 0 & -1 \\ 0 & -1 & 0 \\ -1 & 0 & 0 \end{bmatrix} \tag{7.1}$$

In the example process shown in Figure 7.1, the milling tools are parallel to each other, i.e. z_1 and z_2 are parallel. This is a common configuration seen on parallel machine tools. In this paper, the model is developed for the cases where z_1 and z_2 are parallel but the formulation can also be applied on other cases with slight modifications.

(a)   (b)   (c)
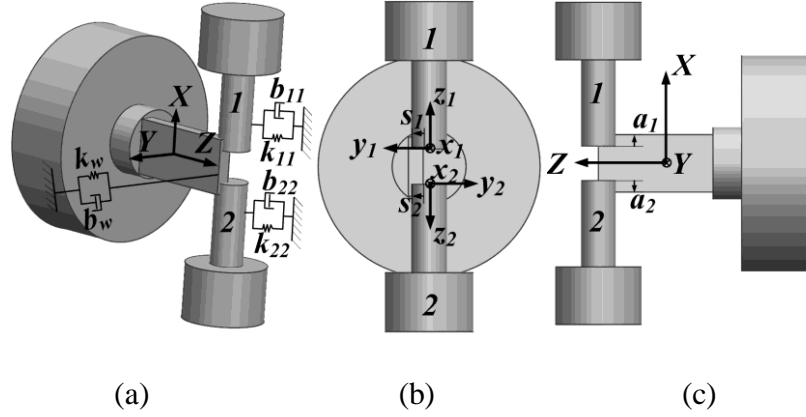
Figure 7.1: An example parallel milling process (a) 3D view (b) XY view (c) XZ view

Since there are two cutting tools in the parallel milling processes, the number of cutting parameters doubles. The process parameters for the ith milling tool are defined here. Axial and radial depths are represented by a_i and s_i as shown in Figure 7.1. The spindle speed and feed per tooth are symbolized by rpm_i and f_i, respectively. The clockwise or counter-clockwise rotating tools can be used at the same time. Depending on the type of the cutting tool, and workpiece orientation with respect to the cutting tools, the cutting types can be up-milling or down-milling. For example, if both of the milling tools are rotating in clockwise direction in the example process (Figure 7.1), the first tool is cutting in up-milling mode while the second tool is cutting in down-milling mode. The immersion angle of the jth cutting flute at the tool tip which is measured from positive y_i direction is represented by φ_{ij}. In general, the cutting tools may not contact the workpiece at the same angular position; hence there can be a lag angle, ψ, between the flutes of milling tools. The lag angle can be controlled if the spindles are vector controlled spindles, otherwise lag angle is not under operator's control.

7.1.2. Chip Thickness

The chip thickness on the ith cutting tool depends on the dynamic displacement vector d_i, the local immersion angle $\varphi_{ij}(z)$ and feed per tooth f_i. The dynamic displacement vector d_i represents the relative displacements of the ith milling tool with respect to the workpiece.

$$d_i = \begin{bmatrix} \Delta x_i \\ \Delta y_i \\ \Delta z_i \end{bmatrix} = \begin{bmatrix} x_{ti}(t) - x_{ti}(t - \tau_i) \\ y_{ti}(t) - y_{ti}(t - \tau_i) \\ z_{ti}(t) - z_{ti}(t - \tau_i) \end{bmatrix} - \begin{bmatrix} x_{wi}(t) - x_{wi}(t - \tau_i) \\ y_{wi}(t) - y_{wi}(t - \tau_i) \\ z_{wi}(t) - z_{wi}(t - \tau_i) \end{bmatrix} \qquad (7.2)$$

where x_{ti}, y_{ti} and z_{ti} represent the present displacements of the ith cutting tool in x_i, y_i and z_i directions. Similarly, x_{wi}, y_{wi} and z_{wi} are the displacements of the workpiece on the region that is in contact with the ith cutting tool. The delayed terms are the corresponding displacements one tooth period τ_i before. τ_i depends on the spindle speed rpm_i and number of flutes n_i on the ith cutting tool.

$$\tau_i = \frac{rpm_i}{60 n_i} \qquad (7.3)$$

The displacements of the tools in the axial direction do not result in regenerative effect. Thus, the dynamic chip thickness is calculated using the following formula:

$$h_i = (f_i + \Delta x_i)\sin \varphi_{ij}(z_i) + \Delta y_i \cos \varphi_{ij}(z_i) \qquad (7.4)$$

The local immersion angle $\varphi_{ij}(z)$ varies along the tool axis depending on the following equation:

$$\varphi_{ij}(z_i) = \varphi_{ij} - \frac{\tan(\beta_i)}{R_i} z_i \qquad (7.5)$$

where β_i and R_i are the helix angle and the radius of the ith milling tool, respectively; z_i represents the axial position on the milling tool.

7.1.3. Dynamic Cutting Forces

Using the linear-edge force model [36], differential cutting forces in radial, tangential and axial directions on the ith cutting tool's j^{th} flute can be written as follows:

$$\begin{aligned}
dFr_{ij}(\varphi_{ij}) &= (K_{re} + K_{rc}h_i)dz_i \\
dFt_{ij}(\varphi_{ij}) &= (K_{te} + K_{tc}h_i)dz_i \\
dFa_{ij}(\varphi_{ij}) &= (K_{ae} + K_{ac}h_i)dz_i
\end{aligned} \qquad (7.6)$$

where K_{rei}, K_{tei}, K_{aei} and K_{rci}, K_{tci}, K_{aci} are radial, tangential, axial edge and cutting force coefficients on the ith tool, respectively. dz_i is the height of the axial differential element. In previous works by Altintas [1] and Budak [97], the calculation of static cutting forces was presented. In this thesis, in order to calculate dynamic cutting forces, the static force formulation in [97] is modified by using the dynamic chip thickness formulation presented in Equation (7.4). Finally, dynamic cutting forces in x_i, y_i and z_i directions are determined for given immersion angle of φ_i as follows:

$$Fx_i(\varphi_i) = \sum_{j=1}^{n_i} \int_{z_{\lim 1}}^{z_{\lim 2}} dFx_{ij}(\varphi_{ij})$$

$$Fy_i(\varphi_i) = \sum_{j=1}^{n_i} \int_{z_{\lim 1}}^{z_{\lim 2}} dFy_{ij}(\varphi_{ij}) \qquad (7.7)$$

$$Fz_i(\varphi_i) = \sum_{j=1}^{n_i} \int_{z_{\lim 1}}^{z_{\lim 2}} dFz_{ij}(\varphi_{ij})$$

$z_{\lim 1}$ and $z_{\lim 2}$, are the integration limits that are also used for modeling of standard 3-axis milling processes (Altintas [1], Budak [97]) .

7.1.4. Tool and Workpiece Dynamics

Tool and workpiece dynamics can be represented by transfer functions, or frequency response function, which are measured by impact hammer tests. The response of the ith tool at the tool tip to the dynamical cutting forces can be obtained using the following relation:

$$\begin{bmatrix} x_i \\ y_i \\ z_i \end{bmatrix} = \begin{bmatrix} G_{x_i x_i} & G_{x_i y_i} & G_{x_i z_i} \\ G_{y_i x_i} & G_{y_i y_i} & G_{y_i z_i} \\ G_{z_i x_i} & G_{z_i y_i} & G_{z_i z_i} \end{bmatrix} \begin{bmatrix} Fx_i \\ Fy_i \\ Fz_i \end{bmatrix} \qquad (7.8)$$

The cross-transfer functions, e.g. G_{xizi}, G_{yizi} etc., are neglected since their magnitudes with respect to the direct ones are considerably low. Moreover, the direct transfer functions in tool axis direction, i.e. G_{zizi}, are also neglected since milling tools are relatively rigid in this direction. So, G_{xixi} and G_{yiyi} are the only transfer functions required in the formulation. In the hammer tests, excitation is given from the tool tip with a hammer and response of the tool is measured by an accelerometer at the tool tip. Since the response at the tool tip is of interest only, only one transfer function measurement is adequate although the tool tip response can include multi-dof behavior.

The modal data is fit to measured transfer functions using Cutpro software [93]. G_{xixi} and G_{yiyi} can be calculated using the following relation:

$$G_{p_i p_i}(j\omega) = \sum_{r=1}^{q} \frac{\frac{1}{m_r}}{(j\omega)^2 + 2\xi_r \omega_{n,r}(j\omega) + \omega_{n,r}^2} \quad , p = x, y \qquad (7.9)$$

where q represents number of modes determined from the transfer function measurement at the tool tip and ω is the frequency variable. m_r, ζ_r and $\omega_{n,r}$ are modal mass, modal damping ratio and modal natural frequency corresponding to the rth mode.

Unless the workpiece is flexible in Y and/or Z directions, the dynamics of the two tools in the considered case are independent of each other. So, in such a case the dynamics and stability of the tools can be analyzed separately. However, the workpiece in the example case considered is flexible; hence, it is a dynamically parallel process. The flexibility of the workpiece in X and Z directions can be neglected since the workpiece is noticeably rigid in these directions with respect to Y direction. The frequency response functions at two different points -one on the upper side and one on the lower side of the workpiece- where the first and second tool is in contact with the workpiece are measured (Figure 7.2). Since the feed in both of the cutting tools is in –Z direction, the workpiece dynamics is variable during the process. The stability analysis is performed for the beginning of the process; hence measurement points are selected close to the beginning of the process as shown in Figure 7.2. The response of the workpiece at two points to the cutting forces on the workpiece can be determined using the following equation.

$$\begin{bmatrix} Y_1 \\ Y_2 \end{bmatrix} = \begin{bmatrix} G_{11} & G_{12} \\ G_{21} & G_{22} \end{bmatrix} \begin{bmatrix} F_1 \\ F_2 \end{bmatrix} \qquad (7.10)$$

where Y_i is the displacement of the workpiece and F_i is the cutting force at the ith point. The transfer functions, G_{ik} can be defined using the following equation [99]:

$$G_{ik}(j\omega) = \sum_{r=1}^{q_w} \frac{\frac{U_{ir}U_{kr}}{m_r}}{(j\omega)^2 + 2\xi_r \omega_{n,r}(j\omega) + \omega_{n,r}^2} \quad , i, k = 1, 2 \qquad (7.11)$$

U_{ir} and U_{kr} are the elements of the modal shape matrix which are obtained by Cutpro modal analysis module [93] and q_w is the number of modes of workpiece in the analysis. The size of the mode shape matrix is 2 by q_w. Modal data and mode shape

matrix are obtained by modal analysis of two measured transfer functions which are G_{11} and G_{12}. The displacements of the workpiece in Equation (7.10) can be transformed to tool coordinate systems using the inverse of transformations presented in Equation (7.1).
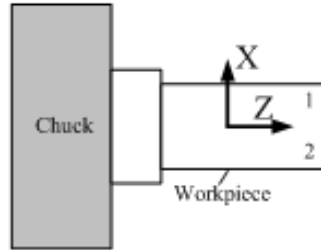
Figure 7.2: Measurement points on the workpiece

7.2. Time-Domain Model

The time-domain model that simulates the dynamical behavior of parallel milling operations needs all the process parameters which are stated in the previous sections. Moreover, dynamic chip thickness, dynamic cutting forces, tool and workpiece dynamics should be written in terms of process parameters. In the model, the parallel milling process is simulated at discrete time intervals in Simulink [98] environment. Each discrete time corresponds to an immersion angle on each tool; at each instant, dynamic displacements of the cutting tools and workpiece are calculated using the measured transfer functions and modal shape matrices by Equation (7.8) and Equation (7.10), respectively. The relative displacements of the tools with respect to the workpiece at the present time and at the time one tooth period before are used to form the dynamic displacement vector d_i by Equation (7.2) that is responsible for the regeneration effect. Since the displacements in the z_i directions do not affect the regeneration mechanism for the presented parallel milling process, the first two terms which include displacements in x_i and y_i directions are used to calculate the dynamic chip thickness using Equation (7.4). Finally, cutting forces corresponding to the calculated chip thickness values and given process parameters are calculated for the present immersion angle. This calculation steps are continued with the next discrete simulation time. The block diagram notation of the presented time domain model is given in Figure 7.3. Depending on the variation of dynamic cutting forces, displacements and/or frequency spectrum of these variations, processes can be classified as stable, marginal or unstable.
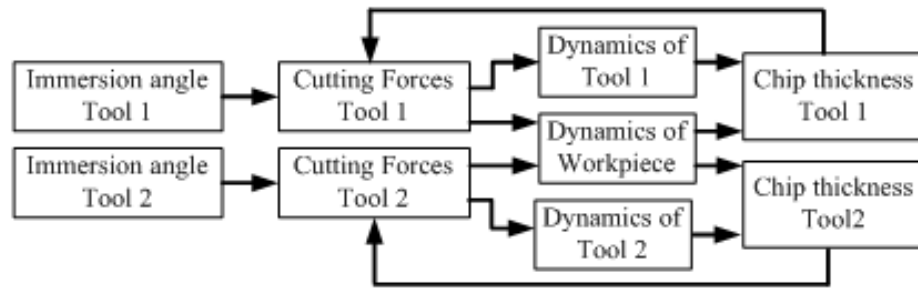
Figure 7.3: Block diagram notation of the time domain model

The stability diagrams are used to determine stable process parameters to avoid chatter vibrations and the presented time-domain model can be used to predict stability diagrams for a parallel milling process. There are two cutting tools in the presented parallel milling process but the stability diagram for each tool cannot be obtained independently since there is dynamic coupling between two tools which is the flexible workpiece. Stability diagram for only one of the tools can be predicted after the process parameters of the other cutting tool are all set. For example assume that the parameters of the first tool are fixed. In this case, stability diagram for the second tool can be predicted using the time domain model after the process parameters except the spindle speed and axial depth of the second tool are set. With that purpose, a spindle speed range of interest for the second tool is selected. For each spindle speed, the time domain model is simulated starting from for low axial depth of cut to higher axial depth of cut. The axial depth of cut is incremented by certain cutting depths, Δa_2, and for each axial depth the presented time-domain model is run until the process becomes unstable. The average of the axial depths at the last stable point and first unstable point is selected as the stability limit for the corresponding spindle speed.

The spindle speeds and number of flutes of the cutting tools can be different in parallel milling which results in different tooth periods, i.e. different delay terms in Equation (7.2). But if the feed velocities in mm/min are different, relative translational motion between the two tools is observed. This makes determination of the interaction between the cutting tools difficult; hence feed per tooth value of the second tool is selected in according to the following equation in order to keep feed velocity in mm/min on the first tool and on the second tool the same.

$$f_2 = f_1 \frac{rpm_1 * n_1}{rpm_2 * n_2} \tag{7.12}$$

7.3. SIMULATION RESULTS

The presented time-domain model is simulated on several example cases. Although the experimental verification has not been presented yet, the measurements for the example cases are performed on an Index ABC parallel machining centre (Figure 7.4). The workpiece and two milling tools are also shown in (Figure 1.5). The workpiece material is 1050 steel. The cutting tools are clock-wise rotating, 12 mm diameter and 2 flute flat-end mills that have 30° helix angle. The overhang lengths of the upper tool and the lower tool are 40.5 mm and 47.8 mm, respectively.

The measured modal data of the first tool and second tool, which include natural frequencies (f_n) damping ratios (ζ) and stiffness values (k), is presented in Table 7.1. The modal data of the workpiece is tabulated in Table 7.2 and the corresponding modal shape matrix U is given in Equation (7.13). It's seen that the first mode is a bending mode while the second mode is a torsional one.

$$U = \begin{bmatrix} U_{11} & U_{21} \\ U_{21} & U_{22} \end{bmatrix} = \begin{bmatrix} 1 & 1 \\ 0.930 & -0.844 \end{bmatrix} \tag{7.13}$$

Figure 7.4: Parallel machining centre

Using the stability model presented in [54], the stability diagram of each tool working in single mode can be determined. The flexibility of the workpiece is also included in the calculations. The first tool's absolute stability limit is determined as 0.5 mm with chatter frequency of 1550 Hz when it's working in up milling (Figure 7.5(a)). The absolute stability of the second tool in down milling is calculated as 0.3mm at chatter frequency of 760 Hz (Figure 7.5 (b)). When the second tool's cutting type is changed to up milling, the absolute stability increases to 0.9 mm at 734 Hz chatter frequency. Comparing the calculated chatter frequencies with the natural frequencies of

the system, it can be concluded that the workpiece flexibilities are dominant in determining the absolute stability limit of the given cases.

Table 7.1: Modal data for the milling tools

Tool 1	x_1 direction			y_1 direction		
Mode#	f_n (Hz)	ζ	k(N/m)	f_n(Hz)	ζ	k(N/m)
1	2127.2	$5.279*10^{-2}$	$9.107*10^6$	2275.2	$6.234*10^{-2}$	$9.459*10^6$
Tool 2	x_2 direction			y_2 direction		
Mode#	f_n (Hz)	ζ	k(N/m)	f_n(Hz)	ζ	k(N/m)
1	1788	$1.048*10^{-1}$	$2.403*10^7$	1731.12	$1.379*10^{-2}$	$1.777*10^8$
2	2036.2	$8.883*10^{-2}$	$4.276*10^7$	1909.9	$3.288*10^{-2}$	$1.400*10^7$
3	-	-	-	2101.6	$2.977*10^{-2}$	$4.910*10^7$

Table 7.2: Modal data for the workpiece

	Y direction		
Mode#	f_n (Hz)	ζ	k(N/m)
1	746.5	$1.691*10^{-2}$	$4.997*10^6$
2	1550.1	$2.165*10^{-3}$	$1.160*10^7$

The effect of parallel milling on stability limits is analyzed on an example case. The cutting parameters for the first cutting tool are fixed as tabulated in Table 7.3. The second tool is also performing a half immersion operation. The specific cutting force coefficients for the second tool are taken as equal to the cutting coefficients of the first tool. Since the edge forces do not affect the regeneration mechanism, edge force coefficients are taken as zero. The stability limits for the second tool are predicted for both up milling and down milling cutting types on several spindle speeds in the spindle speed range of 2950-3200 rpm by the presented time domain model. These limits are presented in Figure 7.6 for up milling and down milling operations, separately. In both of the cases the absolute stability is predicted to be 0.35mm. However, the maximum stability limits at the presented lobes are considerably different. The maximum stability limit of the second tool is 1.5 mm when it is in up milling cutting type whereas it's 3mm when the cutting type is changed to down milling.

(a)   (b)

(c)
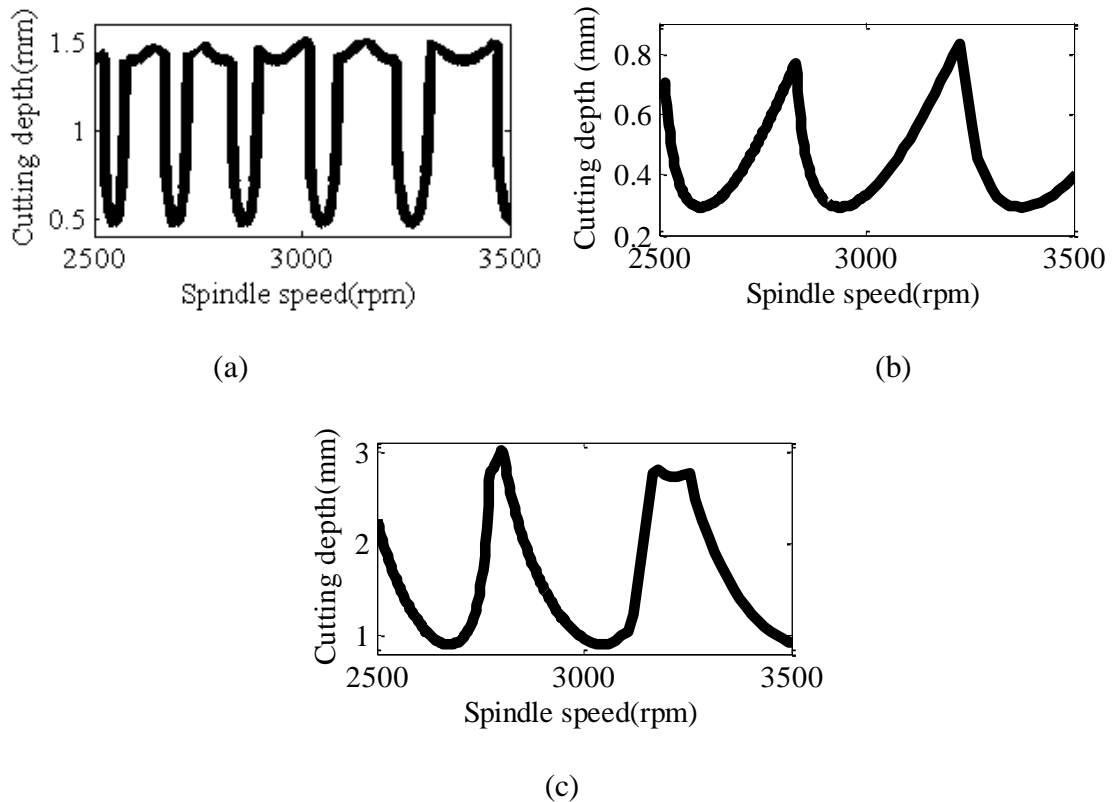
Figure 7.5:Stability limit diagrams of the tools working in single mode (a) Tool 1(up-milling) (b) Tool 2(down milling) (c) Tool 2(up milling)

It is of interest to compare the stability diagrams for single mode operations in Figure 7.5(a) and Figure 7.5(b) with the stability diagrams of the parallel milling process in Figure 7.6. When the second tool is in down milling mode, absolute stability very slightly increased to 0.35 mm from 0.3 mm due to the effect of the first tool. Moreover, the maximum stability at the presented lobes increased to 1.5 mm from 0.8 mm. However, absolute stability limit decreased to 0.35 mm from 0.9 mm under the effect of the first tool when the cutting type of the second tool is up milling. But the maximum stability at the presented lobes left unchanged around 3 mm. As a result, depending on cutting types and on whether the process planner is interested in absolute stability or the maximum stability limits for specific lobes, the parallel milling has certain advantages and disadvantages. However, the additional material removed by the other tool should also be taken into account in such comparisons.

Table 7.3: Cutting parameters of the first tool in the example

a_1	0.5 mm
$nrpm_1$	3000 rpm
f_1	0.05mm
s_1	Half immersion up milling
$K_{rc1},\ K_{tc1}\ K_{ac1}$	484, 1597,517 MPa
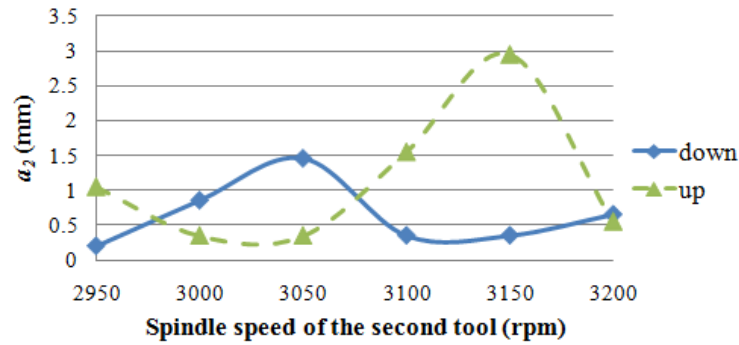
Figure 7.6: Stability limit diagrams of the second tool for half immersion up and down milling cases (The parameters of the first tool are tabulated in Table 7.3)

In order to represent how the presented time domain model is used to determine the stability limits given in Figure 7.6 and show the response of the system at a stable and at an unstable point, the variation of displacements of the workpiece in Y direction at node 1 (Figure 7.2) is presented for two different cases to be representative in Figure 7.7 . The spindle speed of the second tool is 3000 rpm, cutting type is down milling and cutting depth of the second tool is 0.8mm and 1mm in these cases. Since the stability limit at 3000 rpm for down milling case is determined as 0.85 mm as shown in Figure 7.6, cutting depth of 0.8 mm results in a stable process while cutting depth of 1mm results in a stable operation which can be seen in Figure 7.7.

(a)   (b)
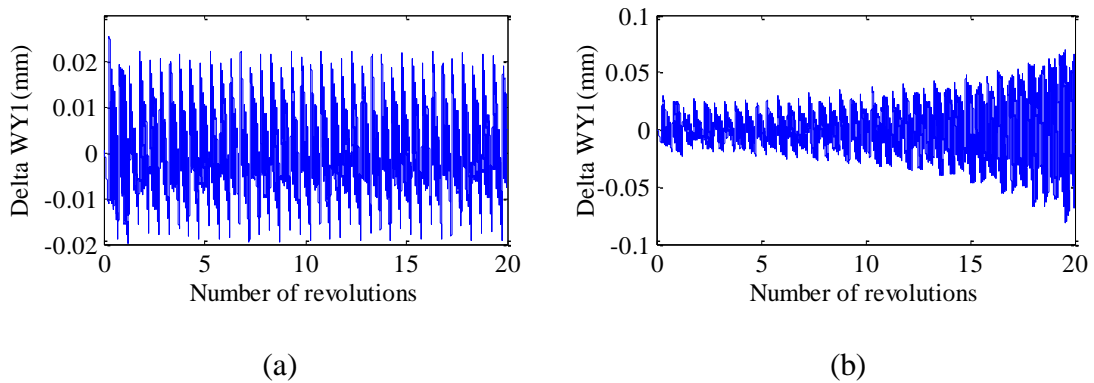
Figure 7.7; Variation of displacements of the workpiece in Y direction at node 1
(a)a_2=0.8mm (b) a_2=1mm
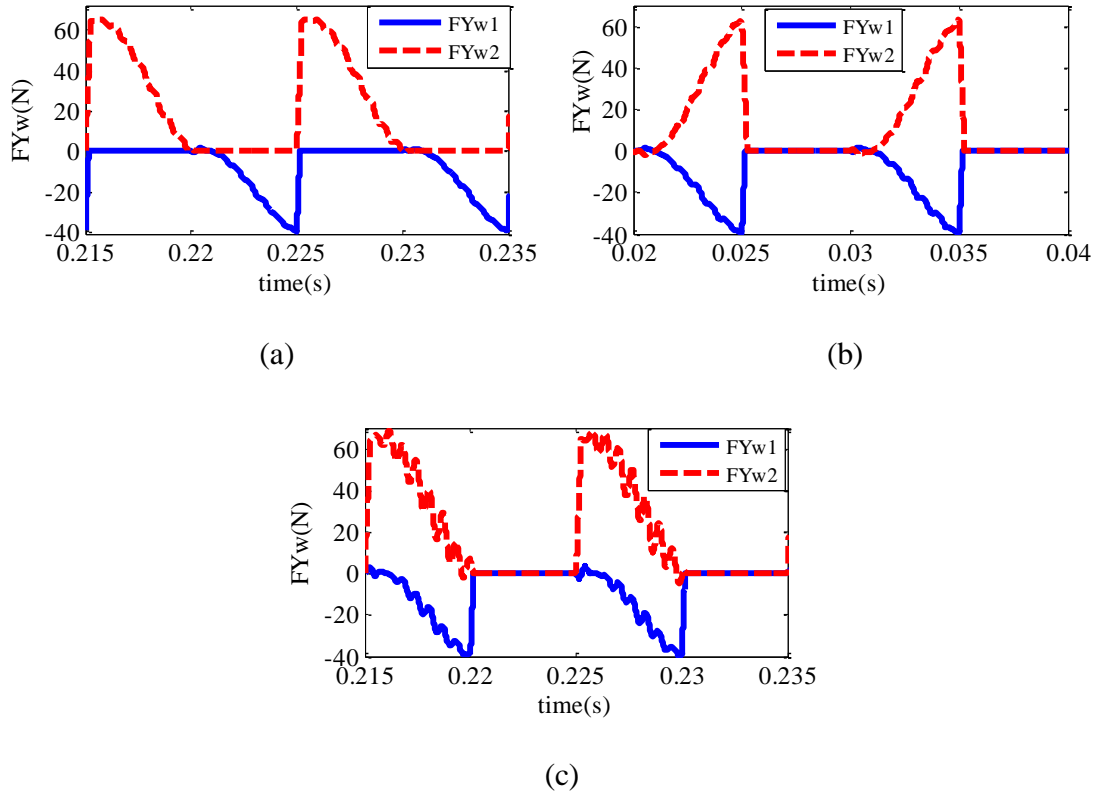
Figure 7.8; Variations of cutting forces, FY_{w1} and FY_{w2} (a_2=0.8mm) (a) down milling (b) up milling (c) down milling, lag angle=90°

It should be noted that selection of up milling and down milling changes the form of variation of cutting forces. Hence interaction of the two cutting tools is affected by selection of cutting types. This effect is shown for a point on Figure 7.6 where a_1 is 0.5mm, a_2 is 0.8mm, rpm_1 and rpm_2 are both 3000 rpm. To be representative, during the parallel milling process, the variations of cutting forces, FY_{w1} and FY_{w2}, are presented for one tool rotation in Figure 7.8(a) and (b). Full lines and dotted lines represent FY_{w1} and FY_{w2}, respectively. FY_{w1} is the cutting force on the workpiece in Y direction due to the first cutting tool whereas FY_{w2} is the cutting force on the workpiece in the same direction due to the second tool. The first tool is in up milling mode while the second tool is in down milling mode in Figure 7.8(a). In this case, there is a phase difference between force values and there is no interaction between them. On the other hand, in Figure 7.8 (b), both of the cutting tools are in up milling mode and it's seen that they are in phase with each other. For that reason, there is more interaction between force values in this case. This behavior also affects the stability of the system, i.e., the first case is stable while the second case is unstable as presented in Figure 7.6.

As presented in the Section 7.1.1, there can be a lag angle, ψ, between the first tool and second tool. Its effect on the variation of forces is presented on Figure 7.8(c). In this case, the lag angle of 90° is applied on the case presented in Figure 7.8(a). It's seen that there is a time shift between the forces FY_{w1} and FY_{w2} when there is lag angle. Due to its effect on the form of variation of cutting forces, lag angle may affect the stability limits. This effect was only seen in the regions close to the stability limits. For example, when lag angle of 90° is applied on the case presented in Figure 7.8(a) where a_2 is 0.8 mm while stability limit is 0.85 mm, originally stable process becomes unstable as shown in Figure 7.9. On the other hand, it was seen that the stability limits are not influenced by the lag angle in the regions away from the stability limits.
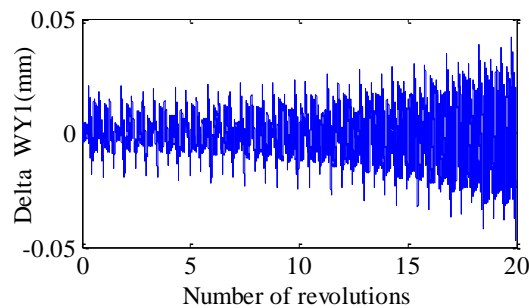
Figure 7.9; Effect of lag angle of 90° on stability (a_2=0.8mm)

8. MECHANICS AND DYNAMICS OF INSERTED FACE-MILLING OPERATIONS

Mathematical models of cutting tools are needed before force and stability models can be developed. Hence, in the next section, geometries of the cutting tools are modeled. Then, cutting force and stability models are presented in Sections 8.1 and 8.2, respectively. Finally, application of the models to the machining of an example die is presented.

8.1. Geometric Model of Inserted Face-Mills

A general mathematical model for inserted cutters is explained in this section as it is required in both force and stability models. The cutting tool geometries commonly used in die machining and modeled in this work are presented in Figure 8.1. In the modeling, positions of points on the cutting edge have to be formulated for which two coordinate systems are used, namely tool and insert coordinate systems. The tool coordinate system consists of X_t, Y_t and Z_t directions. X_t axis represents the feed direction of the cutting tool whereas Y_t and Z_t axes are in the cross-feed and the tool axis directions, respectively. The insert coordinate system consists of u_i, v_i and w_i directions with its origin at the center of the insert face containing the cutting edge. The tool and the insert coordinate systems are aligned with each another when immersion angle of the insert, φ_j, is 90° before orientations on the insert are applied (Figure 8.2, Figure 8.3(a)). φ_j represents the immersion angle of the jth insert center measured from the Y_t axis in the clockwise direction. Position of the jth insert center with respect to the tool coordinate system ($X_t Y_t Z_t$ coordinate system) is defined by V_{IC} vector [87]:

$$V_{IC} = \begin{bmatrix} \sin(\varphi_j)I_R & \cos(\varphi_j)I_R & I_Z \end{bmatrix}^T \tag{8.1}$$

where I_R is the radial offset in the $X_t Y_t$ plane and I_Z is the axial offset in Z_t direction.

Inserts are designed with different orientations on cutting flutes depending on the application. Their orientation on cutting flutes can be defined by three rotation angles, namely, axial rake angle (β_a), lead angle (δ) and index angle (α), respectively (Figure 8.3). β_a is defined as the rotation around X_t-axis, δ is the rotation around Y_t axis and α is the rotation around Z_t-axis when the immersion angle of the corresponding insert is 90°.

Inserts in this work have round shapes with or without a center offset with respect to the insert center. Center offset (O_f) defines the distance between the insert center (O') and center of the curvature of the cutting edge (O_c) as shown in Figure 8.4. An insert with a center offset is presented in Figure 8.2-Figure 8.4; however, the model is general for inserts with round shapes. For example, O_c and O' coincides in the cutting tool presented in Figure 8.1(b), hence center offset is zero in this case. The position of a point on the cutting edge with respect to the insert center is shown with the $\textbf{\textit{V}}_{CE}$ vector in insert coordinate system:

$$\textbf{\textit{V}}_{CE} = \begin{bmatrix} x_m & y_m & z_m \end{bmatrix}^T \tag{8.2}$$

where x_m, y_m and z_m are measure numbers of $\textbf{\textit{V}}_{CE}$ vector in $\textbf{\textit{u}}_i$, $\textbf{\textit{v}}_i$ and $\textbf{\textit{w}}_i$ directions, respectively. These are calculated using the equations below (Figure 8.4):

$$x_m = R\cos\gamma,\ y_m = 0,\ z_m = -R\sin\gamma$$

$$\gamma = \theta + \sin^{-1}(\frac{O_f}{R}\cos\theta)\ \text{for}\ \theta_a \le \theta \le \theta_b \tag{8.3}$$

R is defined as the radius of curvature of the cutting edge and γ is the angle between the $\textbf{\textit{u}}_i$ direction and the line that connects center of the curvature of the cutting edge (O_c) to a point on the cutting edge as shown in Figure 8.4. θ represents the angle between the $\textbf{\textit{V}}_{CE}$ vector and $\textbf{\textit{u}}_i$ direction. θ_a and θ_b represent the limits of cutting edge.

After including the effects of the orientations and rotation effect of the immersion angle φ_j on the inserts, $\textbf{\textit{V}}_{CE}$ vector can be transformed to the tool coordinate system as follows:

$$\textbf{\textit{V}}_{CET} = \textbf{\textit{T}}_M \textbf{\textit{V}}_{CE} \tag{8.4}$$

where $\textbf{\textit{T}}_M$ is a transformation matrix consisting of four rotations $R_X(\beta_a)$, $R_Y(\delta)$, $R_Z(\alpha)$ and $R_Z(\varphi'_j)$ and they are defined in the following equations:

$$\textbf{\textit{T}}_M = R_Z(\varphi_j')R_Z(\alpha)R_Y(\delta)R_X(\beta_a) \tag{8.5}$$

$$R_X(\beta) = \begin{bmatrix} 1 & 0 & 0 \\ 0 & \cos\beta_a & -\sin\beta_a \\ 0 & \sin\beta_a & \cos\beta_a \end{bmatrix}, R_Y(\delta) = \begin{bmatrix} \cos\delta & 0 & \sin\delta \\ 0 & 1 & 0 \\ -\sin\delta & 0 & \cos\delta \end{bmatrix}$$

$$R_Z(\alpha) = \begin{bmatrix} \cos\alpha & -\sin\alpha & 0 \\ \sin\alpha & \cos\alpha & 0 \\ 0 & 0 & 1 \end{bmatrix}, R_Z(\varphi_j') = \begin{bmatrix} \cos\varphi_j' & -\sin\varphi_j' & 0 \\ \sin\varphi_j' & \cos\varphi_j' & 0 \\ 0 & 0 & 1 \end{bmatrix} \tag{8.6}$$

where φ_j' depends on the immersion angle φ_j:

$$\varphi_j{}'=90-\varphi_j \tag{8.7}$$

(a)   (b)
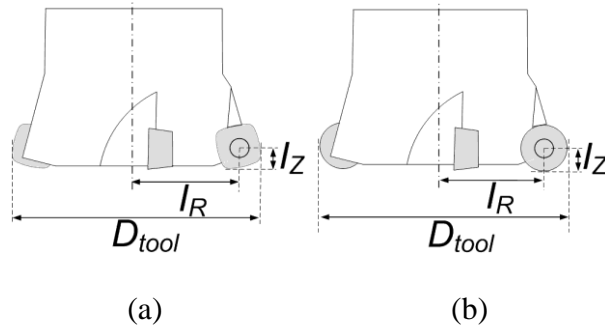
Figure 8.1 : Schematic representation of cutting tools
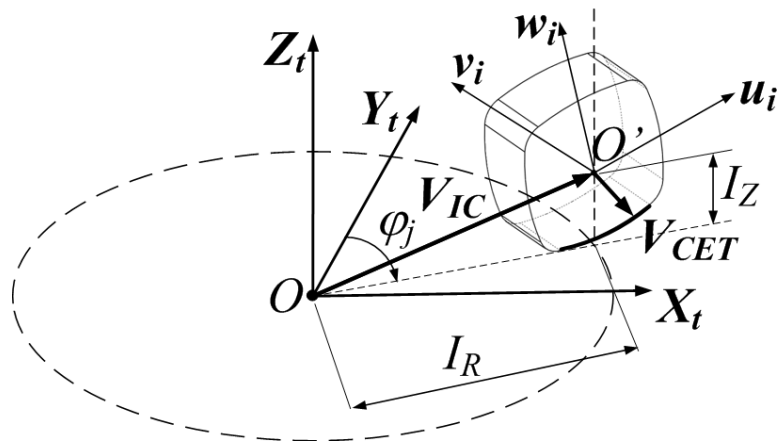
Figure 8.2 : Coordinate systems

The final position vector of the points on the cutting edge (V_P) with respect to the tool coordinate system can be written as (Figure 8.2):

$$V_P = V_{IC} + V_{CET} \tag{8.8}$$

As a result, using the presented procedure, X_t, Y_t and Z_t coordinates of points on cutting edges can be calculated in tool coordinate system. Moreover, local immersion angle, $\varphi_j(Z_t)$, of points on the jth insert's cutting edge can be determined using X_t and Y_t coordinates of the corresponding point on the cutting edge:

$$\varphi_j(Z_t) = a\tan 2(X_t, Y_t) \tag{8.9}$$
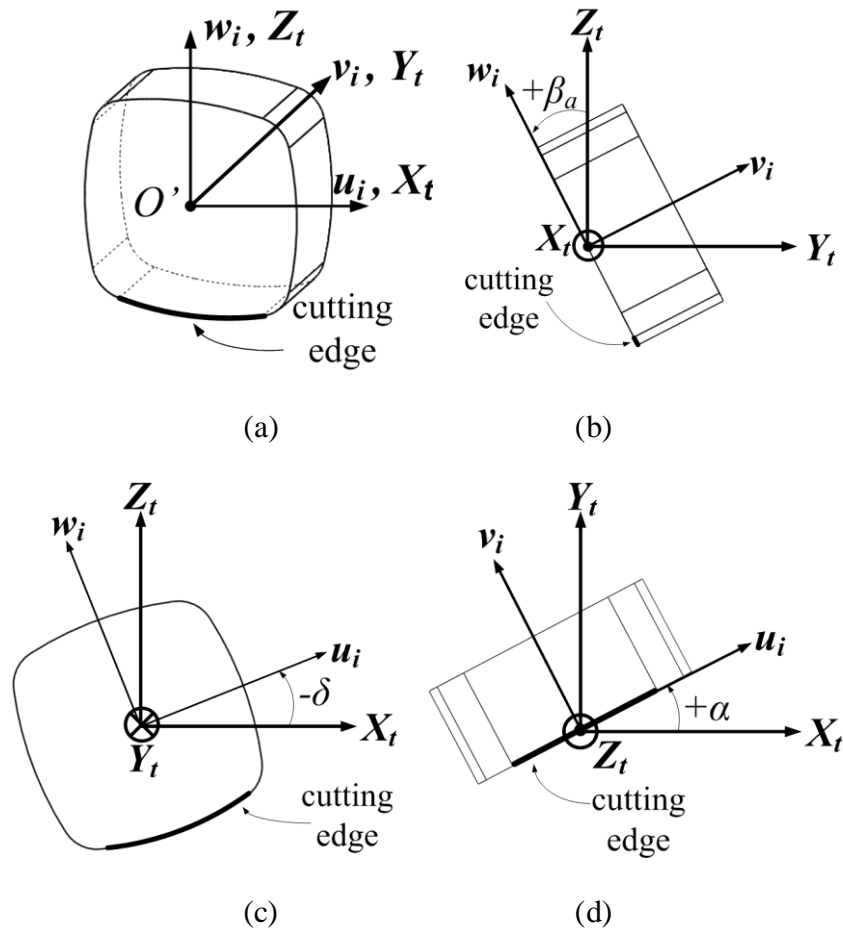
Figure 8.3 (a) Before orientations (b) Axial rake angle, β_a (c) lead angle, δ (d) index angle, α
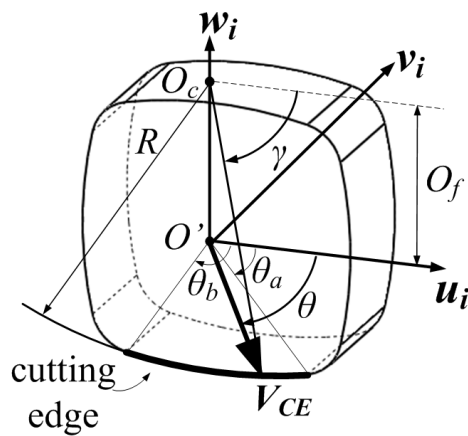
Figure 8.4 : Insert coordinate system

8.2. Cutting force model

In this section, force model is described firstly. In order to verify the force predictions, the predicted cutting forces are compared with measured forces for an example case.

Geometry of inserts and cutting tools are variable along the tool axis direction, Z_t. Thus, the mechanics of the milling process varies along the cutting edge. In order to take these variations into account, the cutting edge is divided into differential elements that have heights of dZ (Figure 8.5). Differential cutting forces in radial, tangential and axial directions on a differential element (Figure 8.5) can be calculated as presented in (3.22)

Chip thickness (ct) is variable in both tangential and axial directions. The chip thickness at a point on the cutting edge is demonstrated in Figure 8.5 and can be calculated as follows:

$$ct = f_t \sin \varphi_j(Z_t) \sin K(Z_t) \tag{8.10}$$

where K is defined as axial immersion angle which is the angle between the unit outward normal vector $\boldsymbol{u}$ and negative Z_t direction (Figure 8.5). K can be calculated by the following equation:

$$K = \cos^{-1}(-u_{Zt}) \tag{8.11}$$

where u_{Zt} is the unit outward normal vector's ($\boldsymbol{u}$ in tool coordinate system) measure number in Z_t direction. In order to determine the unit outward normal vector $\boldsymbol{u}$ in tool coordinate system, firstly, unit outward normal vector in insert coordinate system ($\boldsymbol{u_{insert}}$) is defined as follows:

$$\boldsymbol{u_{insert}} = \begin{bmatrix} \cos \gamma & 0 & -\sin \gamma \end{bmatrix}^T \tag{8.12}$$

where superscript T represents transpose operation. Unit outward normal vector in tool coordinate system ($\boldsymbol{u}$) (Figure 8.5) can be calculated by transforming $\boldsymbol{u_{insert}}$ using transformation matrix $\boldsymbol{T_M}$ as follows:

$$\boldsymbol{u} = (T_M \boldsymbol{u_{insert}})^T \tag{8.13}$$

Chip width (db) on a differential element depends on dz and axial immersion angle K. It can be calculated by (8.11):
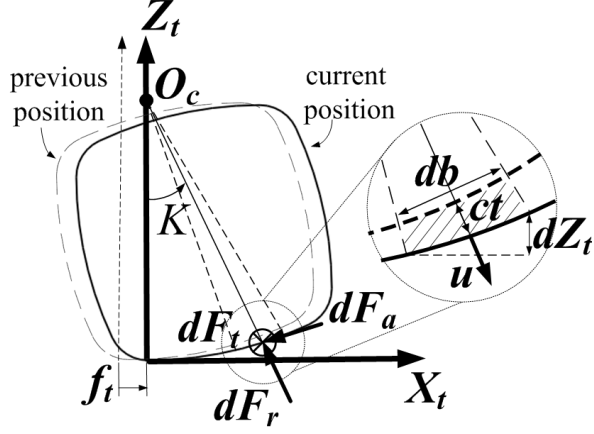
Figure 8.5 : Chip thickness, differential forces

The differential forces in radial, tangential and axial directions can be transformed to X_t, Y_t and Z_t directions using a transformation matrix, which depends on local immersion angle, $\varphi_j(Z_t)$ and axial immersion angle K and is analogous to T_{xyz} matrix in (3.24). The cutting forces on each flute are calculated by integrating the differential forces on the engagement region, and the total cutting forces are obtained by summing the contribution of each cutting insert as follows:

$$F_{X_t}(\varphi) = \sum_{j=1}^{n} \int_{Z_{t1}}^{Z_{t2}} dF_{X_{tj}}(\varphi_j(Z_t))$$

$$F_{Y_t}(\varphi) = \sum_{j=1}^{n} \int_{Z_{t1}}^{Z_{t2}} dF_{Y_{tj}}(\varphi_j(Z_t)) \tag{8.14}$$

$$F_{Z_t}(\varphi) = \sum_{j=1}^{n} \int_{Z_{t1}}^{Z_{t2}} dF_{Z_{tj}}(\varphi_j(Z_t))$$

where n represents the total number of cutting inserts on the tool. The integration limits for each immersion angle, Z_{t1} and Z_{t2}, are determined by a discrete engagement model. The cutting edges of inserts are discretized and the regions where the cutting insert is in contact with the workpiece are determined in this model. There are two engagement criteria for a point on cutting edge to be in cut. If a point is in cut with the workpiece, Z_t coordinate of the corresponding point should be equal or less than the axial depth of cut, and the immersion angle $\varphi_j(Z_t)$ of the corresponding point is between start (φ_{st}) and exit (φ_{ex}) angles [1].

132

8.2.1. Verification test for the force model

A verification test for the force model is presented here. In this case, GH210 steel is cut. The cutting force coefficients are calculated using the orthogonal database for the specified material which consists of empirical relations for shear angle ϕ, friction angle β, shear stress τ_{shear}, radial, tangential and axial edge force coefficients, K_{re}, K_{te} and K_{ae} [36]. For orthogonal database generation, calibration tests were performed in the range of 30-200 m/min for cutting speed and in the range of 0.1-0.3 mm/tooth for feed per tooth using the set-up presented in Figure 8.6. It was observed that effect of the feed per tooth on the orthogonal database is negligible. As a result, the empirical relations obtained for shear angle ϕ, friction angle β, shear stress τ_{shear}, radial, tangential and axial edge force coefficients, K_{re}, K_{te} and K_{ae}, respectively, are presented depending on the cutting speed V (m/min) only in Table 8.1.

The cutting tool is a 66mm diameter tool that has 5 circular, 16mm diameter inserts without center offset. On the inserts, axial rake angle (β) is 7° and the index angle (α) is 18°. Radial depth of cut, axial depth of cut, and spindle speed are 33mm, 0.5mm and 1200rpm, respectively. The process is a down milling operation. Feed per tooth is 0.66mm/tooth which is outside of the calibration range. However, the negligence of the feed per tooth effect on the orthogonal database in the calibrated range is assumed to be valid for the extended feed values including 0.66 mm/tooth.

(a)   (b)
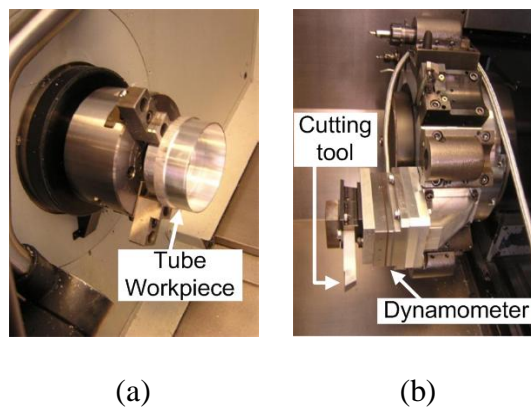
Figure 8.6 : Calibration tests (a) workpiece (b) Force measurement set-up

During the test, cutting forces are measured (Figure 8.7). Comparison of measured and simulated forces in one revolution for the representative case is presented in Figure 8.8 in order to verify the model's predictions for cutting forces in X_t, Y_t and Z_t directions. In the figure, full curves represent simulated forces while dashes curves are experimental forces. It is easily seen that run-out has an effect in this case since the

magnitudes of measured cutting forces are not equal among different inserts. In the simulation, run-out effect was not taken into account. Nevertheless, it can be said that the presented model predicts the cutting forces with a reasonable accuracy.

Table 8.1: Orthogonal database for GH210 material and carbide tools

$$\phi = 32.351 + 0.0403V \text{ (deg)}$$
$$\beta = 29.937 - 0.0805V \text{ (deg)}$$
$$\tau_{shear} = 348.78 - 0.0289V \text{ (MPa)}$$

$$K_{re} = 42.539 + 0.2465V \text{ (N/mm)}$$
$$K_{te} = 62.019 + 0.1349V \text{ (N/mm)}$$
$$K_{ae} = 0$$
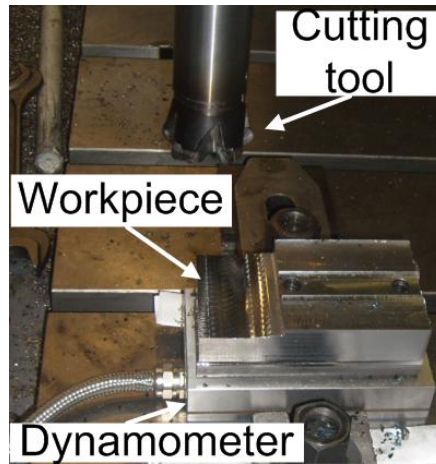
Figure 8.7 : Force measurement set-up

8.1. Stability model

Chatter is a type of self-excited vibration which results due to unstable interaction between dynamic cutting forces and chip thickness. Cutting forces result in displacements on the cutting tool which cause changes in dynamic chip thickness. Consecutively, dynamic chip thickness affects the dynamic cutting forces. This is a closed loop dynamic interaction, and stability of this interaction determines whether the process is stable or unstable.

In this section, firstly dynamic chip thickness is formulated, and then stability formulation is given. Finally, for an example case, the stability diagram predicted by the model is compared with experiments.
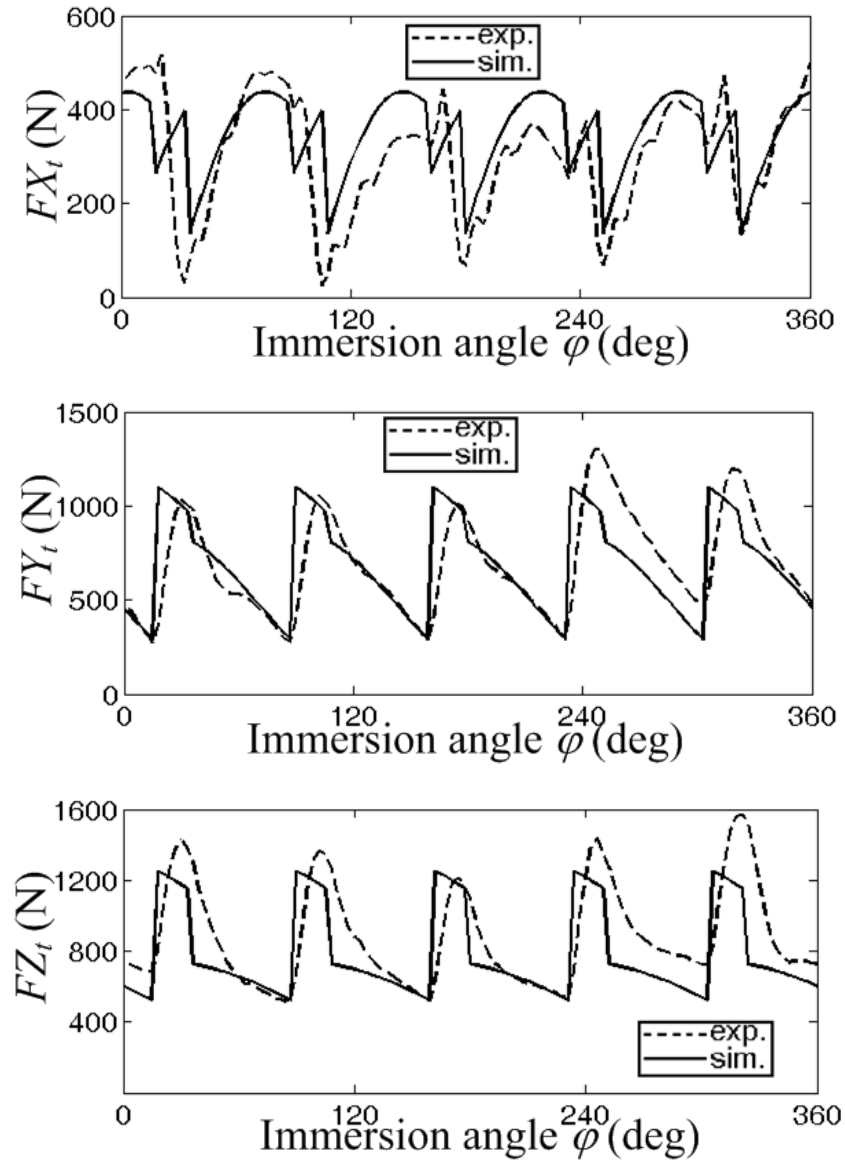
Figure 8.8 : Simulated (full curves) and measured (dashed curves) forces in X_t, Y_t and Z_t directions

8.1.1. The dynamic chip thickness

Chip thickness at a cutting point (h) consists of static and dynamic parts in the existence of vibrations. However, static part of the chip thickness does not contribute to the regeneration mechanism. Hence, only the dynamic part of the chip thickness h_d is considered, it is calculated by the scalar product of the unit outward normal vector $\boldsymbol{u}$ at the corresponding point and the dynamic displacement vector $\boldsymbol{d}$ in tool coordinate system as demonstrated in (4.1).

Unit outward normal vector $\boldsymbol{u}$ at any point on the cutting edge can be calculated using (8.13) Since the automotive dies are very big and stiff compared to the cutting

tools, the workpiece is assumed to be rigid in the stability analysis. Hence, the displacements are referred as the cutting tool displacements only. The dynamic displacement vector $\boldsymbol{d}$ is defined as the difference between the current displacements $([X_{td}(t), Y_{td}(t), Z_{td}(t)])$ and the displacements one tooth period (τ) before $[X_{td}(t-\tau), Y_{td}(t-\tau), Z_{td}(t-\tau)]$ in tool coordinate system (Figure 8.9).
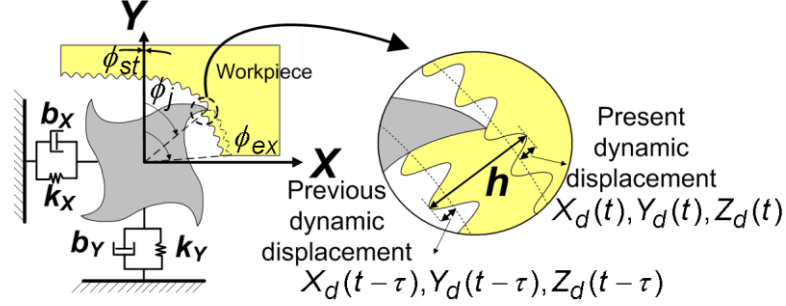
Figure 8.9 : Dynamic chip thickness

$$\boldsymbol{d} = \begin{bmatrix} \Delta X_{td} \\ \Delta Y_{td} \\ \Delta Z_{td} \end{bmatrix} = \begin{bmatrix} X_{td}(t) - X_{td}(t-\tau) \\ Y_{td}(t) - Y_{td}(t-\tau) \\ Z_{td}(t) - Z_{td}(t-\tau) \end{bmatrix} \qquad (8.15)$$

8.1.2. Formulation of the milling stability

The cutting tool geometry is divided into discrete elements along the tool axis direction in order to take the variation of cutting insert geometry into account in the stability formulations (Figure 8.10). An iterative method is applied for the solution of stability limits. In the iterations, axial depth of cut (a) is incremented by steps of ΔZ_t (Figure 8.10). At each iteration, the chatter frequency (ω_c) is swept around the natural frequencies of the system since chatter frequencies are close to natural frequencies. For each ω_c a limiting cutting depth a_{lim} is calculated. The iteration continues by incrementing axial depth of cut (a) until all the calculated limiting cutting depths (a_{lim}) are less than axial depth of cut (a) in the analysis.

Dynamic cutting forces at a cutting point on element l at immersion angle of φ_j can be written as follows:

$$\begin{bmatrix} F_{X_t}{}^l(\varphi_j) \\ F_{Y_t}{}^l(\varphi_j) \\ F_{Z_t}{}^l(\varphi_j) \end{bmatrix} = \boldsymbol{T}_{X_t Y_t Z_t} \begin{bmatrix} K_{rc} \\ K_{tc} \\ K_{ac} \end{bmatrix} h_d \Delta b \qquad (8.16)$$
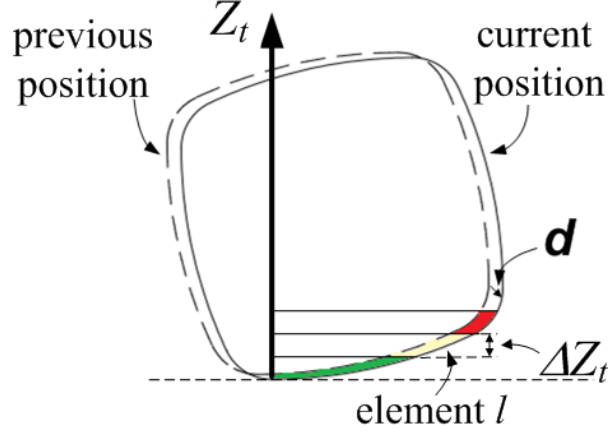
Figure 8.10 : Discrete elements in stability formulation

Discrete chip width Δb can be written in terms of axial immersion angle K and height of the discrete disc element ΔZ_t as in follows:

$$\Delta b = \frac{\Delta Z_t}{\sin K} \tag{8.17}$$

When the relations obtained for dynamic chip thickness (h_d) ((4.1)), the discrete chip width (Δb) (8.17) are substituted into (8.16), and defining $\boldsymbol{B}^{lj}(\varphi_j)$ matrix as follows:

$$\boldsymbol{B}^{lj}(\varphi_j) = \frac{1}{\sin K} \boldsymbol{T}_{X_t Y_t Z_t} \begin{bmatrix} K_{rc} \\ K_{tc} \\ K_{ac} \end{bmatrix} \boldsymbol{u} \tag{8.18}$$

Equation (8.16) can be re-written as:

$$\begin{bmatrix} F_{X_t}{}^l(\varphi_j) \\ F_{Y_t}{}^l(\varphi_j) \\ F_{Z_t}{}^l(\varphi_j) \end{bmatrix} = \Delta Z_t \boldsymbol{B}^{lj}(\varphi_j) \begin{bmatrix} \Delta X_{td} \\ \Delta Y_{td} \\ \Delta Z_{td} \end{bmatrix} \tag{8.19}$$

Summing up the contribution of each cutting insert, dynamic cutting forces at immersion angle φ on element l can be represented as follows:

$$\begin{bmatrix} F_{X_t}{}^l(\varphi) \\ F_{Y_t}{}^l(\varphi) \\ F_{Z_t}{}^l(\varphi) \end{bmatrix} = \Delta Z_t \boldsymbol{B}^l(\varphi) \begin{bmatrix} \Delta X_{td} \\ \Delta Y_{td} \\ \Delta Z_{td} \end{bmatrix} \tag{8.20}$$

where $\boldsymbol{B}^l(\varphi)$ is the summation of $\boldsymbol{B}^{lj}(\varphi_j)$ for all inserts:

$$\boldsymbol{B}^l(\varphi) = \sum_{j=1}^{n} \boldsymbol{B}^{lj}(\varphi_j) \tag{8.21}$$

The Equation (8.20) can also be represented in time domain since immersion angle φ changes with time, t:

$$\begin{bmatrix} F_{X_t}{}^l(t) \\ F_{Y_t}{}^l(t) \\ F_{Z_t}{}^l(t) \end{bmatrix} = \Delta Z_t \boldsymbol{B}^l(t) \begin{bmatrix} \Delta X_{td} \\ \Delta Y_{td} \\ \Delta Z_{td} \end{bmatrix} \tag{8.22}$$

$\boldsymbol{B}^l(t)$ is a periodic function with tooth passing period τ and it can be represented by Fourier series expansion. Altintas and Budak [54] showed that using only the first term of the Fourier series expansion (single frequency method), stability diagrams can be predicted accurately unless radial immersion is very low. Hence, in this paper, $\boldsymbol{B}^l(t)$ matrix is replaced by the first term of the Fourier series expansion which is $\boldsymbol{B_o}^l$. It can be represented in time and angular domain as follows [54]:

$$\boldsymbol{B_o}^l = \frac{1}{\tau}\int_0^\tau \boldsymbol{B}^l(t)dt = \frac{1}{\varphi_p}\int_0^{\varphi_p} \boldsymbol{B}^l(\varphi)d\varphi \tag{8.23}$$

where φ_p is pitch angle between cutting inserts and it equals to $2\pi/n$. The dynamic displacement vector at the limit of stability in terms of the transfer function matrix of the structure and cutting forces can be written as follows:

$$\boldsymbol{d} = \begin{bmatrix} \Delta X_{td} \\ \Delta Y_{td} \\ \Delta Z_{td} \end{bmatrix} = (1 - e^{-i\omega_c\tau})\boldsymbol{G}(i\omega_c) \begin{bmatrix} F_{X_t}(t) \\ F_{Y_t}(t) \\ F_{Z_t}(t) \end{bmatrix} \tag{8.24}$$

Substituting $\boldsymbol{B_o}^l$ and Equation (8.24), cutting forces corresponding to the disc l at the limit of stability takes the following form:

$$\begin{bmatrix} F_{X_t}{}^l \\ F_{Y_t}{}^l \\ F_{Z_t}{}^l \end{bmatrix} e^{i\omega_c t} = \Delta Z_t \boldsymbol{B_o}^l (1 - e^{-i\omega_c\tau})\boldsymbol{G}(i\omega_c) \begin{bmatrix} F_{X_t} \\ F_{Y_t} \\ F_{Z_t} \end{bmatrix} e^{i\omega_c t} \tag{8.25}$$

where $\boldsymbol{G}$ is the 3x3 transfer function matrix of the tool in tool coordinate system and ω_c is the chatter frequency. So far, cutting forces for the element l have been written in terms of the total forces. However, in order to solve the stability limits, all the elements should be solved simultaneously. For that reason, Equation (8.25) is written for all the elements in the analysis and these equations are summed side by side. Then,

the following equation is obtained where the left hand side of the equation is total dynamic cutting forces:

$$\begin{bmatrix} F_{X_t} \\ F_{Y_t} \\ F_{Z_t} \end{bmatrix} e^{i\omega_c t} = \Delta Z_t (1 - e^{-i\omega_c \tau})(\sum_{l=1}^{m} \boldsymbol{B_o}^l) \boldsymbol{G}(i\omega_c) \begin{bmatrix} F_{X_t} \\ F_{Y_t} \\ F_{Z_t} \end{bmatrix} e^{i\omega_c t} \tag{8.26}$$

m is the number of disc elements in the analysis at the current iteration which equals to $a/\Delta Z_t$. After the terms are collected at the left hand side, the equation turns into the following eigenvalue problem.

$$\left[\boldsymbol{I} - \Delta Z_t (1 - e^{-i\omega_c \tau})(\sum_{l=1}^{m} \boldsymbol{B_o}^l) \boldsymbol{G}(i\omega_c) \right] \begin{bmatrix} F_{X_t} \\ F_{Y_t} \\ F_{Z_t} \end{bmatrix} = 0 \tag{8.27}$$

where $\boldsymbol{I}$ is the 3 by 3 identity matrix. Equation (8.27) has nontrivial solutions only if the following determinant is equal to zero:

$$\det\{\boldsymbol{I} + \lambda\boldsymbol{\Phi}\} = 0 \tag{8.28}$$

where $\boldsymbol{\Phi}$ and complex eigenvalue λ are defined as follows:

$$\lambda = -\Delta Z(1 - e^{-i\omega_c \tau})$$

$$\boldsymbol{\Phi} = \left(\sum_{l=1}^{m} \boldsymbol{B_o}^l \right) \left[\boldsymbol{G}(i\omega_c) \right] \tag{8.29}$$

Skipping some intermediate steps which can be found in [54], the elemental stability can be calculated for each eigenvalue. Using the equation below, the eigenvalue that results in the minimum positive elemental depth is selected as solution for the corresponding chatter frequency:

Each chatter frequency ω_c corresponds to several spindle speeds in the stability diagrams. The calculation of these spindle speeds is explained in the Section 4.4.1 [54]. Finally, stability diagrams are obtained by plotting the determined stability limits with respect to the calculated spindle speeds.

8.1.3. Verification test

In order to verify the model's predictions for the stability diagrams, a verification test is presented here. It is a roughing operation where radial depth of cut is 70% of the tool diameter. It's an up milling process and workpiece material is GS47 steel. The orthogonal database obtained for GS47 material is presented in Table 8.2.

Table 8.2: Orthogonal database for GS47 material and carbide tools

$$\phi = 23.383 + 0.0237V \text{ (deg)}$$
$$\beta = 19.083 - 0.0092V \text{ (deg)}$$
$$\tau_{shear} = 676.1 + 0.007V \text{ (MPa)}$$

$$K_{re} = 142.62 - 0.0773V \text{ (N/mm)}$$
$$K_{te} = 46.183 + 0.1125V \text{ (N/mm)}$$
$$K_{ae} = 0$$

The cutting tool is the circular inserted tool without a center offset which is presented in Section 8.2.1. The overhang length of the tool is 170 mm. The frequency response function of the tool in X_t-and Y_t direction is measured. Due to the symmetry of the structure, they are quite similar to each other. Hence, the measured frequency response function in X_t direction, which is plotted in Figure 8.11, is used in the simulation for both X_t and Y_t directions. Predicted stability diagram and results of chatter tests are given in Figure 8.12. Although, there is some discrepancy between experiments and simulations, the difference is reasonable and can be attributed to the measurement errors in FRFs and errors in predictions of cutting force coefficients.
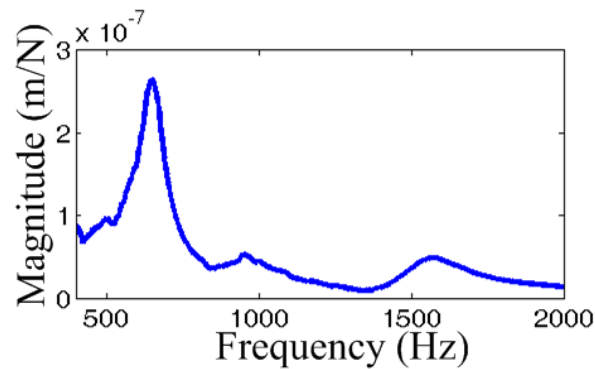
Figure 8.11 : Magnitude of FRF for an example case.
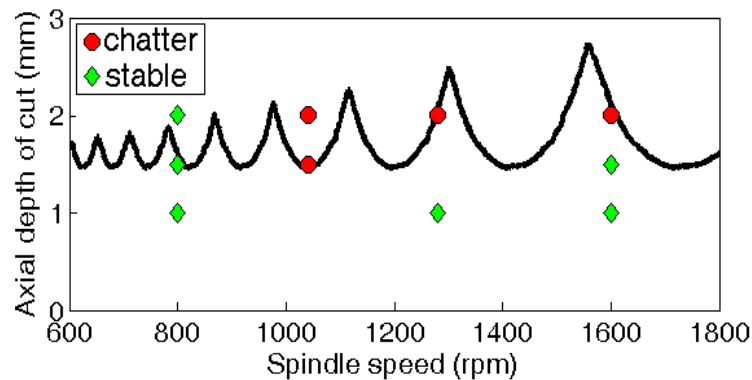
Figure 8.12 : Verification test for stability model

8.2. Application of the Models for Optimization of Real Machining Cases

The developed models are applied for about 10 dies in TOFAS with different materials. The die materials include GH210, GH1090, GS47, FEG52 and 39NiCrMo3. The cutting tool used in the applications is the tool presented in Section 8.2.1. For this tool, feed rate was kept at 1 mm/tooth since feed rate above 1 mm resulted in chipping on the inserts. Moreover, spindle speeds are kept below 1000 rpm since higher cutting speeds resulted in unacceptably high temperature on the inserts. In TOFAS die shop, the axial depth of cut for these tools are set to be 1mm.Using the force and stability models, some modifications on axial depth values in machining of dies are performed and considerable decrease in machining times is achieved without causing any quality problem. Two example die applications are presented here in detail to be representative. Moreover, for 5 different die machining applications, machining time improvements using the force and stability models in parameter selection is presented.

Figure 8.13 :Okuma 3-axis milling machine.

The first example is a roughing operation. The overhang length of the tool is 150 mm. The machine tool is an Okuma 3-axis vertical milling machine. The material is 39NiCrMo3 steel. Radial depth of cut is variable during the process where it changes between 70% and 100% of the tool diameter. Moreover, cutting type is also variable, i.e. process is an up-milling operation at some parts of the tool path and down-milling at other parts. Since cutting forces are higher and stability limits are lower in slotting cases, the process parameters are selected considering the slotting case to stay on the safe side during the whole process.

Stability diagram predicted by the model for slotting case is presented in Figure 8.14 where the predicted for absolute stability is 3.1 mm. Furthermore, effects of axial

depth of cut and feed per tooth on cutting torque and power are calculated, and are demonstrated in Figure 8.15. The torque and power limits of the OKUMA machine tool spindle which are 600 Nm and 22 kW, are also plotted on the corresponding figure. Considering these limits and simulation results presented in Figure 8.14 and Figure 8.15, the axial depth of cut were increased from 1 mm to 3 mm. As a result of the use of models in the parameter selection phase, the operation time has been about one third of the original time (Figure 8.16), which has a considerable impact on the productivity of the process. Some part of the die after the roughing operation is presented in Figure 8.17.
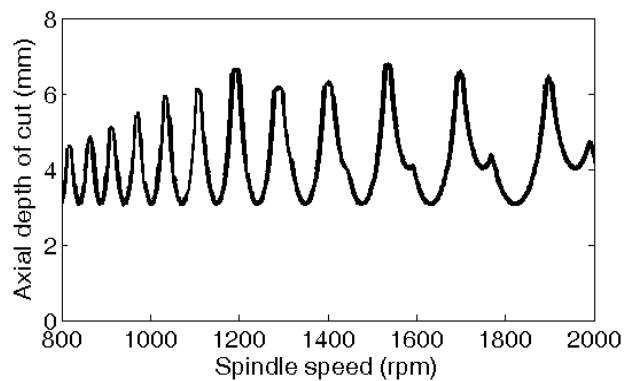
Figure 8.14 : Stability diagram for the example 1.
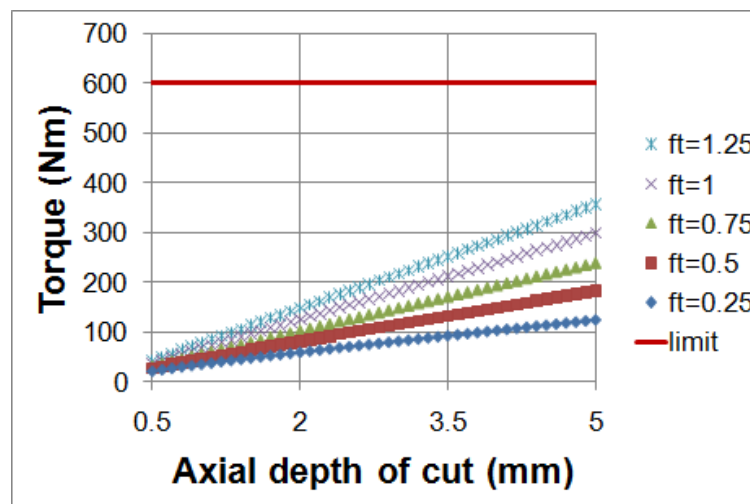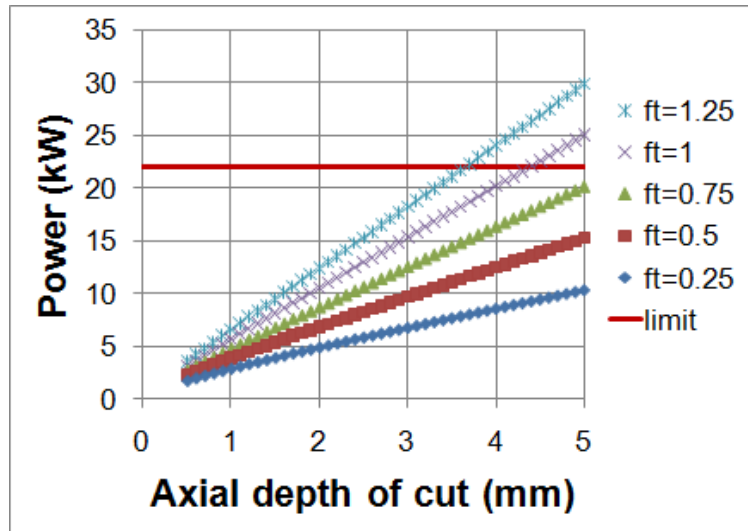
Figure 8.15 : Predicted torque and power values for different axial depth of cut and feed per tooth values for example 1. (Spindle speed=1000 rpm).
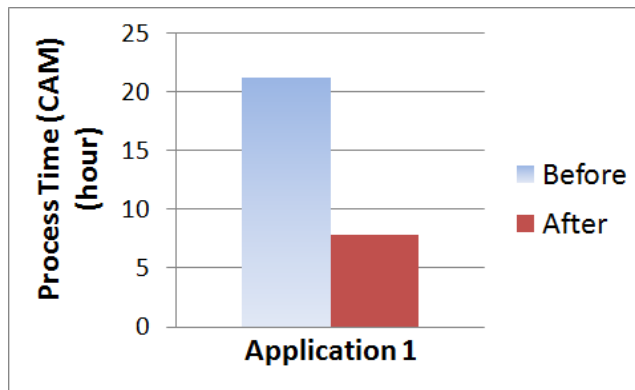
Figure 8.16 : Improvement in the operation time for example 1
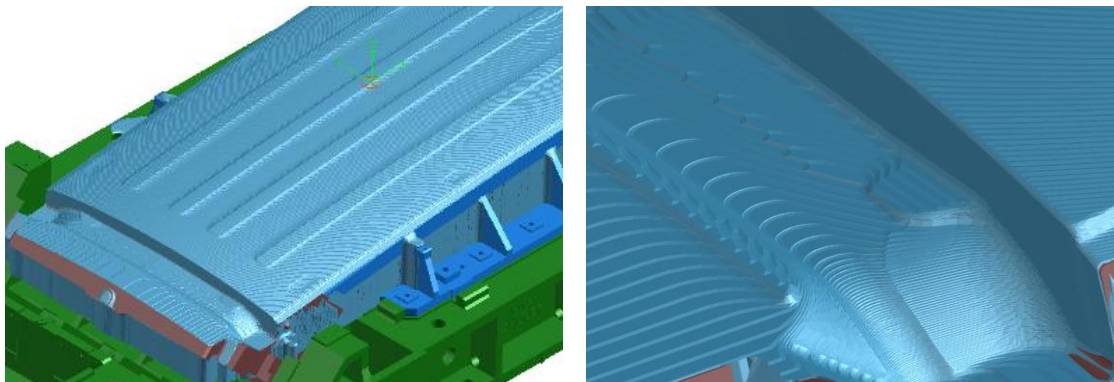
(a) (b)

Figure 8.17 : The first example die after the roughing operation (a) Part of the die (b) Detail view

143

Figure 8.18 : Parpas horizontal 5-axis machining center

The second example is machining of a die made of GH 210 steel in Parpas horizontal 5-axis machining center (Figure 8.18). The overhang length of the tool is 150mm. As radial immersion is variable between 70% and 100% of the tool diameter along the tool path, the simulations are performed for slotting (100% radial immersion) to be on the safe side.

The simulated stability diagram for this case is presented in Figure 8.19 where it is seen that absolute stability is slightly above 3 mm. Considering only stability constraint, the axial depth of cut can be increased from 1mm to 3 mm. However, the cutting torque and cutting power constraints should also be checked. For that reason, simulated cutting torque and power values for different axial depth of cut and feed rate are presented in Figure 8.20. The torque and power limits of Parpas machine tool's spindle are 200 Nm and 30 kW, respectively which are also presented in Figure 8.20. Although axial depth of cut can be increased to 3mm for feed per tooth value of 1 mm/tooth considering stability and power constraints, cutting torque in this case is higher than the torque limit of the spindle (Figure 8.20). For that reason, axial depth of cut is increased to 2mm in this case and operation time nearly halved (Figure 8.21).
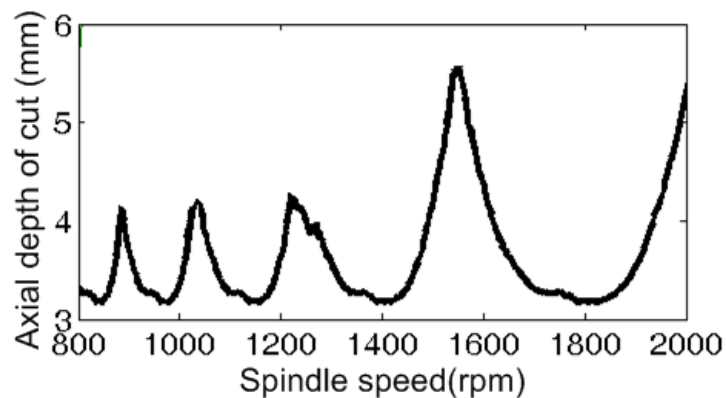
Figure 8.19 : Stability diagram for the example 2.
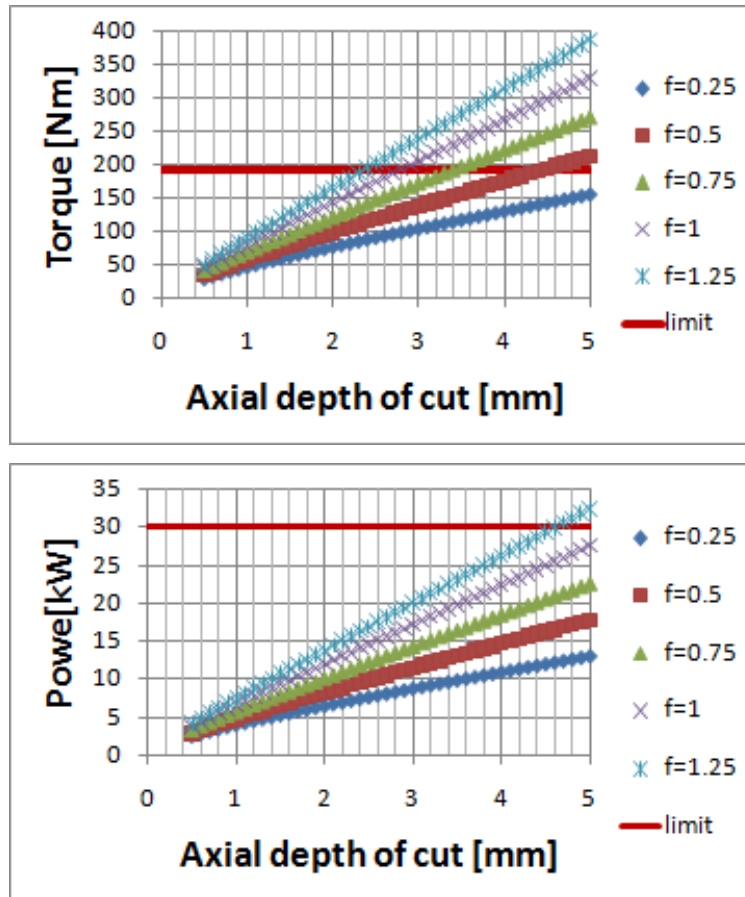
Figure 8.20 : Predicted torque and power values for different axial depth of cut and feed per tooth values for example 2. (Spindle speed=1000 rpm).
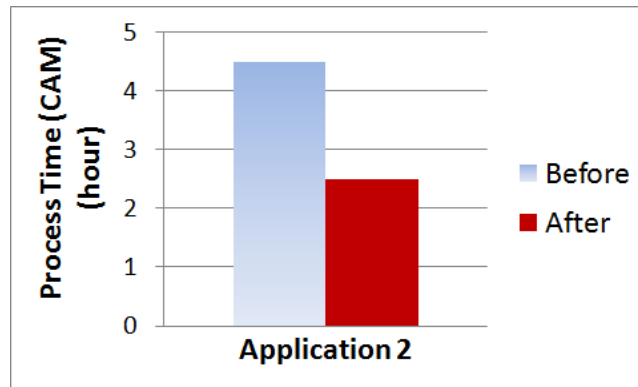
Figure 8.21 : Improvement in the operation time for example 2

Using a similar procedure that is presented in the two examples above, the force and stability model results are used in selection of axial depth of cuts in about 10 die applications in TOFAS die shop. To be representative, the operation times of 5 different applications before and after the models' results are applied, are presented in Figure 8.22. The results are quite promising considering their effects on the productivity on the die shop as in average more than 50% decrease in machining time is achieved.
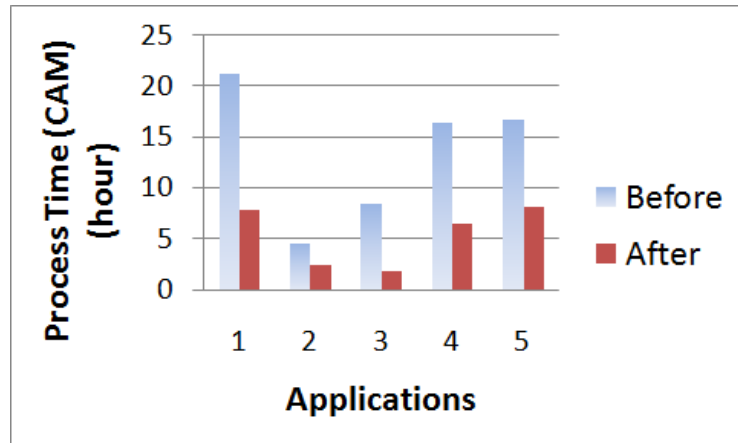
Figure 8.22 : Improvement in the operation time of 5 different die applications

9. CONCLUSIONS

9.1. Conclusions

The contributions of the thesis can be categorized under three main groups which are 5-axis ball-end milling, parallel machining and face-milling with inserted tools.

9.1.1. 5-axis ball-end milling

Process geometry of 5-axis ball-end milling is presented in detail. The understanding of process geometry is important due to two main reasons. Firstly, using process geometry surface quality and productivity measures, namely, scallop height and material removal rate (MRR), respectively, can be calculated. Cutting with tool tip condition can be avoided. The local chip thickness on cutting edge of cutting tools and engagement region between the cutting tool and workpiece can be calculated. Secondly, process geometry provides these as input to the process models for calculation of cutting forces, form errors and stability diagrams. Hence, process geometry knowledge is needed for modeling the mechanics and dynamics of the 5-axis ball-end milling processes.

The terminology in 5-axis ball-end milling which includes the process parameters and coordinate systems is introduced. An engagement model which can calculate the engagement regions between the tool and workpiece is developed. Another engagement model had been proposed in the master thesis work [7], but it was only able to consider the engagements in the ball-region of the cutting tools. The presented engagement model in the thesis can determine engagement zones both on the ball-part and cylindrical part of the ball-end mills. Calculations of scallop heights and material removal rate (MRR) are presented. It was shown that tilt angle may affect scallop height left on the surface depending on the step over value unlike in 3-axis ball-end milling where scallop height only depends on radius of ball-end mill and step over value. Tilt angle affects also the material removal rate (MRR) for cases where cylindrical part of the cutting tool is in cut. Otherwise, i.e., if the ball-part of the tool is incut only, MRR is independent of tilt angle.

Due to the ball-end mill geometry, the cutting speed at the tool tip is zero. Hence, the tool tip cannot perform cutting, instead it indents/ploughs on the workpiece if it is in

contact with the workpiece. Indentation or ploughing process depends on the tool orientation. If lead angle is zero and tool tip is in contact with the workpiece, the tool tip only ploughs over the workpiece since the feed vector is perpendicular to the radial direction at the tool tip. In this case, ploughing occurs, ploughing forces result and surface quality is deteriorated due to the tool tip marks left on the desired surface. On the other hand, when lead angle is negative tool tip may be in contact with the workpiece, but not with the desired surface. In this case, feed vector has a component in the radial direction along the tool tip. For that reason, the tool tip tries to indent into the workpiece. Both indentation and ploughing forces results, however, the desired surface quality is not affected since tool tip is not in contact with the final surface. Nevertheless, the tool tip contact with the workpiece is undesirable and it should be avoided. In the thesis, a systematic tool tip avoidance procedure is developed to guide the process planner during the process parameter selection phase.

Works on modeling the mechanics of the process resulted in force and form error models in 5-axis ball-end milling. They provide capability for prediction of cutting forces, torque and power and form errors. These process models help in two ways. Firstly, they can be used in optimum selection of process parameters considering the cutting forces, torque, power or form errors as constraints. Secondly, they can be used in simulation of a full process once the workpiece geometry and tool path information is given. However, the process parameters at each point along the tool path need to be determined since the process parameters may change along the tool path. Tunc and Budak [6] developed a method where they read CL file of the tool path and determine the process parameters at each CL point. Using this method and developed process parameters, cutting forces, torque, power and form errors can be predicted along a given tool path. If there are any dangerous zones, the tool path can be modified by the process planner and simulated again. This can be repeated until trouble free process is predicted. This way all the iterations on the tool path are made on software environment and iterations that includes hardware such as machine tool equipment are eliminated. This proposed model has been applied on real machining examples in roughing and finishing operations and it proved to be useful. The main criterion in applicability for this method is that process geometry should be able to be defined with standard process parameters along the tool path which may not be the case with workpieces having discontinuous surfaces such as holes or slots. Nevertheless, the method is a practical and efficient method for workpieces with smooth surfaces.

Stability models in frequency and time domain are presented in the thesis. Using the models stability diagrams can be predicted and process parameters that result in chatter free processes can be determined by the stability diagrams. Both single-frequency and multi-frequency solutions are formulated, and they are used in stability predictions. It is shown that the predictions of single- and multi-frequency solutions are much closer to each other compared to the 3-axis flat-end milling since the ratio of the time spent in cutting to non-cutting in 5 axis ball-end milling is not very short even for small radial step over values. Due to the varying cutting force coefficients and engagement boundaries along the tool axis, the cutting tool is discretized along the tool axis in the simulations. It was observed that the elemental disc thickness plays an important role in the accuracy of the results, thus discretization should be made smaller until the convergence is achieved. A time domain model for 5-axis ball-end milling and its results are compared with frequency domain methods. In general, there is satisfactory agreement between the results of the models. Moreover, the predictions of the models are tested experimentally and reasonable agreement is obtained.

Effect of lead and tilt angles on process geometry, mechanics and dynamics are investigated in detail. The effect of lead and tilt angles on engagement regions are shown by CAD models and calculations of the presented engagement model [31]. They change the local chip thickness values but the maximum local chip thickness in the engagement region is independent of lead and tilt angles if only ball-part of the cutting tool is engaged with the workpiece. The maximum chip thickness is affected by lead and tilt angles in cases where cylindrical part of the tool is also included in the process. Tilt angle may affect the scallop height and left on the surface where increase in absolute value of the tilt angle decreases scallop height depending on the step over value. Thus, higher step over can be used for a given scallop height limit which in turn results in less number of cutting steps. At the same time, material removal rate also increases. Finally, an increase in absolute value of tilt angle results in decreased machining time which is also demonstrated with an example.

Lead and tilt angles strongly affect cutting forces, torque, power and form errors since they change the geometry and mechanics of the process. It is demonstrated that in order to minimize the cutting torque and power, the engagement region with the workpiece should be positioned on the lower side of the tool. That is particularly important for roughing operations with relatively large diameter tools where the available torque and power can be the process limitation. Although exact values of the

required lead and tilt angles to minimize these parameters can only be determined by running the process model [30], some qualitative guidelines can be suggested. Tilt angle should be selected such that it has the same sign with the cross-feed direction. On the other hand, lead angle should be kept at a slightly positive value since application of higher positive lead angles shifts the engagement region to the upper parts of the cutting tool and negative lead angles may result in tool tip contact. These qualitative comments are verified by simulations and experiments for several representative cases. Form error due to tool deflections is an important factor for finishing operations. For minimum form error, lead and tilt angles could be selected as zero; however, this would result in tool tip contact marks with the created surface. For that reason, lead angle should be selected slightly positive. For the selection of tilt angle, overcutting is an important consideration. For clockwise rotating tools, when tilt angle is negative, the cutting tool starts cutting from the finished surface. In such a case, depending on the direction of cutting forces, the tool may deflect into the workpiece resulting in overcut. The opposite is true for counter-clockwise rotating tools. Hence, negative tilt angles should be avoided for clockwise rotating tools while use of positive tilt angles should be prevented for counter-clockwise rotating tools where possible.

Lead and tilt angles also affect the dynamics of 5-axis ball-end milling. They change the chatter behavior and stability limits not only due to their effect on the directional coefficient matrix, but also on the feed direction and oriented transfer function matrix depending on the machine tool configuration. For a representative test case, it is demonstrated that combined effect of lead and tilt angles may provide 4 times increase in absolute stability limit.

9.1.1. Dynamics of parallel machining

Dynamics of for parallel machining processes, namely, parallel turning and parallel milling processes are presented in the thesis. Two different parallel turning processes are presented in this paper. In the first case, a specially designed tool holder which can hold two cutting tools is used on a standard turning center. In the second case, the turning tools are clamped on independent turrets on a parallel turning center. Developed time and frequency domain models are useful for understanding the dynamic interaction of parallel working tools and predicting the effect of this interaction on stability limits. The models' results are presented on several examples and advantage of parallel turning with respect to single tool turning is demonstrated. Moreover,

experimental verification for the first turning case is presented. It is demonstrated that the total cutting stability in a parallel turning process can be increased compared to single tool turning due to dynamics interactions between the tools. This effect is enhanced if the modal frequencies of the tools are close to each other similar to the situation in tuned vibration absorbers. Finally, a new phenomenon where there are two stability limit curves on the stability diagram is presented for the parallel turning operations.

A time-domain model that can simulate parallel milling processes is presented in the thesis. The model is able to include the dynamic interactions of two flexible cutting tools and a flexible workpiece. If the workpiece is rigid, the dynamics of two processes can be analyzed separately using a standard milling stability formulation since there is no presence of dynamic coupling. Otherwise, the presented model is needed to incorporate the dynamic interaction between the cutting tools. The simulation results showed that the process stability strongly depends on the milling mode, part flexibility and other process parameters. Stability limits are shown to be affected by lag angle between the tools. It was observed that the total stable material removal rate by two parallel working milling tools may be higher than a single milling tool increasing productivity.

9.1.2. Face milling process with inserted tools

Cutting forces and stability diagrams in die machining operations with inserted cutters can be predicted using the presented process models. Different insert geometries on the tools with different orientations on the cutting tools complicate the mathematical representation of the cutting edges. A vectorial representation is employed with this purpose. Force and stability models which are similar to the ones developed for 5-axis ball-end milling are presented. The predictions of cutting forces and stability diagram are compared with experiments, and it is shown that models' accuracy is reasonable. Using the models, constraint such as cutting torque and power limitations of machine tools and chatter vibrations are taken care of in the parameter selection phase before machining. Finally, positive effect of using process models on productivity of real die machining processes is shown.

9.2. Further research directions

Further research directions are divided into two subsections as future work in 5-axis milling and parallel machining. They are presented in the following two sections.

9.2.1. 5-axis milling

Process geometry, mechanics and dynamics of 5-axis ball-end milling are presented in this thesis. These works can be extended to more general 5-axis milling operations where the workpiece can have discontinuous features or the tool has more complex geometry (tapered, serrated tools). An analytical engagement model was developed to determine the engagement region between the ball-end milling tool and the workpiece but calculation of engagement models for a general case is fairly complex. Because of this complexity, analytical calculation of the engagement region seems to be not possible. Geometric engines like ACIS [26] or Z-mapping method [27] will be necessary for determination of the engagement region.

The developed models can be used in parameter selection during process planning stage. Moreover, certain variables such as cutting forces, torque/power, form errors and stability limits, etc., can be simulated throughout a given tool path. For simulation of a given tool path, the variations of the process parameters along the tool path need to be determined. The determination of process parameters from a given tool path was shown by Tunc and Budak [6]. Combining this work and the presented models in this thesis, the simulations can be performed throughout a given toolpath. This strategy was shown to be working with enough accuracy for roughing of smooth workpieces and finishing operations [100]. The most important constraint of this strategy is that it should be possible to define the engagement regions using standard process parameters which are cutting depth, step over, lead and tilt angle. For example, semi-finishing processes where the left geometry from roughing operation is not smooth, the presented strategy will result in errors, since the engagement regions in this case can not be defined with standard process parameters. Again, geometric engines like ACIS [26] or Z-mapping method [27] should be employed for these cases for increased accuracy.

Effects of multi-frequency solution for 5-axis ball-end milling were shown to be marginal in the thesis. Although the step over is selected as low, the immersions are not that low due to the ball-geometry of the tool. In this case, the ratio of time spent in cutting to non-cutting which is an important criterion for seeing multi-frequency effects is low. For that reason, multi-frequency effects are suppressed. However, for tapered

ball-end milling tools which are used in flank milling operations, tapered part of the tool is usually more involved in cutting with respect to the ball-part, hence immersions can be lower and the ratio of time spent in cutting to non-cutting can also be low. In this case, multi-frequency effects are more likely to be observed. On the other hand, helix angle on the taperd tool can play an important role on the multi-frequency effects. Since the cutting depths in flank-milling are usually high, helix angle decreases the time spent-in cutting to non-cutting, so it has a suppressing effect on the multi-frequency effects. Although flank milling and helix angle have opposing effects, it is worth analyzing the stability of these operations with the multi-frequency method.

Frequency and time-domain models for 5-axis ball-end milling stability are presented in the thesis. Semi-discretization method [59] which is another useful method in stability analysis can also be employed for 5-axis ball-end milling stability and the results of the semi-discretization method can be compared with the methods presented in the thesis.

As shown in the thesis, kinematics of machine tools has effect on the dynamics of the processes. By adding the kinematics of the machine tool, into force and stability models, preferable workpiece clamping positions and orientations could be determined. Furthermore, effect of cutting forces on linear and rotational axes of the machine tool can be predicted during the process simulation. Finally, a given CL file could be checked if it's possible to achieve the given tool path respecting the machine tool limitations such as acceleration or speed.

9.2.2. Parallel Machining

The focus in the parallel turning operations has been on the effect of parallel working turning tools. The parallel turning models have been developed considering the flexibilities in the feed diection only, which resulted in one-dimensional turning stability problem. The turning tools and inserts are selected such that there is no side-edge cutting angle or oblique angle on the cutting edge. As a result, the formulation is kept one dimensional. Using the 1-D stability model, important results such as effects of the tools's effect on each other's stability limit and stability limits with two limits were presented in the paper. However, as a future work, the developed models can be extended to cover a general turning tool where it may have side cutting edge angle or oblique angle on it. Moreover, the workpiece stability can also be included in the model.

The offset between the turning tools in the feed direction have not been considered in the thesis since it does only change the static chip thickness and it does not affect the regeneration mechanism. However, the effect of the offset should be analyzed further if the magnitude of the cutting forces on the turning tools of interest. As an initial analysis, depending on the offset value, the turning tools share the feed per revolution value but how it's shared between the tools is a question of further research.

Dynamics of the parallel milling has been formulated in time domain and a stability diagram calculated with this method is presented in the thesis. Although a frequency domain model has also been formulated for parallel milling stability, it is not presented in the thesis since stability diagrams using the frequency domain model could not be calculated yet. This work is in progress at the moment and is planned to be finished after the thesis.

In the thesis, lag angle between the parallel working milling tools has been shown to affect the stability limits. As Shamoto and Akazawa [65] presented the effect of using different spindle speeds on the stability of parallel milling tools, the effect of lag angle can be analyzed in more detail and its effect can be shown also experimentally. However, it should be noted that vector spindles are required to be able to control lag angle between the tools. Otherwise, it is an uncontrolled parameter.

In parallel milling, different spindle speeds or different number of teeth on cutting tools result in different delays which result in multi-delay stability problem.It is worth investigating the effect of multiple delays on the stability limit as a future work. At the moment, the parallel milling formulation has only been applied to flat-end mills. In the future, it can also be applied to more general tools such as ball-end mill tools, tapered ball-end mill tools or serrated tools. Workpiece play a major role in dynamic behavior of the parallel milling process. Since the material is removed from the workpiece throughout the process, the varying dynamics of the workpiece structure should be taken care of. For that reason, the future research in this field will be important. Moreover, the relative translational motion between the cutting tools was neglected in the current analysis since it results in varying dynamics with time between the milling tools. The varying dynamics could be added to the model in the future.

A. APPENDIX

A.1. The measurement of the centers of revolution of rotary axes in Deckel Maho 50evo Machining Center

The accurate measurement of the centers of revolution of rotary axes in 5-axis machining centers is needed since the postprocessor programs need the kinematic information of the machining centers as they produce G codes from APT codes. The kinematic information given by DMG service was not enough to represent the kinematic chain of the machine tool. Hence, a measurement procedure was developed to measure the important kinematic information of the machine tool.

A.1.1. The data provided by DMG service

DMG service provided the following data and claimed that these data was enough to represent the kinematic chain.

Table A.1: Data given by DMG service in the beginning of August

Measurement	(mm)
M13	-250.621
M 14	-156.035
M 15	-543.407
M 16	-250.622
M 17	
M 18	
M 19a	
M 19b	155.542

However, it was realized that these data was not sufficient for the post-processor program. DMG service gave the missing data by phone; although, they did not measure these dimensions. They probably sent the old values. The final data provided by DMG service.

Table A.2: Final data given by DMG service

Measurement	(mm)
M 13	-250.621
M 14	-156.035
M 15	-543.407
M 16	-250.642
M 17	-1.047
M 18	-388.4
M 19a	-154.988
M 19b	155.007

A.1.2. The measurement procedure

There are 2 rotary axes (C and B) on the machine tool. These axes are illustrated in the following figure.
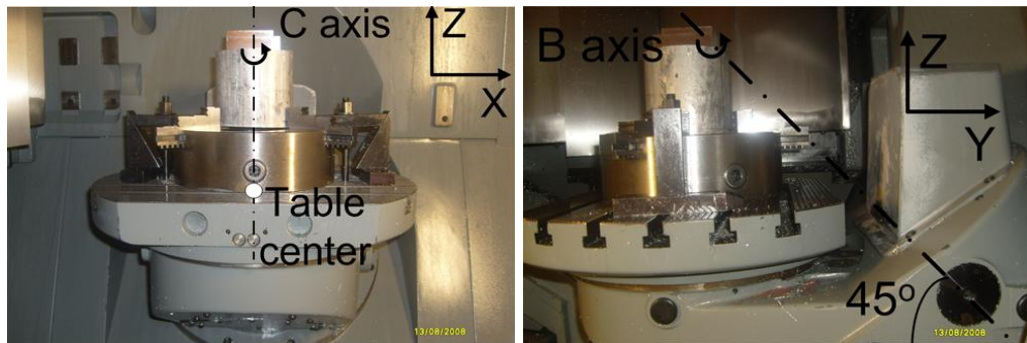
(a)   (b)

Figure A.1 (a) C axis (b) B axis

Firstly, the measurement of the center of C axis is presented. C axis motion defines the rotation of the table along the Z axis of the machine tool. The procedure for calculation of the center of rotation of C axis is listed as follows:

1. In order to measure the center of rotation, an initial value for the coordinates of the center is used. This initial value can be taken as the last measured coordinates of the rotation center which is given in Table A.3.

Table A.3: Inital coordinates of the center of the table (provided by DMG service)

	X(mm)	Y(mm)	Z(mm)
Table center(TC)(X_t, Y_t, Z_t)	-250.621	-156.035	-543.407

2. A rectangular prism is clamped to the table. It should be connected close to the center of rotation as much as possible. All 5 surfaces of the workpiece is machined and a square block with dimension of *a* in X, Y directions is obtained. In the machining process, the X and Y coordinates of the initial rotation center of the table is used as the work offset (WCS) which later becomes the center of the machined square block.

3. After the square block is machined, the four surfaces of it are measured in XY plane using the measurement probe as shown in Figure A.2. Using the values X1, X2, Y3 and Y4 which are the coordinates of the corresponding surfaces in MCS (Machine Coordinate System), the dimensions of the machined square block and the center of the block in X and Y directions can be determined as tabulated in Table A.4.
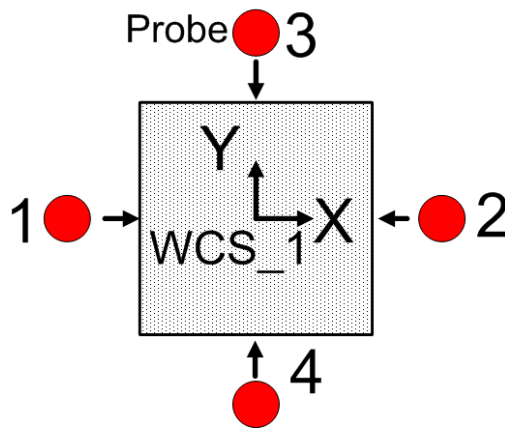
Figure A.2 The measurement of 4 surfaces of the square block

Table A.4: Measured coordinates of the 4 surfaces and calculation of dimensions and center of the square block in X and Y directions

Point	X	Y
1	X1	0
2	X2	0
X length	(X2-X1)	-
X center	(X2+X1)/2	-
3	0	Y3
4	0	Y4
Y length	-	(Y3-Y4)
Y center	-	(Y3+Y4)/2

4. The table is rotated 180° in C axis. Following the procedure in the step 3, X and Y coordinates of the new center of the square block (WCS_2) is determined. If the initial table center was correct, the new center of the square block (WCS_2) would be the same with the WCS_1 measured before the 180° rotation in C axis. However, due to the accuracy characteristics of the measurement probe used, there may be a few micrometers difference between these two centers. If there is a considerable difference of ΔX and ΔY between the initial table center and the real table center, then there would be a difference of $2\Delta X$ and $2\Delta Y$ in WCS_1 and WCS_2. Finally, the X and Y coordinates of the real center of the table is determined by calculating the mid-point between WCS_1 and WCS_2. This is illustrated in Figure A.3.
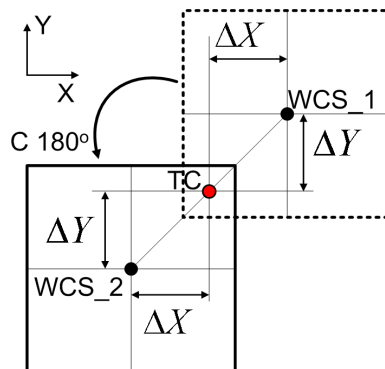
Figure A.3: The determination of the table center (TC) from WCS1 and WCS2

158

5. After the new table center (TC) is determined in XY plane, steps 2-4 are repeated. If the calculated table center is the real table center, the newly calculated table center and the previous table center in XY plane should match with a certain tolerance.

6. The Z coordinate of the table center is measured using a calibration tool holder with known length l_c and a Johnson gage of height 100 mm.

The length of the tool holder is measured using a dial gauge as shown in Figure A.4. Firstly, the spindle's lowest point in Z-direction is measured with the dial gauge (Figure A.4a). It should be paid attention that the point that dial gauge is in contact with is on the rotating part of the spindle. Then, the tool holder is put into the spindle and tool holder's lowest point in Z-direction is measured (Figure A.4b). The difference between these two measurements gives the tool holder's length l_c.

(a)   (b)
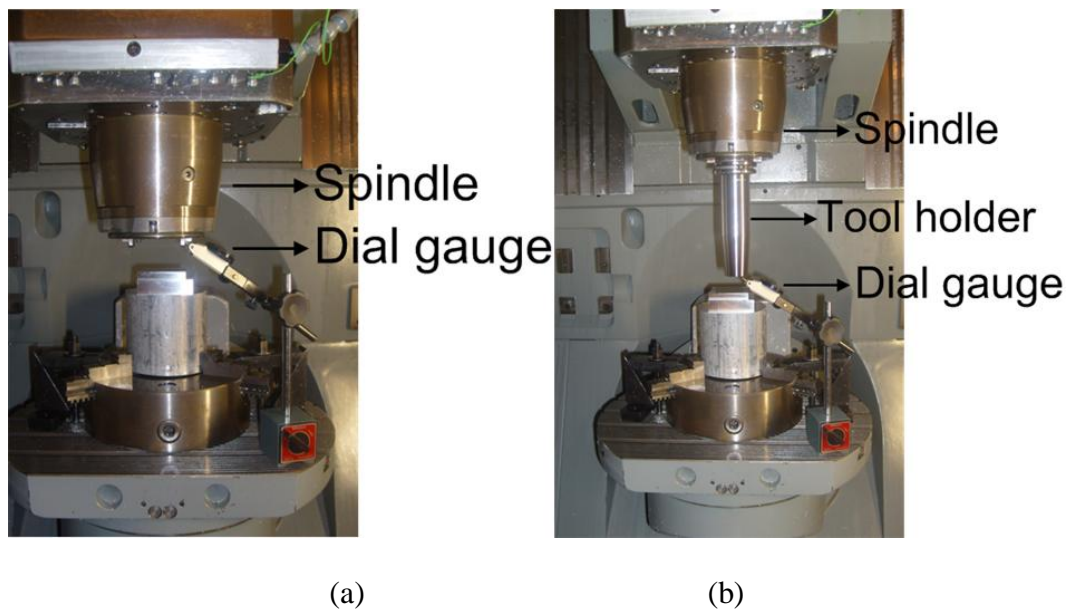
Figure A.4 Measurement of the cutting tool length l_c (a) Measurement of the spindle's lowest point in Z direction (b) Measurement of the tool holder's lowest point in Z direction

The Johnson gage is put on the table. The tool holder is moved down until the tool holder touches the Johnson calibration unit (Figure A.5). At this position, the addition of the Z position in MCS (Machine Coordinate System), length of the tool holder l_c and height of the Johnson gage (100mm) gives the Z-coordinate of the table center (Z_t).

159
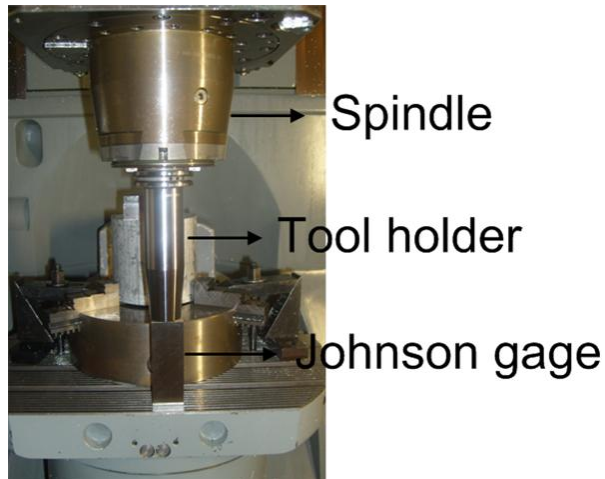
Figure A.5: Measurement of the Z coordinate of the table center

Secondly, the measurement of the B axis is presented. B axis motion defines the rotation of the table along an axis that makes 45° with the horizontal in YZ plane (Figure A.1b). Any point on the rotation axis B can be given as input to the post processor program. The point (B_{center}) in the middle of the line that connects the table center when B-axis is at 0° and table center when B-axis is at 180° is selected to be measured.

After the coordinates of the table center (X_t, Y_t, Z_t) are determined, coordinates of the table center after the B-axis is rotated by 180° which is represented by (X_{tr}, Y_{tr}, Z_{tr}) is needed.

The procedure for calculation of the coordinates of the table center when B-axis is at 180° is listed as follows:

1. The Z-coordinate of the top surface of the square block (Z_w) is measured using the measurement probe when B-axis is at 0°. Since the Z coordinate of the table center (Z_t) is known, height of the square block (h_w) can be calculated by subtracting Z_t from Z_w (Figure A.6).

2. The B-axis is rotated by 180°. The dimension Y_{wr} is measured in Y-axis using the measurement probe. Adding the height of the square block (h_w) to the Y_{wr}, Y coordinate of the table center when B-axis is at 180°. (Y_{tr}) is determined (Figure A.6).

3. The dimension Z_{wr} is measured in Z-axis using the measurement probe. Subtracting half of the width of the square block (a) from Z_{wr}, Z coordinate of the table center when B-axis is at 180°. (Z_{tr}) is determined (Figure A.6).

160
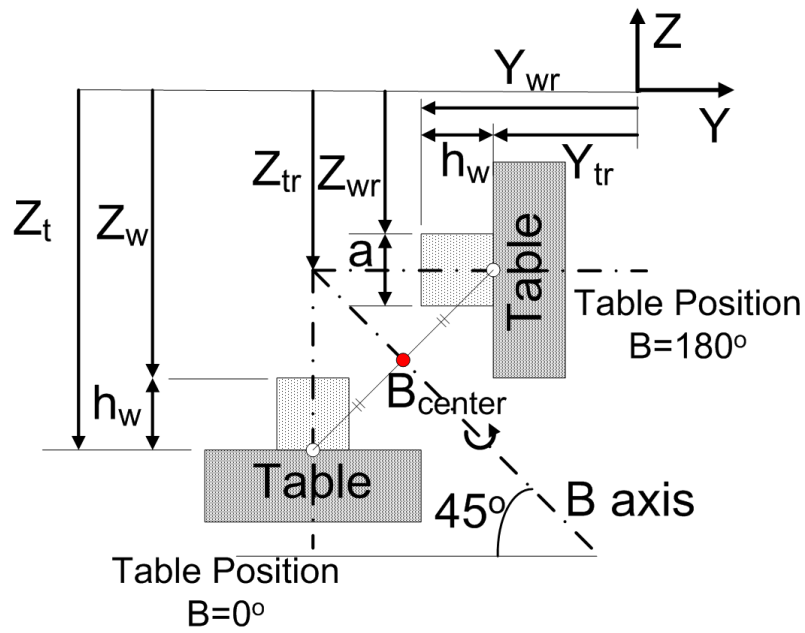
Figure A.6: Measurement of the Y and Z coordinates of the table center (Y_{tr}, Z_{tr}), respectively when B axis is at 180°.

4. X coordinate of the left surface (X_{tr1}) and X coordinate of the right surface (X_{tr2}) are measured using the measurement probe (Figure A.7). The mid-point of these coordinates gives the X_{tr} which is the X-axis coordinate of the table center when B-axis is at 180°. This measurement is illustrated graphically in Figure A.7.
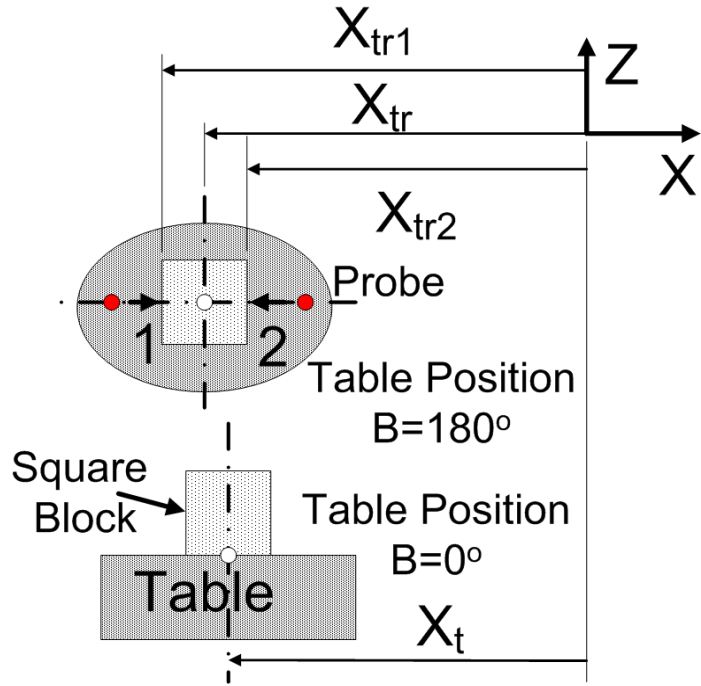
Figure A.7: Measurement of the X coordinate of the table center (X_{tr}) when B axis is at 180°.

After both the coordinates of the table center (X_t, Y_t, Z_t) , and coordinates of the table center after the B-axis is rotated by 180° which is represented by (X_{tr}, Y_{tr}, Z_{tr}) are determined. Point B_{center} is the mid-point of these two positions. The coordinates of the point B_{center} are given as follows:

$$Bcenter=0.5*[(Xt+Xtr), (Yt+Ytr), (Zt+Ztr)] \tag{A.1}$$

A.1.3. The sample measurements and calculations

In this section, the procedure explained in the previous section is implemented on the machining center. Firstly, determination of table center when B-axis is at 0° is presented. Then, the table center when B-axis is at 180° is determined. Finally, the coordinates of point B_{center} is calculated

A.1.3.1.   Table center coordinates (B=0°)

The initial values of the table center are given in Table A.3. A 82 mm square block was machined taking the center of the block as the coordinates in Table A.3. Four surfaces of the block are measured as shown in Figure A.3 and Table A.4 is filled as follows:

Table A.5: Measured coordinates of the 4 surfaces and calculation of dimensions and center of the square block (WCS_1) in X and Y directions

Point	X(mm)	Y(mm)
1	-291.622	0
2	-209.637	0
X length (mm)	81.985	-
X center (mm)	-250.63	-
3	0	-197.048
4	0	-115.077
Y length (mm)	-	81.971
Y center (mm)	-	-156.063

The table is rotated by 180° in C axis and the measurement is repeated. The measurement results are tabulated in Table A.6. It is seen that there is considerable difference between WCS_1 and WCS_2. The table center is in the mid-point of WCS_1 and WCS_2. Hence, the new table center can be calculated as (-250.61,-156.03) mm.

Table A.6: Measured coordinates of the 4 surfaces and calculation of dimensions and center of the square block (WCS_2) in X and Y directions

Point	X(mm)	Y(mm)
1	-291.578	0
2	-209.597	0
X length (mm)	81.981	-
X center (mm)	-250.588	-
3	0	-196.994
4	0	-115.014
Y length (mm)	-	81.98
Y center (mm)	-	-156.004

Using the new table center coordinates, the above procedure was repeated for a square block with dimensions of a=77.980 mm and the new table center was calculated to be (-250.607, -156.029). The new table center in XY plane is taken as the average of these two values. The Z-coordinate of the table center is calculated as explained in the previous section. The new table center is tabulated in the following table:

	X(mm)	Y(mm)	Z(mm)
The new table center(TC)(X_t, Y_t, Z_t)	-250.608	-156.029	-543.331

Table A.7: Calculated coordinates of the center of the table (B=0°)

A.1.3.2.   Table center coordinates (B=180°)

The top surface of the square block is measured as Z_w= -316.484 mm when B axis is at 0°. Height of the square block h_w can be calculated as follows:

$$hw= Zw-Zt =-316.484-(-543.331)= 226.847 \text{ mm} \tag{A.2}$$

After B-axis is rotated by 180°, the dimension Y_{wr} (Figure A.6) is measured as -228.002 mm. Hence, Y_{tr} can be determined:

$$Ytr = Ywr+hw=-228.002+226.847= -1.155 \text{ mm} \tag{A.3}$$

The dimension Z_{wr} (Figure A.6) is measured as -349.455 mm. Since the dimension of the square block is known, the dimension Z_{tr} can be calculated:

$$Ztr= Zwr-a/2=-349.455-77.980/2=-388.445 \text{ mm} \tag{A.4}$$

The dimensions X_{tr1} and X_{tr2} are measured as -289.627 mm and -211.644mm, respectively. Using these two measurements, X_t can be determined:

$$Xtr= 0.5(Xtr1+ Xtr2)=0.5(-289.627-211.644)=-250.635mm \tag{A.5}$$

Finally, the coordinates of table center when B-axis is at 0° and at 180° are tabulated in the following table. The mid-point of these two points gives the coordinates of the point B_{center}. The highlighted coordinates are required by the post processor program. The measurement numbers of the dimensions in DMG service data sheet are given next to them.

Table A.8: Table center coordinates when B=0°. and B=180°, the coordinates of the point B_{center}

The new table center(TC)	X(mm)	Y(mm)	Z(mm)
The new table center(TC) (X_t, Y_t, Z_t) B=0°	M13 -250.608	M14 -156.029	M15 -543.331
The new table center(TC) (X_{tr}, Y_{tr}, Z_{tr}) B=180°	M16 -250.635	M17 -1.155	M18 -388.445
B_{center}	-250.621	-78.592	-465.888

10. REFERENCES

[1] Y. Altintas, Manufacturing Automation Metal Cutting Mechanics, Machine Tool Vibrations, and CNC Design, Cambridge University Press, 2000.

[2] NX CAM, http://www.plm.automation.siemens.com

[3] CATIA Machining, http://www.3ds.com

[4] hyperMILL, http://www.openmind-tech.com

[5] ESPRIT CAM, http://dptechnology.com

[6] Tunc, L.T., Budak, E., 2009, Extraction of Milling Conditions from CAM Data for process simulation, International Journal of Advanced Machining Technology, 43:538-550

[7] Ozturk, E., 2005, Modeling of 5-axis Milling Forces and Form Errors, MSc. Thesis, Mechatronics Engineering, Sabanci University, Istanbul, Turkey

[8] Pi, J., Red, E., Jensen, G., 1998, Grind-free tool path generation for five-axis surface machining ,Computer Integrated Manufacturing Systems, 11, 4, 337-350

[9] Yoon, J., Pottmann, H., Lee, Y., 2003, Locally optimal cutting positions for 5-Axis sculptured surface machining, Computer Aided Design, 35, 1, 69-81

[10] Ming, C.H., Hwang, Y.R., Hu, C.H., 2003, Five-Axis tool orientation smoothing using quaternion interpolation algorithm, International Journal of Machine Tools and Manufacture, 43(12) 1259-1267

[11] Gray, P. J., Ismail, F., Bedi, S., 2004, Graphics- assisted rolling ball-method for 5-Axis surface machining, Computer Aided Design 36 (7) 653-663.

[12] Makhanov, S. S., Anotaipaiboon W., 2007, Advanced numerical methods to optimize cutting operations of five-axis milling machines, Springer Series in Advanced Manufacturing

[13] Bohez, E.L.J., 2002, Five-axis milling machine tool kinematic chain design and analysis, International Journal of Machine Tools and Manufacture, 42, 505–520

[14] Jung, Y. H., Leea, D. W. , Kimb, J. S., Mokc, H. S., 2002, NC post-processor for 5-axis milling machine of table-rotating/tilting type, Journal of Materials Processing Technology,130-131, 641-646

[15] Tsutsumi, M., Saito, A., 2003, Identification and compensation of systematic deviations particular to 5-axis machining centers, International Journal of Machine Tools and Manufacture, 43, 8, 771-780

[16] Sorby, K., 2007, Inverse kinematics of five-axis machines near singular configurations, International Journal of Machine Tools and Manufacture, 47, 299–306

[17] Lin, P. D., Tzenga, C. S., 2008, Modeling and measurement of active parameters and workpiece home position of a multi-axis machine tool, International Journal of Machine Tools and Manufacture, 48, 3-4, 338-349

[18] Anotaipaiboon W., Makhanov, S.S., Bohez, E.L.J., 2006, Optimal setup for five-axis machining, International Journal of Machine Tools and Manufacture, 46, 9, 964-977

[19] Sencer, B., Altintas, Y., Croft, E., 2009, Modeling and Control of Contouring Errors for Five-Axis Machine Tools. Part I: Modeling, Journal of Manufacturing Science and Engineering,131, 3, 031006

[20] Srinivasan, K., Tsao, T. C., 1997, Machine Tool Feed Drives and Their Control- A Survey of the State of the Art, Journal of Manufacturing Science and Engineering,119, ,4B, 743-748.

[21] Altintas, Y., Erkorkmaz, K., Zhu, W.H., 2000, Sliding Mode Controller Design for High Speed Feed Drives, CIRP Annals, 49,1, 265–270.

[22] Lee, K. , Kim, J., 2000, Controller gain tuning of a simultaneous multi-axis PID control system using the Taguchi method, Control Engineering Practice, 8, (8) , 949-958

[23] Yeh, S. Hsu,P. L, 2003, Analysis and Design of Integrated Control for Multi-Axis Motion Systems, IEEE Transactions On Control Systems Technology, 11, 3, 375-382

[24] Sencer, B., Altintas, Y., 2009, Modeling and Control of Contouring Errors for Five-Axis Machine Tools. Part II – Precision Contour Controller Design, Journal of Manufacturing Science and Engineering,131, 3, 031007

[25] Imani, B.M., Sadeghi, M.H., Elbestawi, M.A., 1998, An improved process simulation system for ball end milling of sculptured surfaces, International Journal of Machine Tools & Manufacture 38:1089–1107

[26] ACIS geometric engine, http://www.spatial.com

[27] Kim, G.M., Cho, P.J., Chu, C.N., 2000, Cutting force prediction of sculptured surface ball-end milling using Z-map, International Journal of Machine Tools & Manufacture 40: 277–291.

[28] Lamikiz, A., Lopez de Lacalle, L.N., Sanchez, J.A. Salgado, M.A., 2004, Cutting force estimation in sculptured surface milling, International Journal of Machine Tools & Manufacture, 44:1511–1526.

[29] Fontaine, M., Moufki, A., Devillez, A., Dudzinski D. , 2007, Modelling of cutting forces in ball-end milling with tool–surface inclination Part I: Predictive force model and experimental validation, Journal of Materials Processing Technology, 189: 73–84

[30] Ozturk, E., Budak, E., 2010, Tool Orientation Effects on the Geometry of 5-axis Ball-end Milling, Proceedings of the 36th International MATADOR Conference, 14-16 July 2010, Manchester, United Kingdom.

[31] Ozturk, E., Budak, E., 2007, Modeling of 5-Axis Milling Processes, Machining Science and Technology, Vol. 11, Issue 3, 287-311.

[32] Fontaine, M., Devillez, A., Moufki, A., Dudzinski, D., 2006, Predictive Force Model for Ball-end Milling and Experimental Validation with a Wavelike Form Machining Test. International Journal of Machine Tools and Manufacture,46, 367-380.

[33] Gradisek, J., Kalveram, M., Weinert, K., 2004, Mechanistic Identification of Specific Force Coefficients for a General End Mill, International Journal of Machine Tools and Manufacture, 44, 401-414.

[34] Lazoglu, I., 2003, Sculpture Surface Machining: A Generalized Model of Ball-end Milling Force System. International Journal of Machine Tools and Manufacture, 43, 453-462.

[35] Ozturk, B., Lazoglu, I., Erdim, H., 2006, Machining of Free-Form Surfaces. Part II: Calibration and Forces, International Journal of Machine Tools and Manufacture, 46, 736-746.

[36] Budak, E., Altintas, Y., Armarego, E. J. A., 1996, Prediction of Milling Force Coefficients from Orthogonal Cutting Data. Journal of Manufacturing Science and Engineering, 118, 216-224.

[37] Lee, P., Altintas, Y., 1996, Prediction of Ball-end Milling Forces from Orthogonal Cutting Data, International Journal of Machine Tools and Manufacture, 36, 1059-1072.

[38] Engin, S., Altintas, Y., 2001, Mechanics and Dynamics of General Milling Cutters Part 1: Helical End Mills, International Journal of Machine Tools and Manufacture, 41, 917-924.

[39] Yang, M., Park, H., 1991, The Prediction of Cutting Force in Ball-end Milling. International Journal of Machine Tools and Manufacture, 31 (1), 45-54.

[40] Sadeghi, M. H., Haghighat, H., Elbestawi, M. A., 2003, A Solid Modeler Based Ball-end Milling Process Simulation, International Journal of Advanced Manufacturing Technology, 22, 775-785.

[41] Tai, C., Fuh, K, 1995, The Prediction of Cutting Forces in the Ball-end Milling Process. Journal of Materials Processing Technology, 54, 286-301.

[42] Yucesan, G., Altintas, Y., 1996, Prediction of Ball-end Milling Forces. Journal of Engineering for Industry, 118, 95-103.

[43] Larue, A., Altintas, Y., 2005, Simulation of Flank Milling Processes. International Journal of Machine Tools and Manufacture, 45, 549-559.

[44] Clayton, P. A., El-Wardany, T., Elbestawi, M. A., Viens D. A, 2000, Mechanistic Force Model of the 5-axis Milling Process. Proceedings of the ASME Manufacturing Engineering Division, 11, 979-987.

[45] Zhu, R., Kapoor, S. G., DeVor, R. E., 2001, Mechanistic Modeling of the Ball-end Milling Process for Multi-axis Machining of Free-form Surfaces, Journal of Manufacturing Science and Engineering, 123, 369-379.

[46] Fussell, B.K., Jerard, R. B., Hemmet, J. G., 2003, Modeling of Cutting Geometry and Forces for 5-axis Sculptured Surface Machining, Computer Aided Design, 35, 333-346.

[47] Kim, G. M., Kim, B. H., Chu, C. N., 2003, Estimation of Cutter Deflection and Form Error in Ball-end Milling Processes. International Journal of Machine Tools and Manufacture, 43, 917-924.

[48] Lopez de Lacalle, L. N. , Lamikiz, A. , Sanchez, J. A., Salgado, M. A., 2007, Toolpath selection based on the minimum deflection cutting forces in the programming of complex surfaces milling, International Journal of Machine Tools and Manufacture 47, 2, 388-400

[49] Armarego, E. J. A., Brown, R.H. The Machining of Metals, Prentice-Hall, 1969.

[50] Budak, E., Altintas, Y., 1994, Peripheral Milling Conditions for Improved Dimensional Accuracy, International Journal of Machine Tools and Manufacture, 34 (7), 907-918.

[51] Tobias, S.A., Fiswick, W., 1958, Theory of Regenerative Machine Tool Chatter, The Engineer, London, 205

[52] Tlusty, J., Polacek, M., 1963, The Stability of Machine Tools Against Self Excited Vibrations in Machining, Int. Research in Production Engineering, ASME, 465-474.

[53] Minis, I., Yanushevsky, T., Tembo, R., Hocken, R., 1990, Analysis of Linear and Nonlinear Chatter in Milling, Annals of the CIRP, 39, 459-462.

[54] Budak, E., Altintas, Y., 1998, Analytical Prediction of Chatter Stability in Milling. Part I: General Formulation, Journal of dynamic systems, measurement, and control, 120, 22-30.

[55] Altintas, Y., Budak, E., 1995, Analytical Prediction of Stability Lobes in Milling, Annals of the CIRP, 44(1) 357-362.

[56] Budak, E., Altintas, Y., 1998, Analytical Prediction of Chatter Stability in Milling. Part II: Application of the General Formulation to Common Milling Systems, Transactions of ASME, 120 32-36.

[57] Davies, M. A., Pratt, J. R., Dutterer, B., Burns, T., J., 2002, Stability Prediction for Low Radial Immersion Milling, Journal of Manufacturing Science and Eng., 124, 217-225.

[58] Bayly, P. V, Halley, J. E. , Mann, B.P., Davies, M.A.,2003, Stability of Interrupted Cutting by Temporal Finite Element Analysis, Journal of Manufacturing Science and Engineering, 125, 220-225.

[59] Insperger, T., Stepan, G., 2004, Vibration Frequencies in High-Speed Milling Processes or a Positive Answer to Davies, Pratt, Dutterer and Burns, Journal of Manufacturing Science and Eng., 126, 481-487

[60] Gradisek, J., Kalveram, M., Insperger, T., Weinert, K., Stepan, G., Govekar, E., Grabec, I., 2005, On stability prediction for milling, International Journal of Machine Tools and Manufacture, 45, 769–781.

[61] Merdol, S., D., Altintas, Y., 2004, Multi Frequency Solution of Chatter Stability for Low Immersion Milling, Journal of Manufacturing Science and Engineering, 126 459-466.

[62] Altintas, Y., Shamoto, E., Lee, P., Budak, E., 1999, Analytical Prediction of Stability Lobes in Ball End Milling, Transactions of ASME, 121, 586-592.

[63] Altintas, Y., 2001, Analytical Prediction of Three Dimensional Chatter Stability in Milling, JSME Int Journal. Ser C. Mech Systems, Mach Elem Manuf, 44 (3) 717-723.

[64] Khachan, S., Ismail, F., 2009, Machining chatter simulation in multi-axis milling using graphical method, International Journal of Machine Tools and Manufacture, 49, 163-170.

[65] Shamoto, E., Akazawa, K., 2009, Analytical prediction of chatter stability in ball end milling with tool inclination, CIRP Annals - Manufacturing Technology, 58, 351-354.

[66] Smith, S., Tlusty, J., 1993, Efficient Simulation Programs for Chatter in Milling, Annals of the CIRP, 42(1), pp. 463–466.

[67] Li, H. Z., Li, X. P., Chen, X. Q., 2003, A Novel Chatter Stability Criterion for the Modeling and Simulation of the Dynamic Milling Process in the Time Domain, Int. J. Adv. Manuf. Technol., 22, pp. 619–625.

[68] Campomanes, M. L., Altintas, Y., 2003, An Improved Time Domain Simulation for Dynamic Milling at Small Radial Immersions, Trans. ASME Journal of Manufacturing Science and Engineering, 125, pp. 416–422.

[69] Sims, N. D., 2005, The Self-Excitation Damping Ratio: A Chatter Criterion for Time-Domain Milling Simulations, Trans. ASME Journal of Manufacturing Science and Engineering, 127, pp. 433-445.

[70] Ozturk, E., Budak, E., 2010, Dynamics and Stability of Five-axis Ball-end Milling, Journal of Manufacturing Science and Engineering, 132, 021003-1-13.

[71] Tlusty, J. and Ismail, F., 1981, Basic non-linearity in machining chatter, Annals of the CIRP. 30: 21-25.

[72] Moufki, A., Devillez, A. Segreti, M., Dudzinski, D., 2006, A semi-analytical model of non-linear vibrations in orthogonal cutting and experimental validation, Int. Journal of Machine Tools & Manufacture, 46, 436–449

[73] Chen, C. K., Tsao, Y. M., 2006, A stability analysis of turning a tailstock supported flexible workpiece, International Journal of Machine Tools & Manufacture, 46, 18-25.

[74] Vela-Martinez, L., Jauregui-Correaa, , J. C., Rubio-Cerda, E., Herrera-Ruiz, G., Lozano-Guzman, A. 2008, Analysis of compliance between the cutting tool and the workpiece on the stability of a turning process, International Journal of Machine Tools & Manufacture, 48,1054–1062

[75] Rao, B. C. , Shin, Y. C. , 1999, A comprehensive dynamic cutting force model for chatter prediction in turning, International Journal of Machine Tools & Manufacture, 39, 1631-1654

[76] Ozlu, E., Budak, E., 2007, Analytical Modeling of Chatter Stability in Turning and Boring Operations-Part I: Model Development J. Manuf. Sci. Eng. 129, 726.

[77] Ozlu, E., Budak, E., 2007, Comparison of one-dimensional and multi-dimensional models in stability analysis of turning operations, Int. Journal of Machine Tools & Manufacture, 47, 1875–1883.

[78] Lazoglu, I., Vogler, M., Kapoor, S.G., DeVor, R.E, 1998, Dynamics of the Simultaneous Turning Process, Transactions of the North American Manufacturing Research Conference, NAMRC XXVI, pp. 135-140

[79] Ozdoganlar, O. B., Endres, W. J., 1999, Parallel-Process (Simultaneous) Machining and Its Stability, presented at ASME IMECE'99, Nashville, TN, and in Proc., Symp. on Mach. Sci. and Tech., MED-10, 361-368.

[80] Olgac, N, Sipahi, R., 2005, A Unique Methodology for Chatter Stability Mapping in Simultaneous Machining, Journal of Manufacturing Science and Engineering, Vol. 127, pp. 791-800.

[81] Shamoto,E., Mori,T.,Nishimura, K., Hiramatsu, T., Kurata, Y. ,2010, Suppression of regenerative chatter vibration in simultaneous double-sided milling of flexible plates by speed difference, CIRP Annals - Manufacturing Technology, 59, 387–390

[82] Ozturk, E., Budak, E., 2010, Modeling Dynamics of Parallel Turning Operations, accepted for the Proceedings of the 4th CIRP International Conference on High Performance Cutting, 24-26 October 2010, Nagaragawa Convention Center, Gifu, Japan

[83] Ozturk, E., Budak, E., 2010, Modeling Dynamics of Parallel Milling Processes in Time-Domain, the Proceedings of the 2nd CIRP International Conference, Process Machine Interactions, 10-11 June 2010, The University of British Columbia, Vancouver, Canada.

[84] Altintaş, Y., Lee, P., 1996, A General Mechanics and Dynamics Model for Helical End Mills, CIRP Annals,45/1: 59-64.

[85] Elbestawi , M.A., Chen, L., Becze, C.E., El-Wardany, T.I.,1997, High-Speed Milling of Dies and Molds in Their Hardened State, CIRP Annals, 1: 57-62.

[86] Lia, X.P., Zhenga, H.Q., Wonga, Y.S., Neea, A.Y.C., 2000, An Approach to Theoretical Modeling and Simulation of Face Milling Forces , Journal of Manufacturing Processes, Vol. 2, Issue 4: 225-240

[87] Engin, S., Altintas, Y., 2001, Mechanics and Dynamics of General Milling Cutters, Part II: Inserted Cutters, International Journal of Machine Tools & Manufacture, 41: 2213–2231.

[88] Kim, S.J., Lee, H.U., Cho, D.,W., 2006, Feedrate Scheduling for Indexable End Milling Process Based on an Improved Cutting Force Model, International Journal of Machine Tools and Manufacture, 46,1589-1597.

[89] Lopez de Lacalle , L.N., Lamikiz, A. , Munoa, J., Salgado, M.A., Sanchez, J.A., 2006, Improving the High-Speed Finishing of Forming Tools for Advanced High-Strength Steels (AHSS),   International Journal of Advanced Manufacturing Technology, 29: 49-63.

[90] Campa, F.J., Lopez de Lacalle, L.N., Lamikiz, A., Sanchez, J.A., 2007, Selection of Cutting Conditions for a Stable Milling of Flexible Parts with Bull-Nose End Mills, Journal of Materials Processing Technology, 191: 279-282.

[91] Ozturk, E., Ozkirimli, O., Suren, G., Aksu, B., Budak, E., 2009, Increasing Productivity in Die Machining Through Process Modelling, Proceedings of the 5th International Conference and Exhibition on Design and Production of Machines and Dies/Molds, Kusadasi, Turkey.

[92] O. Ozsahin, H.N. Ozguven, E. Budak, 2009, Mass Loading Effect of Accelerometers on Tool Point FRF and Stability Diagrams, Proceedings of the 12th CIRP Conference on Modeling of Machining Operations, May 7-8 , San Sebastian, Spain.

[93] Cutpro: http://www.malinc.com

[94] Lin, C., Tu, J. F., Kamman, J., 2003, An Integrated Thermo-Mechanical-Dynamic Model to Characterize Motorized Machine Tool Spindles During Very High Speed Rotation, Int. Journal of Machine Tools and Manuf., 43,1035-1050.

[95] Press, W.H.,Teukolsky, S. A., Vetterling , W. T., Flannery, B. P., 2002, Numerical Recipes in C++: The Art of Scientific Computing, Cambridge Univ. Press.

[96] Mann, B.P., Insperger, T., Bayly P. V., Stepan G., 2003, Stability of Up-Milling and Down-Milling, Part 2: Experimental Verification, International Journal of Machine Tools and Manufacture, 43, pp. 35–40.

[97] Budak, E., 2006, Analytical models for high performance milling. Part I: Cutting forces, structural deformations and tolerance integrity, International Journal of Machine Tools & Manufacture 46 , pp. 1478–1488.

[98] Simulink, http://www.mathworks.com/products/simulink

[99] W. de Silva, C. , 2007, Vibration: Fundamentals and Practice, In: CRC Press Taylor & Francis Group, 2007

[100] Budak, E., Ozturk, E., Tunc, L., T., 2009, Modelling and Simulation of 5-Axis Milling Processes, Annals of CIRP, Manufacturing Technology, 58, 347-350.